

**BIOIMPEDANCE OF SOFT TISSUE UNDER  
COMPRESSION AND APPLICATIONS TO  
ELECTROSURGERY**

by

Robert Edward Dodde

A dissertation submitted in partial fulfillment  
of the requirements for the degree of  
Doctor of Philosophy  
(Biomedical Engineering)  
in The University of Michigan  
2011

Doctoral Committee:

Professor Albert J. Shih, Co-Chair  
Associate Professor Joseph L. Bull, Co-Chair  
Professor James D. Geiger  
Assistant Professor Eric Johnsen  
Research Investigator Grant H. Kruger

redieren

© 2011 Robert E. Dodde

## **Dedication**

This dissertation is dedicated to my family and our future together; to my beautiful wife Erica who has shown an incredible amount of strength and faith in myself and us, has sacrificed incredibly to see me through this, and whom I so longingly look forward to getting reacquainted with once this is completed, and to my children, Caden and Lawson, who have given me reasons to laugh when I wanted to cry and made me appreciate the simple things in life when it has seemed so complex.

I also dedicate this work to those who will not be able to celebrate the conclusion of this journey with me, but who have meant so much to me during it; my grandfather Egbert Dodde whose skill at machining inspired me to fabricate much of the hardware for my research, and my fellow Ph.D. candidate who will always be a philosophical doctorate to me, Alan Vincent.

## **Acknowledgements**

Research of this length and depth cannot happen without the help, guidance, and support of many people. It is with great appreciation and humility that I offer this work up for review.

I would like to thank first my advisor, Professor Albert Shih, for his willingness to take on a graduate student with no engineering background and no financial support. It was a leap of faith on both of our parts when we began working with each other as neither of us knew what would happen next. He has given me much freedom to pursue this research where it needed to go, even when he was not sure that the path I was on would bear fruit. With his help and guidance, I have not only been able to develop electrosurgical instrumentation designs, but have received a patent for this research. I have gained extensive experience writing grant proposals, and have even seen a few get accepted, which will undoubtedly serve me well as I pursue my future career.

I would also like to also thank my other committee members, Professor Joseph Bull, Dr. James Geiger, M.D., Dr. Grant Kruger, Ph.D., and Professor Eric Johnsen for their guidance and critiquing of this research as it progressed. I appreciate their support and advice throughout this entire process.

Professor Joseph Bull has been incredibly supportive of me as a student and future researcher. He has always been there to listen and offer advice regardless of the topic of discussion. It is difficult to feel supported working in a traditional manufacturing research lab performing biomedical research. Prof. Bull and his lab have adopted me as one of their own which has been greatly appreciated. With him I have also completed research not included in this dissertation on the splitting of bubble through a bifurcating network of channels. To a student such as myself not having an engineering background, this additional experience is invaluable to me in my future career pursuits and has given me confidence in my ability as an engineer.

Dr. James Geiger, M.D., has been an incredible advocate not only for my research but for me as an individual. His willingness to work with engineering students on a student project to measure tissue temperature during electrosurgery is what allowed Prof. Shih and I to begin working together. He has been an invaluable resource in relating my research to clinical needs. He has also been a great resource for hardware needed to perform my experiments. Much of the work presented here would not have been completed without him.

Dr. Grant Kruger, Ph.D., has proven to be a great blessing to my research. At a point when the circuitry seemed to be incomprehensible to me and I was near the end of my patience with this research, Dr. Kruger was there to offer the needed encouragement and insight I needed to complete the bioimpedance measurement circuitry. I am also grateful for the additional work I have been able to perform in developing other circuits and printed circuit boards for ultrasound and pain testing applications. This broadened scope of electrical work has given me the confidence in my abilities to make and produce my own circuits.

A special thanks goes out to Professor Eric Johnsen, who made himself available to serve as my committee cognate on short notice. His willingness to sit and listen to me go over my defense is much appreciated. Additionally, his critical insights into how the tissue compression research may be applicable to other areas of much different time and length scales has opened my mind to the potential impact that this research may have in the future.

This thesis would also not have been possible without the help of many people from across the University. First, I would like to give my deepest thanks to Toby Donajkowski. His willingness to educate and work with me on machining was instrumental in allowing me to fabricate the components necessary for my research. He never let me settle for a second rate job on machining a part, even if it was only a block of aluminum to space parts with. Toby has made me very proud of the work I have done and continues to be a great example to me of what it means to be a man, husband, and father.

Two University physicians, Dr. William Roberts and Dr. Arnold Advincula, have also been invaluable to my work. From access to tissue, help in animal labs, and

conversations about surgical needs, Will is a greatly appreciated resource. Arnie, despite his busy schedule, has always been such a great cheerleader and together we have done some great work, including much of the research presented in Chapters 2 and 4. He has given me access to venture capitalists interested in my research and, despite having left the University to pursue his career in Florida, continues to support my work.

Professor Kevin Pipe served on both my Master's Thesis and Preliminary Exam committees and unfortunately was not available to participate in the Dissertation Defense. However, he has always been available with his critical insight into my research at multiple points along the way. With his keen engineering and analytical mind, knowledge of both thermal and electrical processes, and desire to see my research be all that it can be, he routinely could be counted on to give critical insights to the problems I ran into with my research and the analysis of the data I collected.

Professor William (Rick) Weitzel has been an incredible support and has offered much insight into areas bioimpedance may have clinical relevance that I had not even thought of prior to meeting him. We have had a great symbiotic relationship where I have been able to grow and strengthen my interest in electronics and circuits as well as become acquainted with ultrasound technologies. His innovative mindset is refreshing and inspiring.

Scott Merz has also been a great example to me of what it means to be a biomedical engineer. His intellect and insight into the clinical relevance of experimental research has been instrumental in how I think about the future potential of my research. We have worked on a few proposals attempting to elevate my electrosurgical and bioimpedance research into the clinical space and I have enjoyed the education I have received in reshaping how I think and present my research to different groups of people.

I would like to thank Gail Rising, Sandy Holmes, and Kimberly Ives for their help in running animal labs and getting me access to tissue, especially at those times when I desperately needed it, they were there to support me with their skills and time.

I must give thanks to my fellow lab mates, and a special thanks to Matthew Chastagner, my ally and friend for many of the years of my research. His decision to join me in looking at the effects of tissue compression gave me much needed support in

making my way through this research. When things were the worst, we were there for each other to give support, advice, and a listening ear. I would like to thank Jacob Gee, Roland Chen, and Scott Miller for their help with conducting the experiments within this thesis. Lastly, I would like to thank Carl McGill and Jason Moore for their support and encouragement.

Finally, I owe my largest thank you to my family, for their encouragement and patience throughout this process. It has not been easy and I know it would not have been possible without my loving wife. I entered into this research married to a incredible woman and find myself, as my Ph.D. research wrapped up, with two adorable children who mean everything to me. Erica has sacrificed her career as a social worker to raise our children and support our family, and for that I am endlessly appreciative. Thank you from the bottom of my heart for your encouragement and love; I will love you always. To my parents, who have always been so proud of me, thank you not only for the encouragement, but for everything you have given me over the years. I owe much of what I have become to you. To the rest of my family, some of whom I have not even seen in many years, I love you all and look forward to seeing you again soon.



## Table of Contents

|  |              |
|--|--------------|
| <b>Dedication</b> .....  | <b>ii</b>    |
| <b>Acknowledgements</b> .....  | <b>iii</b>   |
| <b>List of Figures</b> .....   | <b>x</b>     |
| <b>List of Tables</b> .....  | <b>xvii</b>  |
| <b>List of Appendices</b> .....  | <b>xviii</b> |
| <b>Abstract</b> .....  | <b>xix</b>   |
| <b>Chapter 1 Introduction</b> .....  | <b>1</b>     |
| 1.1 Motivation.....  | 1            |
| 1.2 Literature Review.....   | 3            |
| 1.2.1 Review of Electrosurgery and Thermal Spread Monitoring .....                   | 3            |
| 1.2.2 Review of Electrosurgical Modeling.....  | 6            |
| 1.2.3 Review of Thermal Management in Electrosurgical Applications .....             | 6            |
| 1.2.4 Review of Tissue Electrical Characterization .....                             | 7            |
| 1.2.5 Review of Tissue Mechanical Property Modeling .....                            | 11           |
| 1.1. Research Objectives and Tasks.....  | 12           |
| 1.2. Outline.....  | 13           |
| <b>Chapter 2 Thermal Profiling of the Energy-Based Surgical Procedure</b> .....      | <b>15</b>    |
| 2.1 Introduction.....  | 15           |
| 2.2 Materials and Methods.....   | 16           |
| 2.3 Results.....   | 20           |
| 2.4 Discussion .....   | 21           |
| 2.5 Conclusion .....   | 22           |
| <b>Chapter 3 Finite Element Model of the Bipolar Electrosurgical Procedure</b> ..... | <b>24</b>    |
| 3.1 Introduction.....  | 24           |
| 3.2 Experimental Setup for In-Vivo Electrosurgical Temperature<br>Measurement.....   | 27           |
| 3.3 Finite Element Modeling .....  | 29           |
| 3.3.1 Thermal-Electric FEM Formulation.....  | 29           |

|   |  |           |
|---|--|-----------|
| 3.3.2   | Properties of Biological Tissue .....  | 31        |
| 3.3.3   | FEM Techniques .....   | 32        |
| 3.3.4   | Electrode Design .....   | 34        |
| 3.3.5   | Boundary Conditions.....   | 35        |
| 3.3.6   | FEM Electrical Input.....  | 37        |
| 3.4   | Experimental and FEM Results .....   | 37        |
| 3.4.1   | Experimental Validation and Effect of Compression.....                           | 37        |
| 3.4.2   | Effect of Temperature-Dependent Electrical and Thermal<br>Conductivities.....    | 40        |
| 3.5   | Discussion of FEM Results.....   | 41        |
| 3.5.1   | Temporal and Spatial Temperature Distributions .....                             | 41        |
| 3.5.2   | Effect of Compression on Temporal and Spatial Temperature<br>Distributions ..... | 42        |
| 3.6   | Conclusions.....   | 44        |
| <br>  |  |           |
| <b>Chapter 4 Bipolar Electrosurgery Using Active Cooling Channels for the<br/>Minimization of Thermal Spread .....</b>        |  | <b>47</b> |
| 4.1   | Introduction.....  | 47        |
| 4.2   | Materials and Methods.....   | 48        |
| 4.2.1   | Spleen Coagulation.....  | 51        |
| 4.2.2   | Mesenteric Vessel Sealing.....   | 52        |
| 4.3   | Results.....   | 52        |
| 4.4   | Discussion.....  | 57        |
| 4.5   | Conclusions.....   | 59        |
| <br>  |  |           |
| <b>Chapter 5 Development and Validation of a Bioimpedance Measurement<br/>System Using a New Constant Current Source.....</b> |  | <b>60</b> |
| 5.1   | Introduction.....  | 60        |
| 5.2   | Equivalent Circuit Analog for Soft Tissue.....                                   | 61        |
| 5.2.1   | Complex and Polar Impedance Representations .....                                | 62        |
| 5.2.2   | Depressed loci .....   | 63        |
| 5.3   | Bioimpedance Measurement Circuit.....  | 64        |
| 5.3.1   | Voltage-Controlled Current Source Circuitry .....                                | 67        |
| 5.3.2   | Current-to-Voltage Converter Circuitry .....                                     | 68        |
| 5.3.3   | Buffered Differential Voltage Measurement Circuitry .....                        | 69        |
| 5.3.4   | PCB Layout .....   | 71        |
| 5.4   | Bioimpedance Measurement Circuit Validation.....                                 | 72        |
| 5.4.1   | Current-to-Voltage Circuit Characterization.....                                 | 72        |
| 5.4.2   | Voltage-Controlled Current Source Characterization .....                         | 73        |
| 5.4.3   | Buffered Differential Voltage Measurement Characterization .....                 | 74        |
| 5.5   | Bioimpedance Probe .....   | 77        |
| 5.6   | Bioimpedance Probe Characterization.....   | 78        |
| 5.7   | Hook Effect.....   | 81        |

|  |  |            |
|--|--|------------|
| 5.8  | Experimental Methodology .....               | 82         |
| 5.9  | Results.....                                 | 84         |
| 5.10   | Discussion.....                              | 86         |
| 5.11   | Conclusions.....                             | 87         |
| <b>Chapter 6 Bioimpedance of Porcine Spleen under Compression.....</b> |  | <b>88</b>  |
| 6.1  | Introduction.....                            | 88         |
| 6.2  | Experimental Set-up and Procedure.....       | 89         |
| 6.2.1  | Characterization of the Tissue Chamber ..... | 90         |
| 6.2.2  | Experimental Procedure .....                 | 93         |
| 6.2.3  | Experimental Calibration .....               | 94         |
| 6.2.4  | Non-linear Least Squares Fitting.....        | 96         |
| 6.3  | Results.....                                 | 97         |
| 6.3.1  | Bioimpedance Measurements.....               | 98         |
| 6.3.2  | Pressure Measurements .....                  | 100        |
| 6.3.3  | Histology .....                              | 100        |
| 6.4  | Discussions .....                            | 103        |
| 6.5  | Conclusions.....                             | 105        |
| <b>Chapter 7 Conclusions.....</b>                                      |  | <b>107</b> |
| 7.1  | Major Achievements.....                      | 107        |
| 7.2  | Original Contributions .....                 | 110        |
| 7.3  | Future Work.....                             | 111        |
| <b>Appendices .....</b>  |  | <b>115</b> |
| <b>References .....</b>  |  | <b>136</b> |

## List of Figures

|   |    |
|---|----|
| Figure 1.1. Representation of tissue under compression during electrosurgery. ....  | 3  |
| Figure 1.2. Frequency-dependance of polarization resistance ( $R_p$ ) and capacitance ( $C_p$ ) for a 1.4 mm <sup>2</sup> platinum electrode. ....  | 8  |
| Figure 1.3. Summary of complex plane and frequency for bioimpedance. ....   | 10 |
| Figure 2.1. (a) Photograph of exteriorized porcine spleen and (b) in situ temperature acquisition set-up. ....  | 15 |
| Figure 2.2. Photograph of top and front views of actual polycarbonate fixtures used for positioning of both the instrument jaws and the thermistors. ....   | 16 |
| Figure 2.3. Computer Aided Design (CAD) drawing of polycarbonate fixtures displaying distances of thermistors from instrument jaw edge. ....  | 17 |
| Figure 2.4. Schematic diagram of the temperature acquisition system used. The signal conditioner consists of a Wheatstone bridge powered by 10V, with $R_1=R_2=R_3=10k\Omega$ . ....  | 19 |
| Figure 2.5. (a) Post-operative spleen from 5 mm Gyrus Plasmakinetic Cutting Forceps and (b) post-operative spleen from Ethicon Harmonic Ace. ....   | 20 |
| Figure 2.6. Thermal Profiles for each of the energized instrument trials performed. (a) Gyrus 5mm Cutting Forceps, (b) Ethicon Harmonic Ace – ‘Min 3’ setting for 5 s, (c) Ethicon Harmonic Ace – ‘Min 3’ setting until tissue transaction, and (d) Ethicon Harmonic Ace – ‘Min 3’ setting for 5 s followed by ‘Max 5’ setting until tissue transaction. .... | 21 |
| Figure 3.1. The Gyrus ACMI 5 mm bipolar cutting forceps. Note the end of the device is magnified to show electrode detail. ....   | 26 |
| Figure 3.2. Experimental set-up showing positioning of tissue, electrode, and thermistors. ....   | 27 |
| Figure 3.3. Voltage input for FEM (a) measured alternating current (AC) voltage signal and close up view of the 350 kHz waveform and (b) resultant direct current (DC) approximation of the waveform equivalent to the root-mean-square (RMS) value of the RF signal. ....  | 29 |
| Figure 3.4. Schematic of the 3D FEM model showing (a) the tissue, electrodes, and symmetry plane defined by points EACG , (b) a representative mesh case, (c) top view of tissue regions identified for the compression-dependent regions (I, II and III) and thermistor. ....  | 32 |

|  |    |
|--|----|
| Figure 3.5. Two electrodes: (a) Flat electrode (FE), (b) Grooved electrode (GE) in Gyrus ACMI bipolar instrument used in the experiment, and (c) dimensions of the cross-section for GE. ....  | 34 |
| Figure 3.6. FEM of the effect of temperature-dependent $\sigma$ and $k$ on tissue temperature. $k_{Tref}$ and $k(T)$ are constant and temperature-dependent thermal conductivity, respectively. $\sigma_{Tref}$ and $\sigma(T)$ are constant and temperature-dependent electrical conductivity, respectively. ....   | 36 |
| Figure 3.7. Comparison of thermal profiles for in-vivo experiments and FEM using a GE under a constant thermal conductivity, temperature-dependent electrical conductivity, and (a) compression-independent and (b) compression-dependent simulation. ....   | 38 |
| Figure 3.8. Cross-sectional view of temperature profiles on a plane offset from plane ABDC by 6 mm at different times for a constant thermal conductivity, temperature-dependent electrical conductivity, and compression-independent simulation using a GE. Times (a)-(e) correlate to the end of each pulse and (f) correlates to the end of the simulation after sufficient cooling. .... | 39 |
| Figure 3.9. Cross-sectional view of temperature profiles at 3.22 s on different planes offset from plane ABFE for a constant thermal conductivity, temperature-dependent electrical conductivity, and compression-independent simulation using a GE (distances indicating the offset from Plane ABFE) (same temperature scale as in Figure 3.8). ....  | 40 |
| Figure 3.10. Cross-sectional view of temperature profiles for a constant thermal conductivity, temperature- and compression-dependent electrical conductivity simulation using a GE on a plane offset from plane ABDC by 6 mm at various times. Times (a)-(e) correlate to the end of each pulse and (f) correlates to the end of the simulation after sufficient cooling. ....              | 41 |
| Figure 3.11. Cross-sectional view of temperature profiles at 3.22 s for a constant thermal conductivity, temperature- and compression-dependent electrical simulation using a GE on different planes offset from plane ABFE (distances indicating the offset from Plane ABFE) (same temperature scale as in Figure 3.10). ....   | 42 |
| Figure 3.12. Effect of grooved electrode (GE) and flat electrode (FE) on temperature profiles. ....  | 44 |
| Figure 4.1. Images of the electrodes for the (a) Gyrus 5mm Forceps (standard bipolar forceps) with thermistor fixture and (b) the modified Gyrus 5mm Forceps (actively cooled bipolar forceps) incorporating an active cooling channel around the outside of the bipolar electrodes with thermistor fixture attached. ....   | 48 |
| Figure 4.2. Schematics for the two devices used in this experiment. (a) Standard bipolar forceps and a top view showing thermistor fixture and position of the thermistors. (b) Actively cooled bipolar forceps incorporating cooling  |    |

|   |    |
|---|----|
| channels around both bipolar electrodes and top view showing thermistor fixture and position of the thermistors.....  | 49 |
| Figure 4.3. Schematic diagram of data acquisition system for electrical and temperature data recording. The experimental components, including the electrosurgical system and tissue, are shown within the dashed rectangle. Thermistors were inserted into the tissue to record temperature measurements while the current and voltage probes were connected to the leads of the electrosurgical devices to record electrical measurements. Data was brought into the computer via a NI PXI-6221 Data Acquisition Card and an Agilent 54833A Oscilloscope. ....  | 50 |
| Figure 4.4. Experimental set-up for coagulation experiments using (a) the unmodified Gyrus 5mm Forceps and (b) the modified Forceps incorporating an active cooling channel around the bipolar electrodes. ....   | 52 |
| Figure 4.5. Typical thermal and electrical profiles for coagulation studies on splenic tissue using the standard bipolar forceps and the actively cooled forceps with a cooling channel around the bipolar electrodes. (a) Standard bipolar forceps. Midline temperature reached 90% of maximum value in 2.5 s. Average power for first 2 pulses was 125 W and dropped down to 40 W by the 5th and 6th pulses (indicative of the VP3 40 setting). Impedance averaged 450 $\Omega$ over the 4th-6th pulses. (b) Actively cooled forceps. Midline temperature reached 90% of maximum value in 2.5 s. Average power for first 4 pulses was 140 W and dropped down to 85 W for the 6th-8th pulses. Impedance remained lower than 50 $\Omega$ for the first 4 pulses and averaged 200 $\Omega$ over the 6th-8th pulses.....  | 54 |
| Figure 4.6. Typical thermal and electrical profiles for coagulation studies on mesenteric tissue using the standard bipolar forceps and the actively cooled forceps with a cooling channel surrounding the bipolar electrodes. (a) Standard bipolar forceps. Midline temperature reached 90% of maximum value in 4 s. Average power for first 3 pulses was 135 W and dropped down to 30 W by the 7th and 8th pulses (indicative of the VP1 30 setting). Impedance slowly rose to ~240 $\Omega$ in the later pulses. The steeper temperature drop-off at the 1.0 mm point once power input stopped indicates maximum temperatures were reached not in the midline but outside the profile of the forceps. Temperature data not available for the 3.5 mm distance. (b) Actively cooled forceps. Midline temperature reached 90% of maximum value in 7 s. Average power for first 8 pulses was 110 W while impedance never reached more than 40 $\Omega$ ..... | 55 |
| Figure 4.7. Summary of thermal and temporal development for coagulation experiments on splenic (a) and mesenteric (b) tissues. (a) SPLN data comes from experiments using standard bipolar forceps while the SPLC data comes from experiments with the actively cooled forceps. Midline temperatures were seen to increase by a statistically significant larger amount (p-value = 0.009) with the actively cooled forceps as compared to the standard bipolar forceps while temperatures taken adjacent to the actively cooled forceps   |    |

increased less than 2°C. Adjacent points to the standard bipolar forceps saw temperature changes slowly decline from 30°C at 1.0 mm to 4°C at 3.5 mm. (b) MESN data comes from experiments using standard bipolar forceps while the MESC data comes from experiments with the actively cooled forceps. Midline temperatures were seen to increase slightly more in the cooled case as compared to the standard case while temperatures taken adjacent to the cooled device rose minimally. Adjacent points to the standard bipolar forceps saw temperature changes slowly decline from 40°C at 1.0 mm to 10°C at 3.0 mm (data not available for 3.5 mm distance). .....56

Figure 4.8. Detailed summary of thermal development during each pulse for coagulation experiments on splenic (a) and mesenteric (b) tissues. (a) SPLN data comes from experiments using normal 5 mm forceps while the SPLC data comes from experiments with the custom adjacent cooling channels. Midline temperatures were seen to increase significantly more during each pulse in the cooled case as compared to the standard case while temperatures taken adjacent to the cooled device rose minimally. Adjacent points to the normal device saw temperature changes increase even more at the 1.0 mm location compared to the midline temperatures during the first pulse. More distant locations saw similar slowly declining slopes for temperature increases during each pulse through 1.5 mm. Points at 3.0 mm and 3.5 mm saw greater temperature increases at later pulses due to conductive heating. (b) MESN data comes from experiments using normal 5 mm forceps while the MESC data comes from experiments with the custom adjacent cooling channels. Midline temperatures were seen to increase at nearly equal rates, although the standard device heated up quicker during the beginning pulses and the modified device heated up more quickly during the later pulses. However, hardly any temperature increase was seen at points adjacent to the cooled device while similar, shifted temperature profiles were seen for the standard device at distances adjacent to the tool edge.....58

Figure 5.1. Overview of how alternating current passes through cellular tissue. ....60

Figure 5.2. Schematic of tissue as an equivalent circuit analog.  $R_{ext}$  is the resistance of the extracellular fluid,  $R_{int}$  is the resistance of the intracellular fluid,  $C_m$  is the bulk capacitance of the cellular membranes, and  $R_m$  is the bulk resistance of the cellular membranes. ....61

Figure 5.3. (a) Overview of polar and complex representations of data (b) equivalent circuit diagram for tissue.....62

Figure 5.4. Example of depressed loci in the complex plane.  $R$  represents resistance and  $X$  represents reactance.....63

Figure 5.5. Schematic overview of bioimpedance circuitry. Circuit components are located within the dashed box.  $I_{OUT}$ ,  $V1$ ,  $V2$ , and  $I_{IN}$  connect to the probe and then to the tissue.  $VS$  is the signal source from the function generator.  $V(V)$  is the voltage signal proportional to the voltage difference between  $V1$  and  $V2$ .  $V(I)$  is a voltage signal proportional to the current

|   |    |
|---|----|
| injected into the tissue. $V(V)$ and $V(I)$ connect to an oscilloscope for measurement. ....  | 66 |
| Figure 5.6. Circuit schematic for (a) the voltage-controlled current source (VCCS) used to drive the tissue load and (b) the current-to-voltage converter (C2V) used to monitor the input current from the VCCS.....  | 69 |
| Figure 5.7. Detailed schematic of the buffered voltage differentiator circuit. ....   | 70 |
| Figure 5.8. (a) Top side view of the bioimpedance measurement PCB. And (b) bioimpedance measurement PCB encased in housing unit.....  | 71 |
| Figure 5.9. Characterization of the C2V subcircuit for the bioimpedance measurement circuit. (a) Measured current for various input voltages and (b) deviation of phase shift from expected value of $180^\circ$ . The black lines in (b) represent one degree of phase shift. ....   | 72 |
| Figure 5.10. Characterization of the VCCS subcircuit for various targeted output currents.....  | 74 |
| Figure 5.11. Bandwidth details for the differential voltage amplifier circuit with a gain of 20 in (a) dB and (b) phase shift. ....   | 75 |
| Figure 5.12. Cole-Cole plots for $R=1\text{ k}\Omega$ (red), $R=2\text{ k}\Omega$ (blue). (a) $C = 100\text{ pF}$ (102.2 pF measured) (b) $C = 1\text{ nF}$ (1.04 nF measured) (c) $C = 45\text{ nF}$ (44.4 nF measured) (d) $C = 100\text{ nF}$ (98 nF measured).....  | 76 |
| Figure 5.13. (a) Bioimpedance probe and (b) exploded view of the probe. ....  | 77 |
| Figure 5.14. Estimated contact impedances based on Schwan data [39] assuming a $0.05\text{ mm}^2$ platinum electrode. Total contact impedance for the circuit would be double.....  | 78 |
| Figure 5.15. Experimental ( $ Z _{exp}$ ) vs theoretical ( $ Z _{theo}$ ) impedance values for NaCl solutions. ....   | 80 |
| Figure 5.16. Experimental Set-up (a) and process flow diagram and (b) for bioimpedance measurements. ....   | 83 |
| Figure 5.17. (a) Raw (raw), corrected ( $I_A$ and $I_{AC_p}$ ), and fitted data ( $Z_{fit}$ ) for one example bioimpedance measurement on porcine spleen tissue and (b) Comparison of electrical conductivity ( $\sigma$ ) and electrical permittivity ( $\epsilon$ ) experimental results for porcine spleen with the literature (note literature based on a range of animal spleen values at various temperature ranges)..... | 85 |
| Figure 6.1. Experimental set-up for tissue compression experiments.....   | 89 |
| Figure 6.2. (a) Measured $ Z $ versus frequency for various depths above the bottom of the tissue chamber and (b) Average current at each frequency point for given saline concentrations. ....   | 90 |
| Figure 6.3. Effect of insertion depth ( $h$ ) on $ Z $ . (a) At higher frequencies, effect is seen to be concentration dependent, but for frequencies below 100kHz, the effect is constant. (b) Average normalized impedance vs. insertion depth for  |    |



|   |     |
|---|-----|
| 0.01, 0.02, 0.05, and 0.125% saline concentrations (frequency range of readings is from 100Hz – 100kHz).....  | 91  |
| Figure 6.4. Impact of probe insertion depth (h) on the measured phase angle. (a) For high frequencies, impact is concentration dependent. (b) For the frequency range 100 Hz – 100 kHz, the average phase shift is seen to be less than one degree regardless of insertion depth.....   | 92  |
| Figure 6.5. Dielectric properties for saline solutions versus frequency. (a) electrical permittivity ( $\epsilon$ ) and (b) electrical conductivity ( $\sigma$ ).....   | 93  |
| Figure 6.6. Decision and process flowchart for compression of spleen tissue.....  | 94  |
| Figure 6.7. Progression of data from the initial collection to the final fitting to the Cole-Cole model. Raw data (Raw), data after calibrating for voltage differentiator (IA), data after further correcting for depth effect (IAd), after next correcting for the Hook Effect (IAdC <sub>p</sub> ), and the final fitted data (Z <sub>fit</sub> ). Data was collected at a height (h) of 6.20 mm. ....                                     | 96  |
| Figure 6.8. Final summary of strain-dependent Cole-Cole terms. (a) Normalized $R_{ext}$ and $R_{int}$ as a function of compressive ratio, (b) normalized $C_{mem}$ as a function of compressive ratio, and (c) normalized $\alpha$ as a function of compressive ratio. ....   | 97  |
| Figure 6.9. Mean and standard deviation (error bars) of the RMSE for data fitting to a Cole-Cole model for eight samples over 0-80% compression.....  | 98  |
| Figure 6.10. Overview of the development of the impedance loci during tissue compression. Note the shift of the loci to the right for lower compression levels and then a dramatic shift to the left and collapse of the loci at higher compression levels. ....  | 99  |
| Figure 6.11. Plot of pressure ( $\sigma$ ) versus time (s) for strain measurements. Each ramp up of pressure and subsequent relaxation is for an incremental increase in strain of 10%. X-axis is in time (s), with the length of the last relaxation for 80% compression being 120 s.....  | 100 |
| Figure 6.12. Histology at 10X magnification for (a) 80% tissue compression and (b) control. ....  | 101 |
| Figure 6.13. Histology at 40X magnification for (a) 80% tissue compression and (b) control. ....  | 102 |
| Figure 6.14. Plot showing the strain dependence of the resistance at 500 kHz. Compression is defined as $\frac{h_m - h_i}{h_i}$ where $h_m$ is the measured tissue thickness and $h_i$ is the initial tissue thickness. This is a common frequency used in electrosurgical instrumentation where large strains are commonly imposed on tissue. From 50-80% compression there is seen to be a 31% change in the resistance of the tissue. .... | 104 |
| Figure A.1. Load curves for each of the VPC modes within the Gyrus PlasmaKinetic® Generator. ....   | 117 |

|  |     |
|--|-----|
| Figure B.1. (a) Overview of polar and complex representations of data and (b) equivalent circuit analog for tissue. ....   | 118 |
| Figure B.2. Graphical view of transformations required to represent complex data in the impedance, $Z^*$ , admittance, $Y^*$ , modulus, $M^*$ , and capacitance, $C^*$ , planes. ....                        | 119 |
| Figure C.1. Block diagram of the Labview program. The numbered rounded rectangles indicate (1) while loop, (2) case structure, (3) shift register, (4) cluster, (5) array, and (6) enumerated text box. .... | 125 |
| Figure C.2. Detailed view of (a) the enumerated text box showing all of the states within the program and (b) the cluster containing all of the different data type variables used in the program. ....      | 126 |
| Figure C.3. Front panel of the bioimpedance Labview program. ....  | 127 |
| Figure D.1. Full schematic for bioimpedance measurement circuit. DC bypass coupling, BNC connections, and offset voltage potentiometers are shown along with power supply lines for clarification. ....      | 129 |
| Figure D.2. (a) Eagle board layout of bioimpedance measurement circuit (b) bottom view of final PCB board (c) top view of final PCB board. ....  | 130 |
| Figure D.3. AMP03 datasheet. ....  | 131 |
| Figure D.4. AD711 datasheet. ....  | 132 |
| Figure D.5. AD8065 datasheet. ....   | 133 |
| Figure D.6. INA111 datasheet. ....   | 134 |
| Figure D.7. LM7171 datasheet. ....   | 135 |

## **List of Tables**

|  |     |
|--|-----|
| Table 2.1. Comparison of Two Energized Surgical Instruments.....   | 18  |
| Table 2.2. Comparison of mean peak temperatures, standard deviations, and procedural times for the 5 mm Gyrus Cutting Forceps and Ethicon Harmonic Ace ..... | 22  |
| Table 3.1. Properties used in the FEM.....   | 31  |
| Table 3.2. FEM boundary conditions as marked in Figure 3.4.....  | 35  |
| Table 5.1. Summary of bioimpedance probe calibration data .....  | 81  |
| Table A.1. Summary of VPC modes within the Gyrus PlasmaKinetic <sup>®</sup> Generator. ....  | 116 |

## **List of Appendices**

|  |     |
|--|-----|
| <b>Appendix A</b> Gyrus PlasmaKinetic <sup>®</sup> Surgical Generator Overview ..... | 116 |
| <b>Appendix B</b> Cartesian and Polar Bioimpedance Representations .....             | 118 |
| <b>Appendix C</b> Bioimpedance Labview Program .....                                 | 122 |
| <b>Appendix D</b> Bioimpedance Measurement Circuit Details.....                      | 128 |

## **Abstract**

This research studies the impact of compression on the electrical impedance of soft tissue. Soft tissue compression occurs in many ways, either physiologically or through forces imposed by the outside world. While much work has been done in characterizing the electrical properties of soft tissues, little work has been done in correlating the compression of tissue to the subsequent changes in the electrical properties. This lack of knowledge has led to the use of less than ideal instrumentation within electrosurgery resulting in unnecessary quality of life reduction in patients post-operatively.

This research aims to quantify the impact of compression on the bioimpedance of tissue. First, a baseline for understanding thermal spread is developed by documenting the thermal history of tissue during energized surgical procedures. Then, a finite element model of the bipolar electrosurgical procedure is performed and analyzed to suggest various mechanisms that can be at play during this procedure that affect the resulting thermal profile. Next, a new instrument design is developed and tested based on these findings to eliminate thermal spread. To perform more detailed research on electrical impedance changes in compressed tissue, a bioimpedance measurement system is then developed and validated. Finally, basic tissue compression tests are performed where mechanical and electrical properties of the tissue are monitored during the tissue compression. These findings are finally correlated to suggest a mechanism for the process of tissue compression.

# Chapter 1 Introduction

## 1.1 Motivation

Over the last two decades dramatic advances in surgery have allowed increasingly complex operations to be completed using minimally invasive surgery (MIS). MIS is accomplished by passing laparoscopic ports through very small incisions. Specialized instruments are passed through the ports to complete the operation. A number of potential advantages are thus offered including reduced pain, scarring, and convalescence periods. Advancements in energy-based dissection and vessel sealing (ligation) devices have been critical to broadening the MIS applications. These energy-based surgical devices (EBSD) use a variety of energy sources (electrical, radiofrequency, ultrasonic, and laser) to provide effective and rapid hemostasis and are approved for ligating blood vessels up to 7 mm in diameter [1]. Use of EBSDs has allowed successful dissection of very vascular organs such as the prostate, liver and uterus. They are now adapted for nearly all types of surgery including neurosurgery, orthopedics, gynecology, urology, general surgery, plastic surgery, and otolaryngology. While originally developed for laparoscopic surgery, EBSDs are now used in open surgery where they are replacing traditional suture ligation of blood vessels. EBSD success has been tempered somewhat by recognition of possible collateral tissue damage due to thermal or electrical spread from the instrument tip.

These EBSDs are used in thousands of operations yearly and complications associated with them are thus magnified. Annually 600,000 hysterectomies and 220,000 prostatectomies (29,000 deaths) are performed and they are the second most widely performed surgeries among respective genders [2]. These patients are also younger and healthier than those diagnosed in the past. Side effects from these procedures include urinary incontinence (UI) in males and females and erectile dysfunction (ED) in males. A study performed by Brown et al. [3] suggests the extent of uterine removal, and thus increased potential for neurovascular bundle (NVB) damage, is correlated to risk of UI. A

technique to spare NVBs around the prostate has been developed. Widespread adoption of this technique (meticulous dissections and preservation of the neurovascular bundles without use of electrosurgical devices) has resulted in improved post-operative potency rates of 68% to 86% at centers of excellence [4, 5]. Within the last ten years, advanced laparoscopic and robotic techniques have been applied to these procedures, including laparoscopic radical prostatectomy (LRP). Although long-term data are not yet available, results with respect to biochemical progression free survival and continence appear equivalent to open techniques. However, a great variability is still seen in postoperative potency rates [6]. The majority of published techniques of laparoscopic prostatectomy rely on bipolar, monopolar, or ultrasonic energy sources for hemostasis. Successful preservation of potency has recently been reported from centers specializing in LRP with results ranging from 23% to 82%. This wide variability is likely multifactorial but may be in part due to the method of nerve dissection and use of hemostatic energy sources. Additionally, it has been demonstrated by Ong et al. in a canine model that dissection utilizing any EBSD can result in NVB damage and poor post-operative potency outcomes due to large thermal spread [7].

It has been suggested that one of the primary reasons for these complications is due to the excessive thermal energy developed in the region during energized surgical procedures [8]. Considering the high compression levels (>60%) used during these procedures, complex mechanical changes occur which are hypothesized to also impact other tissue characteristics such as fluid distribution and the electrical conductivity of the tissue.

This research aims to quantify the impact of high compression on the electrical properties of tissue. First, a baseline for understanding thermal spread is developed by documenting the thermal history of tissue during energized surgical procedures. Then, a finite element model of the bipolar electrosurgical procedure is performed and analyzed to suggest various mechanisms that can be at play during this procedure that affect the resulting thermal profile. Next, a new instrument design is developed and tested based on these findings to eliminate thermal spread. To perform more detailed research on electrical impedance changes in compressed tissue, a bioimpedance measurement system is then developed and validated. Finally, basic tissue compression tests are performed

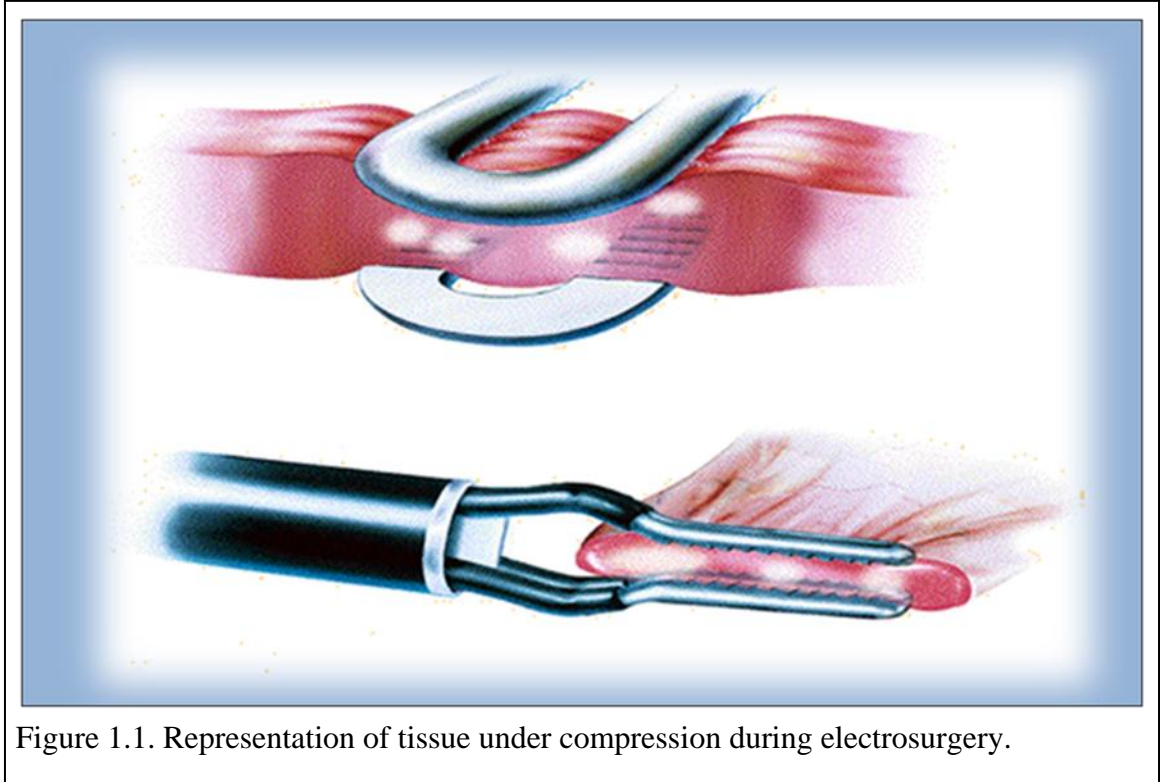


Figure 1.1. Representation of tissue under compression during electrosurgery.

where mechanical and electrical properties of the tissue are monitored during the tissue compression. These findings are correlated at the end to suggest a mechanism for the process of tissue compression.

## 1.2 Literature Review

### 1.2.1 *Review of Electrosurgery and Thermal Spread Monitoring*

Collateral thermal damage, or thermal spread, from energized surgical instruments has been shown to vary widely by the instruments being used, the modality being used, the environment they are being used in, and the tissue they are being used on.

It has been well documented that tissue damage occurs thermally through an Arrhenius-type dependence on temperature and time [9]. The longer tissue is held at a certain temperature above a threshold, the greater amount of damage occurs, and the amount of time a tissue can withstand a temperature decreases rapidly with increasing temperature. Industry standards take 43°C as the starting temperature where damage can occur at, but it takes a considerably long time to cause permanent damage, on the order of



200 minutes. In contrast, tissue held at 65°C for as short a time as one second can cause permanent damage [10].

Electrosurgery is the descendant of electrocautery and differs primarily from its predecessor in that it passes current into the body to generate heat using the resistance of the tissue instead of using electric current to directly heat the tip of the electrode [10]. It is largely considered to be developed by Harvey Cushing and William T. Bovie in 1926 but others have had major contributions, including William Clark who first described the desiccating properties of electrosurgery in 1914 [11].

In monopolar electrosurgery, the whole patient becomes part of the circuit. Current from the active electrode seeks the shortest path back to the return electrode. This concentrates current along less electrically resistive conduits such as nerves or vascular structures. The path current takes may therefore have no correlation with anatomical distance. Partly due to this, the bipolar electrode was introduced by Jeffrey Greenwood in 1942 to eliminate the patient from the circuit [12]. The active and return electrodes are in close proximity, thus minimizing potential injury. However, as tissue is desiccated, its resistance increases. Current may spread to surrounding lower resistive tissue and widen the area of damage.

Additionally, current leakage from the bipolar device may cause it to behave like a monopolar electrical source. Bipolar cautery has been associated with thermal spread up to 6 mm [13]. Newer forms of bipolar energy devices, using a generator with a feedback-controlled circuit to determine the conductivity and amount of tissue in the instrument's grasp, deliver appropriate amounts of high-current, low voltage energy to seal tissue. The high current melts collagen and elastin in the tissue, forming a durable, thin seal. LigaSure™ Lap (LS) sealing device (Valleylab) and the PlasmaKinetics™ (PK) sealer (Gyrus Medical) are touted to reliably seal vessels up to 7 mm in diameter with minimal thermal spread. The Ligasure device uses continuous bipolar waveforms while the Gyrus-PK sealer uses pulsed bipolar waveform, with inactive periods between energy bursts. Gyrus theorizes this pulse/cool-off period allows instrument jaw cooling, thus reducing desiccation at the contact point, and resulting in less electrode sticking. While thermal spread with these devices is less than traditional bipolar it is still significant and can be

greater than 3mm. Prior research examining electrosurgery has identified heat as a cause of neural injury, which may occur as low as 41°C [7]. Because of this, irrigation is routinely used to cool tissue during head and neck surgery. This practice is corroborated by studies finding clear neuro-protective effects with using irrigation during bipolar cautery of the rat sciatic nerve.

Ultrasonic shears have been developed to obviate the need for electrical current and may be more suitable for use around neural structures. However, in pre-clinical and clinical studies it is clear that thermal spread may be significant, often as much as 3-4 mm, and can lead to complications including hollow viscous (bowel, bladder, etc) perforation and significant nerve injuries. For example, many surgeons began to use the ultrasonic shears for laparoscopic radical prostatectomy due to its excellent haemostatic properties. However, Owaki et al. found the ultrasonic shear blades become hot, increasing to 63°C in 3 s and 150°C after 30 s [14]. They suggested blade contact with neural structures immediately following use caused recurrent injury in their patients undergoing endoscopic parathyroid surgery. This is important as the surgeon has no indication of the instrument tip temperatures or the degree of thermal spread during laparoscopic surgery.

Methods for monitoring the thermal history of tissue have been varied. Currently, thermographic imaging techniques are being widely used to demonstrate surface temperatures of both the tissue and the electrode during procedures. Thermocouple and thermistor use has also been used in the past, but restricted to imbedding the sensor into the electrodes themselves. Post-operatively, histopathologic studies can also be performed and used in coincidence with thermal data to correlate damages seen histologically and thermally.

The extent of the collateral damage done using energized procedures has been studied previously with varying degrees of cross-correlation [15, 16]. Traditionally the thermal spread from these instruments is determined with a combination of in-situ dynamic thermography and histopathologic studies [17].

### **1.2.2 *Review of Electrosurgical Modeling***

Thermal spread in biological tissue is difficult to measure and predict. Modeling is a necessary tool to understand temperature distribution and tissue damage from thermal spread. However, research is lacking in this area. Research in the modeling of radiofrequency (RF) ablation has been reviewed by Berjano [18]. Past research has focused on FEM of tissue RF ablation and shortening the design time for new RF instrumentation. Several researchers have modeled RF ablation using a finite element approach [19-21]. However, the literature has been limited primarily to the area of tumor ablation in the liver and heart, which is characterized by low voltage inputs and procedural times on the order of 480–720 s and 60-120 s, respectively. Cautery is a technique characterized by high voltage inputs and procedural times on the order of 3–10 s, almost two orders of magnitude shorter than liver RF ablation and one order shorter than cardiac RF ablation. To date, detailed FEM on the cautery procedures is still new and not well studied. Pearce et al. [22] published the finite difference determinations for the potential gradient from a smooth rectangular electrode. The modeling of such procedures can be important to further the understanding of how tissue responds to RF energy, resulting in improvements to instrumentation design.

### **1.2.3 *Review of Thermal Management in Electrosurgical Applications***

To mitigate the natural consequences of energized surgical devices, various techniques have been utilized. These include the use of saline irrigation, internal heat pipes, and control algorithms within the generator.

Saline flushes have found good use for hepatic tissue ablation where deep, wide lesions are needed [23-27]. Cauterized tissue at the surface of the liver creates an impeditive barrier to further cauterization and is therefore unwanted. By flooding the area with saline, both the surface of the tissue and the electrode are maintained at lower temperatures, keeping the tissue conductive to electrical current longer, thereby increasing the lesion depth with time [28]. This technique has recently been advanced through the use of cold irrigation to further prohibit lateral thermal damage to the tissue [29, 30].

Heat pipes have been used with the development of hollow electrodes to promote passive cooling of the electrodes primarily in response to tissue charring and a resultant sticking of tissue to the electrode which results in risks of breaking open sealed and/or cauterized tissue once the procedure has completed [31, 32].

With the onset of solid-state circuitry in the 1970's, surgical generator design began to advance rapidly [10]. Most electrosurgical generators employ a constant power control on the electrical output to the surgical devices. This serves to automatically adjust output voltage to the changing electrical properties of the tissue during a procedure. Additional proprietary algorithms are also incorporated into most modern surgical generators [33].

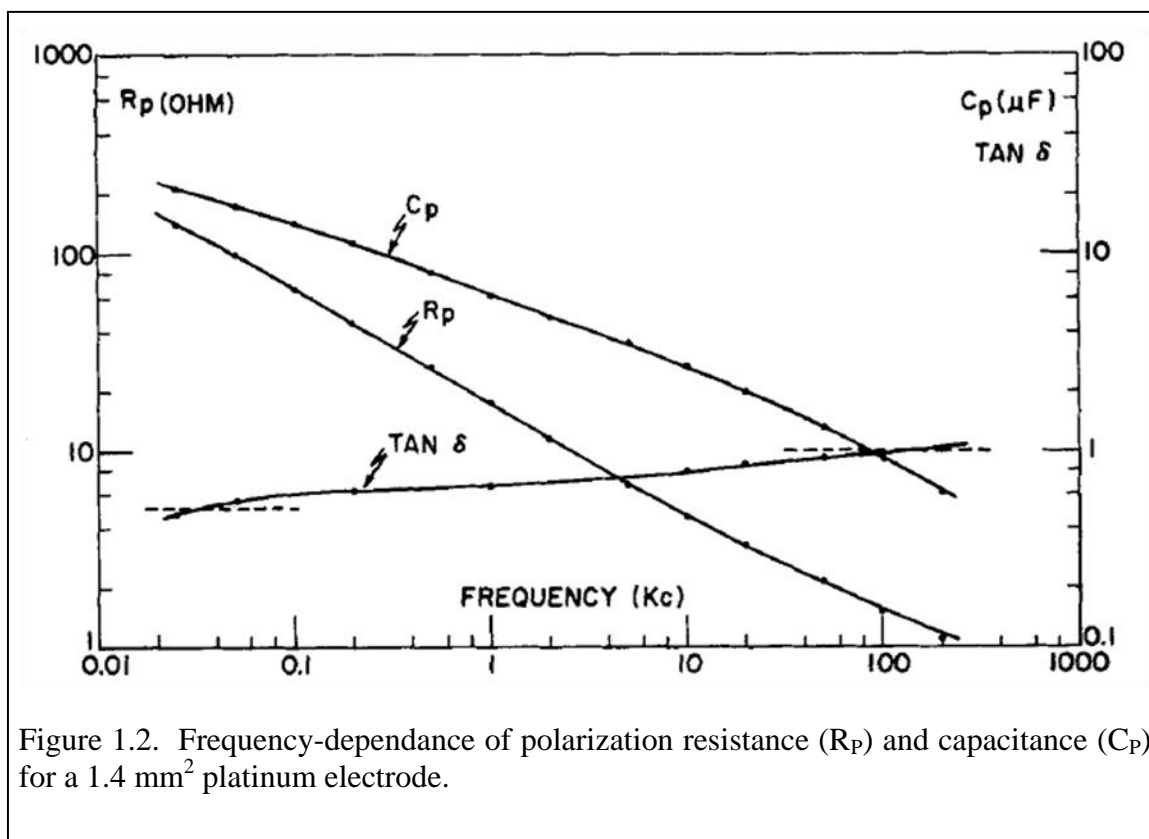
Of note is an additional technology being currently used to control thermal spread. EnSeal uses a micro-carbon electrode along with an I-beam compressor to coagulate tissue [34]. The electrode is proposed to microscopically short-circuit at high temperatures, thus avoiding additional electrical current from being injected into the tissue.

#### ***1.2.4 Review of Tissue Electrical Characterization***

Electrical stimulation and measurement had been initially limited to frequencies above 5 kHz for safety reasons expressed by Geddes et al. [35]. At 50 Hz and using trans-thoracic electrodes, currents of 50 mA stimulate the Vegas nerve producing a slowing of the heart. At 5 kHz, about 12 to 15 times more current (600 to 750 mA) is needed to produce the same effect. At 3 kHz, the current required to produce a ventricular fibrillation (approximately 4-6 A) is 20 times greater than that at 60 Hz (200-300 mA). With recent advances in instrumentation technology, it is now possible to use currents in the  $\mu\text{A}$  range, thus permitting safe physiological measurements even at low frequencies.

#### **Contact Impedance**

The ability to fully characterize the electrical response of tissue and electrolytes is a relatively recent phenomenon [36]. Up until the turn of the 20<sup>th</sup> century, it was difficult to measure even the impedance of simple electrolytes accurately due to frequency and current-density dependencies of the contact impedance of the electrode/electrolyte interface. In 1897 Kohlrausch minimized the electrode impedance problem by



developing the platinum-black electrode, which has a low impedance and allowed for resistivity measurements at 1000 Hz with a bipolar electrode [37]. However, in 1884 Bouty had already resolved the electrode/electrolyte impedance problem in a different way by introducing the tetrapolar method [38]. In this method, a constant current is injected between two outer electrodes and a potential difference is measured between two inner electrodes each having input impedance much greater than the contact impedances of the potential-measuring electrodes. Bouty called the potential-measuring electrodes ‘parasitic electrodes.’ It is common practice to use the terms polarization resistance and polarization capacitance to describe the processes involved with current moving from an electrode to an electrolyte.

Since the discovery and subsequent understanding of contact impedance, much work has been performed on the interaction between electrodes and electrolytes [39-42]. In general, the contact impedance can be modeled as an equivalent electrical circuit by placing a resistor and capacitor in parallel with each other. As mentioned above, the

terms are called the polarization resistance ( $R_p$ ) and the polarization capacitance ( $C_p$ ). The total impedance that the electrode/electrolyte interface has to current can be expressed as the sum of the separate impedances, or

$$\text{---} \tag{1-1}$$

where  $Z_p$  is the polarization impedance.

As shown in Figure 1.2 [39],  $R_p$  and  $C_p$ , and thus  $Z_p$ , are frequency dependent. However,  $R_p$  and  $C_p$  are related to each other through the following equation

$$\text{---} \tag{1-2}$$

which is fairly frequency-independent, as shown in Figure 1.2 [39].

### **The Cell Membrane and Bioimpedance**

It wasn't until the early 1930s that it was understood how critical a component the reactance of tissue is to biological impedance measurements. Early efforts of researchers such as Philippon [43], Fricke [44], McClendon [45, 46], and Cole [47-49] demonstrated the presence of a cell membrane capacitance. Using the potential theory originally developed by Maxwell [50] which was later applied to particle suspensions by Fricke [51, 52], these investigators confirmed the presence of a 'relaxation-type' conduction process associated with the cell membrane capacitance.

### **Equivalent Circuit for Bioimpedance**

Just prior to the establishment of the membrane capacitance, Carter published work in 1925 on the representation of two terminal impedance networks containing reactive elements [53]. In this work Carter represented impedance as a variable in the complex plane and it was soon quickly adopted by Cole as an analysis method for biological impedance [54]. Together with equivalent circuit analogues, this representation of biological impedance has greatly simplified an otherwise difficult task of analyzing complex electrical interactions. In 1941, Cole and Cole published what has become known as the Cole-Cole model for biological tissue [55, 56] which follows the form

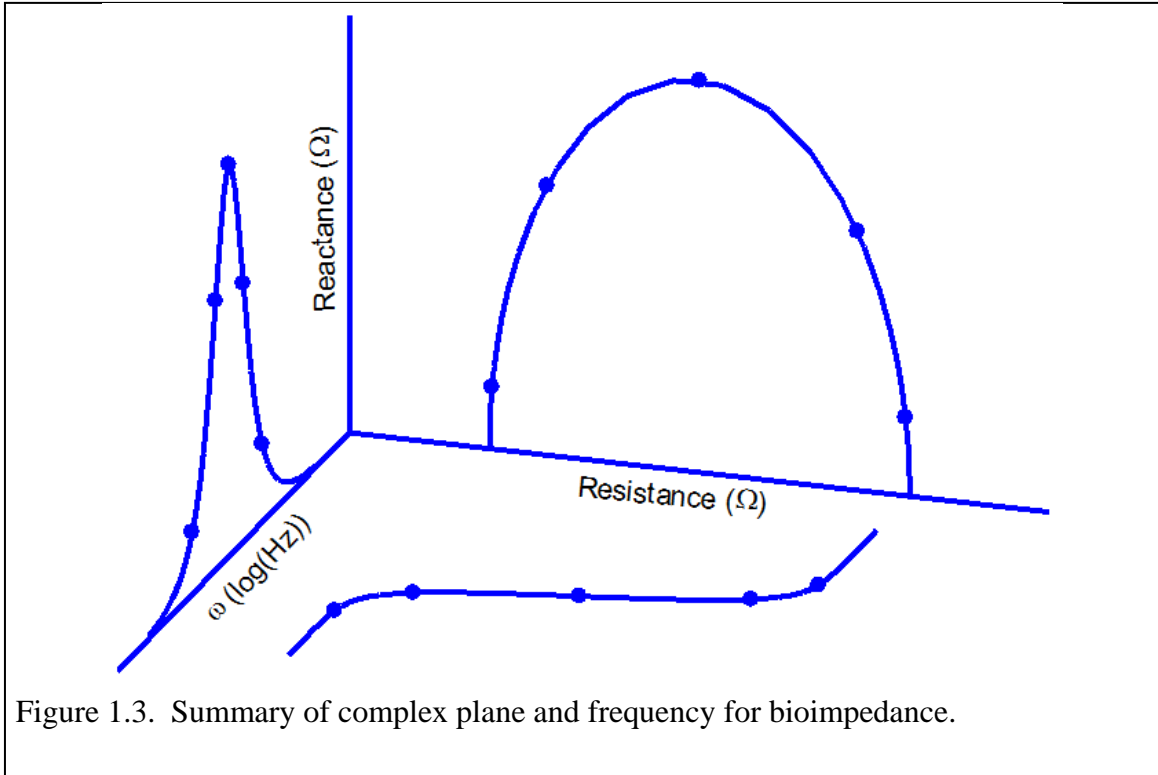


Figure 1.3. Summary of complex plane and frequency for bioimpedance.

where  $Z$  is the impedance,  $\omega$  is the natural frequency,  $R_\infty$  is the resistance at infinite frequency,  $R_0$  is the resistance at zero frequency (DC),  $j$  is the imaginary unit,  $\tau$  is the relaxation constant for the system, and  $\alpha$  is the dispersion coefficient for the system. It should be noted that there is discrepancy in who originally posted this relationship, with some giving credit only to Kenneth Cole, citing a 1940 paper he published [57].

Plots of the real (resistance) versus the imaginary (reactive) parts are semicircular in nature having centers which lie below the real axis. Also, plotting the real and imaginary parts separately against frequency provides characteristic shapes as well. Figure 1.3 shows a graphical summary of these plots and how they relate to each other. Analyzing Eq. 1-3 as a function of frequency, the impedance can be shown to equal  $R_0$  as  $\omega$  approaching zero Hz (DC). This is due to the high cell membrane resistance in relation to the interstitial fluid, along with the capacitance of the cell membrane acting as an open circuit as low frequency [58]. As  $\omega$  approaches infinity, the impedance becomes equal to

$R_\infty$ , due to the cell membrane capacitance acting as a short circuit allowing current to cross the cell membrane unimpeded.

### **Modern Uses of Bioimpedance**

Today bioimpedance measurements are used in a variety of ways and have matured beyond a research tool. Bioelectrical impedance analysis (BIA) is currently used to determine total body water and body fat in individuals. Multi-frequency bioelectrical impedance analysis (MF BIA) uses impedance measurements over a range of low to high frequencies to determine the extracellular fluid volume (low frequencies) and total body fluid volume (high frequencies) [59, 60]. This practice is also being used on a partial, or segmental, portion of the body for the characterization of edema in dialysis [61] and to determine hydration status and predisposition to hypotension [62].

Bioimpedance tomography, or electrical impedance tomography (EIT), has matured to the point that it can be used to produce precise 3D images of the body [63]. EIT does not have the spatial resolution of MRI or CT, but has a key advantage in its temporal resolution, which can be down to the order of milliseconds [64]. This technology has been used in areas such as the detection of breast cancer and the monitoring of brain function and stroke [65, 66]. While it has yet to be used routinely in everyday clinical practice, it has great value in being both safe and cheap compared to alternative imaging technologies [63].

### **1.2.5 Review of Tissue Mechanical Property Modeling**

Initial looks at tissue can take an equivalent mechanical model approach by combining springs and dashpots in series and in parallel with each other. Major problems with these approaches arise when creep and relaxation are looked at, where each has its own flaws. Fung's *Biomechanics* is classical literature describing the quasi-linear viscoelasticity (QLV) of soft tissue [67]. An excellent review was performed by Humphrey [68] on the continuum biomechanics of soft tissue.

Since the introduction of this theory, much research has been performed analyzing tissues from this approach, whereby a range of relaxation times are seen to drive the tissue response to strain. The two main areas that QLV theory has been put to use are in the modeling of tendons and ligaments [69-71] and in the modeling of abdominal soft



tissue [72-75]. Much of this work continues to be performed for use in developing realistic computer-based surgical software as well as in the design of surgical robots and their associated tools.

Considering the number of parameters that must be fit to solve for the QLV model (as many as eight or more depending on the functions that are defined), a number of papers have been written concerning the solution of the QLV problem [76-78].

Apart from Fung's QLV theory, work done by Mow [79] and more recently carried on by Ateshian [80, 81] has looked at the harder of the soft tissues, primarily cartilage, from the standpoint of tissue being viscoelastic. A model, termed the biphasic model, has been developed describing how these tissues respond to stress and strain which shows marked differences with QLV theory. An important outcome of this research is the determination of the protective qualities that fluid has in absorbing stress due to high strains.

The bioimpedance of tissue undergoing compression has natural logical connections with the mechanical properties of tissue. Tissue compression results in the loss of fluid and solid material from the compressed space simply by volume reduction. This impacts cell membranes, interstitial fluid, and intracellular fluid, which are the principal components involved in the electrical relaxation seen in bioimpedance readings of tissue [82]. Monitoring both bioimpedance and the relaxation pressure of tissue can lead to improved understanding of the mechanics underlying tissue compression.

### **1.1. Research Objectives and Tasks**

The primary objective of this research is to characterize the electrical properties of tissue under compression and correlate these to the mechanical changes seen in tissue under compression. As discussed above in the motivation (Section 1.1) collateral thermal damage resulting from electrosurgery is primary concern for using these devices in critical surgical areas such as the reproductive areas for prostatectomy and hysterectomy. Secondary objectives accomplished throughout this process include:

- a) the development of a subsurface temperature sensing system for monitoring tissue temperature during energized surgical procedures

- b) the finite element modeling of a bipolar electrosurgical procedure
- c) the development of a surgical thermal management system for electrosurgery
- d) the development of a custom experimental procedure for monitoring bioimpedance under compression

## 1.2. Outline

This dissertation presents the concept and application of a compression-dependent electrical conductivity of tissue. Layout of this dissertation is described in the following paragraphs.

Chapter 1 of the dissertation provides primary motivations for this doctoral research as well as a literature review of related research work.

Chapter 2 describes a method for measuring the real-time temperature of tissue during the use of energy-based surgical devices. The ability of capturing sub-surface temperatures during energized surgical procedures is validated.

Chapter 3 undertakes the finite element modeling of the bipolar electrosurgical procedure. Previous knowledge on the modeling of monopolar and RF ablation techniques is expanded here to include the bipolar technique, with improvements in matching to the experimental results seen by allowing for a theoretical strain-dependent electrical conductivity.

Chapter 4 is comparative research performed with bipolar electrosurgical instruments validating a method for combating thermal spread. Active cooling channels are utilized adjacent to bipolar electrodes to act as a heat sink and a non-energized compressor to adjacent tissue. The results not only show a dramatic decrease in thermal spread laterally from the bipolar device, but also indicate a more efficient coagulation process as tissue temperatures at the center of the actively cooled device get hotter more quickly than for the standard bipolar device.

Chapter 5 leverages the use of the four electrode technique to analyze the real-time electrical conductivity of tissue. The idea of compression-dependent electrical conductivity is introduced. A series of probes are tested, combined with an LCR meter and a custom front-end amplifier, in *ex-vivo* tissue to validate the approach. The chapter

culminates in both *ex-vivo* and *in-vivo* studies analyzing the electrical conductivity of tissue under varying compression levels for multiple tissues.

Chapter 6 develops an extended Cole-Cole model to include compression-dependent terms allowing for an accurate prediction of electrical conductivity of tissue at varying compressive strains. A strongly non-linear capacitive term is included, indicating the point at which cell membrane rupture occurs. Moreover, the resistive terms are also coupled to this capacitive term to properly demonstrate the combining and mixing of interstitial and intracellular fluids during cell rupture.

Chapter 7 concludes this research and provides ideas for future work in this field along with the author's original contributions.

## Chapter 2 Thermal Profiling of the Energy-Based Surgical Procedure

### 2.1 Introduction

The work presented in this chapter has been published previously in *The Journal of Minimally Invasive Gynecology* [83].

The use of energized dissection systems has dramatically improved laparoscopic dissection and hemostasis while allowing more procedures to be performed in a minimally invasive fashion [84]. Through the years, researchers have worked to improve this technology in order to enhance its execution both in open and endoscopic cases. However, thermal collateral damage associated with the use of energized surgical instrumentation detracts from the usefulness of these devices. The extent of this collateral damage has been studied previously with varying degrees of cross-correlation [15, 16]. Traditionally the thermal spread from these instruments is determined with a combination of in-situ dynamic thermography and histopathologic studies [17]. Currently the primary methods for obtaining hemostasis during minimally invasive surgery include using ultrasonic energy and radiofrequency current.

Despite reports of minimal thermal spread from today's energized instruments, it

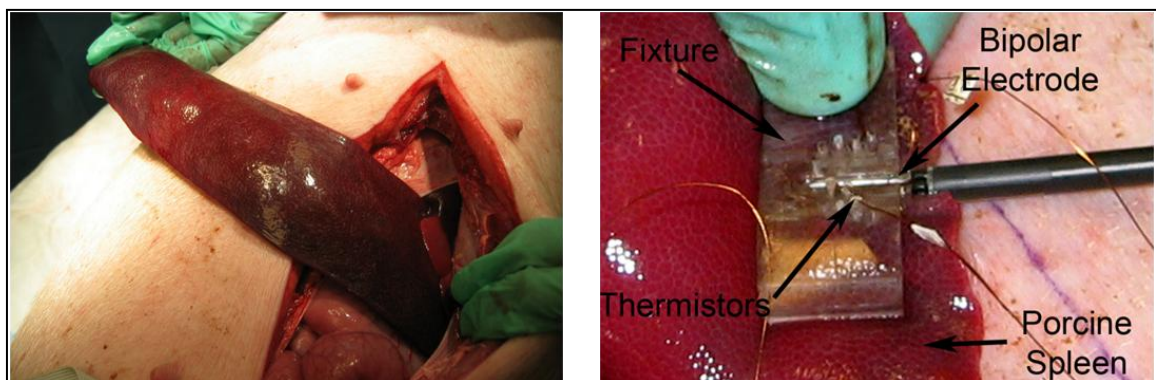


Figure 2.1. (a) Photograph of exteriorized porcine spleen and (b) in situ temperature acquisition set-up.

is impossible for the surgeon to be entirely confident that he or she is not causing collateral damage. Although thermography in its present form could accompany energized surgery in open procedures to guide the surgeon, this is not feasible in laparoscopy. The ability to obtain this data during laparoscopic surgery would require real-time thermal spread determinations to be made immediately without the use of a standard thermal imaging camera. If accomplished, this would not only provide the surgeon with real-time feedback on thermal spread and tissue temperature but also potentially allow for the cessation of a procedure once critical temperatures have been reached. Additionally, thermal measurements and thermal spread calculations could be incorporated into device designs to allow effective control over tissue temperature. The aim of this preliminary study was to validate the ability of determining sub-surface tissue thermal profiles in real-time during surgical procedures using either an advanced bipolar or ultrasonic device.

## 2.2 Materials and Methods

The setting was an animal surgery operating room at the University of Michigan School of Medicine. The protocol was approved by the University Committee on Use and Care of Animals (UCUCA). Funding was secured through an unrestricted educational grant from Gyrus Medical/ACMI. The experiment was carried out on one large (~50 kg), white, landrace cross pig.

Anesthesia was induced in the animal with intramuscular injections of telazol (6 mg/kg) and xylazine (2.2 mg/kg), and then the animal was intubated, positioned supine

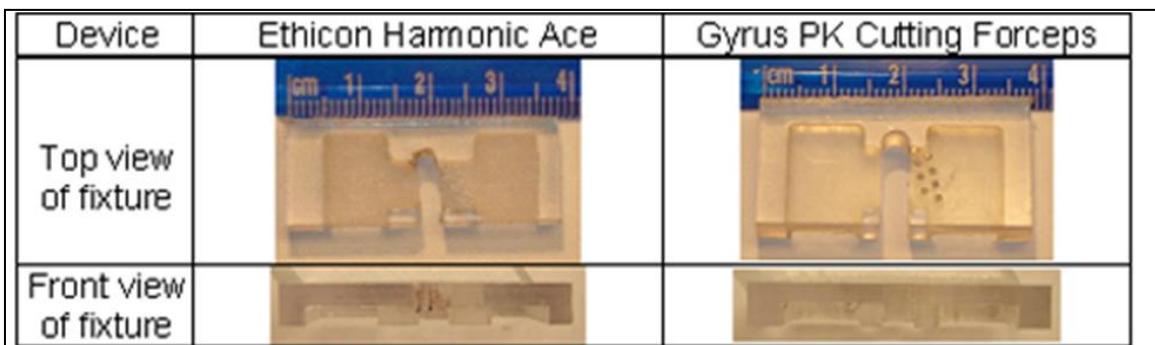


Figure 2.2. Photograph of top and front views of actual polycarbonate fixtures used for positioning of both the instrument jaws and the thermistors.

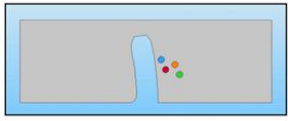

|                | Device  |  | Distance from tool edge (mm) |
|----------------|---|--|------------------------------|
|                | Ethicon Harmonic Ace  | Gyrus PKCutting Forceps  |                              |
| Fixture Symbol |  |  | 1.0 (A)                      |
|                |   |  | 1.5 (B)                      |
|                |   |  | 3.0 (C)                      |
|                |   |  | 3.5 (D)                      |

Figure 2.3. Computer Aided Design (CAD) drawing of polycarbonate fixtures displaying distances of thermistors from instrument jaw edge.



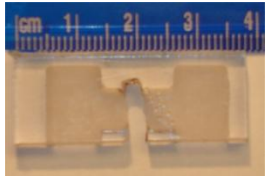
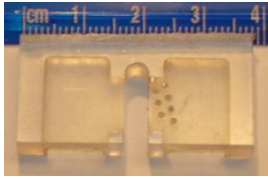


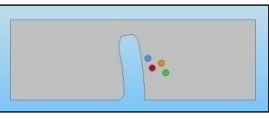
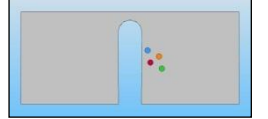
on the operating table, and maintained under general anesthesia with isoflurane (2 to 2.5%) while on a ventilator. Oxygen saturation, pulse rate, respiratory rate, mucous membrane color, and blinking reflex were monitored with pulse oximetry at regular intervals. Upon completion of the experiment, the animal was euthanized via barbiturate overdose.

During the course of the operation, a long midline laparotomy incision was made to expose the abdominal cavity and allow access to the spleen which was the target organ for the experiment. This decision was based on the target organ’s size and uniform thickness. The spleen was exteriorized to perform the instrument measurements and was replaced within the abdominal cavity during periods of no testing (see Figure 2.1(a)).

Two energized 5 mm laparoscopic devices were used: an ultrasonic instrument as represented by the Harmonic ACE (Ethicon EndoSurgery, Cincinnati, OH); and an advanced bipolar electrocautery instrument as represented by the Gyrus Plasmakinetic Cutting Forceps (see Table 2.1). The tissue temperature was measured at a depth of 2.0 mm under the tissue surface using thermistors placed at 1.0 mm from each tool edge. Polycarbonate fixtures were created for each of the devices tested to ensure temperature measurements were recorded at precise distances from the tool edge (see Figure 2.2 and Figure 2.3). The additional thermistor ports present in the fixture were incorporated for future use in acquiring multi-point thermal profiles. Upon tissue clamping the fixture for each device was placed around the device as shown in Figure 2.1(b) and held in place while the trial proceeded. Voltage measurements were recorded using a Wheatstone Bridge circuit and the signals were transmitted and converted in Labview to temperatures

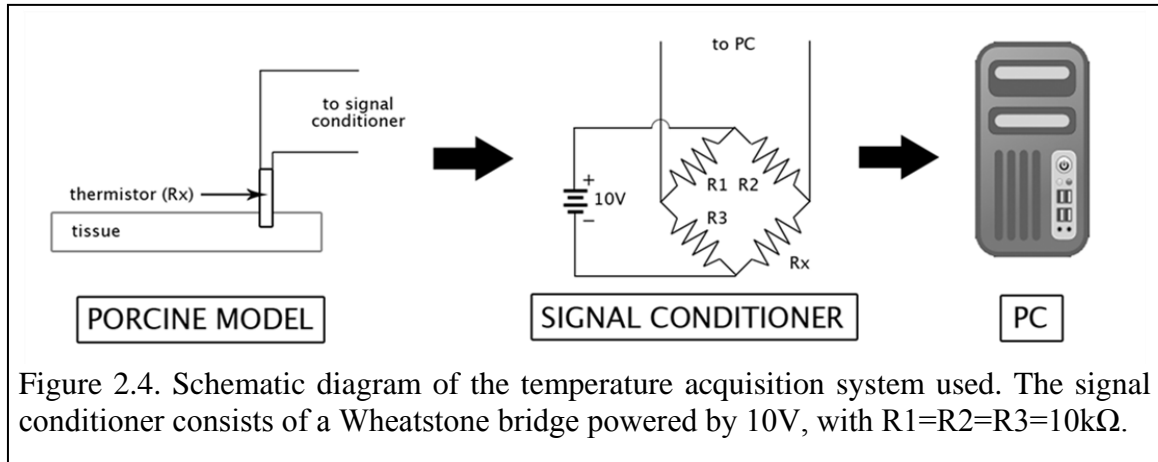
via a Data Acquisition System (DAS). A schematic diagram of the complete temperature data collection system is shown in Figure 2.4.

Table 2.1. Comparison of Two Energized Surgical Instruments.

| Modality              | Ultrasonic  | Bipolar  |
|-----------------------|---|--|
| Company               | Ethicon   | Gyrus  |
| Model                 | Harmonic Ace  | 5 mm Cutting Forceps   |
| Generator             | G300  | PlasmaKinetic  |
| Setting               | Min 3   | VP-35  |
| Surgical tool         |    |   |
| Top view of fixture   |    |    |
| Front view of fixture |  |  |
| Fixture symbol        |  |  |

Within each device, the bite size for the surgical procedures was limited to  $\frac{3}{4}$  of the jaw length to avoid variations in tissue effect at the jaw hinge area. Lateral tension to the tissue was avoided and rotational motions were used only when required for by the device to ensure effects were limited to the devices. Default power settings were used for each device as listed in Table 2.1.

For the Gyrus Plasmakinetic Cutting Forceps, the tissue was clamped using the built-in ratchet. Bipolar energy was applied until 4 stars were indicated on the generator impedance graph. This indicated that a significant change in tissue impedance had occurred. Further generator details are listed in Appendix A. The seal was then transected with the Gyrus device's cold blade (Figure 2.5(a)). Any trial resulting in less



than 3 s to reach 4 impedance stars was omitted as a representative temperature profile would not have been created in that timeframe.

For the Harmonic ACE, the active jaw was placed under the spleen to allow the cut process to be applied upwards (Figure 2.5(b)). The tissue was clamped using the ratchet ensuring it was locked into position. Three clinical scenarios were tested:

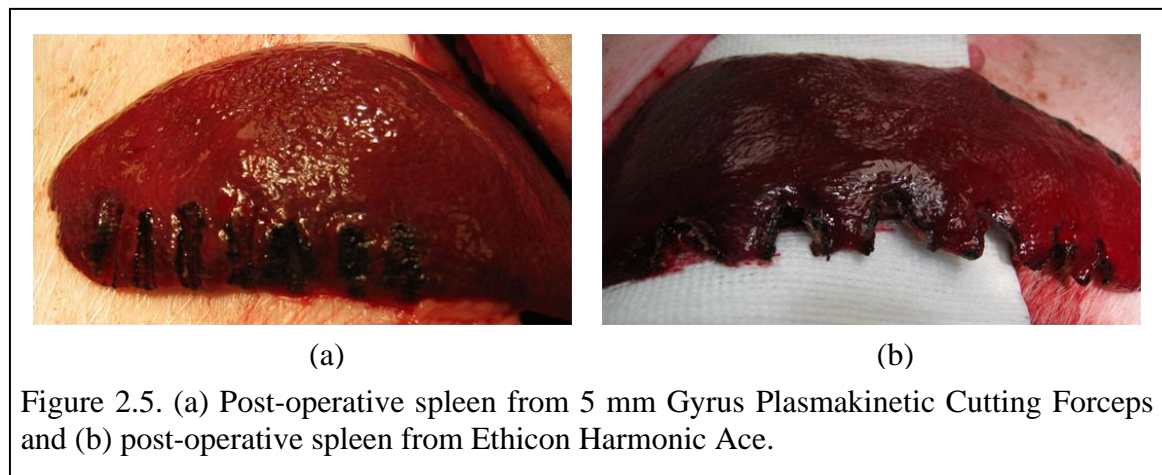
- **Coagulation only** – “Min 3” setting applied to only coagulate tissue for a set time of 5 seconds
- **Coagulation until cut** – “Min 3” setting applied until the surgeon believed adequate coagulation had occurred and then upward force was applied on the tissue with the active jaw until the coagulated tissue was divided, still using “Min 3” setting.
- **Coagulation and then cut** – “Min 3” setting to only coagulate tissue for a set time of 5 seconds and then the “Max 5” setting was used with upward force applied on the tissue with the active jaw until the coagulated tissue was divided



### 2.3 Results

The Gyrus Plasmakinetic Cutting Forceps was tested in seven separate trials with a complete set of thermal profiles as shown in Figure 2.6(a). The average maximum temperature and standard deviation (SD) at 1.0 mm away from the tool edge was 56.8°C (SD 8.5°C) with an average procedural time of 5.7 s (SD 2.7 s).

Three different modes were used with the Harmonic ACE to benchmark its performance as routinely used in surgical procedures. The device was used to perform a strict coagulation at the 'Min 3' setting (Figure 2.6(b)), a coagulation at the 'Min 3' setting which was continued until a full transection was achieved (Figure 2.6(c)), and finally a coagulation at the 'Min 3' setting followed by a transection using the 'Max 5' setting (Figure 2.6(d)). Each modality was run three times for a total of nine trials. The average maximum temperatures at 1.0 mm were as follows - coagulation only: 57.5°C (SD 7.7°C); coagulation until cut 61.9°C (SD 9.6°C); coagulation and cut 56.4°C (SD 3.1°C). The average procedural times were 5.2 seconds (SD 0.9 s) for coagulation only, 10.3 seconds (SD 0.9 s) for coagulation until cut, and 6.0 seconds (SD 0.7 s) for cut.



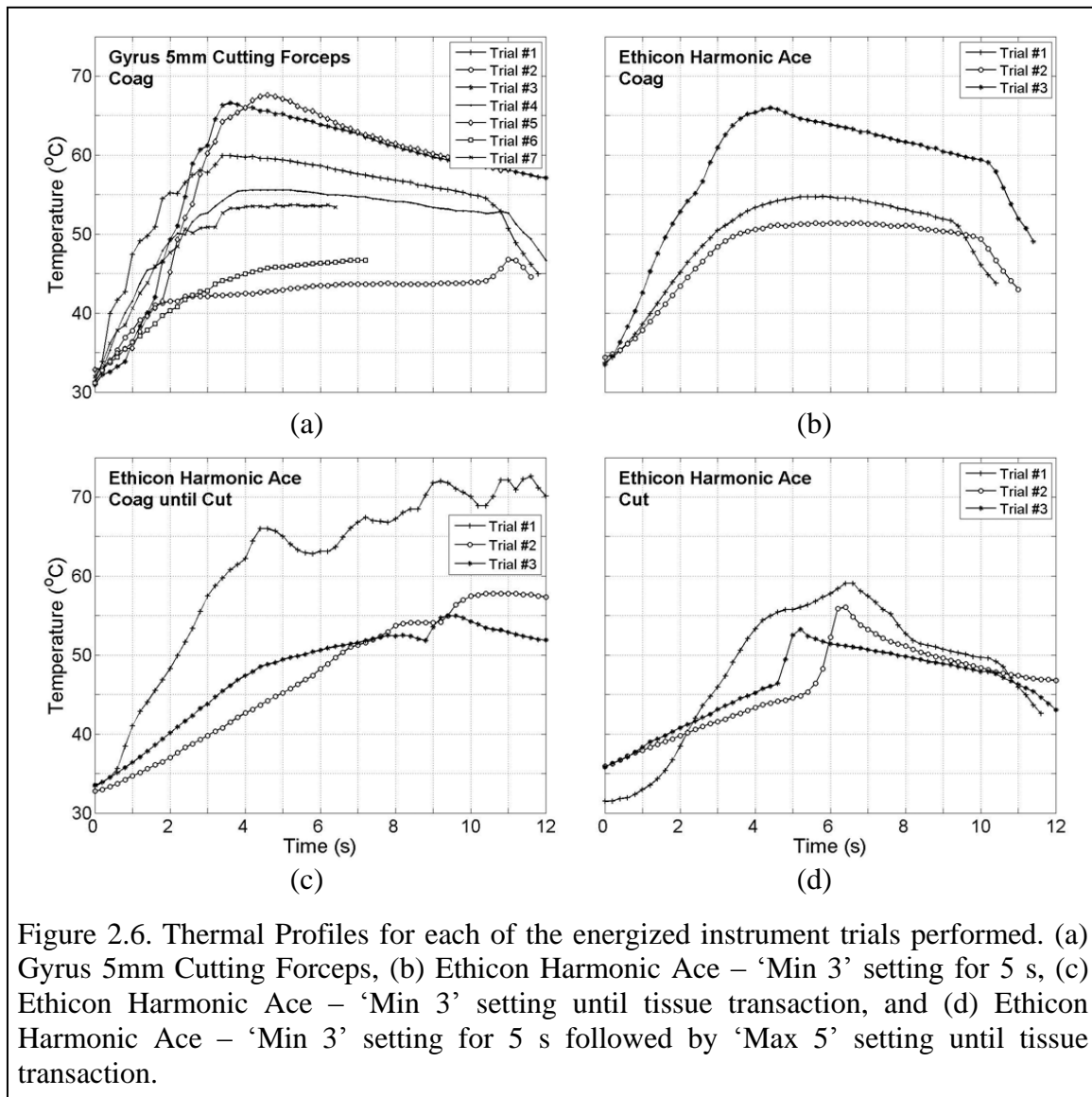


Figure 2.6. Thermal Profiles for each of the energized instrument trials performed. (a) Gyrus 5mm Cutting Forceps, (b) Ethicon Harmonic Ace – ‘Min 3’ setting for 5 s, (c) Ethicon Harmonic Ace – ‘Min 3’ setting until tissue transaction, and (d) Ethicon Harmonic Ace – ‘Min 3’ setting for 5 s followed by ‘Max 5’ setting until tissue transaction.

## 2.4 Discussion

The results in Table 2.2 demonstrate the proof of concept ability to obtain real-time sub-surface tissue thermal profiles of energized surgical instruments with the novel temperature acquisition system described. The average maximum temperatures observed at the 1.0 mm thermistor position for both of the tools tested as well as the average time it took to achieve them are listed in Table 2.2. Although the Gyrus Plasmakinetic Cutting Forceps operated cooler than the Ethicon Harmonic ACE at a 1.0 mm distance measured from the tool edge, the difference in all cases was less than 5°C and not statistically

Table 2.2. Comparison of mean peak temperatures, standard deviations, and procedural times for the 5 mm Gyrus Cutting Forceps and Ethicon Harmonic Ace

| Device                     | Application             | Tissue Temperature and Surgical Time |                      |                      |                     |
|----------------------------|-------------------------|--------------------------------------|----------------------|----------------------|---------------------|
|                            |                         | T <sub>avg</sub> (°C)                | T <sub>SD</sub> (°C) | t <sub>avg</sub> (s) | t <sub>SD</sub> (s) |
| Gyrus 5mm Forceps<br>(n=7) | Coag                    | 56.8                                 | 8.5                  | 5.7                  | 2.7                 |
| Harmonic ACE<br>(n=9)      | Coag (n=3)              | 57.5                                 | 7.7                  | 5.2                  | 0.9                 |
|                            | Coag until Cut<br>(n=3) | 61.9                                 | 9.6                  | 10.3                 | 0.9                 |
|                            | Coag & cut (n=3)        | 56.4                                 | 3.1                  | 6.0                  | 0.7                 |

significant. Also there were no significant differences in temperature amongst the three ultrasonic energy modes.

The similar thermal range for the two devices would indicate a similar thermal tissue margin as well; however, the lack of histopathology after the lab precludes this observation from being made in complete confidence. In fact, previous published reports have actually shown the level of thermal spread measured via histological analysis to be less than that of real-time thermography [17]. Based on these reports, collateral thermal damage may be a function of both the maximum temperature to which the tissue was exposed and the duration of the application. A more consistent correlation with histopathology may exist with the use of tissue sub-surface thermistors versus thermography. Overall, the lack of a difference between the operating temperatures of the Gyrus Plasmakinetic Cutting Forceps and Ethicon Harmonic ACE demonstrates their comparable thermal profiles during energized dissection and hemostasis.

## 2.5 Conclusion

This laboratory experiment represents the first known successful attempt of measuring sub-surface tissue temperatures in real-time during energized dissection. The ability to acquire instant temperature information within tissue during an operative procedure is a major advance not only for the study of surgical tool performance but for

the safety of surgical procedures in general. Since thermistors are dependent solely on their own resistance they are believed to be capable of relaying even laparoscopic thermal information in real-time to the surgeon. This advance has the potential to enhance the surgeon's ability to minimize unwanted thermal damage to surrounding tissues during surgical procedures if incorporated into instrument designs. Currently, for practical studies, traditional in situ dynamic thermography with thermal imaging cameras is limited to open cases.

The initial success achieved in this laboratory experiment warrants the continuation of this research coupled in the future with histopathologic analysis. The additional thermistor ports present in the fixture will need to be used to develop multi-point thermal profiles. Correlating these results with a histopathologic analysis and integration of this technological concept into instrument design could allow for more accurate determination of collateral tissue damage during energized dissection and hemostasis thereby minimizing both intra- and post-operative complications.

## **Chapter 3 Finite Element Model of the Bipolar Electrosurgical Procedure**

### **3.1 Introduction**

The work presented in this Chapter has been published previously in the ASME Journal of Manufacturing Science and Engineering [85].

In this study, a finite element model (FEM) of the bipolar electrosurgical cautery procedure is performed to investigate the thermal spread and temperature distribution in biological tissue. In-vivo surgical experiments are conducted in a porcine model for temperature measurement in the spleen. The measured temperatures during bipolar electrosurgery are compared with simulation results to validate the FEM model.

Cautery, or the coagulation of tissue, is a surgical technique that has long been used to denature proteins and minimize bleeding during surgical procedures [10]. One method to perform cautery is electrosurgery, which uses radiofrequency (RF) electrical currents to actively heat biological tissues with high power density [10]. Because human nerve and muscle stimulation cease at frequencies over 100 kHz, the electrical energy in RF alternating current can be delivered safely to generate the heat necessary for coagulation. Without coagulation, the internal bleeding from the cut area is a danger to the patient and affects the surgeons' field of view. Electrosurgery provides a major advance in surgery by minimizing blood loss and reducing operation time. Miniaturization of the electrosurgical instrument has enabled the use of minimally invasive or laparoscopic surgical procedures, thereby reducing patient recovery time. The success of laparoscopic surgery from both the surgeon and patient perspective has provided the inertia for using these instruments in increasingly complex procedures. However, their success in procedures such as prostatectomy and hysterectomy has been hampered by collateral damage to local neural structures impacting patient post-operative quality of life [3, 4, 7].

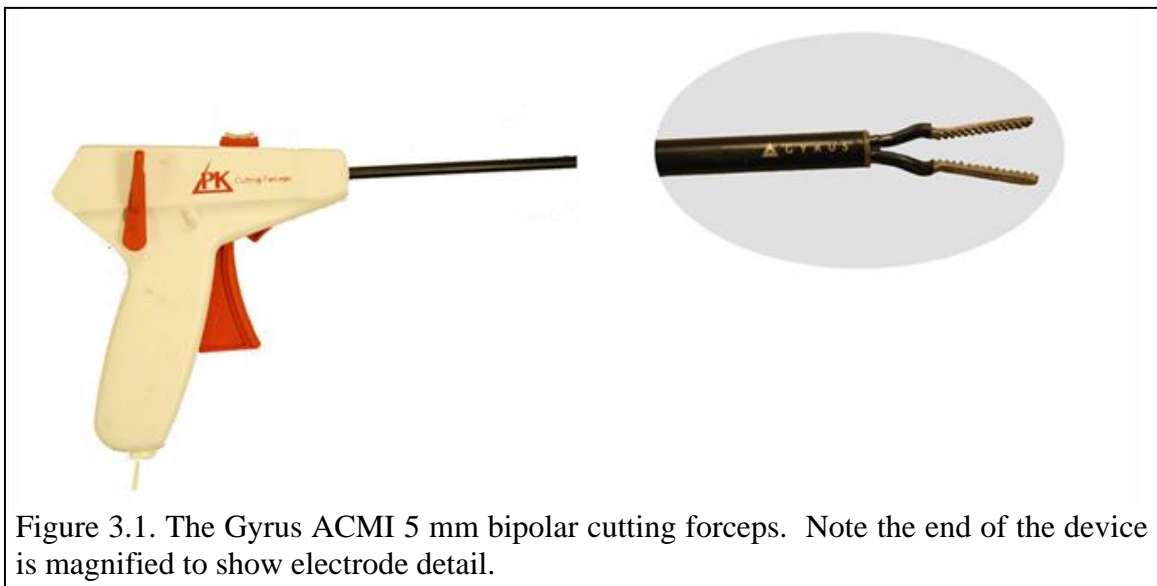
Electrosurgery can be categorized as monopolar and bipolar. Monopolar electrosurgery uses current in the gap between tool and tissue to generate heat and ablate tissue. It functions under the same principle as electrical discharge machining (EDM). Bipolar electrosurgery employs dispersive electrodes, called forceps, as shown in Figure 3.1. The RF electrical current supplied by an electrical generator flows through only the tissue between the two electrodes to complete the circuit. As electrical current passes through tissue its resistance generates heat for cautery. It functions under the same principles as resistive spot welding. Bipolar electrosurgery is investigated in this study.

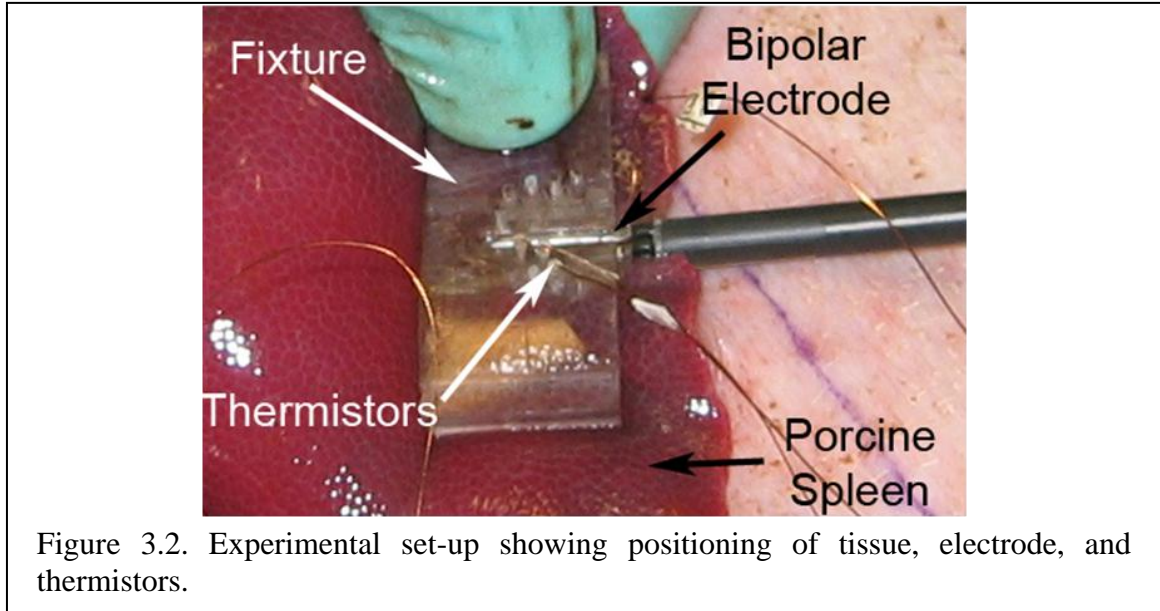
Heat generated from electrosurgery has a harmful side effect of spreading and damaging the surrounding tissue and, more importantly, the nerves in the neurovascular bundle (NVB) in surgery. This phenomenon is referred to as thermal spread in surgery [16]. Collateral tissue damage has been highlighted as a major concern for post-operative side effects, especially for procedures occurring near critical nervous regions such as prostatectomy and hysterectomy [7]. These side effects include impotence and incontinence with varying lengths of duration from temporary to permanent. Recent advances have been made in generator and control technologies that pulse the input voltage and turn off the power once the tissue has been determined to be coagulated. Nevertheless, these advances still report thermal spreads of 3–5 mm in ideal situations, which can cause irreversible side effects during procedures as it is difficult for the surgeon to control thermal spread from the electrosurgical instrument. The purpose of this research is to better understand heat transfer in biological tissues in cautery procedures to further improve the design of surgical bipolar devices.

Thermal spread in biological tissue is difficult to measure and predict. Modeling is a necessary tool to understand temperature distribution and tissue damage from thermal spread. However, research is lacking in this area. Research in the modeling of RF ablation has been reviewed by Berjano [18]. Past research has focused on FEM of tissue RF ablation and shortening the design time for new RF instrumentation. Several researchers have modeled RF ablation using a finite element approach [19-21]. However, the literature has been limited primarily to the area of tumor ablation in the liver and heart, which is characterized by low voltage inputs and procedural times on the order of 480–720 s and 60-120 s, respectively.

Cautery is a technique characterized by high voltage inputs and procedural times on the order of 3–10 s, almost two orders of magnitude shorter than liver RF ablation and one order shorter than cardiac RF ablation. To date, detailed FEM on the cautery procedures is still new and not well studied. Pearce et al. [86] published the finite difference determinations for the potential gradient from a smooth rectangular electrode. The modeling of such procedures can be important to further the understanding of how tissue responds to RF energy, resulting in improvements to instrumentation design. In this study, a finite element analysis (FEA) of bipolar electrosurgery cautery is performed to investigate the thermal spread and temperature distribution in biological tissue. In-vivo surgical experiments are conducted in a porcine model for temperature measurement in the spleen. The measured temperatures during bipolar electrosurgery are compared with simulation results to validate the FEM model.

In this study, COMSOL was used to model the heat transfer through in-vivo tissue during bipolar cautery using the Gyrus ACMI 5 mm Cutting Forceps, as shown in Figure 3.1. The results for temperature-dependent and -independent models are compared to experimentally measured tissue temperature for validation. In addition, theoretical compression-dependent effects on electrical conductivity are modeled. The FEM is lastly used to analyze the thermal profiles of different electrode designs to see how geometry can be used to reduce thermal spread.





### 3.2 Experimental Setup for In-Vivo Electrosurgical Temperature Measurement

Experiments were conducted, as shown in Figure 3.2, to measure temperature in the porcine spleen tissue during an electrosurgical procedure with a Gyrus ACMI 5 mm Cutting Forceps along with the Gyrus PlasmaKinetic<sup>®</sup> generator. As seen from Figure 3.1, the instrument consists of two electrodes, each 13 mm long and 1.15 mm wide. The distal 20 mm of this probe is made of 301 stainless steel and the proximal 4.0 cm of the probe is covered with an electrically insulating polytetrafluoroethylene (PTFE) coating.

A porcine (50% duroc, 25% yorkshire and 25% landrace) model weighing about 45 kg was anesthetized and ventilated for use in the in-vivo tissue coagulation experiments. An Agilent (Santa Clara, CA) 54833A 1 GHz oscilloscope in peak detect mode (PDM) with an Agilent 10076A 100:1 high voltage probe was used to measure the electrical voltage input to the tissue. PDM was used due to the limited memory of the oscilloscope as this only collects the peak readings from each waveform. Data was acquired via the Labview software. Tissue temperature was measured with micro-thermistors (Alpha Technics 56A1002-C3, Irvine, CA) with a 0.48 mm outside diameter and 0.25 s thermal response time. Thermistors were selected over thermocouples and other temperature sensors due to the high sensitivity and stability in the targeted temperature range (30–100°C) and their relative immunity to electromagnetic interference. The thermistor



relies on the change in resistance for temperature measurement and is relatively immune to the significant electromagnetic field generated during electrosurgery.

To maintain the same distance from the cutting edge, a fixture made of polycarbonate, as shown in Figure 3.2, was custom made that fits the shape of the forceps. The overall dimension of the fixture is 20 x 38.2 x 5.4 mm. The fixture can stand firmly on the tissue and has a 2.8 mm tall cavity to allow space for vapor to escape, a groove in the shape of the surgical tool tip, and several 0.5 mm diameter holes at specific distances, 1.0, 1.5, 3.0, and 3.5 mm, from the edge of the forceps. The micro-thermistors were inserted through these holes to measure the temperature inside the tissue at a set distance and depth in relation to the forceps for comparison to the temperatures obtained from the FEM.

The electrical input was provided by the Gyrus ACMI PlasmaKinetic<sup>®</sup> generator, commonly used in surgery. Generator details are listed in Appendix A. The measured AC voltage vs. time between two electrodes in the experiment is shown in Figure 3.3(a). The voltage signal has two modes. The ON mode is a  $\pm 100$  V, 350 kHz frequency sine wave input for about 0.22 s duration. A close-up view of this mode, as illustrated in Figure 3.3(a), shows the shape and period of the sine waveform. This ON mode is repeated five times. The second mode is an OFF mode. The voltage signal detected during this time is a factor of the amplification of noise from the voltage probe, which uses a 100:1 scaling of the signal in order to protect the oscilloscope from the high voltage signal.

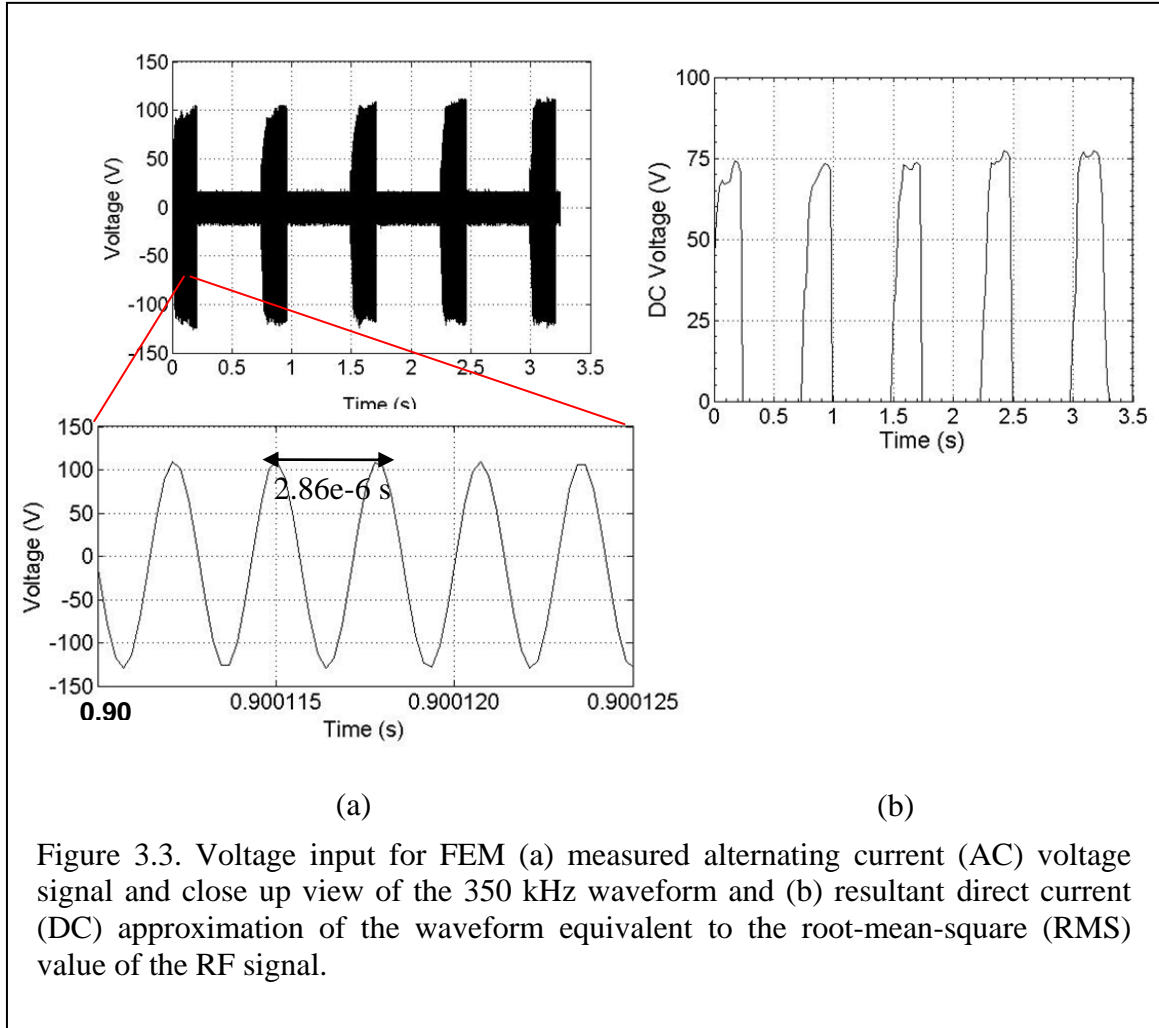


Figure 3.3. Voltage input for FEM (a) measured alternating current (AC) voltage signal and close up view of the 350 kHz waveform and (b) resultant direct current (DC) approximation of the waveform equivalent to the root-mean-square (RMS) value of the RF signal.

### 3.3 Finite Element Modeling

#### 3.3.1 Thermal-Electric FEM Formulation

The analytical modeling of heat transfer in tissue, or bio-heat transfer, was pioneered by the work of Pennes [87] to represent heat sources from metabolism and blood perfusion. The model was refined and studied extensively in the 70s, 80s, and 90s [88-91]. The advancement of finite element and finite difference methods in the 90s has enabled the numerical solution of the bioheat transfer equation for several specific tissue problems. The bio-heat transfer model of tissue includes coupled thermal and fluid (blood) transport phenomena. Through the advances in the modeling of bio-heat transfer,

it is assumed that the solid elements can be used to model the tissue, a multi-phase material consisting of both solid and liquid, with sufficient accuracy.

The linear bio-heat transfer equation for tissue is the general heat equation for conduction with added terms for heat sources, and can be expressed as [87]:

$$\text{---} \tag{3-1}$$

where  $\rho$ ,  $c$ , and  $k$  are tissue density, heat capacity, and thermal conductivity, respectively,  $w_b$  is the effective blood perfusion parameter,  $c_b$  is the blood heat capacity,  $T$  is the local tissue temperature,  $T_a$  is the blood inlet temperature or steady-state temperature of the tissue,  $q_m$  is the metabolic heat generation rate of the tissue,  $q_g$  is the external induced heat generation rate due to electro-surgical heating of the tissue, and  $t$  is time. For all cases, it was assumed that the metabolic heat source and blood perfusion were insignificant ( $q_m = 0$  and  $w_b = 0$ ) as the energy input into the system is much greater than that produced during metabolism [92] and the compression of the tissue from the electrodes inhibits local blood flow. Since the main interest is to simulate the temperatures achieved throughout a cautery procedure, a time-dependent solution is considered.

A quasi-static electrical conduction model was applied to solve the electric field in the tissue using Laplace's equation [93].

$$\tag{3-2}$$

where  $\sigma(T)$  is the temperature-dependent electrical conductivity, and  $V$  is the electric potential. RF coagulation devices operate between 300–550 kHz. At these frequencies, the wavelength is several orders of magnitude larger than the size of the electrode. Thus, the majority of the energy generated by the electrosurgical device is dissipated through electrical conduction rather than capacitive coupling [21].

The difference in the methodology used to solve these governing equations for the cases of constant and temperature-dependent conductivity stems from the method in which Laplace's equation (Eq. 3-2) is solved. In the case where the electrical conductivity is constant, Laplace's equation can be solved independently from the bio-

heat transfer equation (Eq. 3-1). The electric potential ( $V$ ) can be solved quickly over the entire volume and the solution can be implemented into the source term of the heat conduction equation. Since temperature varies spatially, temperature-dependent electrical conductivity is a function of both temperature and position. This dependence requires that Eqs. 3-1 and 3-2 be solved simultaneously which requires iterative computation of both the electrical conductivity and temperature.

Table 3.1. Properties used in the FEM.

| Parameter  | <i>In-vivo</i> spleen<br>[20, 94-96] | Electrode [20]       |
|--|--------------------------------------|----------------------|
| Thermal conductivity ( $k_{T_{ref}}$ ) {W/(m·K)}             | 0.533                                | 70                   |
| Density * Specific heat ( $\rho*c$ ) {J/(K·m <sup>3</sup> )} | 3.9 x10 <sup>6</sup>                 | 2.8 x10 <sup>6</sup> |
| Electrical conductivity ( $\sigma_{T_{ref}}$ ) {S/m}         | 0.33                                 | 4.0x10 <sup>6</sup>  |

### 3.3.2 Properties of Biological Tissue

The electrical and thermal properties of the tissue were available in Refs. [20, 94-96]. The properties for the *in-vivo* spleen and electrodes are shown Table 3.1. For cases using a temperature-dependent electrical conductivity,  $\sigma(T)$ , a standard increase of 2%/°C was used in accordance with Scwhan et al. [97]. Thereby the equations used to determine  $\sigma(T)$  was:

$$3-3$$

where  $T_{ref}$  is the baseline temperature for the conductivity.

There has been work performed on the temperature dependent thermal conductivity,  $k(T)$ , of porcine spleen by Valvano [96] where the relation can be expressed linearly as:

$$3-4$$

### 3.3.3 FEM Techniques

In the multi-physics software COMSOL ver. 3.3, a variation of the heat transfer equation in the Bioheat Transfer Module enables Eq. 3-1 to be solved. This equation is coupled simultaneously in the software with the Conductive Media DC Module to solve Eq. 3-2. The coupling term is the externally induced heat generation term ( $q_g$ ) from Eq. 3-1. This is the resistive heating of the tissue from the RF energy and is defined as  $q_g = \mathbf{J} \cdot \mathbf{E}$ , where  $\mathbf{J}$  is the current density in the unit of  $A/m^2$  and  $\mathbf{E}$  is the electric field in the unit of  $V/m$ .

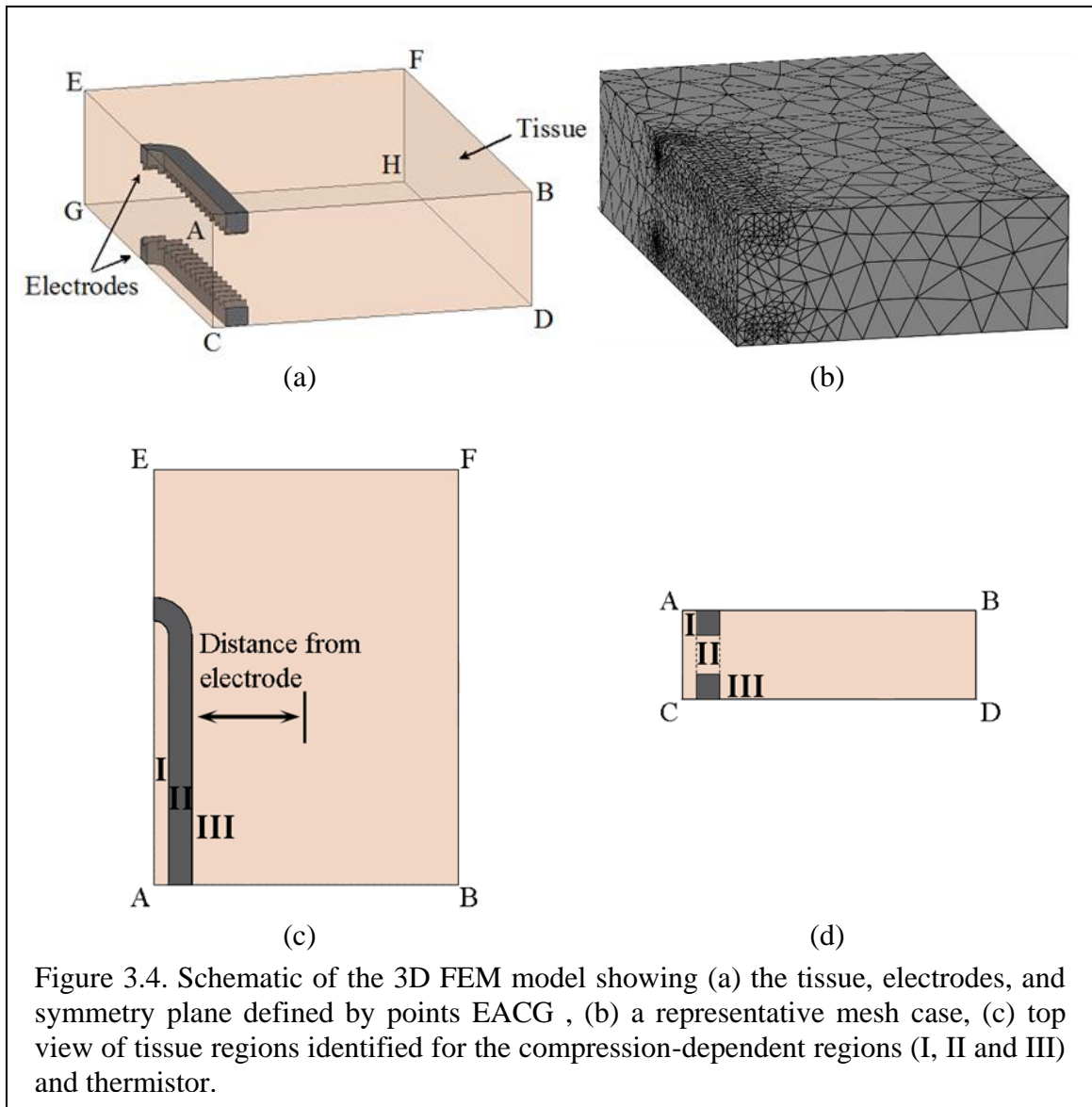


Figure 3.4. Schematic of the 3D FEM model showing (a) the tissue, electrodes, and symmetry plane defined by points EACG , (b) a representative mesh case, (c) top view of tissue regions identified for the compression-dependent regions (I, II and III) and thermistor.

A schematic of the 3D FEM for this study is shown in Figure 3.4. The grooved electrode (to be discussed in Section 3.3.4) embedded in the tissue is illustrated in Figure 3.4(a). The original mesh of the tissue was generated using COMSOL's automatic meshing generator and contained 35,269 of the 3D 4-node linear tetrahedral elements. The mesh refinement feature was used to create a denser mesh in regions near the electrode where temperature information is critical. The mesh was progressively refined until the peak temperature solution at 0.5 mm from the side of electrode did not vary by more than 2%. This resulted in a mesh of 79,476 elements, as shown in Figure 3.4(b), and all other cases except for the flat electrode (to be discussed in Section 3.3.4) were performed with this mesh. For each simulation, the electric field ( $E$ ) and temperature ( $T$ ) were calculated.

The COMSOL PARDISO [98] direct solver using matrix row elimination to solve for the temperature and electrical field was chosen for all analyses. Four input combinations for electrical conductivity and thermal conductivity material properties were compared in the model:

1. Constant electrical conductivity and thermal conductivity ( $\sigma = \sigma_{T_{ref}}$  and  $k = k_{T_{ref}}$ ).
2. Temperature-dependent electrical conductivity, constant thermal conductivity ( $\sigma = \sigma(T)$  and  $k = k_{T_{ref}}$ ).
3. Constant electrical conductivity, temperature-dependent thermal conductivity ( $\sigma = \sigma_{T_{ref}}$  and  $k = k(T)$ ).
4. Temperature-dependent electrical conductivity and thermal conductivity ( $\sigma = \sigma(T)$  and  $k = k(T)$ ).

All variable material properties were determined according to Table 3.1 and Section 3.3.2.

In a separate study, the electrical conductivity of the porcine spleen tissue between the bipolar electrodes was decreased to simulate the impact of tissue compression. Preliminary experiments demonstrate that compression influences the tissue electrical conductivity. This is an area that has limited research but is critical to accurately predict thermal profiles [99, 100]. Preliminary *ex-vivo* tests by the authors demonstrate a tissue electrical resistivity increase of 4 times under 55% compression. In this study, a

simulation was executed with electrical conductivity  $\frac{1}{2}$ – $\frac{1}{4}$  times that of  $\sigma_{T_{ref}}$  while still allowing temperature-dependence of the electrical conductivity but not the thermal conductivity. The tissue in the model was divided into three discrete sections, marked as I, II, and III in the cross-sectional view of the FEM in Figure 3.4(c) and Figure 3.4(d). Tissue between the symmetry plane and the electrodes (I), tissue directly between the electrodes (II), and tissue outside the electrode profile (III) were modeled with electrical conductivity of  $\frac{1}{2}\sigma(T)$ ,  $\frac{1}{4}\sigma(T)$ , and  $\sigma(T)$ , respectively.

### 3.3.4 Electrode Design

The effect of the design of electrode surface in contact with the tissue was studied. The Gyrus ACMI bipolar grooved electrode (GE) design was compared to a flat electrode (FE) design, as shown in Figure 3.5. For both the FE and GE, the model can be defined using a symmetry plane running through the middle of the electrode as seen in Figure 3.4(a). The upper and lower electrode geometries were created by first extruding a 1.25 x 1.15 mm rectangle 12.25 mm in length. This rectangle was then revolved 180° in a circular arc with a 0.725 mm inner radius. For the GE, material was removed from the base rectangular electrode to create the groove profile shown in Figure 3.5(c).

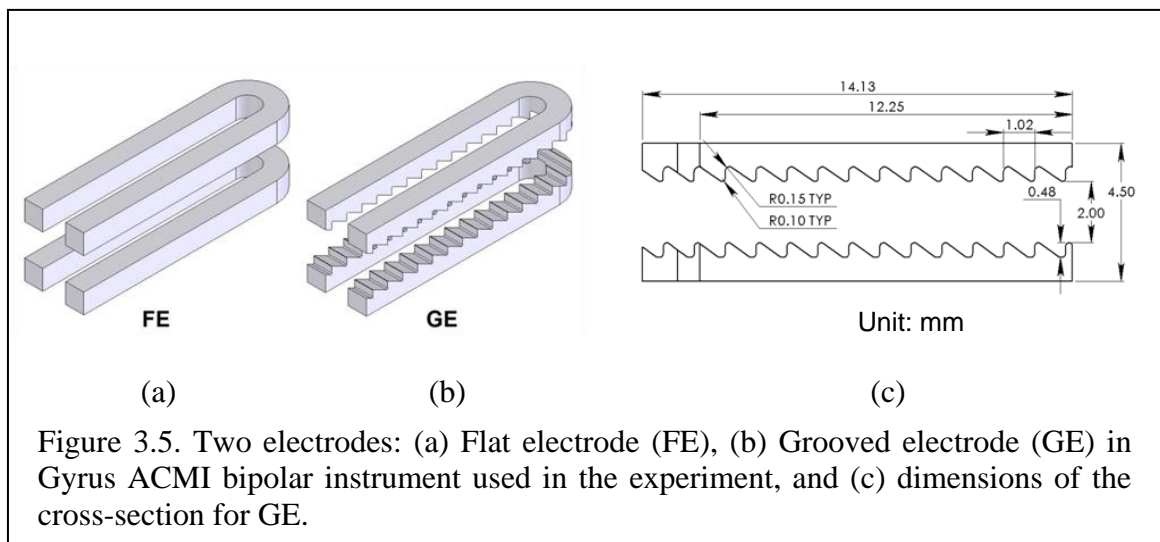


Table 3.2. FEM boundary conditions as marked in Figure 3.4

| Plane | Electrical boundary condition                            | Thermal boundary condition                          |
|-------|--|---|
| ABDC  | Insulated, $\mathbf{n} \cdot (\sigma \nabla V) = 0$      | Free convection, $h = 25 \text{ W/m}^2\text{K}$     |
| ACGE  | Symmetry plane, $\mathbf{n} \cdot (\sigma \nabla V) = 0$ | Symmetry plane, $\mathbf{n} \cdot (k \nabla T) = 0$ |
| ABFE  | Insulated, $\mathbf{n} \cdot (\sigma \nabla V) = 0$      | Free convection $h = 25 \text{ W/m}^2\text{K}$      |
| BDHF  | Insulated, $\mathbf{n} \cdot (\sigma \nabla V) = 0$      | $T_0 = 31^\circ\text{C}$                            |
| CDHG  | Insulated, $\mathbf{n} \cdot (\sigma \nabla V) = 0$      | Free convection $h = 25 \text{ W/m}^2\text{K}$      |
| EFHG  | Insulated, $\mathbf{n} \cdot (\sigma \nabla V) = 0$      | $T_0 = 31^\circ\text{C}$                            |

The seeding of the FE electrodes was identical to that of the GE electrodes for meshing in order to approximate the mesh density of the GE model near the electrodes. This resulted in a mesh of 64,932 3D 4-node tetrahedral elements. In the model temperature was estimated at the midline,  $T_{\text{mid}}$ , of the electrodes and at different distances from the electrode edge in positions corresponding to the thermistors in the *in-vivo* tissue temperature experiments, as shown in Figure 3.4(c). Electrical conductivity was modeled as temperature-dependent ( $+2\%/^\circ\text{C}$ ) while the thermal conductivity was maintained constant for computational efficiency. A separate modeling study was conducted by the authors to investigate the impact of varying temperature dependent electrical and thermal conductivities.

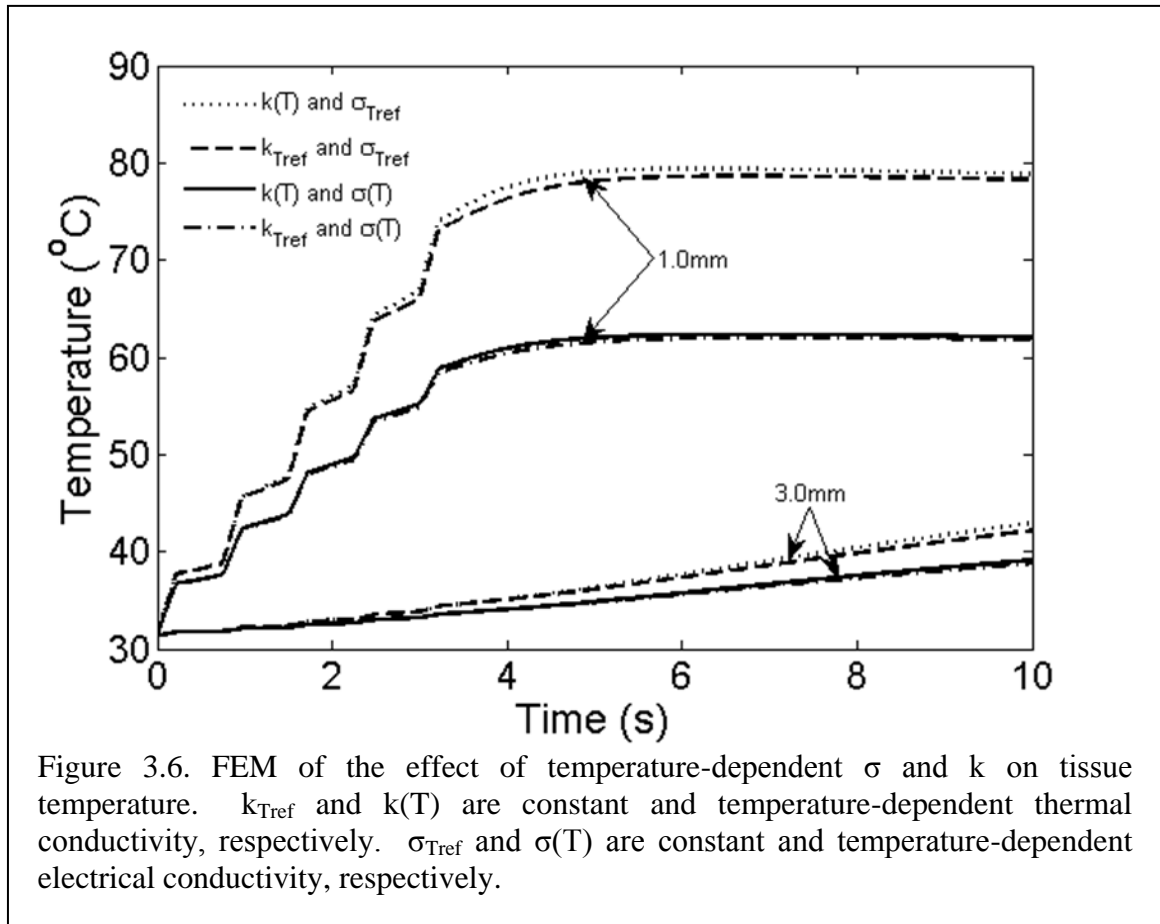
### 3.3.5 Boundary Conditions

As shown in Figure 3.4(a) the active portions of the forceps are embedded into a 25 mm (length AE)  $\times$  15 mm (width AB)  $\times$  4.5 mm (depth AC) region simulating the tissue acted on by the forceps. The boundary conditions were the same for all simulations. Table 3.2 specifies the boundary condition for planes marked by letters A–H in Figure 3.4(a).



The thermal boundary conditions for the surfaces of the tissue not contacting an electrode (planes BDHF and EFHG) are set at a constant temperature  $T_0$ , which is  $31^\circ\text{C}$  in this study. Convection (planes ABFE, ABDC, and CDHG in Figure 3.4(a)) was assumed for all surfaces contacting the electrode except the symmetry plane. In this study, a convection coefficient of  $25 \text{ W/m}^2\text{K}$  is utilized. The symmetry plane (plane ACGE in Figure 3.4(a)) was modeled with zero heat flux such that  $\mathbf{n} \cdot (k \nabla T) = 0$ . Initial condition for temperature was  $T_0=31^\circ\text{C}$  (measured porcine body temperature) for all simulations with the ambient temperature set to  $T_{\text{amb}}=25^\circ\text{C}$  (room temperature).

Insulative electrical boundary conditions were used for all surfaces of the tissue except along the symmetry plane to ensure the current flowed only between the two electrodes. A symmetry plane boundary condition was used along the symmetry plane to mirror the electrical input along that plane.



### **3.3.6 FEM Electrical Input**

Modeling the AC voltage in the 350 kHz frequency range is typically performed by converting the signal to a DC voltage by calculating its root-mean-square (RMS) [18]. For each ON mode the AC signal was divided into ten sections (0.022 s in each section), and RMS averaged resulting in the signal input shown in Figure 3.3(b). Five RF energy pulses with pulse ON mode of 0.22 s and OFF mode of 0.53 s can be identified.

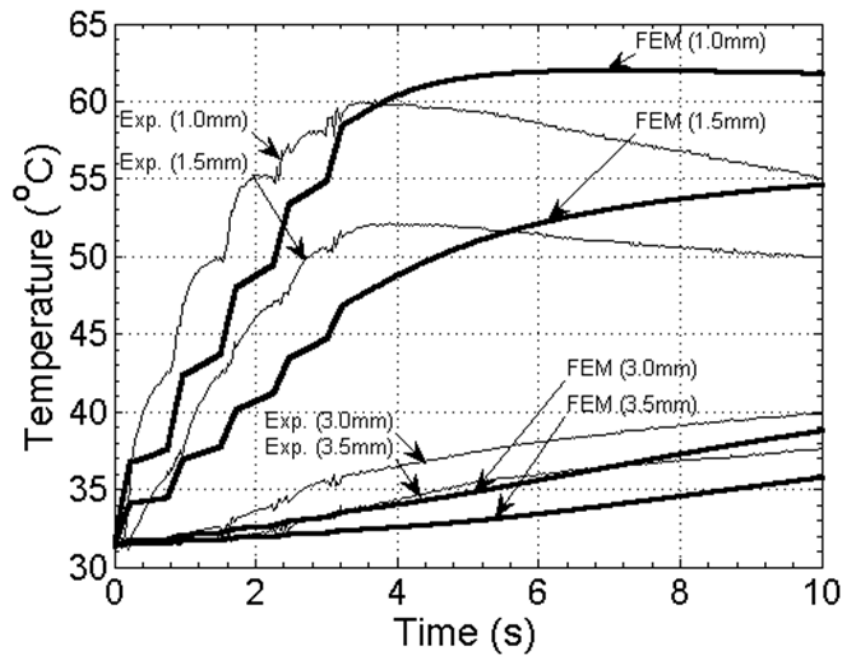
## **3.4 Experimental and FEM Results**

### **3.4.1 Experimental Validation and Effect of Compression**

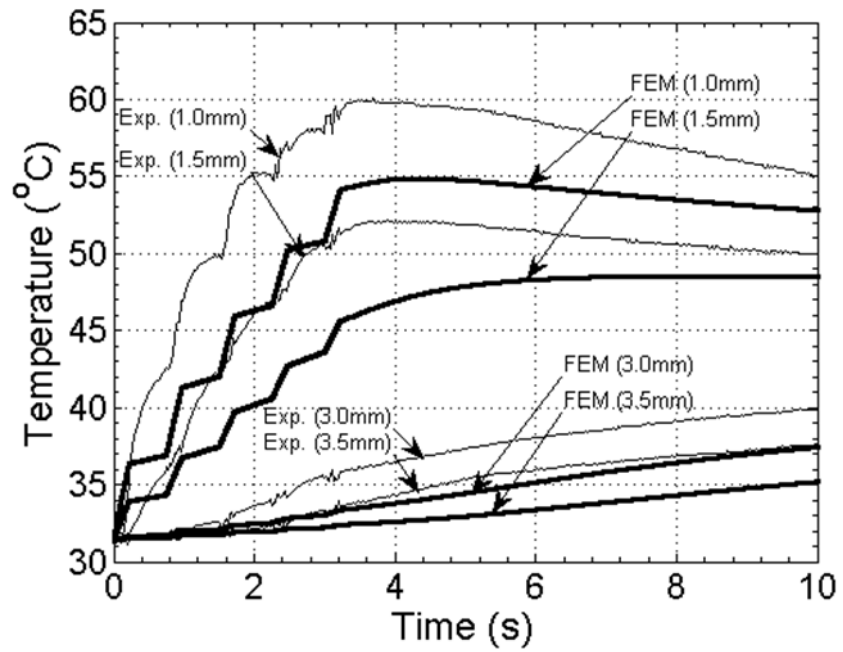
Figure 3.7(a) shows the comparison of measured tissue temperature with FEM predictions during electro-cautery in porcine spleen. The temperatures at four points; 1.0, 1.5, 3.0, and 3.5 mm distance from the tool electrode are presented. The FEM predicts general trends for thermal profiles during active electrosurgical heating compared to the experimental values obtained but is not able to model the post-surgical cooling as accurately. Tissue temperatures reach maxima as late as 7.2 s at 1.0 mm adjacent to the electrode whereas experimental tissue temperatures drop more quickly after cessation of RF energy.

The tissue temperature was observed to rise in a stepped manner near the tool electrode (1.0 and 1.5 mm) from the pulsed electrical input described in Sec. 2. At 3.22 s, the temperature measured at 1.0 mm adjacent to the instrument edge was 60.1°C in the experiment and 58.4°C in the model. These temperatures are above the 50°C threshold identified in Berjano [18] at which proteins denature causing tissue coagulation and permanent thermal damage.

Temperature increased slower in the model than the experiments. This is because of lack of knowledge about how material properties vary according to temperature and compression. Future work identified from this research includes more accurate measurement of the coupled temperature- and compression-dependent properties of biological tissue. Other, less significant sources of error could be the generalized electrical potential input used to simplify the FEM process, the thermistor sensitivity, and variability of thermistor placement.



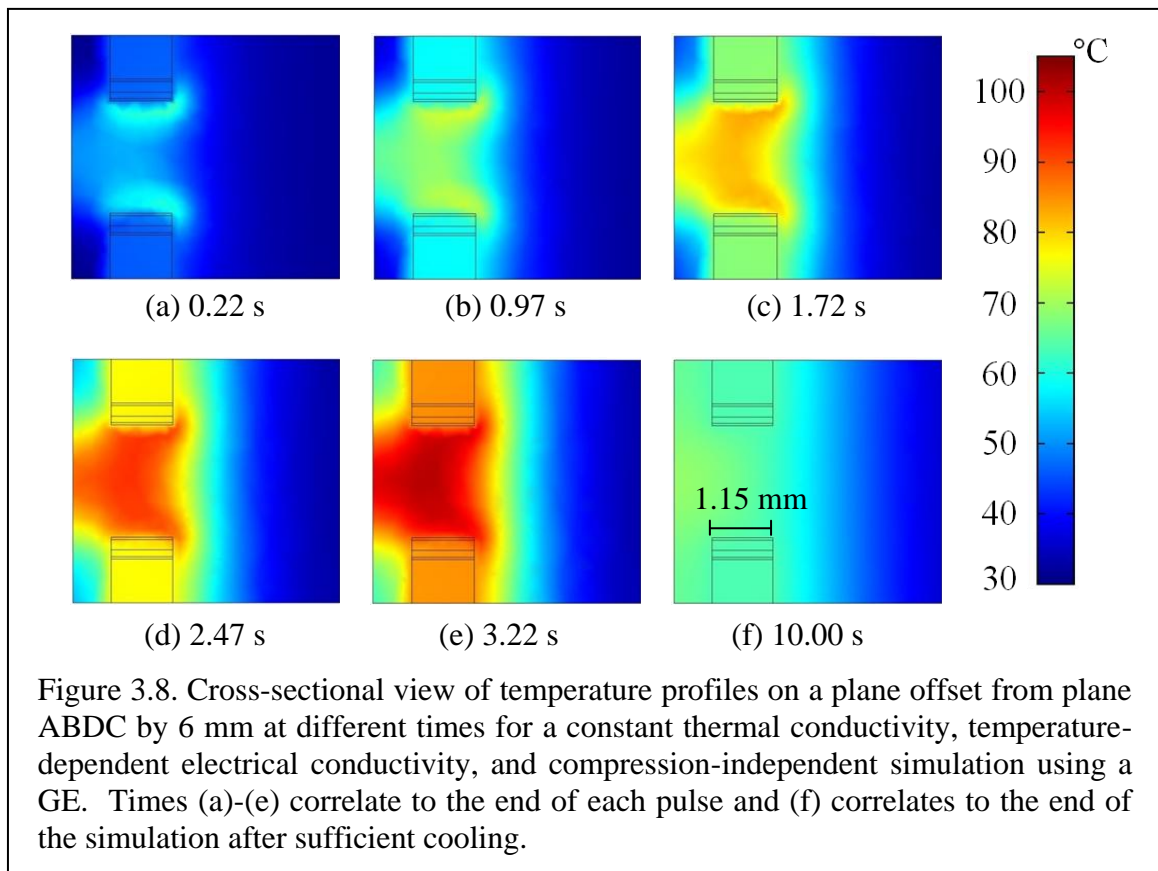
(a)

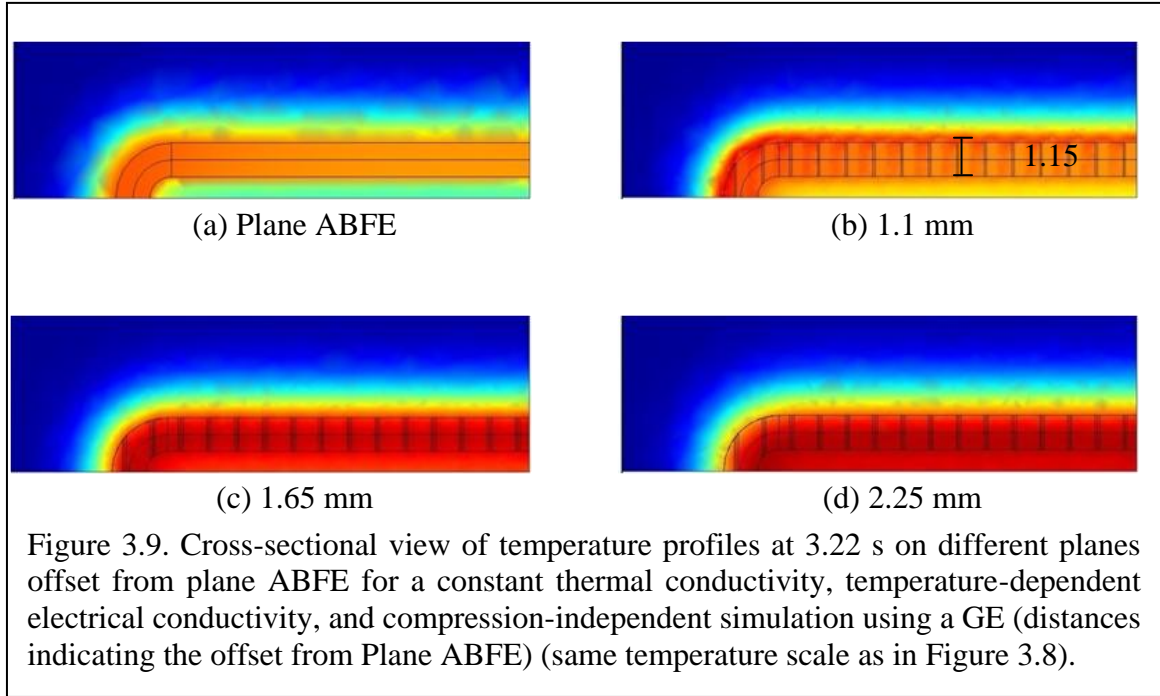


(b)

Figure 3.7. Comparison of thermal profiles for in-vivo experiments and FEM using a GE under a constant thermal conductivity, temperature-dependent electrical conductivity, and (a) compression-independent and (b) compression-dependent simulation.

Figure 3.7(b) shows the FEM temperature vs. time results including the compression effect on tissue electrical conductivity. The temperature in this model drops more quickly than the one without compression-dependency (Figure 3.7(a)), more closely reflecting the cooling time scale noticed in the experiment. The maximum FEM predicted temperature in Figure 3.7(b) at 1 mm and 3.22 s (54.1°C) is much lower than the experimental temperature (60.1°C) and implicates the need for a more accurate compression-dependent tissue electrical conductivity data. Further insight into the compression effect will be given by the temporal and spatial temperature distributions discussed in Section 3.5.1.





### 3.4.2 Effect of Temperature-Dependent Electrical and Thermal Conductivities

Figure 3.6 shows the effect of temperature-dependent thermal and electrical conductivity on temperature profiles at 1.0 and 3.0 mm from the electrode. The simulation results reveal significant differences for different temperature-dependence conditions. The model with temperature-dependent thermal conductivity ( $k(T)$ ) estimated temperatures 0.88°C and 0.02°C higher than the model without  $k(T)$  at 1.0 mm and 3.0 mm adjacent to the tool edge, respectively, at 3.22 s, resulting in only a maximum of 1% temperature change.

The model with temperature-dependent electrical conductivity ( $\sigma(T)$ ) estimated temperatures 14.7°C and 0.85°C lower than the model without  $\sigma(T)$  at 1.0 mm and 3.0 mm from the tool edge, respectively, at 3.22 s, resulting in a maximum of 20% temperature change. The  $\sigma(T)$  has a significant impact and is vital in developing an accurate FEM for bipolar electrosurgery. Therefore, the results in the following sections are for simulations with temperature-dependent  $\sigma(T)$  and constant  $k(T)$ .

### 3.5 Discussion of FEM Results

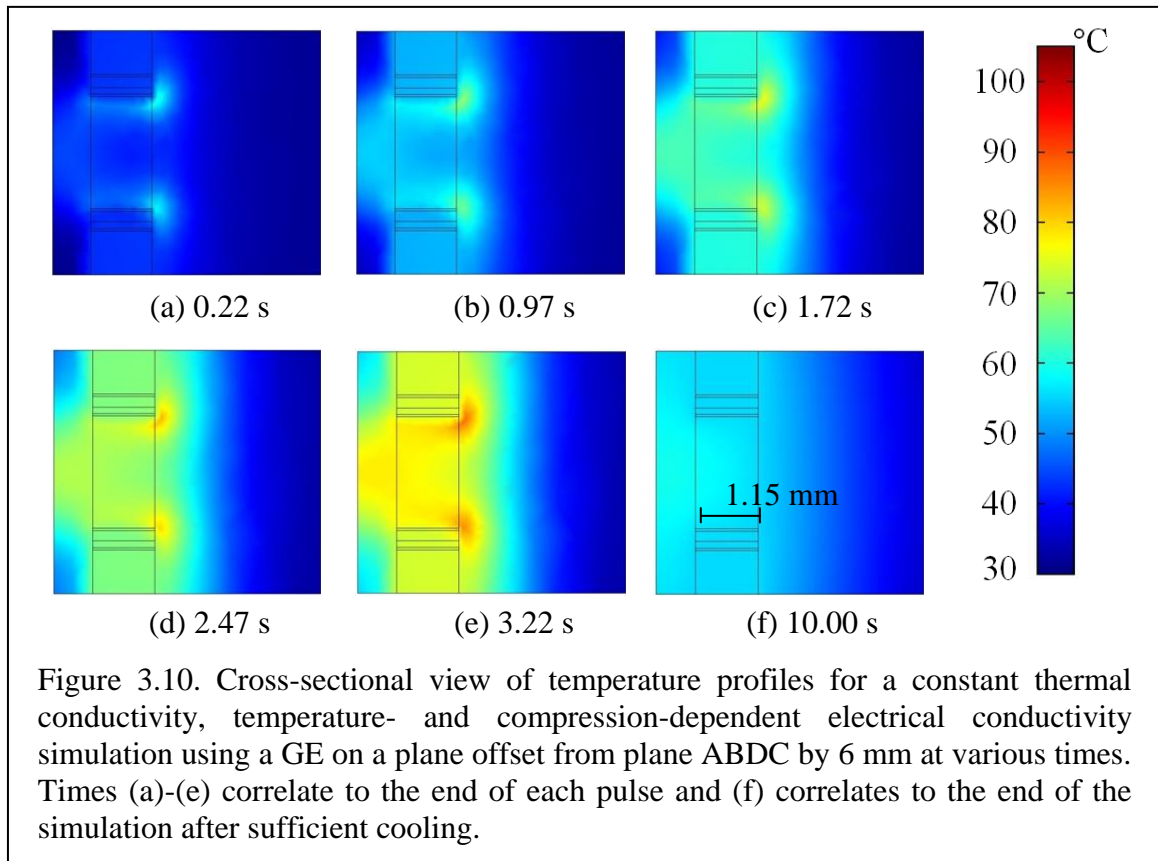
An advantage of FEM is the temperature estimation for different conditions, which would be costly to measure experimentally. The following sections present effects of variations in material properties and electrode design on tissue temperature. The change in internal energy,  $\Delta Q$ , in the unit of J, was determined by:

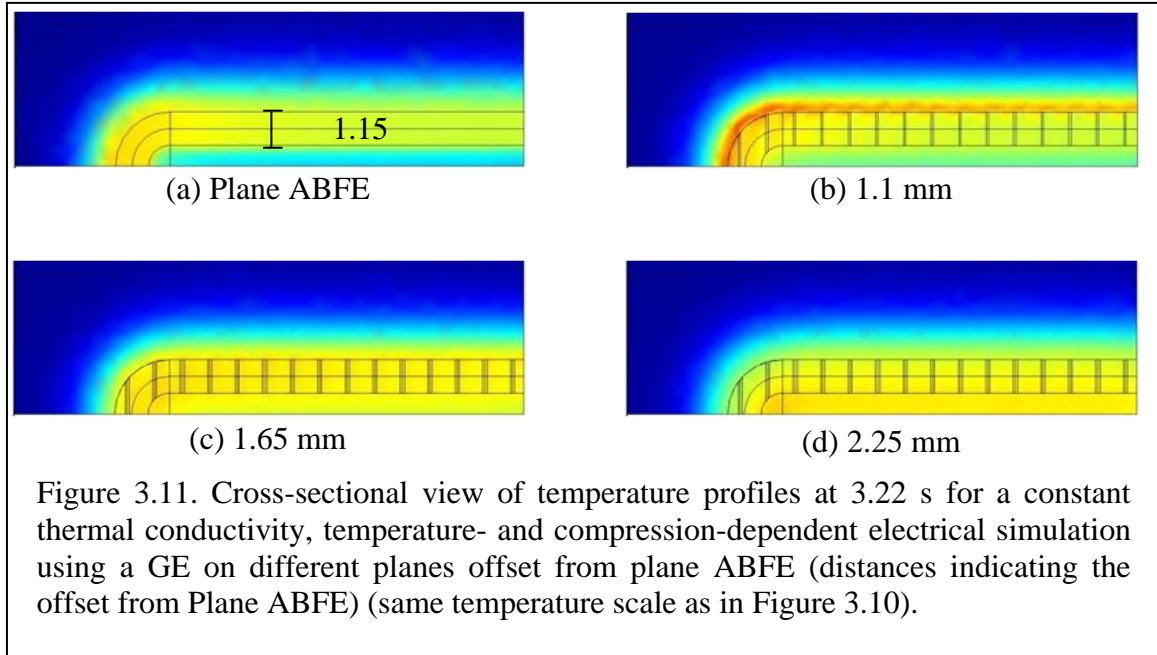
3-5

where  $V^*$  is the tissue volume,  $T_0$  is the tissue temperature at  $t = 0$  s, and  $T_1$  is the tissue temperature at  $t = 3.22$  s.  $\Delta Q$  is calculated in this study for comparison of the energy input between models incorporating compression-dependent and compression-independent electrical conductivity values.

#### 3.5.1 Temporal and Spatial Temperature Distributions

Figure 3.8 shows temporal cross sections of a plane offset from Plane ABDC (as





shown in Figure 3.4(a)) by 6 mm at the end of each of the RF pulses in the simulation. The temperature distribution with a hot spot in the tissue between the electrodes is shown with the symmetry plane on the left side. The temperature is shown to change progressively from the resistive heating until it reaches a maximum temperature of 102.7°C at the end of the last pulse, 3.22 s into the simulation (Figure 3.8(e)).

During each of the pulses the resistive heating happened between the electrodes and near the symmetry plane. The net increase of internal energy in the tissue was  $\Delta Q = 37.3$  J from the resistive heating at the end of the last RF pulse at 3.22 s. Figure 3.8(f) shows the tissue after sufficient cooling and the temperature is more evenly distributed.

Figure 3.9 shows a top view of different planes offset from Plane ABFE (as shown in Figure 3.4(a)) at 3.22 s in the simulation. A large spatial temperature gradient can be seen from the top to the bottom of the electrode. Figure 3.9(d) shows the maximum temperature for the tissue of 102.2°C at the mid plane.

### 3.5.2 *Effect of Compression on Temporal and Spatial Temperature Distributions*

Altering the electrical conductivity of the tissue due to a compression applied by the electrodes (discussed in Section 3.3.3) has a significant role in shaping the resultant

temperature distribution, especially in the modeled post-operative cool down. This dramatic impact is shown in Figure 3.10. Simulations with compression-dependent electrical conductivity show ‘hot-spots’ in the tissue. The temperature is shown to grow progressively until it reaches a maximum temperature of 91.1°C at the end of the last pulse, 3.22 s into the simulation (Figure 3.10(e)). The calculated  $\Delta Q = 6.1$  J is much lower than the 37.3 J of energy added in the compression-independent simulation. The temperatures are much lower in the simulation with compression-dependent electrical conductivity as seen in Figure 3.8-3.11. The reason the temperature rises and falls more accurately in Figure 3.7(b) is the position of the temperature measurement is closer to the hot spots as shown in Figure 3.10 and Figure 3.11. The current density becomes focused at the outer edges of the electrode due to the increased electrical resistivity in the tissue directly between the electrodes, thereby preferentially heating tissue outside of the profile of the instrument.

As shown in Figure 3.12, electrode design plays a significant role in shaping the resultant thermal profiles for bipolar electro-cautery instrumentation. The temperature at 1.0 mm distance from the tool electrode, similar to the simulations of Figure 3.7 and Figure 3.6, is presented. The simulation shows the smooth electrode producing a higher  $T_{\text{mid}}$  of 106.3°C with the difference in temperature between the midline and 1.0 mm from the electrode edge  $\Delta T = 40.4$ °C. The grooved electrode produced a lower  $T_{\text{mid}}$  at 96.6°C with a  $\Delta T = 34.6$ °C. These results suggest that the electrode geometry can be redesigned for control of temperature distributions,  $T_{\text{mid}}$ , and  $\Delta T$  to minimize collateral tissue damage.

In general, including grooves in the electrode minimizes heat generation through a reduction in current density. The collateral tissue damage can be reduced by decreasing the current density, although surgical efficiency drops and surgical time is increased to achieve a similar internal temperature. It was observed by Richter et al. [101] that smooth electrodes tended to not stick as much to tissue as grooved electrodes but also were less effective in vessel sealing. The FEM results presented here raise questions about the role temperature plays in tissue sticking and the creation of an effective seal.



### 3.6 Conclusions

This study demonstrated the capability of using a FEM to study bipolar electrosurgical procedures and demonstrated the importance of incorporating appropriate temperature-dependent tissue properties, electrode geometry, and compression-dependent properties in the FEM model. Incorporating the temperature-dependent thermal conductivity values from the literature into the FEM resulted in only a 1% increase in tissue temperature at 1.0 mm adjacent to the electrode at 3.22 s. However, incorporating the temperature-dependent electrical conductivity in the FEM model resulted in a significant 20% decrease in temperature at 1.0 mm adjacent to the electrode at 3.22 s. FEM results showed the Gyrus ACMI 5mm Cutting Forceps generated a peak temperature at 1.0 mm adjacent to the electrode of 58.4°C at 3.22 s while an identical model imposing compression-dependent tissue electrical conductivity estimated a peak

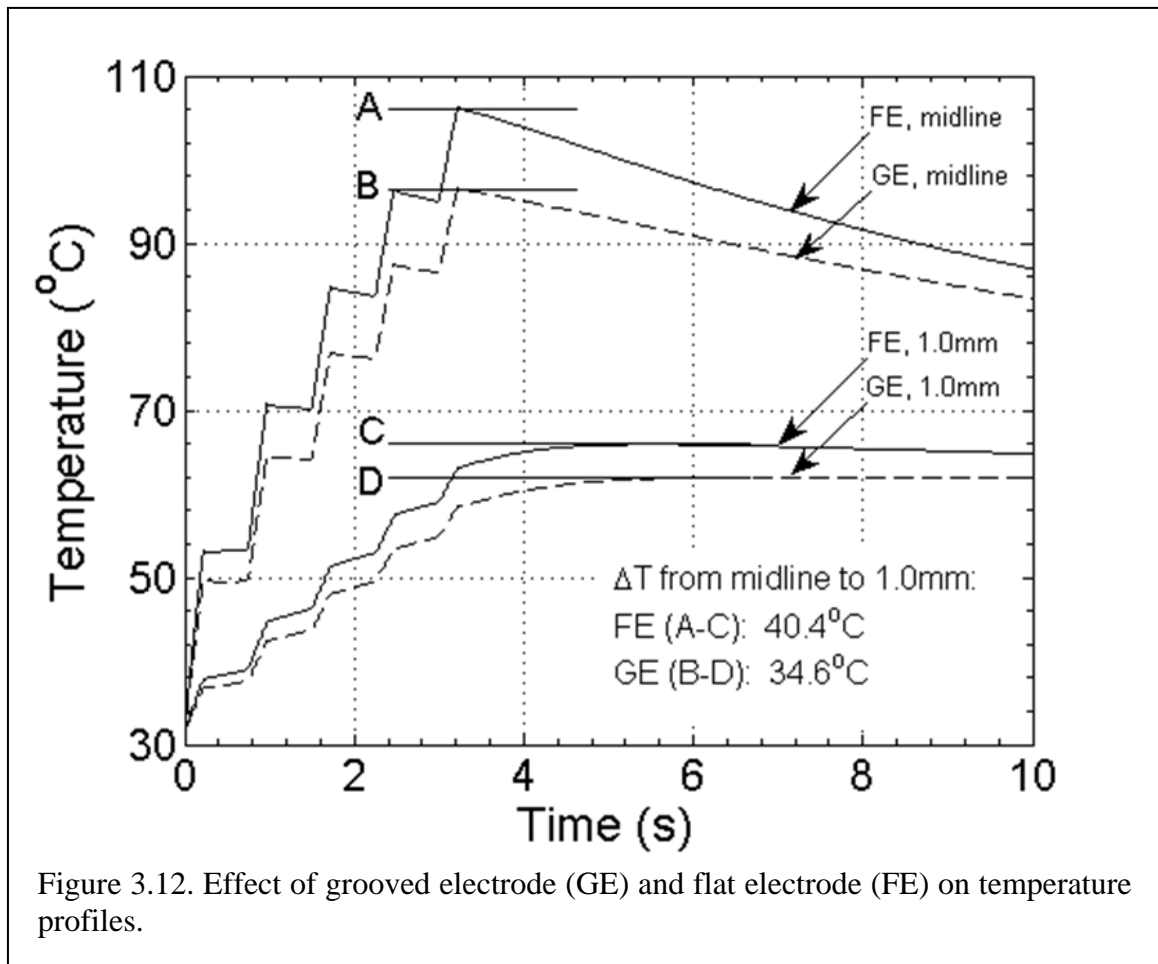


Figure 3.12. Effect of grooved electrode (GE) and flat electrode (FE) on temperature profiles.

temperature at 1.0 mm adjacent to the electrode of 54.1°C at 3.22 s. This compared to an experimentally measured peak temperature of 60.1°C at 1.0 mm adjacent to the electrode at 3.22 s. The 83.6% difference in  $\Delta Q$  from the compression-independent to the compression-dependent simulations confirmed significantly less heating took place in the compression-dependent model. While the model without compression-dependent electrical conductivity more closely matched the temperature values of the experiment during heating, the model with compression-dependent electrical conductivity more closely matched the overall temperature profile for the heating and cooling of the tissue, thus providing a better comparison of the heat transfer time scale. Flat electrodes (FE) were shown to generate temperatures 9.7°C hotter at the symmetry plane and 3.9°C hotter at 1.0 mm adjacent to the electrode as compared to the grooved electrode (GE) design.

Limitations of this model include its assumption of a continual electrode-tissue contact which may not be realistic in all situations. While the voltage signal was seen to be nearly constant for this case, a more versatile model would include a capability to reproduce a constant power setting. It is known that at temperatures near 100°C temperature-dependent material properties experience non-linear phenomenon due to interstitial fluid phase changes. Therefore, at these high temperatures, the model will need refinements to accommodate analyses in these ranges. Also, the impact of the load transmitted to the tissue by the forceps and consequent compression exerted on the tissue during such a procedure is unknown and currently being investigated. This compression may greatly impact tissue material properties, particularly the electrical conductivity, and therefore temperature distributions and thermal energy flow throughout the tissue. As shown in the compression-dependent model, allowing for a more resistive tissue between the electrodes resulted in tissue heating occurring most quickly outside the profile of the instrument. However, for the model without compression-dependent electrical conductivity, the quickest tissue heating is seen to occur throughout the tissue between the electrodes. In this model discrete conductivity changes were imposed on the tissue, but future models will incorporate compression-dependent material properties on a continuum.

The impact that electrode geometry design has on thermal penetration into tissue lateral to the electrode could play a major role in the future design of bipolar instrumentation. It is shown in this study that electrode geometry changes can lead to increased temperatures and thermal gradients. Advanced design considerations can play an important role in minimizing collateral tissue damage and should be implemented whenever feasible.

## **Chapter 4 Bipolar Electrosurgery Using Active Cooling Channels for the Minimization of Thermal Spread**

### **4.1 Introduction**

Electrosurgery, which uses radio frequency (RF) electrical currents to actively heat biological tissues with high power density, is a surgical technique that has long been used to coagulate and remove tissue while minimizing bleeding during surgical procedures [10]. The use of energized dissection systems has dramatically improved laparoscopic dissection and hemostasis while allowing more procedures to be performed in a minimally invasive fashion [84]. Through the years, researchers have worked to improve this technology in order to enhance its execution both in open and endoscopic cases. Miniaturization of the electrosurgical instrument has enabled the use of minimally invasive or laparoscopic surgical procedures, thereby reducing patient recovery time. The success of laparoscopic surgery from both the surgeon and the patient perspective has provided the inertia for using these instruments in increasingly complex procedures. However, their success in procedures, such as prostatectomy and hysterectomy, has been hampered by collateral damage to local neural structures impacting patient postoperative quality of life [3, 4, 7]. The extent of this collateral damage has been studied previously with varying degrees of cross-correlation [15, 16].

Heat generated from electrosurgery has a harmful side effect of spreading and damaging the surrounding tissue and, more importantly, the nerves in the neurovascular bundle (NVB) in surgery. This phenomenon is referred to as thermal spread in surgery [16, 32, 102, 103]. Collateral tissue damage has been highlighted as a major concern for postoperative side effects, especially for procedures occurring near critical nervous regions, such as prostatectomy and hysterectomy [3, 7, 104]. These side effects include impotence and incontinence with varying lengths of duration from temporary to permanent. Recent advances have been made in generator and control technologies that pulse the input voltage and turn off the power once the tissue has been determined to be

coagulated. Nevertheless, thermal spreads of 3–5 mm are still reported in ideal situations, which can cause irreversible side effects during procedures as it is difficult for the surgeon to control this thermal spread.

One method for controlling thermal damage during electrosurgery is the use of saline irrigation to either remove thermal energy from the surgical area (bipolar) or maintain a cool electrode and therefore maximize the injection of current into the tissue for longer ablations (monopolar). A new method of cooling is introduced in this paper, whereby cooling channels placed alongside the powered bipolar electrodes actively sink thermal energy away from the tissue, thereby protecting adjacent tissue from thermal energy. Using this technique in bipolar electrosurgery will allow the use of these instruments in critical techniques.

The purpose of this study is to validate the use of actively cooled channels alongside bipolar electrodes to compress and sink thermal energy away from adjacent tissue to create an actively cooled bipolar forceps capable of efficiently coagulating tissue while minimizing collateral damage to surrounding tissues.

#### 4.2 Materials and Methods

The setting was an animal surgery operating room at the University of Michigan School Of Medicine. The protocol was approved by the University Committee on Use and Care of Animals (UCUCA). The experiment was carried out on one large (~50kg),

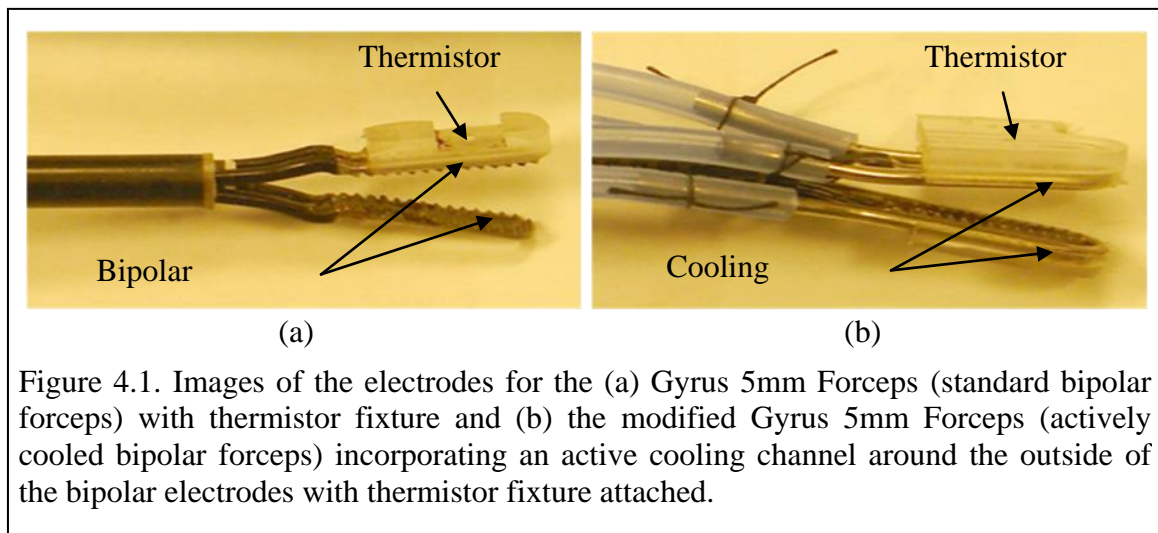


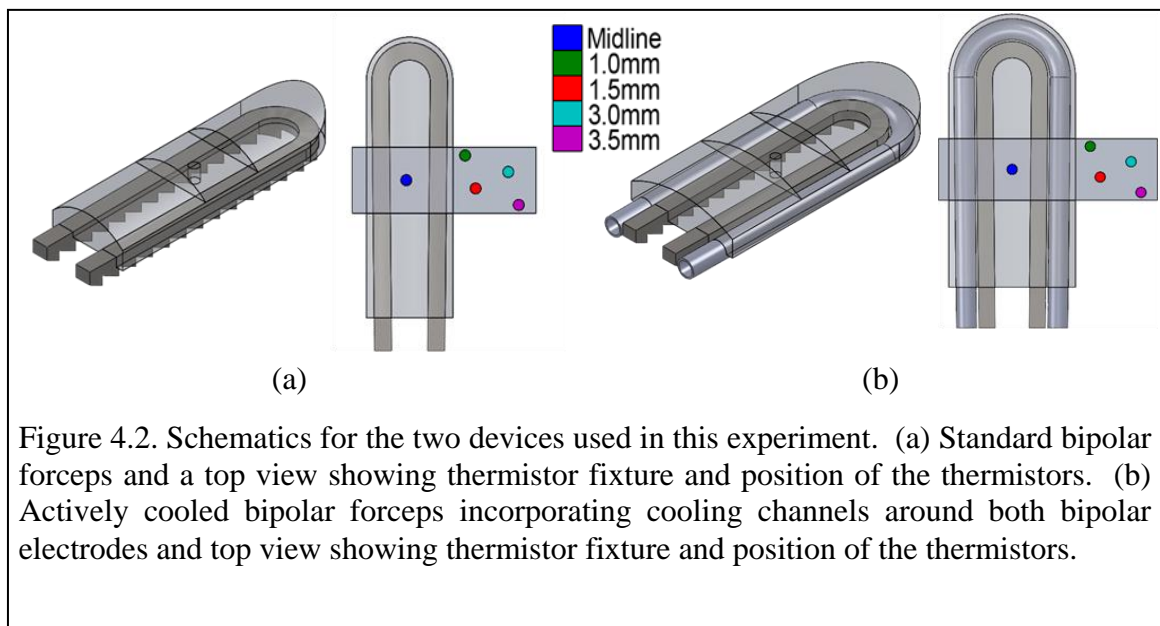
Figure 4.1. Images of the electrodes for the (a) Gyrus 5mm Forceps (standard bipolar forceps) with thermistor fixture and (b) the modified Gyrus 5mm Forceps (actively cooled bipolar forceps) incorporating an active cooling channel around the outside of the bipolar electrodes with thermistor fixture attached.

white, landrace cross pig.

Anesthesia was induced in the animal with intramuscular injections of telazol (6 mg/kg) and xylazine (2.2 mg/kg), and then the animal was intubated, positioned supine on the operating table, and maintained under general anesthesia with isoflurane (2 to 2.5%) while on a ventilator (10 ml/kg) at 12 bpm. Oxygen saturation, pulse rate, respiratory rate, mucous membrane color, and blinking reflex were monitored with pulse oximetry at regular intervals. Upon completion of the experiment, the animal was euthanized via barbiturate overdose.

During the course of the operation, a long midline laparotomy incision was made to expose the abdominal cavity and allow access to the spleen and mesentery, which were the target tissues for the experiment. This decision was based on the target organ's size and uniform thickness. The spleen and mesentery were exteriorized to perform the instrument measurements and were replaced within the abdominal cavity during periods of no testing.

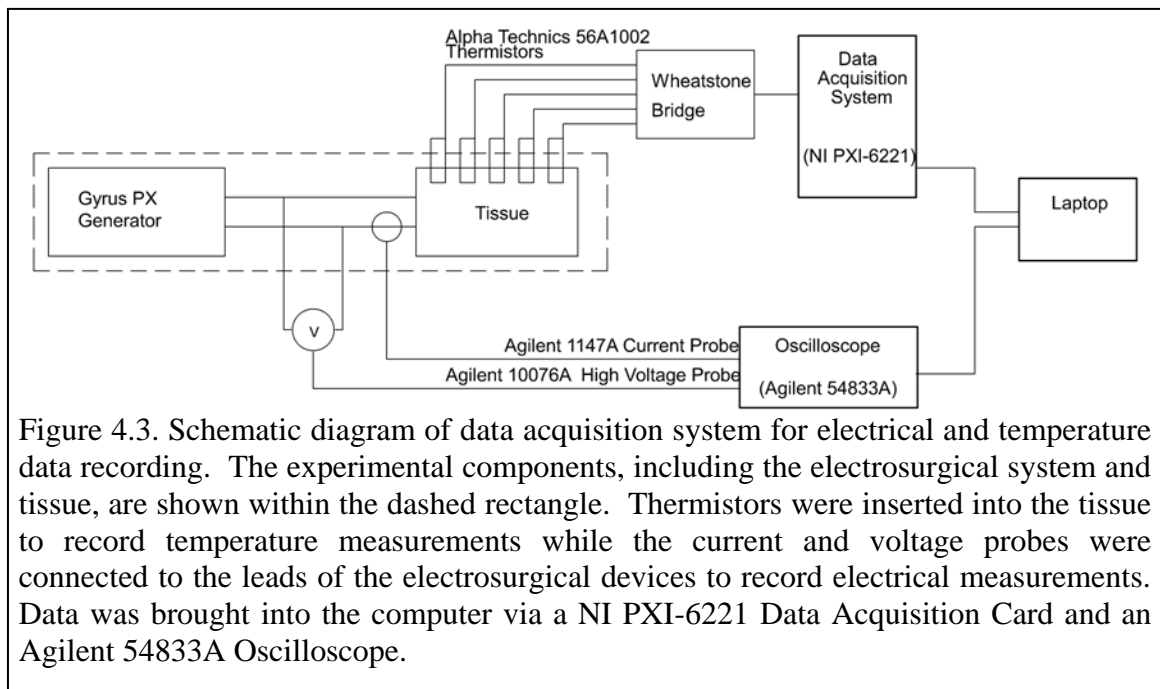
Two energized 5 mm laparoscopic devices were used: an advanced bipolar electrocautery instrument as represented by the Gyrus Plasmakinetic<sup>®</sup> Cutting Forceps; and a modified bipolar electrocautery instrument fitted with an active cooling channel around both the bipolar electrodes, as shown in Figure 4.1. From this point onward, the



two devices will be referred to as standard bipolar forceps and actively cooled bipolar forceps, respectively. Both devices were powered by the Gyrus PlasmaKinetic<sup>®</sup> Surgical Generator. Further generator details are listed in Appendix A.

Tissue temperatures were measured at a depth of 2.0 mm below the tissue surface using thermistors placed at 1.0, 1.5, 3.0, and 3.5 mm from each tool edge as well as at the midline of the device (see Figure 4.2) as described in Dodde et al. [83]. Each thermistor was housed inside a hypodermic stainless steel tube for increased stability. Polycarbonate fixtures created for each of the devices ensured temperature measurements were recorded at precise distances from the tool edge. Each fixture was custom designed for the instrument with an appendage extending from the side of the instrument allowing for thermistor deployment adjacent to the device.

Temperatures were measured using Alpha Technics (Irvine, CA) 56A1002-C3 micro-thermistors with 0.46 mm outside diameter. Temperature data was collected using a NI PXI-1033 Chassis fitted with a NI PXI-6221 data acquisition card using a five channel parallel Wheatstone bridge circuit for signal conditioning. Electrical waveform data was acquired using an Agilent (Santa Clara, CA) 54833A 1 GHz oscilloscope in peak detect mode (PDM). An Agilent 10076A 100:1 250 MHz High Voltage Probe was used to



measure the voltage signal and an Agilent 1147A 50 MHz/15A AC/DC Current Probe was used to measure the current signal. PDM was used to maximize the use of the limited on-board memory of the oscilloscope (256kB). A Labview<sup>®</sup> program was used to monitor the data acquisition and the signal from the current probe was used as a trigger for data collection initiation. Details about the Labview program are in Appendix C Bioimpedance Labview Program. A schematic of the overall experimental procedure is shown in Figure 4.3.

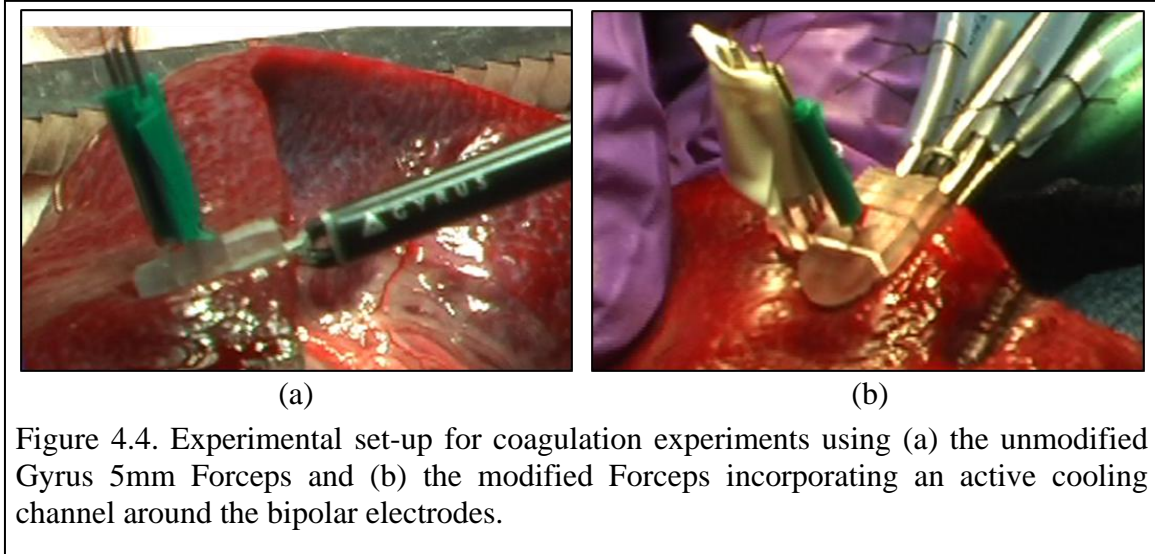
Within each device, the bite size for the surgical procedures was limited to  $\frac{3}{4}$  of the jaw length to avoid variations in tissue effect at the jaw hinge area. Lateral tension to the tissue was avoided and rotational motions were used only when required to position the instruments. Default power settings were used for each device as described below.

#### **4.2.1 *Spleen Coagulation***

An incision was made with a cold scalpel to expose the abdominal cavity and allow access to the spleen. The spleen was removed far enough to perform the surgical procedures and will be replaced within the abdominal cavity during periods of no surgery. The experimental set-up for the standard bipolar forceps coagulation is shown in Figure 4.4(a) and the experimental set-up for the actively cooled bipolar forceps coagulation is shown in Figure 4.4(b).

Five (5) coagulations were performed with each of the devices on separate sides of the spleen at a power setting of VP3 40 which corresponds to the Gyrus vapor pulse coagulation setting for vascular, high impedance tissue with 40 W of targeted output power. A minimum of 6 mm was kept from each coagulation trial to ensure previous thermal effects are not impacting current trials. Tissue temperatures were monitored as described above for each of the cases.





#### 4.2.2 Mesenteric Vessel Sealing

The abdominal incision was enlarged to allow access to the mesenteric vasculature. Vessels were chosen based on their diameter being in the range of 2-4 mm. The experimental set-up is similar to that for the splenic coagulation, as shown in Figure 4.4.

Six (6) groups of vessels were sealed with the standard bipolar forceps and ten (10) groups of vessels were sealed with the actively cooled bipolar forceps. Both devices were operated at a power setting of VP1 30 which corresponds to the Gyrus vapor pulse coagulation setting for thin, low impedance tissue with 30 W of targeted output power. Surface vessel temperatures were recorded only so as not to allow the thermistors to penetrate the vessels.

#### 4.3 Results

The standard bipolar forceps and the actively cooled bipolar forceps were tested a total of five times each on splenic tissue with representative thermal profiles for each device shown in Figure 4.5. The average maximum temperature at the midline and at 1.0 mm adjacent to the tool edge for the standard bipolar forceps were 65.2°C (SD 11.7°C) and 63.8°C (SD 6.9°C), respectively. The average maximum temperature at the midline and at 1.0 mm adjacent to the tool edge for the actively cooled bipolar forceps were 88.6°C (SD 3.6°C) and 29.9°C (SD 2.0°C), respectively. Note that temperature data for

the standard bipolar forceps at a distance of 3.5 mm adjacent to the device edge is not available.

The standard bipolar forceps was tested a total of six times and the actively cooled bipolar forceps was tested a total of ten times on mesenteric tissue with representative thermal profiles for each device shown in Figure 4.6. The average maximum temperature at the midline and at 1.0 mm adjacent to the tool edge for the standard bipolar forceps were 81.8°C (SD 5.4°C) and 74.0°C (SD 6.7°C), respectively. The average maximum temperature at the midline and at 1.0 mm adjacent to the tool edge for the actively cooled bipolar forceps were 77.1°C (SD 13.2°C) and 24.0°C (SD 1.0°C), respectively. The starting midline temperatures for the actively cooled forceps are seen to be lower than those for the standard bipolar forceps due to the flow of coolant through the channels. The  $\Delta T$  is also seen to be greater at the midline, on average, for the actively cooled bipolar forceps as compared to the standard bipolar forceps (see Figure 4.5).

For experiments on both the splenic and mesenteric tissues, the modified, actively cooled device shows greater changes in midline temperature when compared to the standard, unmodified device (see Figure 4.7). For the splenic tissue, the average  $\Delta T$  at the midline was 31.6°C (SD 12.4°C) for the unmodified device and 59.1°C (SD 5.0°C) for the actively cooled device. For the mesenteric tissue, the average  $\Delta T$  at the midline was 50.5°C (SD 6.4°C) for the unmodified device and 54.3°C (SD 13.0°C) for the actively cooled device.

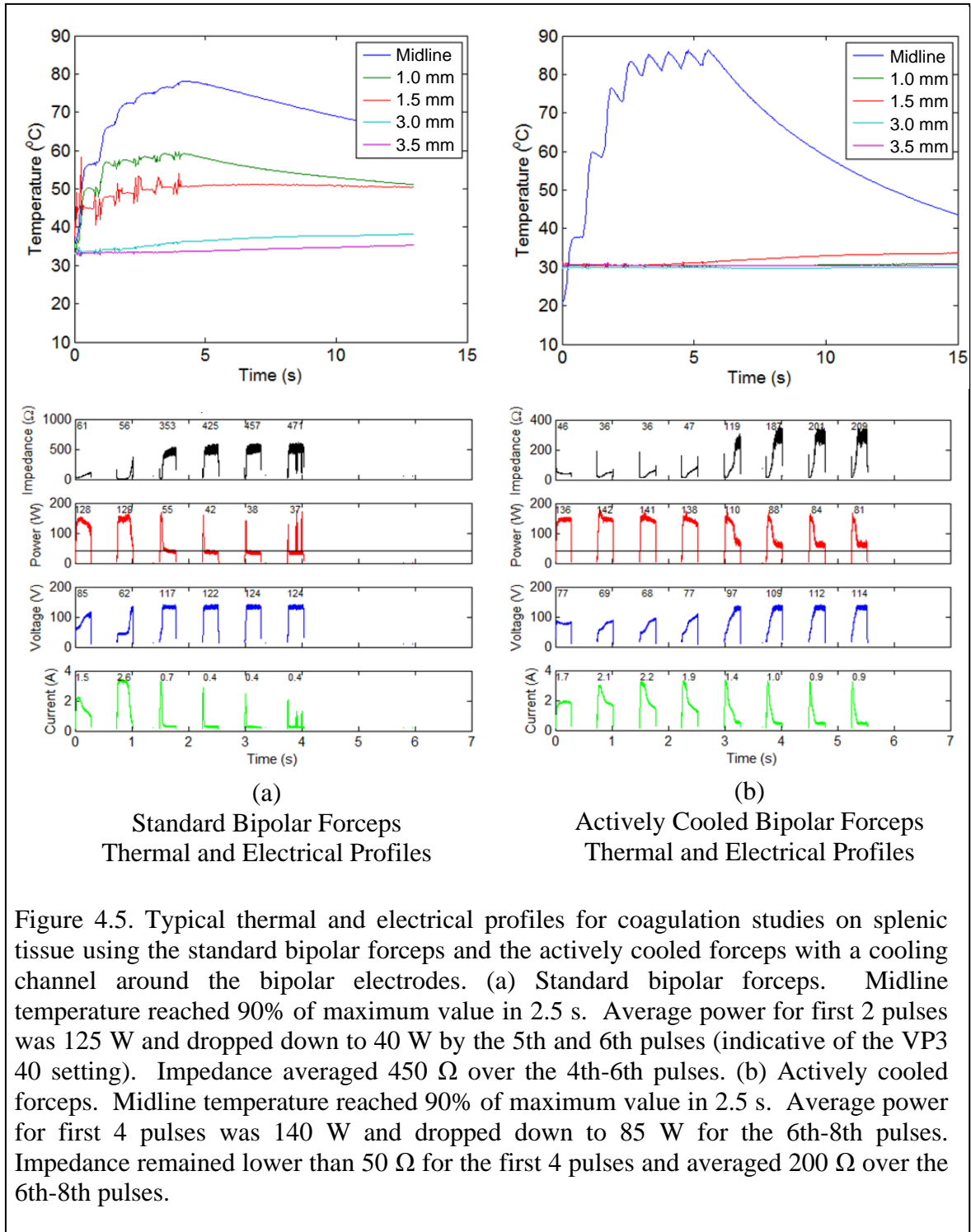


Figure 4.5. Typical thermal and electrical profiles for coagulation studies on splenic tissue using the standard bipolar forceps and the actively cooled forceps with a cooling channel around the bipolar electrodes. (a) Standard bipolar forceps. Midline temperature reached 90% of maximum value in 2.5 s. Average power for first 2 pulses was 125 W and dropped down to 40 W by the 5th and 6th pulses (indicative of the VP3 40 setting). Impedance averaged 450  $\Omega$  over the 4th-6th pulses. (b) Actively cooled bipolar forceps. Midline temperature reached 90% of maximum value in 2.5 s. Average power for first 4 pulses was 140 W and dropped down to 85 W for the 6th-8th pulses. Impedance remained lower than 50  $\Omega$  for the first 4 pulses and averaged 200  $\Omega$  over the 6th-8th pulses.

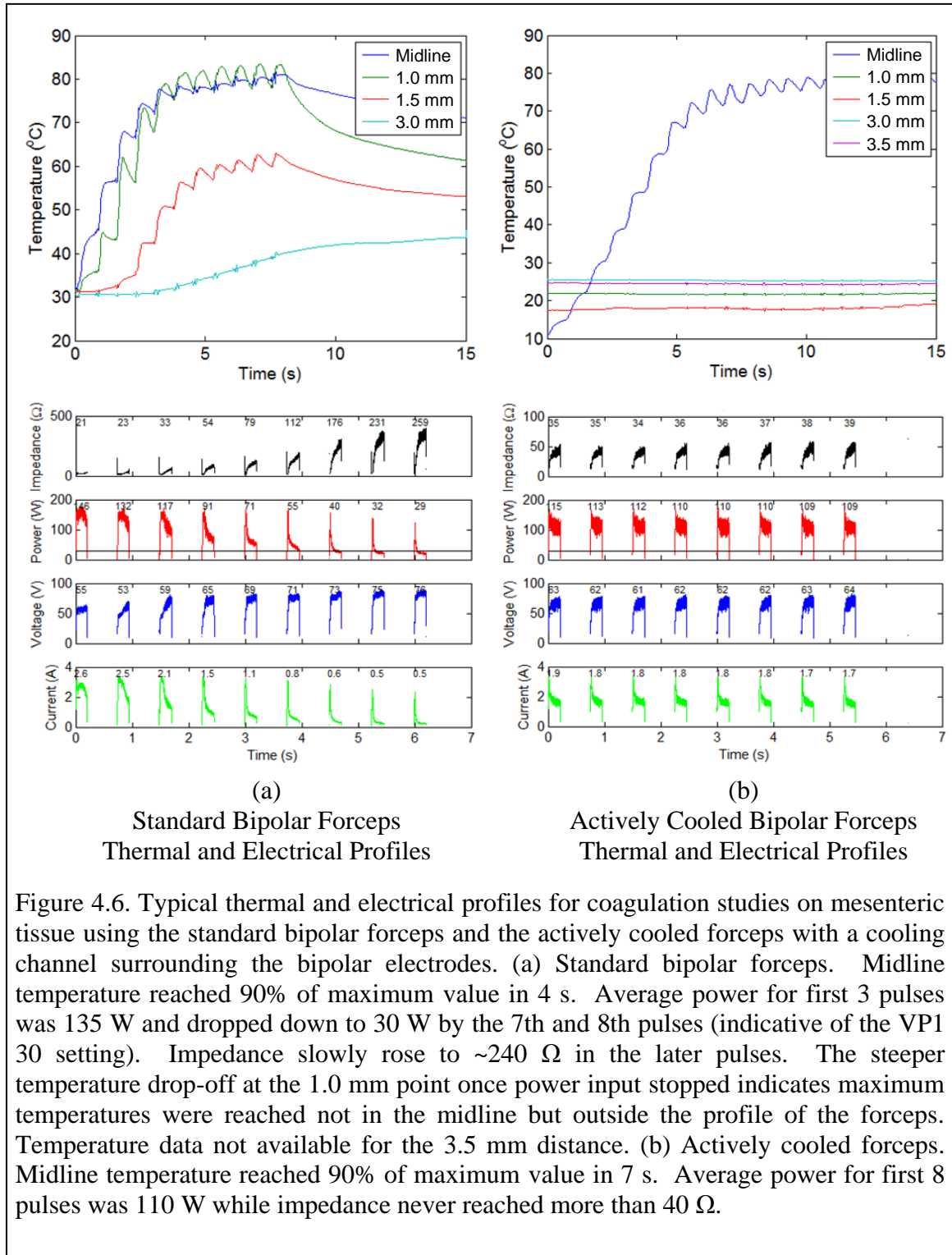


Figure 4.6. Typical thermal and electrical profiles for coagulation studies on mesenteric tissue using the standard bipolar forceps and the actively cooled forceps with a cooling channel surrounding the bipolar electrodes. (a) Standard bipolar forceps. Midline temperature reached 90% of maximum value in 4 s. Average power for first 3 pulses was 135 W and dropped down to 30 W by the 7th and 8th pulses (indicative of the VP1 30 setting). Impedance slowly rose to  $\sim 240 \Omega$  in the later pulses. The steeper temperature drop-off at the 1.0 mm point once power input stopped indicates maximum temperatures were reached not in the midline but outside the profile of the forceps. Temperature data not available for the 3.5 mm distance. (b) Actively cooled forceps. Midline temperature reached 90% of maximum value in 7 s. Average power for first 8 pulses was 110 W while impedance never reached more than  $40 \Omega$ .

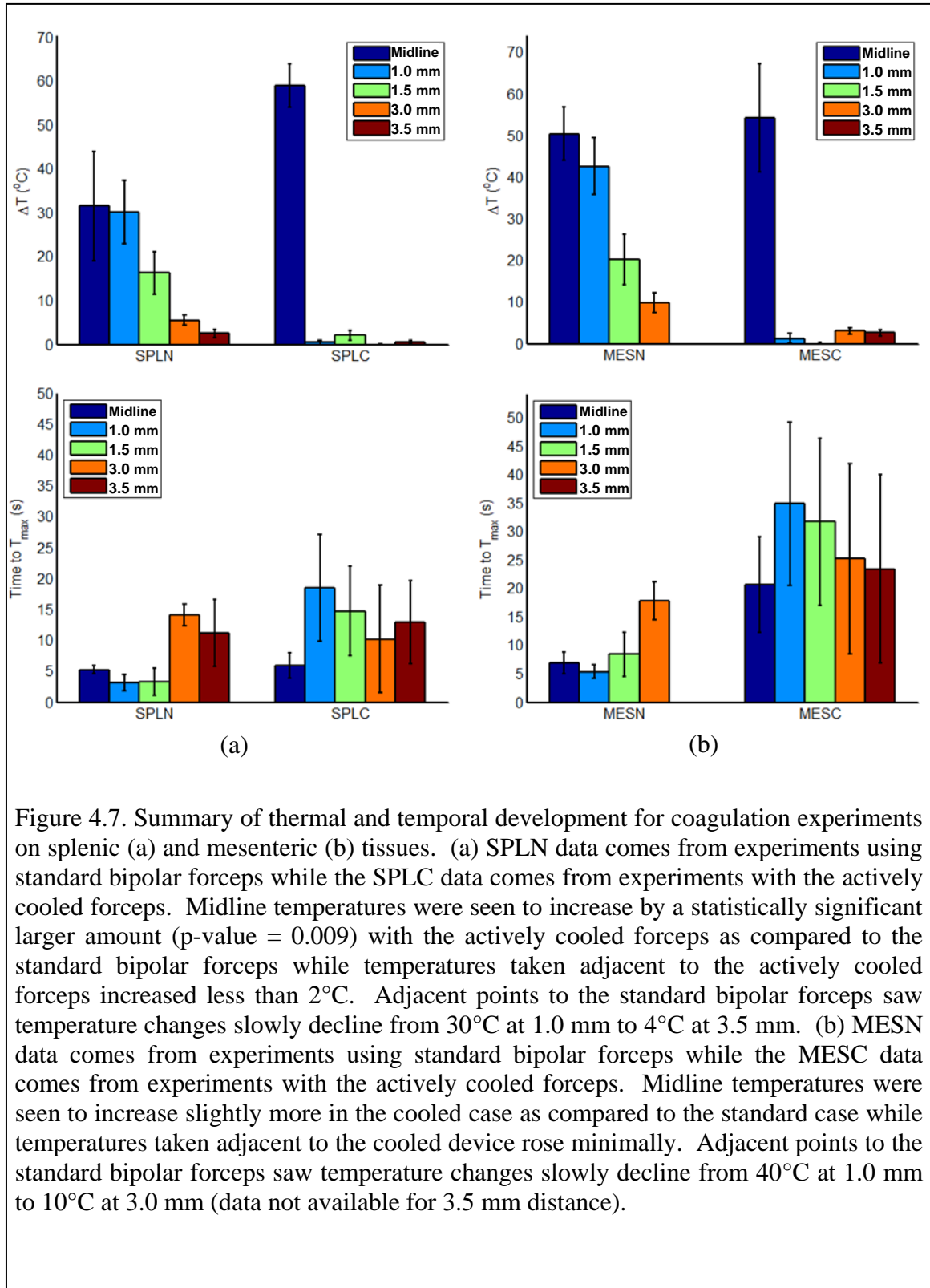


Figure 4.7. Summary of thermal and temporal development for coagulation experiments on splenic (a) and mesenteric (b) tissues. (a) SPLN data comes from experiments using standard bipolar forceps while the SPLC data comes from experiments with the actively cooled forceps. Midline temperatures were seen to increase by a statistically significant larger amount ( $p$ -value = 0.009) with the actively cooled forceps as compared to the standard bipolar forceps while temperatures taken adjacent to the actively cooled forceps increased less than  $2^{\circ}\text{C}$ . Adjacent points to the standard bipolar forceps saw temperature changes slowly decline from  $30^{\circ}\text{C}$  at 1.0 mm to  $4^{\circ}\text{C}$  at 3.5 mm. (b) MESN data comes from experiments using standard bipolar forceps while the MESC data comes from experiments with the actively cooled forceps. Midline temperatures were seen to increase slightly more in the cooled case as compared to the standard case while temperatures taken adjacent to the cooled device rose minimally. Adjacent points to the standard bipolar forceps saw temperature changes slowly decline from  $40^{\circ}\text{C}$  at 1.0 mm to  $10^{\circ}\text{C}$  at 3.0 mm (data not available for 3.5 mm distance).

A detailed look at the changes seen in each individual pulse is shown in Figure 4.8. For both of the devices, similar heating regimes are seen at the midline, although in both cases there are changes in the magnitudes seen for each device. In the splenic tissue coagulations, the maximum midline temperature change is highest for the first pulse and continues to drop off for subsequent pulses. In the mesenteric tissue coagulations, the maximum midline temperature change occurs after the first pulse. For the standard bipolar forceps it occurs during the second pulse and for the actively cooled bipolar forceps it occurs during the third pulse. The most striking difference for both cases; however, is the minimal temperature increases seen at points adjacent to the device edge for the actively cooled bipolar forceps. In general, this device showed comparable, if not greater, thermal performance at the midline with dramatically lower temperature changes adjacent to the device.

#### **4.4 Discussion**

The results shown in this experiment validate the concept of using active cooling and compression adjacent to electrosurgical instruments to minimize collateral thermal damage while maintaining adequate, and potentially increased, coagulative properties seen in current electrosurgical instrumentation.

For the splenic tissue coagulations midline maximum temperatures for the actively cooled bipolar forceps showed a statistically significant higher value (p-value = 0.009) compared to the standard bipolar forceps. Times to  $T_{max}$  at the centerline of both devices were seen to be not significantly different. These results suggest that an increase in surgical efficiency is gained by using the active cooling bipolar forceps as procedural times could be decreased along with a minimization of thermal damage.

A statistically significant difference in maximum temperatures was not seen between the two devices in the mesenteric coagulations (p-value = 0.818). However, with the actively cooled bipolar forceps powered for more than 15 seconds, tissue temperatures adjacent to the device profile remained unchanged by the continuous pulsatile energy input into the tissue. Therefore, the actively cooled device could be used at higher powers without degrading its ability to minimize thermal spread.

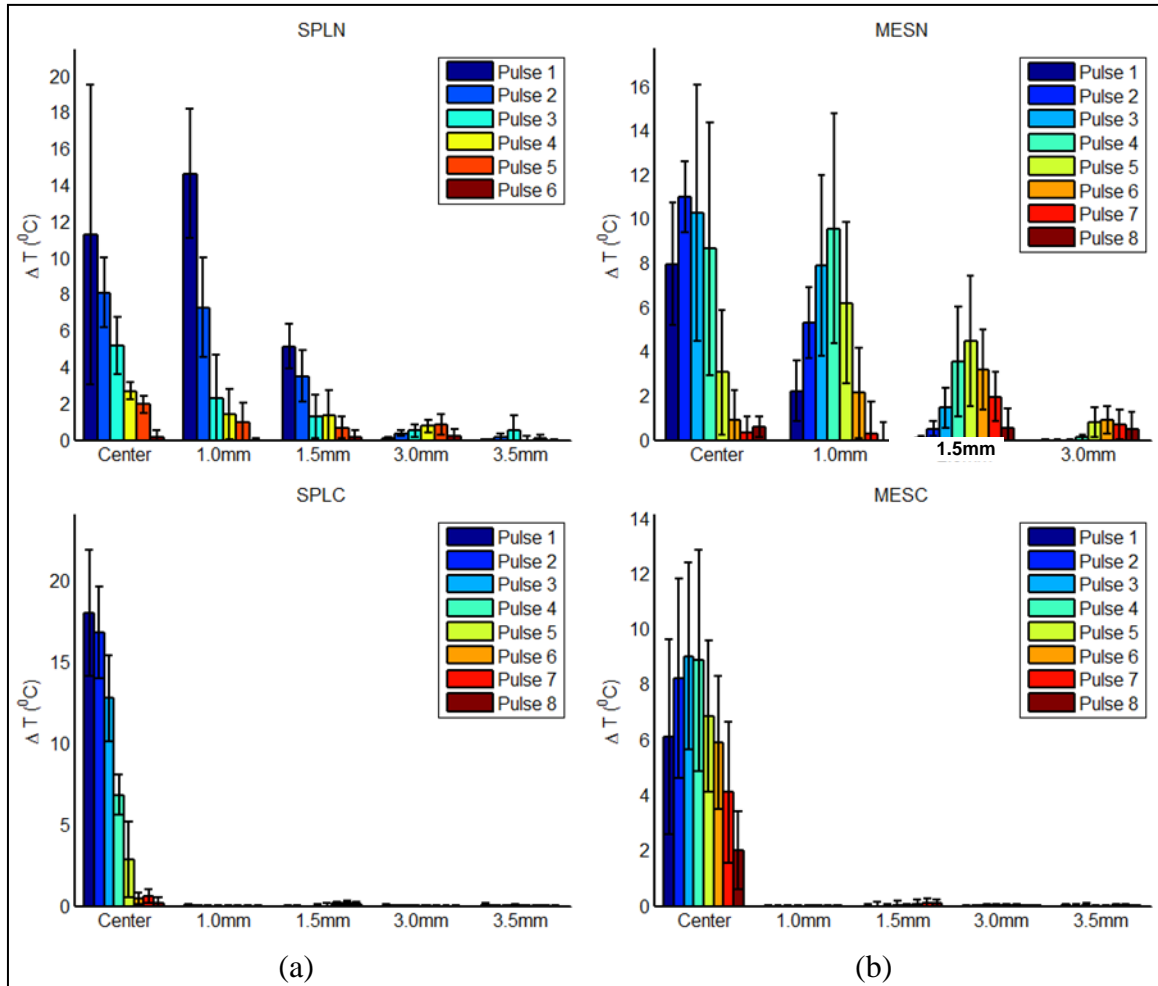


Figure 4.8. Detailed summary of thermal development during each pulse for coagulation experiments on splenic (a) and mesenteric (b) tissues. (a) SPLN data comes from experiments using normal 5 mm forceps while the SPLC data comes from experiments with the custom adjacent cooling channels. Midline temperatures were seen to increase significantly more during each pulse in the cooled case as compared to the standard case while temperatures taken adjacent to the cooled device rose minimally. Adjacent points to the normal device saw temperature changes increase even more at the 1.0 mm location compared to the midline temperatures during the first pulse. More distant locations saw similar slowly declining slopes for temperature increases during each pulse through 1.5 mm. Points at 3.0 mm and 3.5 mm saw greater temperature increases at later pulses due to conductive heating. (b) MESN data comes from experiments using normal 5 mm forceps while the MESC data comes from experiments with the custom adjacent cooling channels. Midline temperatures were seen to increase at nearly equal rates, although the standard device heated up quicker during the beginning pulses and the modified device heated up more quickly during the later pulses. However, hardly any temperature increase was seen at points adjacent to the cooled device while similar, shifted temperature profiles were seen for the standard device at distances adjacent to the tool edge.

## **4.5 Conclusions**

This experiment validates the use of actively cooled electrosurgical devices to be used during laparoscopic surgery to minimize collateral thermal damage to tissue while maintaining appropriate coagulative properties seen in traditional bipolar devices. Minimal levels of temperature increase were seen outside the profile of the actively cooled instrument for both spleen and mesenteric tissues that were tested. Additionally, for the spleen coagulations, a statistically significant higher temperature was also seen at the midline for the actively cooled device. It is postulated that compression of the tissue by the cooling channels may be focusing the electrical energy towards the midline of the instrument due to increased impedance to the current outside of the instrument profile. If true, then a significant added benefit to actively cooling adjacent tissues would be decreased procedural times as it will take less time to achieve proper coagulation. These results show the foundation for a surgical thermal management system (STMS) that could provide both the patient and surgeon increased protection from unwanted side effects due to collateral thermal damage and thermal spread during electrosurgical procedures.

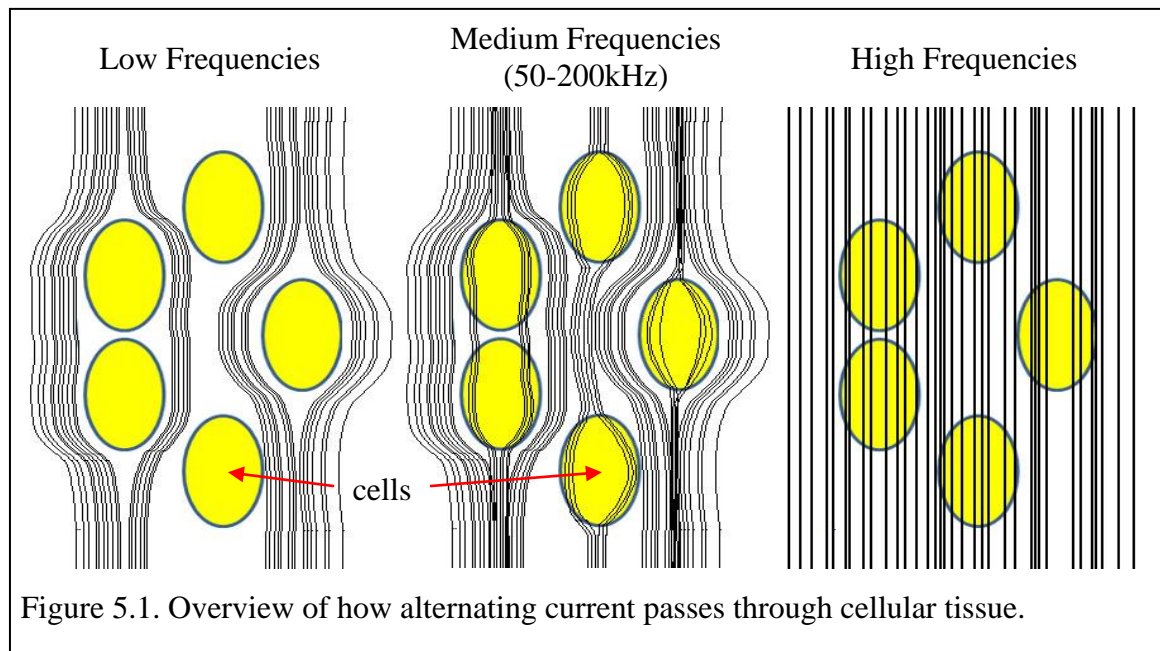


## Chapter 5 Development and Validation of a Bioimpedance Measurement System Using a New Constant Current Source

### 5.1 Introduction

A custom bioimpedance measurement system is described here for the study of soft tissue bioimpedance including the development of a bioimpedance measurement circuit and bioimpedance probe (BP). A new approach to remove DC bias current is included in the development of a constant current source for the bioimpedance measurement circuit. This technique uses a DC bootstrapping technique within a traditional modified Howland current pump. Additionally, the BP is constructed such that it can be used simultaneously as a compressive device in future testing. The entire bioimpedance measurement system is designed to be incorporated into a low-cost solution for bioimpedance measurements.

Measuring the bioimpedance of soft tissue has allowed for the understanding of many different physiological systems. The ability to measure the electrical resistivity of body tissues and fluids is of importance to the researcher, physiologist, and the clinician [105].

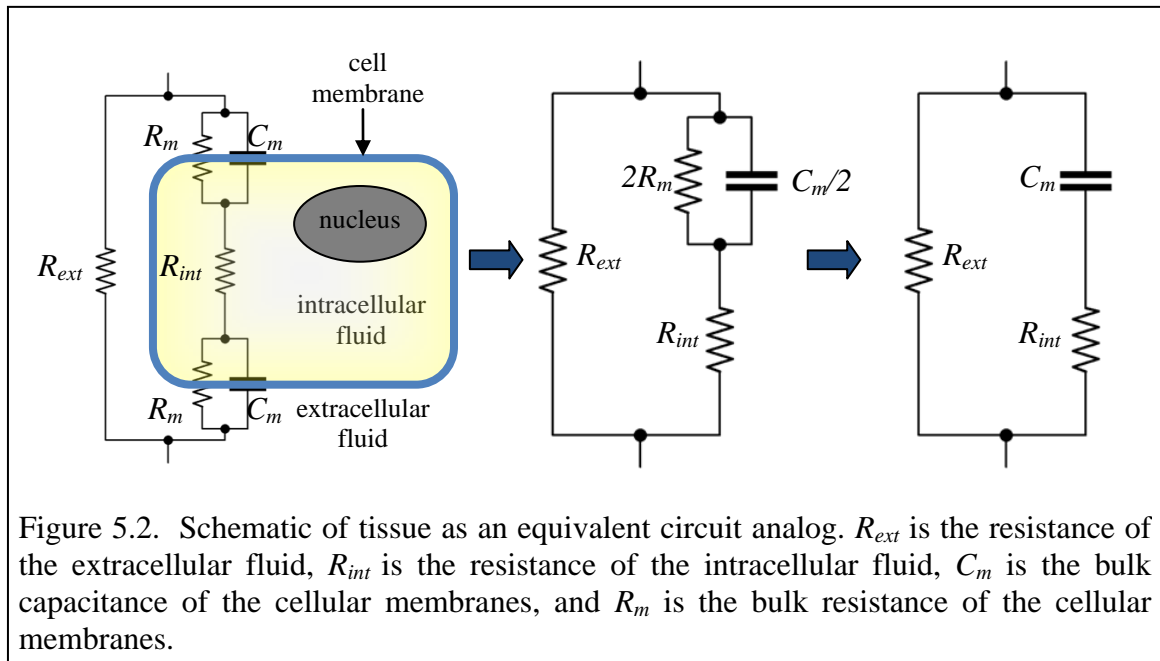


For example, in the measurement of both cardiac stroke volume and cardiac output by impedance cardiography, changes in blood resistivity can be used. Bioimpedance measurements have found use in the analysis and monitoring of several physiological processes. Heart stroke and respiration volume, edema, urological tissue characterization, myography, body composition analysis, and electroporation monitoring are all areas where bioimpedance has been used previously to measure physiological events [82]. Beyond these examples, resistivity reflects the ionic concentration of any electrolyte, thus providing useful information [82].

As shown in Figure 5.1, electric current passes through tissue in a frequency-dependant manner. At low frequencies, current is limited to the extracellular space due to the high cell membrane impedance relative to the impedance of the interstitial space. Increasing frequency results in decreasing cell membrane impedance due to the capacitive nature of the cell membrane. This allows more current to pass through the intracellular space [106].

## 5.2 Equivalent Circuit Analog for Soft Tissue

An equivalent circuit model, known as the Cole-Cole model, can be developed from the interactions of current with cells and tissue, as shown in Figure 5.2. Due to the



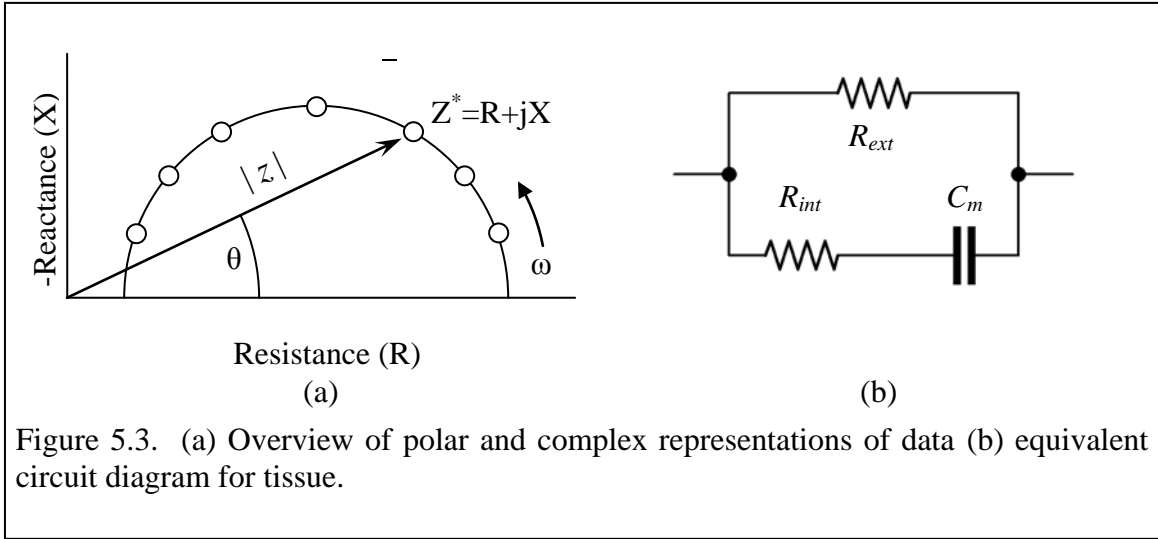


Figure 5.3. (a) Overview of polar and complex representations of data (b) equivalent circuit diagram for tissue.

capacitive nature of the cellular membrane, electrical current passes through the intracellular fluid only at frequencies high enough to overcome the cell membrane reactance. Thus, by monitoring the electrical impedance over a range of frequencies useful information about the intracellular and extracellular tissue spaces as well as the bulk makeup of the cellular membranes can be obtained.

**5.2.1 Complex and Polar Impedance Representations**

The impedance of soft tissue ( $Z^*$ ) can be broken up into the resistance ( $R$ ) and reactance ( $X$ ) components such that

$$5-1$$

as shown in Figure 5.3(a)

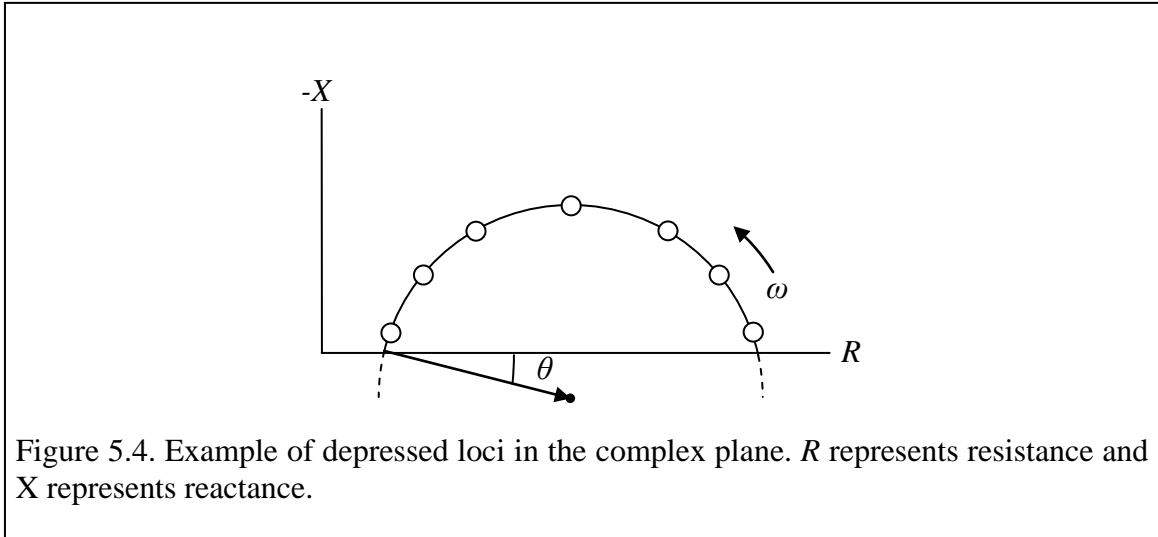
This data can also be transformed into polar coordinates of the form

$$5-2$$

where  $|Z|$  is the impedance modulus and  $\theta$  is the impedance phase. This is accomplished through the following relationships between the polar and Cartesian coordinate systems

$$\text{---} \quad 5-3$$

$$\text{---} \quad 5-4$$



Relevant correlations to the values in the equivalent circuit shown in Figure 5.3(b) can be made through the following relationships

5-5

—————

5-6

5-7

### 5.2.2 Depressed loci

While equivalent circuit analogs can contribute much toward understanding of physiological impedance, one major significant deviation exists between observed physiological impedance and what can be explained by an ideal equivalent circuit analog. The center of the complex impedance loci for many biologic specimens tends to appear depressed from the real axis (see Figure 5.4). There are several theories concerning the origins of this behavior and, while the actual origin of this deviation is unknown, the model proposed by Cole and Cole [56] continues to be the most widely assumed.

Cole and Cole analyzed the dielectric dispersion (complex permittivity) of collected impedance data. Adapting the Debye equation with a variable exponent ( $\alpha$ ) such that

—————

5-8

they were able to mathematically verify this relationship to correspond with the dispersion from the real axis [55]. The exponent represents a distribution of relaxation time constants most commonly thought of as the cell membrane encasing a wide variety of structures that vary in size and shape [58]. This dispersion relates to  $Z$  similarly such that

### **5.3 Bioimpedance Measurement Circuit**

Numerous methods for detecting the bioimpedance of tissue have been developed in the past. The most common are the use of a balanced bridge, impedance analyzers, and lock-in amplifiers [82]. Additionally, several custom circuits have been developed in the literature.

A balanced bridge uses the standard concept of three known impedances connected with the load impedance. By balancing the bridge, the unknown impedance is thus known. However, it is time intensive to perform bridge balancing for numerous frequencies and thus this method is best suited for single, low frequency measurements [82].

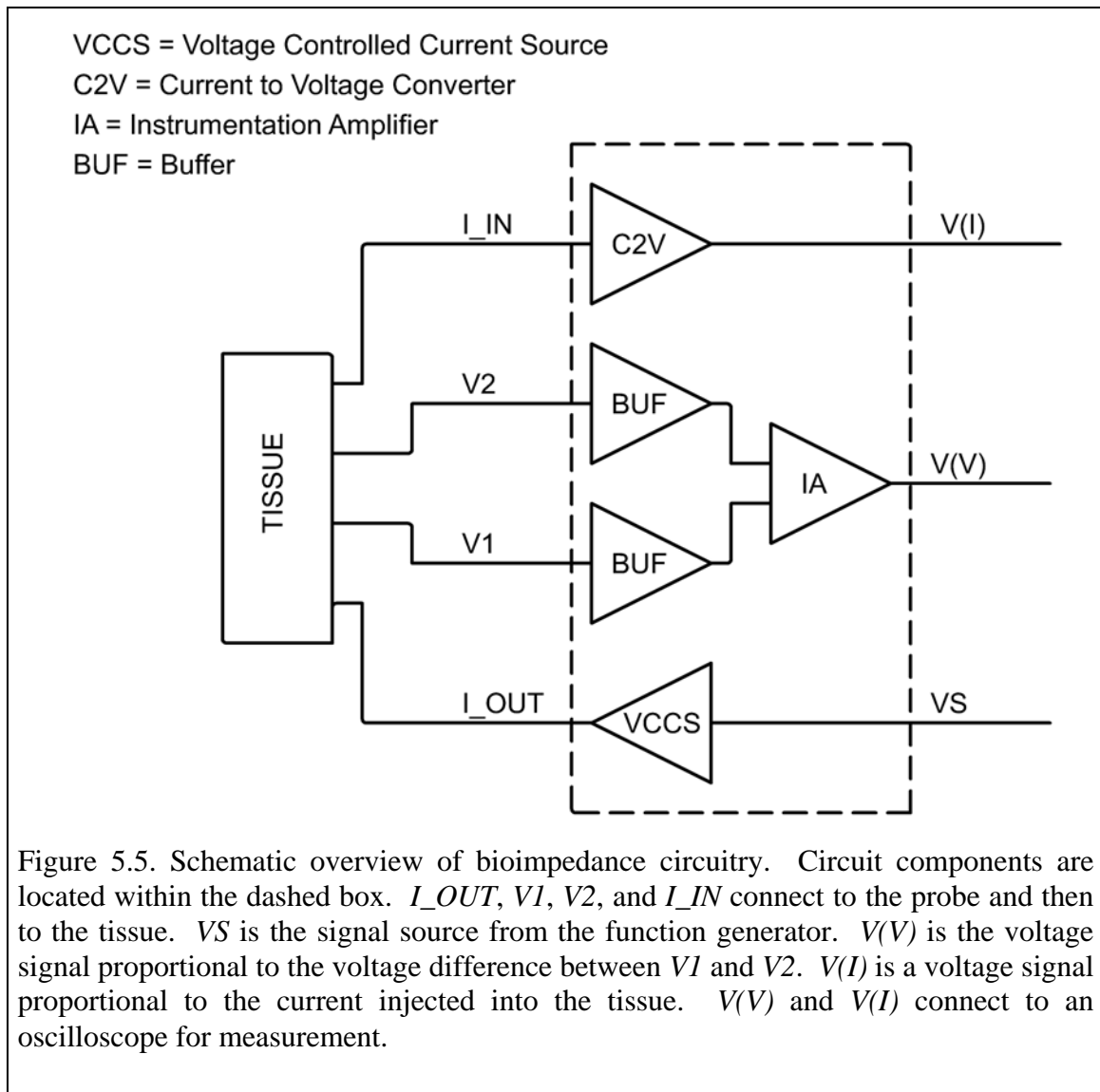
Lock-in amplifiers are used especially when the signals being analyzed are buried in large amounts of noise. The lock-in amplifier works by multiplying the detected signal by a reference signal and then sending this signal through a low-pass filter, resulting in a signal composed only of the frequency of interest. However, most lock-in amplifiers have upper frequency limits of 100 kHz due to the speed and conversion time needed by the analog to digital converters [82].

Impedance analyzers are automated instruments that also include LCR-meters. The difference between the two is that LCR-meters only use an auto-balancing bridge technique for impedance measurements, whereas impedance analyzers use multiple measurement techniques in order to cover a wider frequency range. LCR-meters typically have a measurement range from 5 Hz – 2 MHz while impedance analyzers can extend out to over 100 MHz. However, these instruments typically are not used for tissue

impedance measurements where contact impedances are extremely high and therefore need a front-end amplifier system to be used effectively [107-110].

Custom circuits have been developed and reported in the literature as well. Typically these systems include a voltage or current source, an instrumentation amplifier with high input impedance, and a method for detecting how much current passed through the biological sample [36]. The output signals are either converted into DC voltages proportional to the magnitude and phase of the reading or are sent out to an oscilloscope [106, 111-117]. However, most current sources have problems with bandwidth due to either circuit constraints or load impedance [118-124]. Therefore, a low-cost bioimpedance measurement circuit is developed in this research incorporating a constant current source capable of driving a 5 k $\Omega$  load at frequencies up to 1 MHz.

A bioimpedance circuit needs to be able to measure the current traveling through the tissue, a voltage drop between two reference points within the tissue, and the phase difference between the current and voltage signals. An overview of the circuit developed for this research is shown in Figure 5.5. A Labview-programmable Agilent 33120A function generator is used to provide a constant AC voltage source (VS) to a Voltage-Controlled Current Source (VCCS) which is used to drive current into the tissue sample. Voltage readings are first buffered (BUF) and then differentially amplified through an instrumentation amplifier (IA). The current return path is directed through a Current-to-Voltage converter (C2V) circuit to provide a voltage measurement proportional to the current passing through the tissue.



The circuit is coupled to the tissue through a custom bioimpedance probe (discussed in Section 5.5). The output current from the VCCS ( $I_{OUT}$ ) is sent through the tissue. The input to the C2V circuit ( $I_{IN}$ ) is held at virtual ground and therefore all current flowing through the tissue exits out this electrode. Signals  $V1$  and  $V2$  serve as voltage reference points within the tissue for the impedance measurement. The output signals ( $V(V)$  and  $V(I)$ ) are passed to a PXI-5114 oscilloscope for post-processing. A detailed description of each of the three sub-circuits is given in the sections following this section.

### 5.3.1 *Voltage-Controlled Current Source Circuitry*

Due to the temperature-dependent nature of tissue electrical conductivity, it is best to drive the tissue with a constant current as opposed to a constant voltage to avoid accidentally driving too much current through the tissue. As discussed in Section 3.3.3, tissue is heated proportionally to the current density flowing through it. By maintaining a low current density and only allowing current to flow through the tissue when measurements are being performed, the temperature rise in tissue can be made negligible.

Much research has been performed in developing a wide bandwidth VCCS. The VCCS needs to be designed to output a constant current through a wide range of frequencies while maintaining high output impedance due to the varying magnitude of the contact impedance. Design configurations have included the use of current mirrors, modified Howland current pumps (MDCP), and current conveyors [118-124].

For this research, a modified version of a constant current source described by Analog Devices along with a DC bias bootstrapping technique is developed [118, 120, 125] as shown in Figure 5.6(a). The basic design of the Analog Device circuit is a MDCP with an integrated circuit (IC) chip within the feedback loop to provide for low-current stability.

The MDCP uses an Analog Devices AMP03 differential amplifier. This IC is chosen based on its large internal resistor network (25 k $\Omega$ ) and excellent high frequency bandwidth (3 MHz). The feedback loop IC (AD8065) is chosen so as to have both low input bias current and low offset voltage, thus negating the relatively high input bias current from the differential amplifier. As this circuit is in a voltage buffer configuration, the output signal from this IC is also used to drive the coaxial cable shield with a low impedance voltage equal to the signal line voltage, thus dramatically reducing the stray capacitance from the coaxial cable [126].

Due to the frequency-dependent nature of tissue impedance as well as the contact impedance between the electrode and tissue, the current source will experience much larger impedance from DC current as opposed to AC current. Therefore, minimizing DC offset voltages from the output is critical to ensure good circuit bandwidth. To achieve this, an additional DC feedback circuit is used (LM7171) as shown in Figure 5.6(a). As



this IC has no major frequency considerations and the voltages are low, a basic IC would suffice as well.

The characteristics of this VCCS are such that the output current is proportional to the input voltage through

—

5-10

where  $I_{out}$  is the output current,  $V_{in}$  is the input voltage, and  $R_{set}$  is the sense resistor. To ensure that all the current is directed through  $R_{set}$ , the resistor connecting the output of the AMP03 to the inverting input should be much larger than  $R_{set}$ . As such,  $R_{set}$  is set to 1 k $\Omega$  (+-1%), or 4% of the resistance leading to the inverting input of the AMPO3 IC chip.

To ensure that the current density is not inducing unwanted temperature rises in the tissue, rectification currents, and bubble formation, the current level needs to be kept less than 100  $\mu\text{A}_{\text{RMS}}$  [127], where the RMS subscript stands for the root mean square value. A current output of 60  $\mu\text{A}_{\text{RMS}}$  is chosen which results in a current density of 1.18 mA/mm<sup>2</sup> for electrodes with a diameter of 0.254 mm. This is achieved by using a 60 mV<sub>RMS</sub> driving signal from an Agilent 33120A function generator.

### 5.3.2 *Current-to-Voltage Converter Circuitry*

Two basic ways to measure current are by monitoring the voltage drop across a current-sense resistor in series with the load or by using a current-to-voltage converter (C2V) circuit [128]. The current-sensing resistor technique relies on the load being much larger than the current-sense resistor, so typically values less than 1  $\Omega$  are used. The C2V method is utilized in this circuit due to the inverting nature of the output signal allowing for very small phase shifts to the signal at high frequencies.

The C2V is made up of a single IC in an inverting op amp configuration with a single resistor connected from the output of the IC back to the inverting input as shown in Figure 5.6(b). By connecting the non-inverting input to ground, the inverting input is kept at a virtual ground and all the current flows through the feedback resistor. This produces an output voltage from the IC ( $V_o$ ) inversely proportional to the input current ( $I$ ) such that

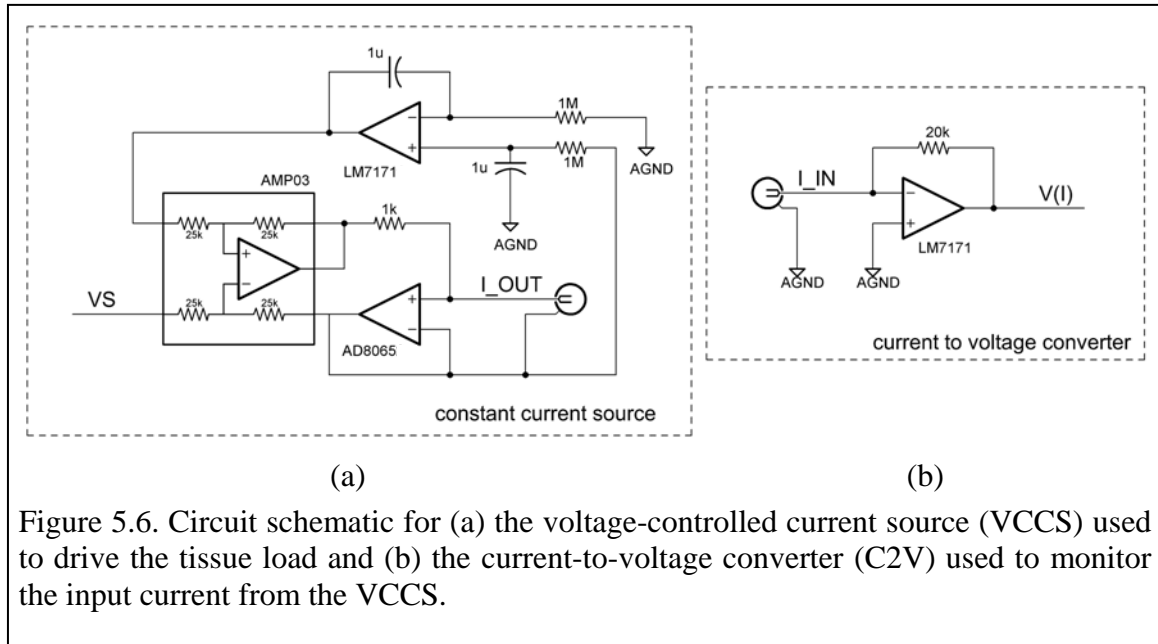


Figure 5.6. Circuit schematic for (a) the voltage-controlled current source (VCCS) used to drive the tissue load and (b) the current-to-voltage converter (C2V) used to monitor the input current from the VCCS.

5-11

where  $R_F$  is the feedback resistor [128-130]. The value of  $R_F$ , assuming a  $60 \mu A_{RMS}$  current as determined in Section 5.3.1 and a maximum voltage output to the oscilloscope of  $8.5 V_{RMS}$ , is equal to

— — — — —

5-12

To allow for additional headroom in calibrating the circuitry and measuring larger currents, a value of \_\_\_\_\_ was selected, resulting in a theoretical voltage output of  $1.2 V_{RMS}$ .

### 5.3.3 Buffered Differential Voltage Measurement Circuitry

Knowledge of the voltage drop across the tissue sample of interest is critical for the bioimpedance measurement. In two-electrode configurations it becomes impossible to know this voltage drop due to the large voltage drop from the current crossing the electrode/electrolyte barrier [82]. Therefore, the tetrapolar technique is nearly always used for measurements where contact impedance cannot be ignored [131]. This technique used extremely high input impedances on voltage sensing electrodes in order to monitor the voltage drop with reference to a common voltage across two reference points.

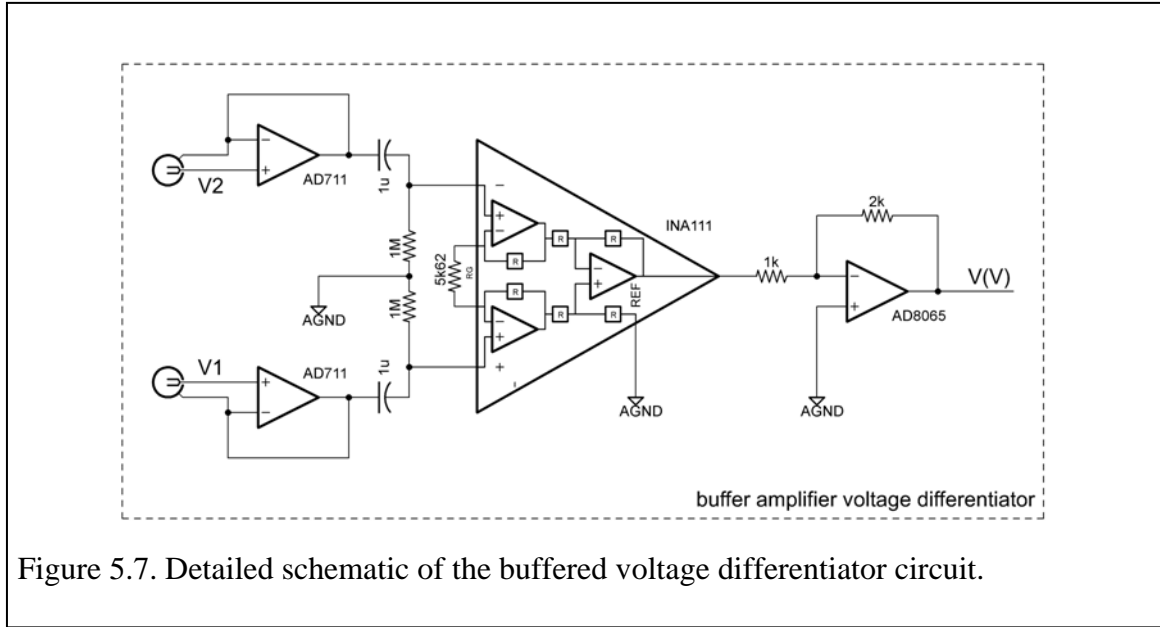


Figure 5.7. Detailed schematic of the buffered voltage differentiator circuit.

The high input impedance ensures that no current exits out of the tissue through these reference points. To determine the voltage drop between the two points, a differential circuit is used whose output is proportional to the difference between the two voltages.

The buffered differential voltage circuit is responsible for measuring the voltage difference between the two reference electrodes positioned in the middle of the current injecting electrodes. This comprises both of the BUF icons and the IA icon in Figure 5.5. The full schematic of the voltage circuit is shown in Figure 5.7.

To ensure that no current leaves the tissue through these electrodes high input impedance is needed for these signals relative to the contact impedance of the electrode-electrolyte interface [82]. This is accomplished by using two voltage buffers at the inputs from the BNC probe. AD711 ICs are used with a bandwidth of 2 MHz and an input impedance of  $10^{13} \Omega$ . The output from each of these ICs is also used to drive the shielding of the coaxial cable with a low impedance voltage equal to that in the signal lead, thus minimizing stray capacitance losses from the BNC cables. Bootstrapping the shielding of the coaxial cables with the same level signal negates the cable capacitance due to the lack of a voltage drop from the signal line to the shielding.

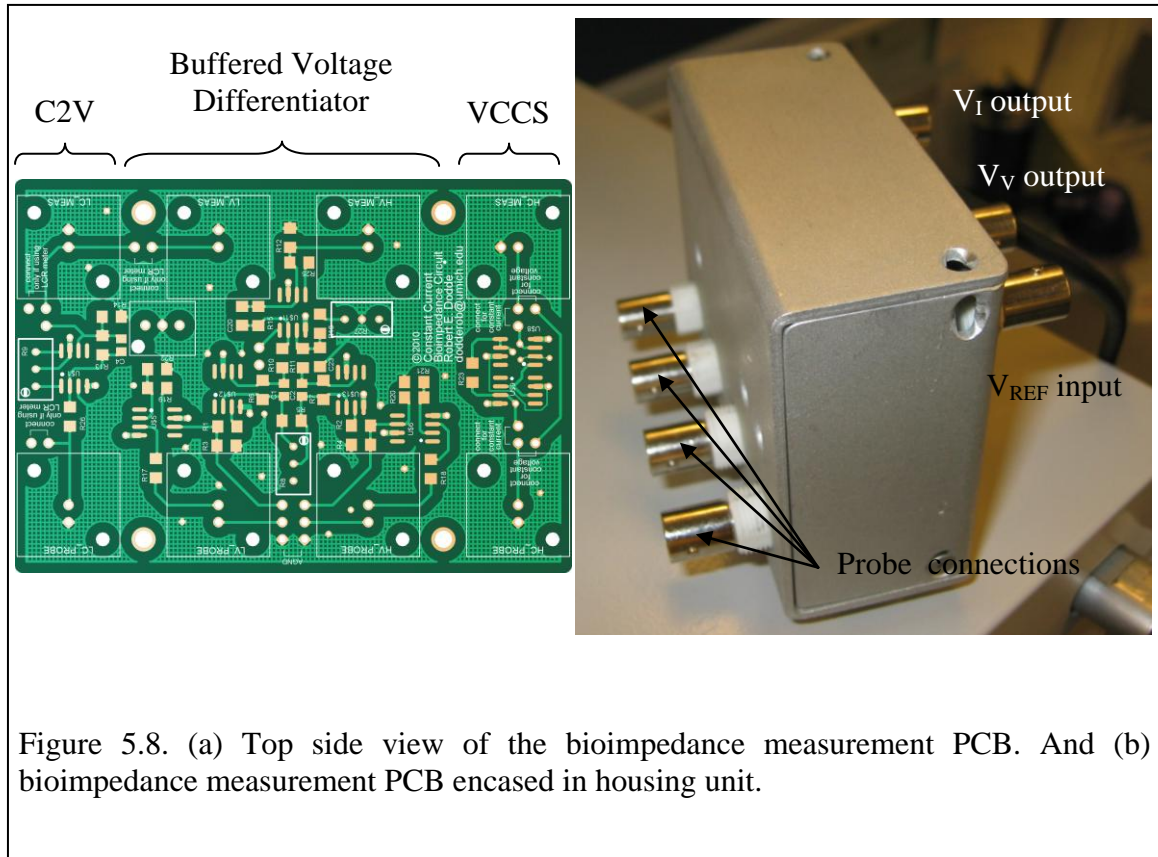


Figure 5.8. (a) Top side view of the bioimpedance measurement PCB. And (b) bioimpedance measurement PCB encased in housing unit.

As the voltage drop between these two electrodes is equal to the difference in the voltages at each electrode referenced to ground, an instrumentation amplifier (IA) is used to convert the two voltage signals to a single-ended differential signal. The two buffered signals are capacitively coupled to the inputs of IA. The IA acts as a differential input to single-ended output transducer such that  $V_{out} = G(V_2 - V_1)$  [132]. The gain term,  $G$ , can be set by an external resistor. Additional gain is also added by an inverting amplifier connected in series with the output of the IA. This serves to both avoid saturating the IA signal as well as inverting the signal to be aligned with the output signal from the current-to-voltage converter which is also inverted (see Section 5.3.2).

### 5.3.4 PCB Layout

The circuit design was realized on a printed circuit board (PCB) in order to minimize stray capacitance and allow for the use of smaller components. The PCB was laid out using Eagle 4.10 which is a schematic and PCB design software package (CadSoft USA, Pembroke Pines, FL). The top side of the PCB is shown in Figure 5.8(a). Care was taken

to ensure that the input pins for each integrated circuit were spaced from the ground plane. Each sub-circuit is also isolated from the other sub-circuits by a cross-hatched ground plane. The board is powered by  $\pm 12\text{V}$  and power supply lines are decoupled as per the recommendation of the manufacturer for each IC. BNC connectors are used for all input and output connections to the board and mounting holes are placed on the board to allow the circuit to be contained in a housing. The complete circuit contained within the housing is shown in Figure 5.8(b).

## 5.4 Bioimpedance Measurement Circuit Validation

To ensure that the bioimpedance measurement circuit performs as designed and to compensate out any circuit-dependent changes to the signals, a series of calibration tests are performed in order to characterize the circuit. Each subcircuit is tested over relevant voltage and/or current ranges as well as over the frequency span of 100 Hz – 1 MHz. Deviations from the theoretical output for each subcircuit are compensated for mathematically during post-processing.

### 5.4.1 Current-to-Voltage Circuit Characterization

For a given input current to the C2V circuit, a proportional voltage output  $180^\circ$  out of phase (due to the inverting nature of the circuit) with the input voltage and equal to Eq. 2 is expected. To characterize this circuit, a constant voltage ( $V_{in}$ ) was supplied to a range

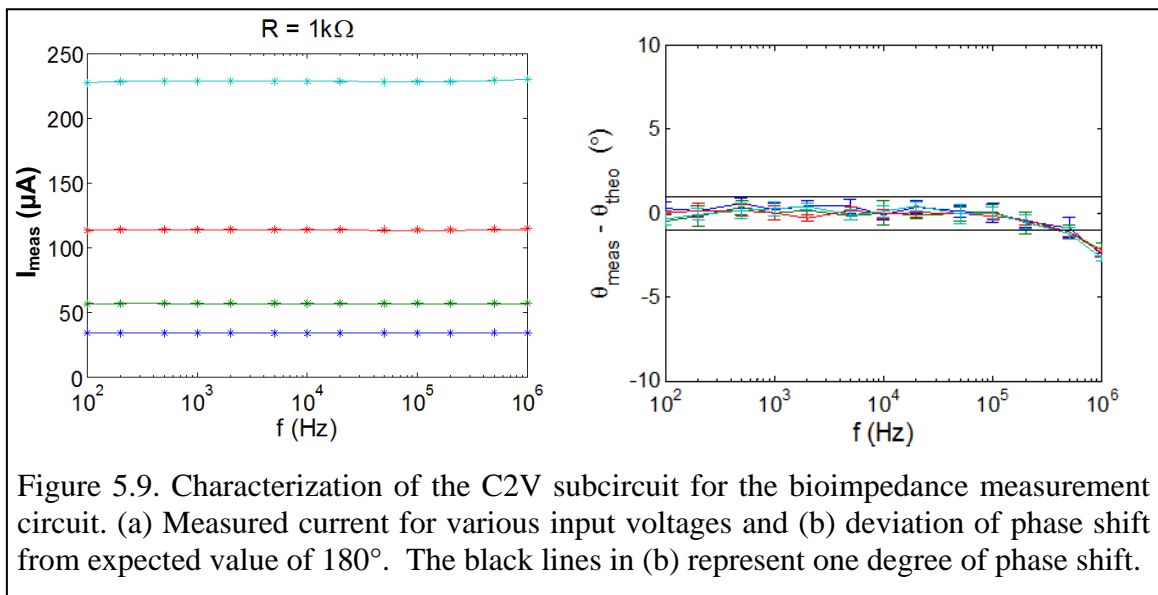


Figure 5.9. Characterization of the C2V subcircuit for the bioimpedance measurement circuit. (a) Measured current for various input voltages and (b) deviation of phase shift from expected value of  $180^\circ$ . The black lines in (b) represent one degree of phase shift.

of calibration resistors ( $R_{cal}$ ) for 30 – 200  $\mu\text{A}$  over the frequency range 100 Hz – 1 MHz.  $V_{in}$  and the output voltage from the C2V circuit ( $V_{out}$ ) were both monitored on a PXI-5044 oscilloscope and  $V_{RMS}$  and phase shift data recorded using a custom Labview® program. More details on the program are given in Appendix C Bioimpedance Labview Program. The current measured ( $I_{meas}$ ) is calculated as

$$\text{---} \tag{5-13}$$

and the theoretical current ( $I_{theo}$ ) is calculated as

$$\text{---} \tag{5-14}$$

Results for the characterization of the C2V subcircuit are shown in Figure 5.9. In Figure 5.9(a), the output current signal for 30  $\mu\text{A}_{RMS}$ , 60  $\mu\text{A}_{RMS}$ , 120  $\mu\text{A}_{RMS}$ , and 240  $\mu\text{A}_{RMS}$  input currents is shown. The output signal is flat through 1 MHz for each of these input currents. In Figure 5.9(b), the phase shift relative to the input signal is for 30  $\mu\text{A}_{RMS}$ , 60  $\mu\text{A}_{RMS}$ , 120  $\mu\text{A}_{RMS}$ , and 240  $\mu\text{A}_{RMS}$  input currents. For all frequencies the resultant phase shift on the output signal is less than 2 degrees, with all frequencies except 1 MHz having less than 1 degree of phase shift. This is well within measurement requirements for the bioimpedance measurement circuit.

#### 5.4.2 Voltage-Controlled Current Source Characterization

Based on known values for spleen tissue as well as theoretical contact impedance values of the bioimpedance probe (see Section 5.5), the VCCS needs to output a constant current through a load impedance ( $R_L$ ) of 5 k $\Omega$  for at 1 MHz increasing to 100 k $\Omega$  of load at 100 Hz. To characterize the VCCS a constant input voltage ( $V_{in}$ ) is used to drive various values of load impedance. The C2V subcircuit is used to measure  $I_{meas}$  using Eq. 5-13 and the theoretical current output,  $I_{theo}$ , is calculated from Eq. 5-14.

The results for the VCCS characterization are shown in Figure 5.10 for 30  $\mu\text{A}_{RMS}$ , 60  $\mu\text{A}_{RMS}$ , 120  $\mu\text{A}_{RMS}$ , and 240  $\mu\text{A}_{RMS}$  expected output current. Each target output current results in similar normalized reactions to loads as seen by the similar shapes of each graph. For 100 k $\Omega$  loads at 120  $\mu\text{A}_{RMS}$  and 240  $\mu\text{A}_{RMS}$ , the reduced magnitude of the curve is due to the required voltage output being too high for the supply voltages (+- 12

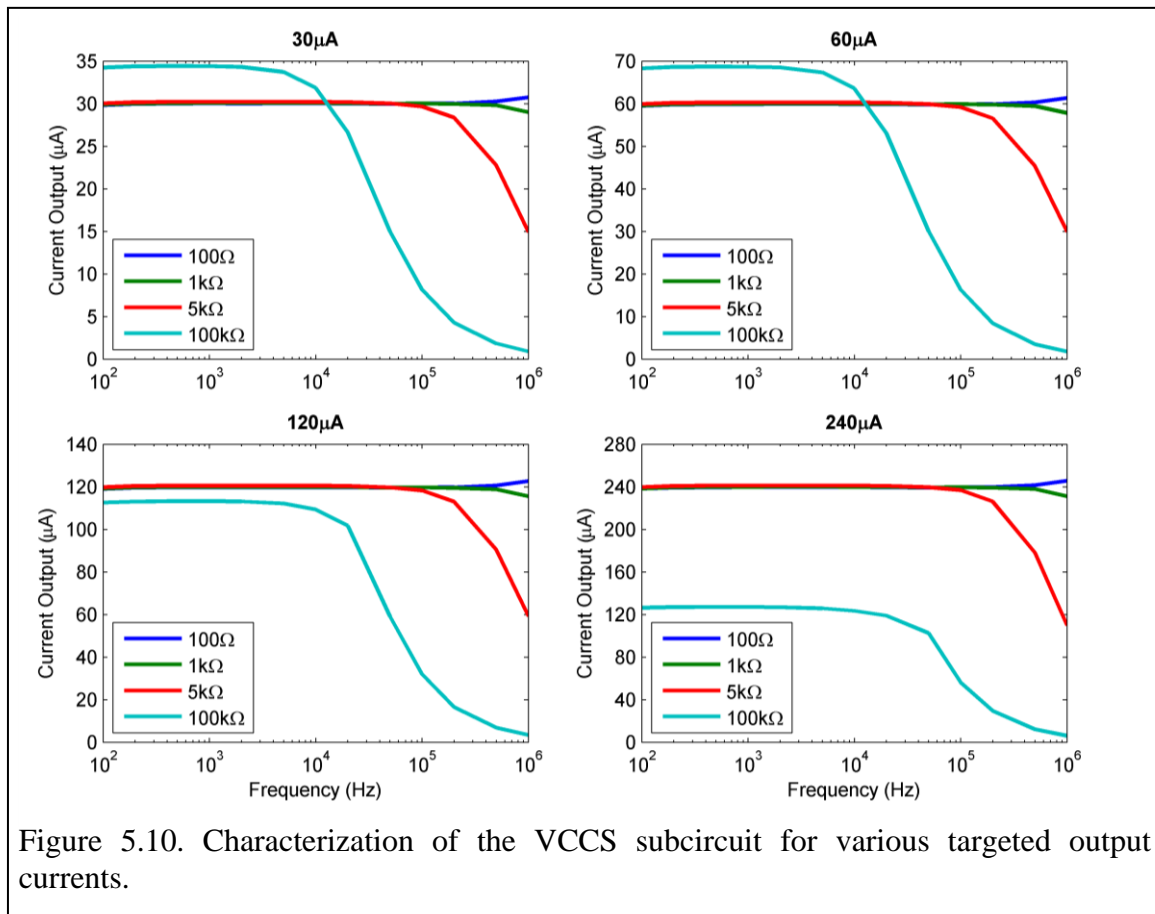


Figure 5.10. Characterization of the VCCS subcircuit for various targeted output currents.

V) and not a direct problem with the circuit itself. The VCCS is seen to be able to drive a  $100\Omega$  and  $1\text{k}\Omega$  load through  $1\text{MHz}$  with less than a 5% error in output current. It is also capable of driving a  $5\text{k}\Omega$  at up to  $\frac{1}{2}$  of its expected output through  $1\text{MHz}$ .

As a design criteria, bioimpedance data is considered usable as long as  $I_{meas}$  is  $\frac{1}{2}$  the expected output current due to sensitivity constraints on the oscilloscope. Measured current can be different than theoretical current output due to circuit limitations as well as losses due to stray capacitance. Based on this criterion, the circuit developed here can output  $60\mu\text{A}_{\text{RMS}}$  through the whole frequency range tested up to a  $5\text{k}\Omega$  load, and can output  $60\mu\text{A}_{\text{RMS}}$  through a  $100\text{k}\Omega$  load up to  $50\text{kHz}$ .

### 5.4.3 Buffered Differential Voltage Measurement Characterization

The differential voltage measurement needs to differentiate and amplify signals differential signals from  $3\text{-}300\text{mV}_{\text{RMS}}$  over a frequency range of  $100\text{Hz-}1\text{MHz}$ . To characterize the circuit developed for this purpose, differential signals were input into the

circuit and this input and the output from the circuit were recorded with the PXI-5044 oscilloscope.

The results for the buffered differential voltage circuit are shown in Figure 5.11. In Figure 5.11(a), the dB response of the expected output signal is plotted against frequency for various input differential voltages. For differential voltages up to 300 mV, the response is independent of the input. However, there is nearly a 2 dB drop-off from the expected signal at high frequencies, which needs to be accounted for in post-processing. Additionally, as shown in Figure 5.11(b), the phase shift is also independent of differential voltage for inputs up to 300 mV. However, a gradual drop off in phase, up to 57 degrees at 1 MHz, is imposed on the output signal which also must be accounted for in post-processing.

The bioimpedance measurement circuit was tested using a series of resistors and capacitors in a typical Cole-Cole model arrangement. The results are shown in Figure 5.12. Each of the graphs shows results for arrangements using resistor values of 1 k $\Omega$  (red) and 2 k $\Omega$  (blue). However, each graph uses a separate capacitor value ranging from 100 pF to 100 nF. The values represent a range of values seen in spleen tissue within the literature [133]. The measured values are plotted with filled in circles and the calibrated data accounting for the magnitude and phase deviations from the buffered differential voltage amplifier are plotted with open circles. The black curve is the non-linear least squares fitted model to calibrated data. created

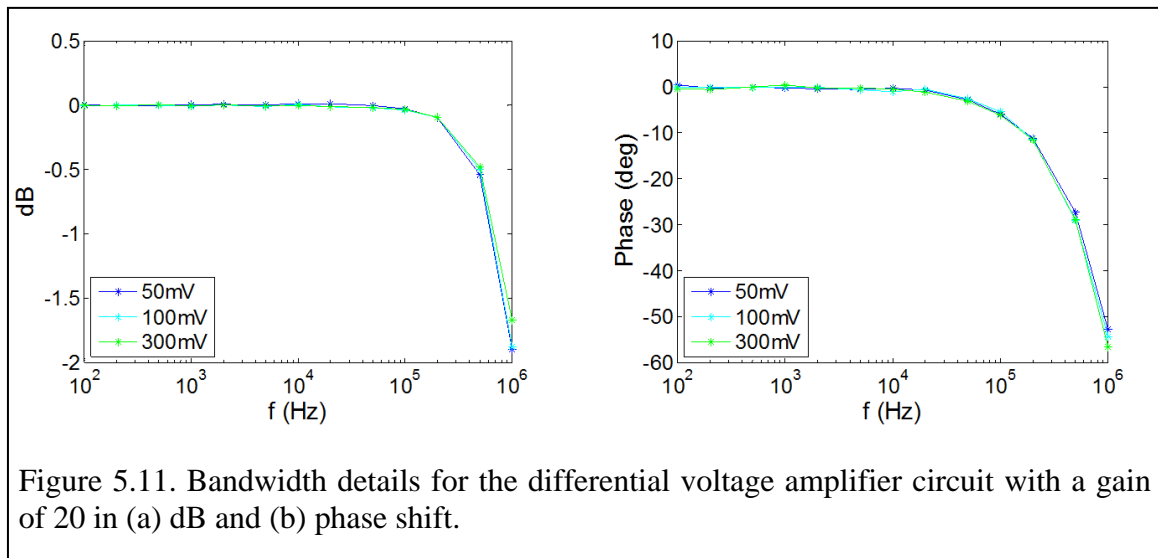
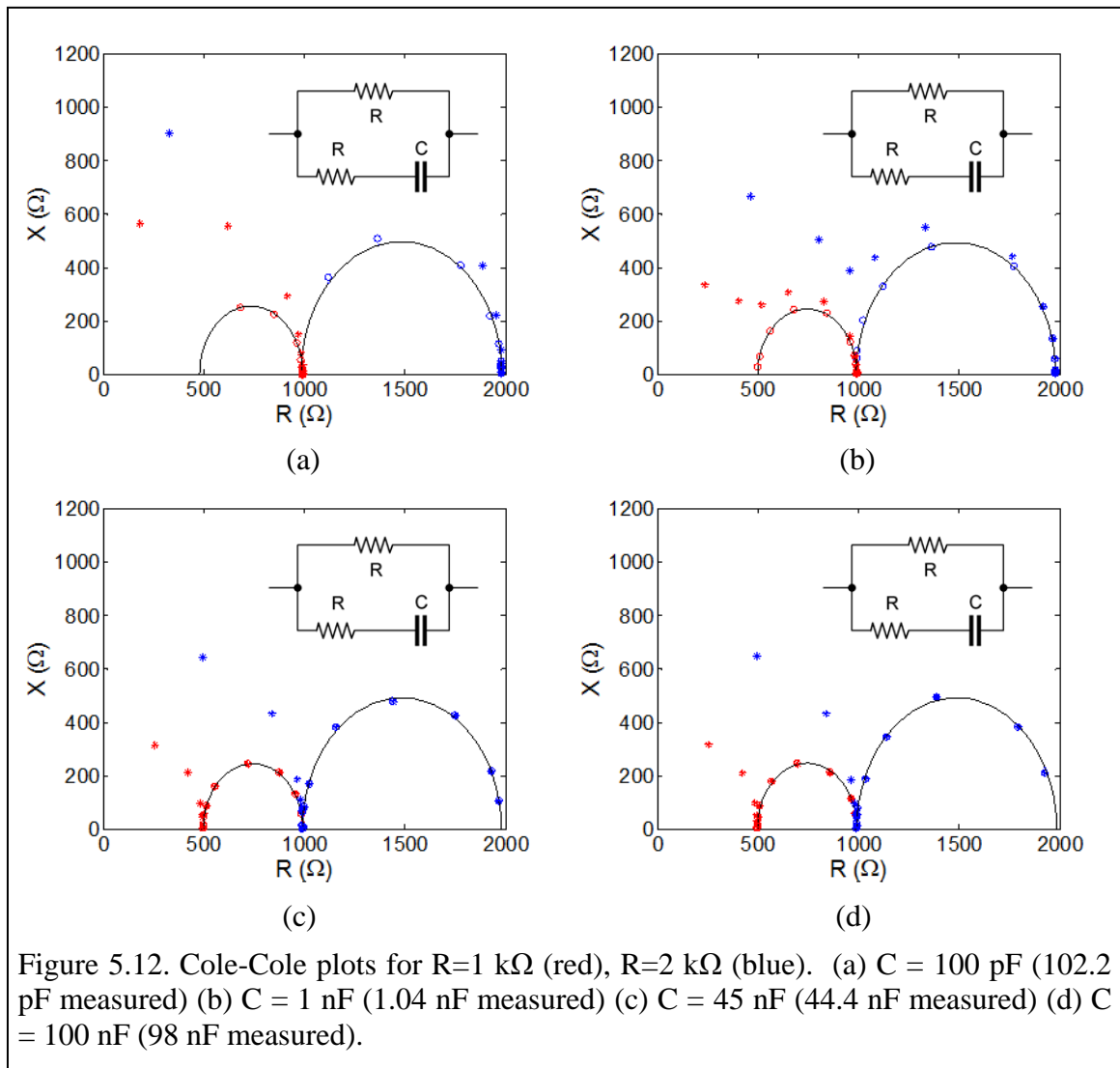


Figure 5.11. Bandwidth details for the differential voltage amplifier circuit with a gain of 20 in (a) dB and (b) phase shift.





The points at which the fitted curve crosses the real axis are easy to see and should be at 500  $\Omega$  and 1 k $\Omega$  for the 1 k $\Omega$  resistor arrangement and at 1 k $\Omega$  and 2 k $\Omega$  for the 2 k $\Omega$  resistor arrangement. The fitted values are within 1% of these expected values. The 100 pF capacitor used was measured at 102.2 pF, the 1 nF capacitor was measured at 1.04 nF, the 45 nF capacitor was measured at 44.4 nF, and the 100 nF capacitor was measured at 98 nF. Considering the 10% manufacturer tolerance on each of the capacitors used, the values are acceptable and show that the calibrating for the buffered differential voltage amplifier is sufficient for a wide range of values typical of physiological tissue.

## 5.5 Bioimpedance Probe

The bioimpedance probe (BP) was designed to allow for the measurement of bioimpedance in soft tissue under various compression levels. The probe consists of four platinum electrodes encased in a 19 mm diameter acrylic cylinder as shown in Figure 5.13. After placement of the electrodes, the cavity in the back of the acrylic is backfilled with epoxy. This is then press fit into a larger fixture allowing the probe to be mounted to a linear stage for tissue compression experiments.

The electrodes are made from 0.25 mm diameter platinum wire and are machined flush with the surface of the probe. The platinum electrodes are soldered into the leads of coaxial cables, extended one meter in length and terminated with BNC connectors. The electrodes are equally spaced with a 3 mm distance between each electrode.

Based on data from Schwan [39] shown in Figure 1.2 and discussed in Section 1.2.4, the contact impedance for the BP for a platinum electrode is shown in Figure 5.14. The high contact impedance of 25 k $\Omega$  at 100 Hz is seen to drop off to only 25  $\Omega$  at 1 MHz and is nearly all due to the contact capacitance. This contact impedance is expected to be

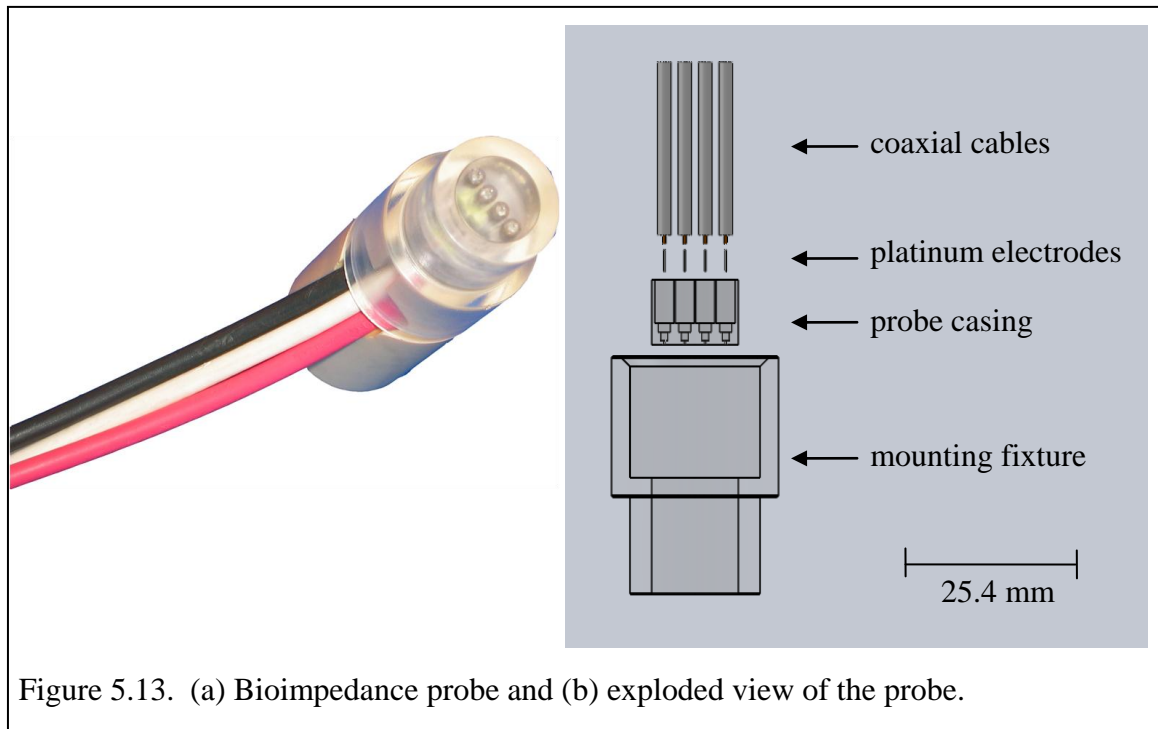


Figure 5.13. (a) Bioimpedance probe and (b) exploded view of the probe.

double this as what is graphed is only for one electrode and the current must cross two electrodes in the BP.

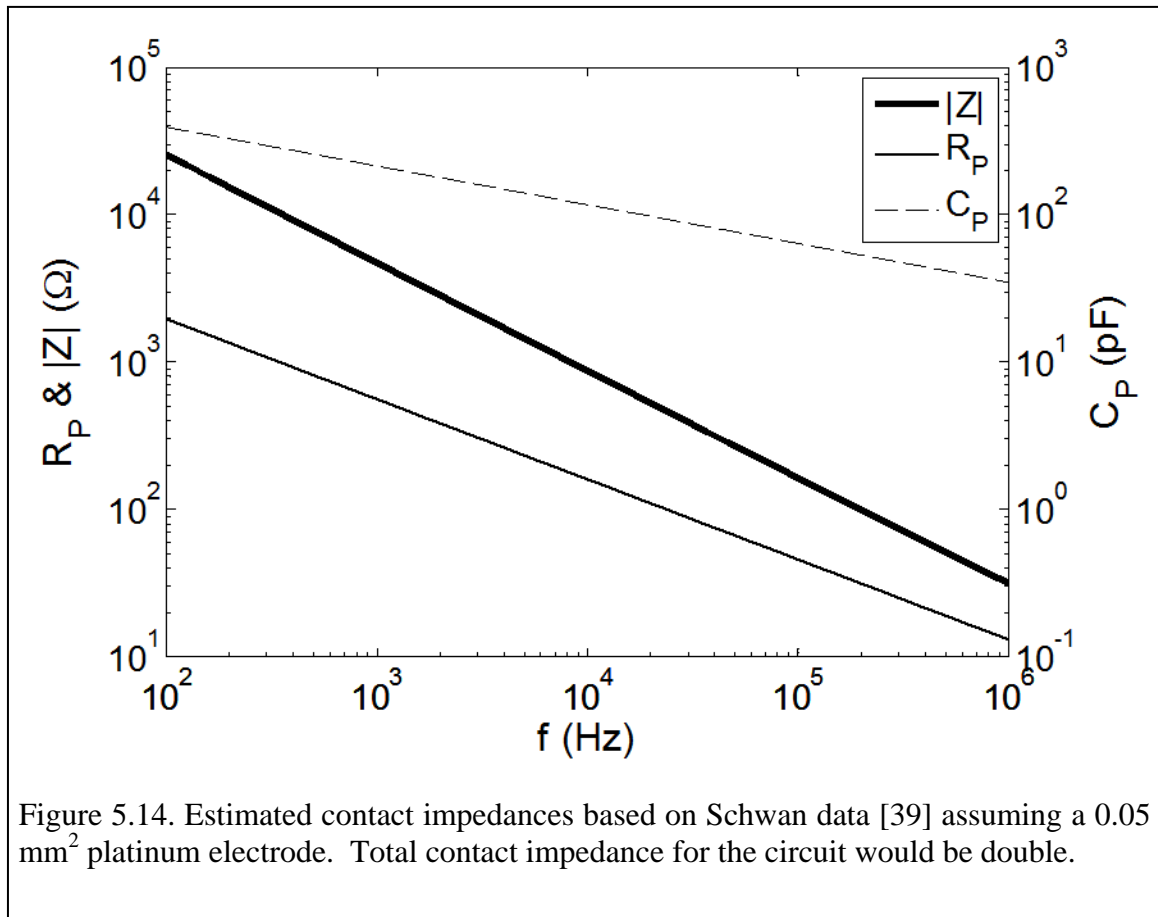
## 5.6 Bioimpedance Probe Characterization

The potential measured between two electrodes in a tetrapolar impedance probe is, through Ohm's Law, equal to the product of the current injected into the medium ( $I$ ) and the apparent resistance ( $R$ ) between the electrodes.  $R$  depends both on the resistivity ( $\rho$ ) of the medium and the geometry of the probe used to measure the potential by

5-15

where  $k$  is known as the cell constant [134]. The cell constant, or proportionality constant, is a parameter that can be used to characterize any BP. Thus, the resistivity ( $\rho$ ) of an unknown solution can be determined by

5-16



For a point electrode in an infinite homogenous medium between two current injecting electrodes, the voltage potential at a point P is

$$\text{---} \text{---} \text{---} \tag{5-17}$$

where  $V_P$  is the voltage at point P,  $I$  is the current injected into the medium,  $\rho$  is the resistivity of the medium, and  $r_1$  and  $r_2$  are the distances between the point electrode and each of the current injecting electrodes [135].

Analyzing this geometry for the four-electrode case it can be shown that the cell constant for a tetrapolar probe is

$$\text{---} \text{---} \tag{5-18}$$

where  $k$  is the cell constant,  $L$  is the distance between the current injecting electrodes, and  $\alpha$  is the ratio of  $\frac{d}{L}$ , where  $d$  is the distance between the voltage-sensing electrodes [136].

Simplifying the equation for the specific case where the distances between each electrode are held constant yields the following equation for the cell constant [136]

$$\text{---} \tag{5-19}$$

For the tetrapolar probe used in this study, the electrodes are encased in an insulating medium and, therefore, only one-half of the infinite space should be considered as the acrylic is much more resistive than the saline. This results in one-half the space for current to travel through, or a doubling of the resistance and therefore a doubling of the cell constant. The final equation for the cell constant of the BP then is [135]

$$\text{---} \tag{5-20}$$

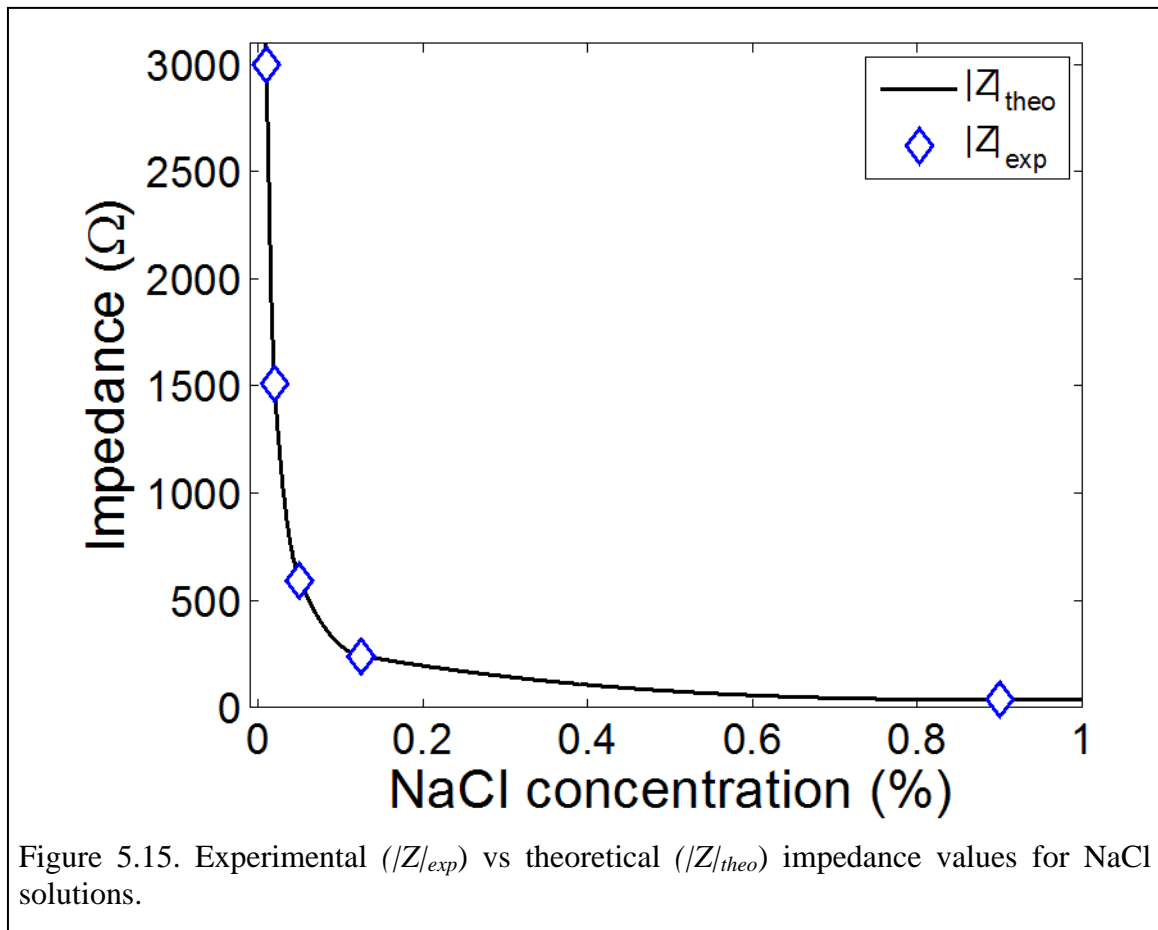
where  $k$  has units of  $\text{mm}^{-1}$ . Considering  $L=9 \text{ mm}$  for the probe used in this study, the theoretical value for  $k=0.0531 \text{ mm}^{-1}$ .

The conductivity of saline solutions has been studied extensively and is known to be strongly dependent on both temperature and molarity. For saline solutions with molarity less than 1M, this relationship has been shown to follow the exponential equation

$$5-21$$

where  $\sigma$  is the conductivity of the solution (S/m) and  $M$  is the molarity (moles/liter) of the solution [137]. The resistivity of a solution is defined as the inverse of its conductivity.

For the BP calibration, five (5) saline solutions of varying concentrations were prepared. These solutions were 0.9%, 0.125%, 0.05%, 0.02%, and 0.01% NaCl. This is equal to molarities of 0.1540 M, 0.0214 M, 0.0086 M, 0.0034 M, and 0.0017 M. The conductivity and resistivity of these solutions, as determined from Eq. 5-21, are listed in Table 5.1.



For each of the prepared solutions, three impedance measurements were taken and averaged to determine the conductivity of the solution. The expected and measured apparent resistances for each of the prepared saline solutions are shown in Table 5.1. The resistances are shown to differ by less than 0.5% at an apparent resistance of 3 k $\Omega$  and less than 5% at an apparent resistance of 36  $\Omega$ .

Table 5.1. Summary of bioimpedance probe calibration data

| NaCl (%) | NaCl (M) | $\sigma$ (S/m) | $\rho$ ( $\Omega$ m) | $R_{th}$ ( $\Omega$ ) | $R_{ap}$ ( $\Omega$ ) | $\Delta R$ (%) |
|----------|----------|----------------|----------------------|-----------------------|-----------------------|----------------|
| 0.9      | 0.154    | 1.547          | 0.647                | 34.3                  | 36.0                  | 4.96           |
| 0.125    | 0.0214   | 0.221          | 4.520                | 239.8                 | 237.3                 | 1.04           |
| 0.05     | 0.0086   | 0.089          | 11.268               | 597.8                 | 590.3                 | 1.25           |
| 0.02     | 0.0034   | 0.036          | 28.136               | 1492.7                | 1510.4                | 1.19           |
| 0.01     | 0.0017   | 0.018          | 56.250               | 2984.1                | 2999.0                | 0.05           |

## 5.7 Hook Effect

It is quite common to obtain bioimpedance measurements impacted by parasitic capacitances in parallel with the load being measured [138, 139]. These stray parasitic capacitances will create a characteristic deviation in the data especially recognizable at high frequencies [138, 140]. This deviation is commonly known as the Hook Effect because it resembles a hook when the impedance data is graphed in the impedance plane, similar to that shown in Figure 5.12(b), although it should be noted that the shape of the curve in that graph can be explained entirely from the magnitude and phase deviations on the output voltage signal from the buffered differential voltage amplifier circuit.

Typical correction used to compensate for the stray capacitance has been fitting the recorded data to an expanded Cole-Cole model of the form

where  $T_D$  is a scalar factor used to compensate out the phase shift induced by a parasitic capacitance. However, the stray capacitance impacts the magnitude of the impedance as well and thus this approach is only partially useful.

A more complete compensation for this effect is given by Buendía [141]. In this work, a complex-valued multiplier is suggested whereby both the magnitude and the phase of the measured impedance can be appropriately compensated for by a given parasitic capacitance. The final equation used to compensate a measured data point is [142]

5-23

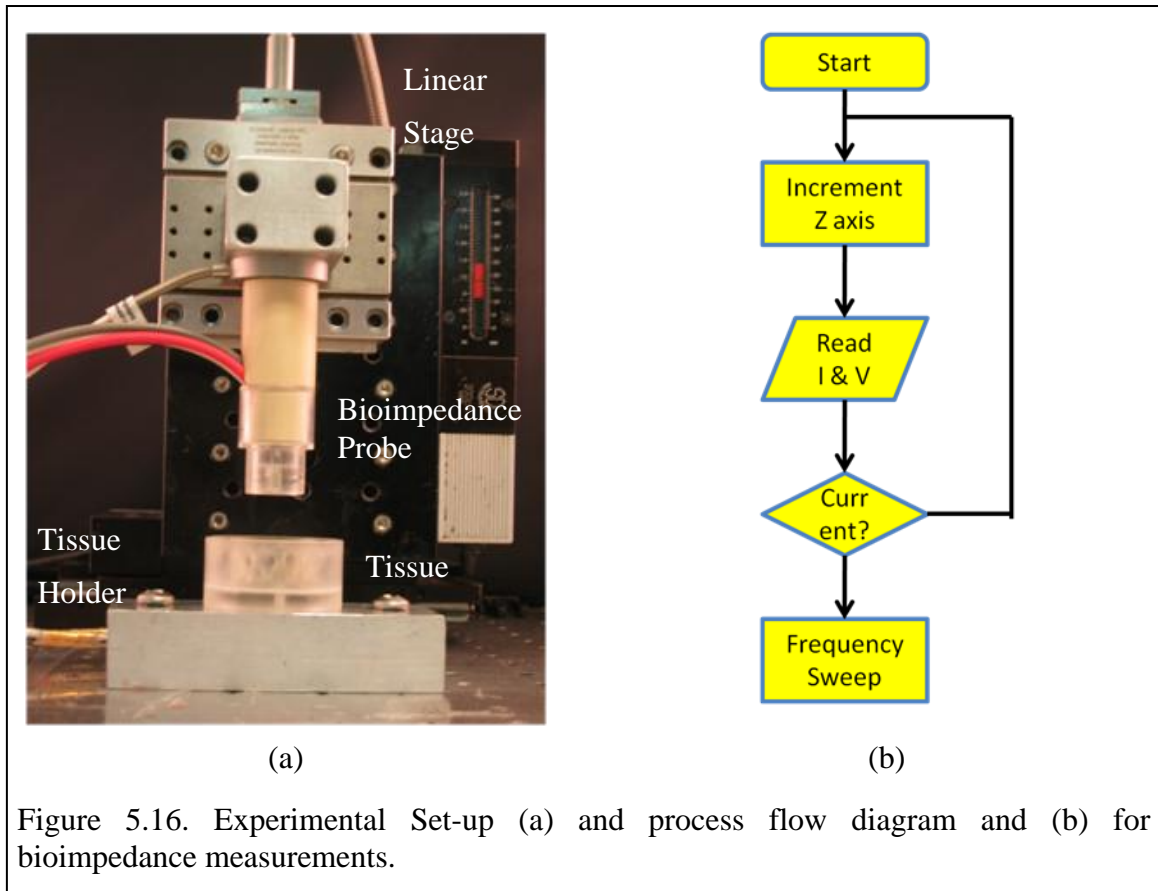
where  $Z_{DUT}$  is the impedance of the ‘device under test,’  $Z_{meas}$  is the measured impedance value, and  $C_p$  is the parasitic capacitance.

For biological samples, the susceptance approaches zero at infinite frequency. Therefore, a good estimate of  $C_p$  can be determined by plotting the susceptance of the data against the angular frequency. The limit of the slope of this graph at high frequency will approach the value of  $C_p$ .

## 5.8 Experimental Methodology

*Ex-vivo* porcine spleen is used to validate the measurement process. Splenic tissue is due to the relative evenness of the tissue physically and access to the known electrical properties of the tissue from within the literature.

The complete experimental set-up is shown in Figure 5.16 . It consists of a custom machined acrylic chamber with a 25.4 mm diameter central housing to hold the tissue. The bioimpedance probe is connected to a Siskiyou 200cri-R linear stage with micrometer positioning accuracy. The BNC extensions of the bioimpedance probe are connected to the bioimpedance measurement circuit, whose outputs are connected to the PXI-5044 oscilloscope. A custom Labview® program is used to process and store the data as described in Appendix C Bioimpedance Labview Program.



Spleen samples were punched out of whole spleen using a sharpened 25.4 mm diameter leather punch (McMaster-Carr, Cleveland, OH). After placing the tissue into the acrylic holder, the bioimpedance probe was moved incrementally with the linear stage until continuity was proven by monitoring the current recorded by the C2V subcircuit. A 13 point logarithmic frequency sweep is performed and  $V_{RMS}$ ,  $I_{RMS}$ , and the phase shift data are recorded by the oscilloscope. This data can be converted from polar into rectangular coordinates as shown in Appendix B Cartesian and Polar Bioimpedance Representations. A non-linear least squares fitting using a trust-region algorithm is used to fit the real part of the impedance data to



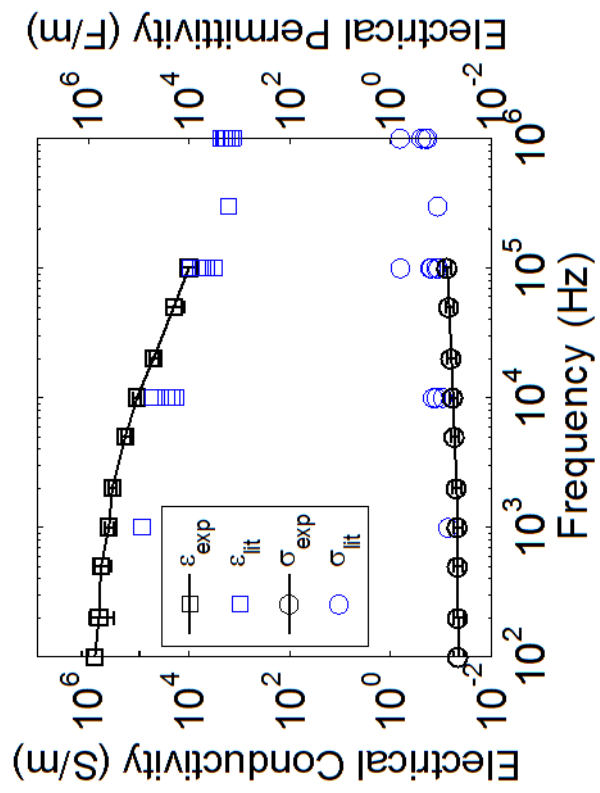
as proposed previously due to the Kramers-Kronig relation coupling the real and imaginary parts of a complex function which is also analytic in the upper half-plane of an impedance plot [143-145].

## 5.9 Results

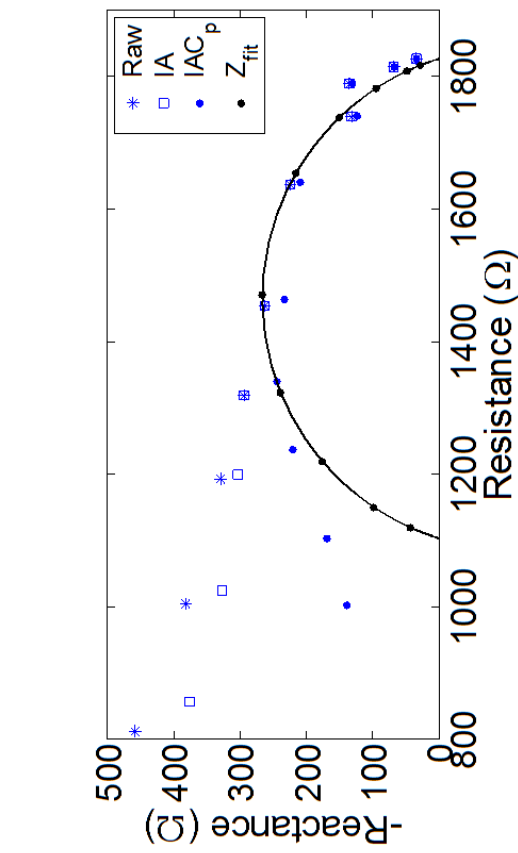
Five porcine spleen tissue samples were tested with the bioimpedance system described above. Results from a representative bioimpedance reading are shown in Figure 5.17(a). Results for the average conductivity and permittivity measurements are shown in Figure 5.17(b) along with values previously reported in the literature [133].

As a design requirement for the bioimpedance measurement circuit was for the output current to be at least  $\frac{1}{2}$  of the expected value, the data was fitted only to frequency measurements up to 100 kHz. In Figure 5.17(a), the raw data is shown (raw) along with the data after calibrating for the buffered differential voltage circuit (IA) and after accounting for the Hook effect ( $IAC_p$ ). The black curve ( $Z_{fit}$ ) shows the non-linear least squares fitted result for the Cole-Cole model.

In Figure 5.17(b), the calculated average permittivity and conductivity values for the five samples tested are plotted in black along with literature values plotted in blue. The conductivity values found here are slightly low compared to the literature values while the permittivity values are found to be slightly high.



(a)



(b)

Figure 5.17. (a) Raw (raw), corrected (IA and IAC<sub>p</sub>), and fitted data ( $Z_{fit}$ ) for one example bioimpedance measurement on porcine spleen tissue and (b) Comparison of electrical conductivity ( $\sigma$ ) and electrical permittivity ( $\epsilon$ ) experimental results for porcine spleen with the literature (note literature based on a range of animal spleen values at various temperature ranges).

## 5.10 Discussion

The results shown in Figure 5.17 validate the use of a new constant current source for use in a bioimpedance circuit. Additionally, incorporating a microprocessor onto the circuit would negate the need for the oscilloscope to make measurements and the entire bioimpedance system could be developed as a low-cost solution for bioimpedance measurements.

The inability to use frequency measurements above 100 kHz is believed to be due to stray capacitance losses. As the contact impedance at high frequencies is expected to become negligible (see Figure 5.14), the total expected impedance (that of the tissue plus the contact impedance) at high frequencies is expected to be nearly all from the tissue, which is well below the 5 k $\Omega$  rated output impedance of the VCCS. Therefore, it is believed that the estimated 400 pF stray capacitance from the Hook Effect acts as a current divider causing significantly less current to pass through the tissue at high frequencies.

The results reported with this device for spleen tissue are low compared to published reports for the dielectric properties of spleen tissue reported elsewhere in the literature [133]. However, these measurements were taken at 24°C and, accounting for a 2%/°C increase in conductivity of tissue, these results lie within 10% of the previously reported values. Additionally, the range of reported values is seen to deviate by as much as an order of magnitude which can result from differing measurement techniques used as well as tissue temperatures at the time of measurement. This wide discrepancy within the literature is quite large compared to the offset of the data collected here.

It is well known that the electrical conductivity of tissue exhibits a temperature dependence of approximately 2%/°C [146]. Both high current densities and high strain rates can potentially increase tissue temperature. Due to this, the current used to drive the tissue load was purposely maintained at levels to ensure current densities remained below levels high enough to increase the temperature of the tissue. In addition, the circuitry was only powered up while measurements were being taken to avoid unnecessary temperature heating. While thermal monitoring was not included in this current experimental setup,

the addition of thermal monitoring would allow for thermal effects to be determined and compensated for.

Due to the robustness of the bioimpedance probe constructed for this research, the system could work well in a research capacity for understanding physiological changes in tissue over time. Specifically, as is presented in the next chapter, this system can be used to monitor the bioimpedance of soft tissue under compressive strain.

## **5.11 Conclusions**

In this research a low-cost, custom bioimpedance system utilizing a new constant current source to actively compensate for DC bias current has been developed allowing for the measurement of bioimpedance of soft tissue. Further refinement of this system, including incorporating a microprocessor on the PCB, incorporating smaller electrodes and decreasing electrode spacing will allow for a truly portable and robust system. Additionally, ensuring stray capacitances in the experimental set-up are minimized will allow for the full bandwidth of the circuit to be used. The research potential for this bioimpedance system includes whole body or segmental edema monitoring, blunt trauma, and electrosurgery.

## **Chapter 6 Bioimpedance of Porcine Spleen under Compression**

### **6.1 Introduction**

Tissue undergoes compression in a variety of physiological and clinical experiences. Examples include the pressure exerted on vessel walls during blood flow, blunt trauma injuries, use of the “nephrologist’s handshake” in determining hydration status in dialysis patients, and during the use of electro-surgical forceps when cauterizing tissue.

Despite the prevalence of tissue compression in such relatively common and important processes, little within the literature has been published on how tissue responds to compression. Typical assumptions include the loss of extracellular fluid from the compressed tissue space [147]. For the case of electro-surgery, this loss of fluid would directly impact the ability of the electro-surgical generator to coagulate tissue as ionic content within the fluid is responsible for the conduction of current through the tissue. Bioimpedance techniques, as described in Chapter 5, can distinguish between intracellular fluid, extracellular fluid, and the bulk capacitance of the cellular membranes. Together with pressure relaxation monitoring and histology, bioimpedance measurements offer a complimentary methodology for a more complete analysis of what occurs to tissue during compression.

Previous literature has noticed a change in electrical readings with an increase in pressure applied to measurement devices. Gonzalez-Correa et al. [147] showed that for various tissues the resistivity increases as pressure is increased to the measurement probe. Keshtkar et al. [148] showed that independent of pressure readings, the ratio of probe size to effective electrode size must be considered as well. Larger probes tend to report lower impedance readings than smaller probes given a constant pressure and electrode size.

Both papers assert the loss of extracellular fluid for the increase in electrical impedance readings, however, complex impedance data that could be gathered using bioimpedance techniques is not shown. Additionally, the effect of the bottom of the

measuring device on their readings is not discussed in either paper. It has been shown that bioimpedance readings are affected by the insertion depth of the probe, or the proximity of the measuring electrodes to the bottom of the measuring device [117].

It is the goal of this research to identify the affect tissue compression has on bioimpedance readings as well as fluid levels between various compartments in tissue. Based on these values, an extended Cole-Cole model utilizing strain-dependent values is suggested for analysis of compressed tissue. As the components of the Cole-Cole model can be mapped to the intracellular and extracellular fluid compartments of tissue as discussed in Section 5.2.1, a hypothesis for what happens to tissue during compression is also developed.

## 6.2 Experimental Set-up and Procedure

The experimental set-up for these experiments is identical to that used in Chapter 5 with the incorporation of a load cell and pressure sensor. In addition to the linear stage (Siskiyou, Inc., Grants Pass, OR), bioimpedance probe, and acrylic tissue chamber, a load cell (LC8125, Omega, Stamford, CT) is used in series with the bioimpedance probe and a pressure sensor (NPC-1210, GE Measurement and Control Solutions, Billerica, MA) is incorporated into the bottom of the tissue chamber to monitor tissue relaxation during and after compression. The complete experimental set-up is shown in Figure 6.1. The

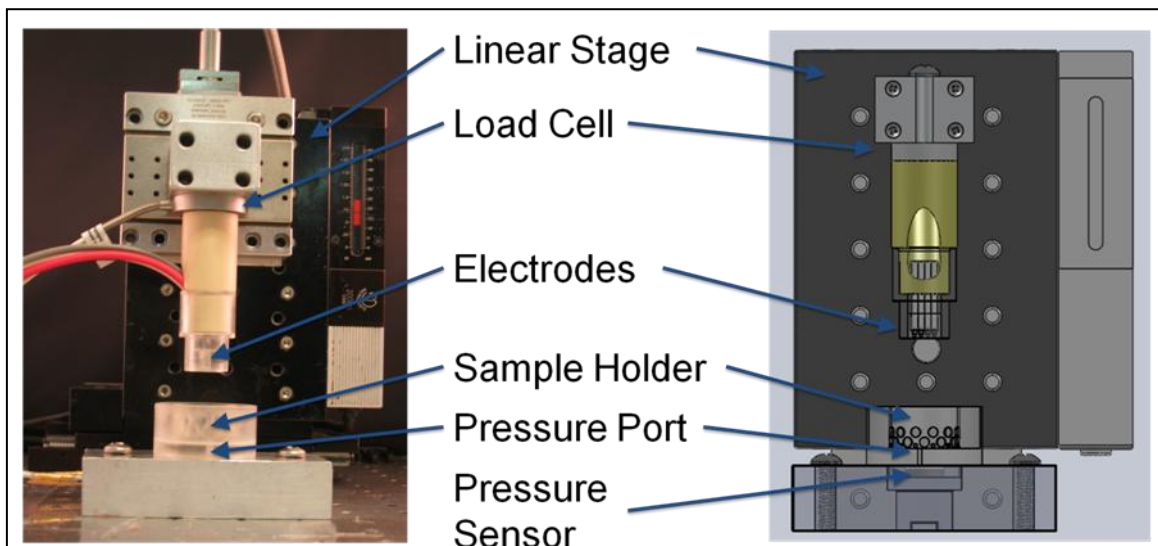


Figure 6.1. Experimental set-up for tissue compression experiments.

pressure sensor is coupled to the underside of the tissue chamber through a 3 mm diameter hole through the bottom of the acrylic. An array of holes drilled radially through the acrylic chamber allow for the free flow of fluid out of the tissue into an outside collection well built around the tissue chamber.

### 6.2.1 Characterization of the Tissue Chamber

Including the calibrations for the circuitry and the Hook Effect described in Section 5.7, the experimental set-up was additionally calibrated for effects due to the proximity of the probe to the floor of the tissue chamber. It has previously been shown that impedance measurements are dependent on insertion depth, especially as the change in impedance between differing layers increases [117, 149, 150]. As the bioimpedance probe gets closer to the bottom of the acrylic chamber used to hold the tissue, field lines associated with the passage of current through the tissue will be affected by the impedance of the acrylic. This depth-dependent apparent resistance must be taken into account for accurate impedance measurements of tissue under higher compression levels.

Results for the measurement of  $|Z|$  as a function of frequency for various insertion depths are shown in Figure 6.2(a). The measured impedance is seen to increase as the distance from the bottom of the tissue chamber decreases. However, as shown in Figure 6.3, the increase is independent of saline concentration over the frequency range of 100

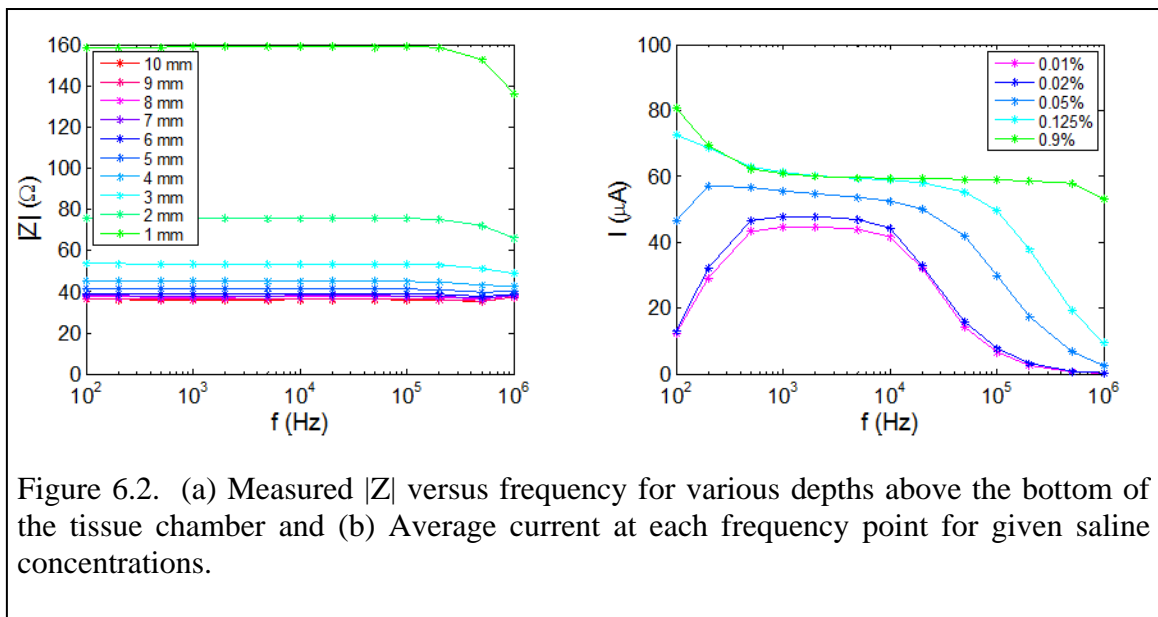


Figure 6.2. (a) Measured  $|Z|$  versus frequency for various depths above the bottom of the tissue chamber and (b) Average current at each frequency point for given saline concentrations.

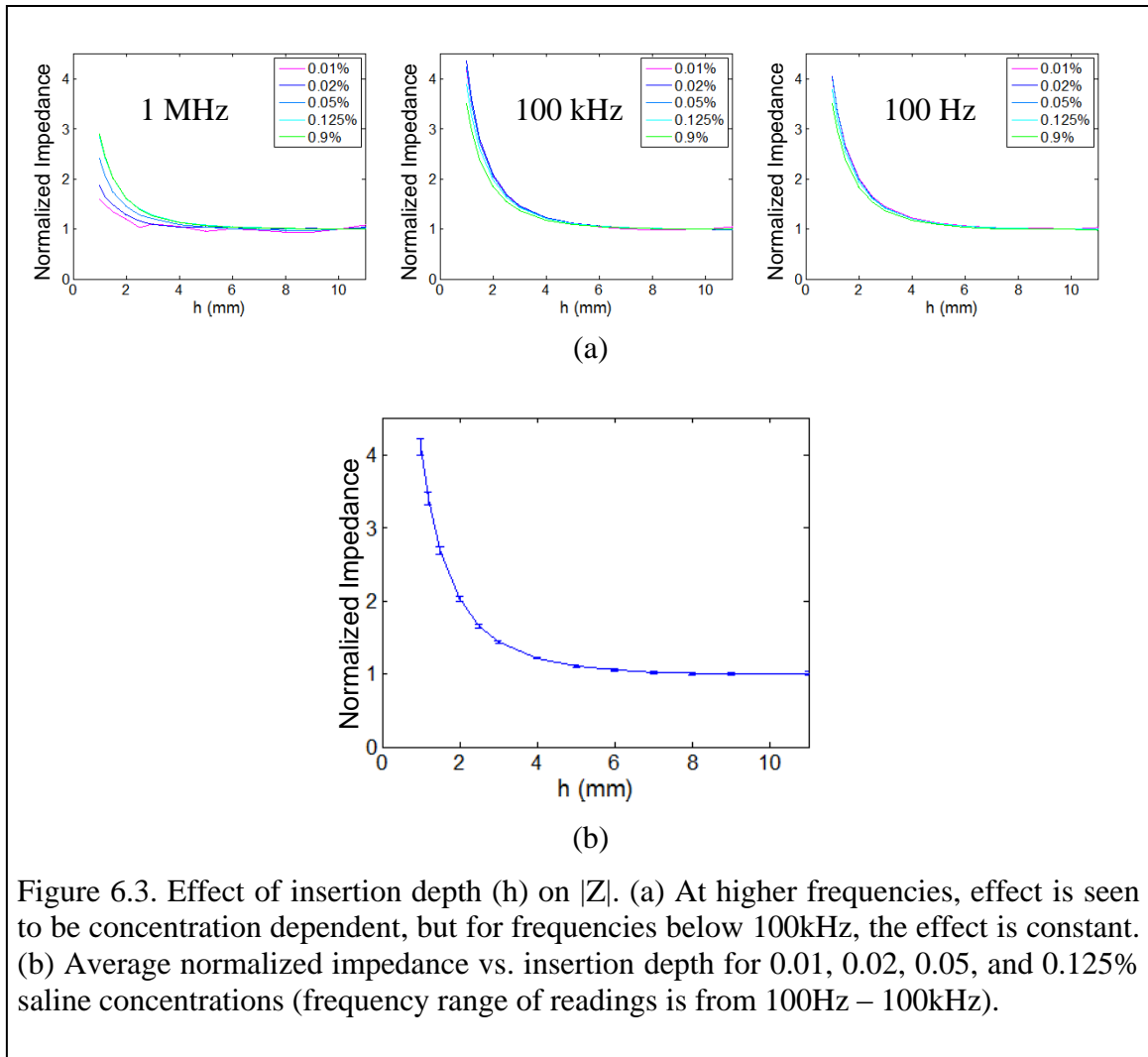


Figure 6.3. Effect of insertion depth ( $h$ ) on  $|Z|$ . (a) At higher frequencies, effect is seen to be concentration dependent, but for frequencies below 100kHz, the effect is constant. (b) Average normalized impedance vs. insertion depth for 0.01, 0.02, 0.05, and 0.125% saline concentrations (frequency range of readings is from 100Hz – 100kHz).

Hz – 100 kHz and is only dependent on the insertion depth. Similarly, the impact on the measured phase shift is also seen to be concentration and frequency-independent for the frequency range of 100 Hz – 100 kHz. For all depths the change is seen to be less than one degree. Considering the standard deviation of the data, it is assumed that the impact on phase shift is negligible for data within the above frequency range.

The measured current at each frequency measurement point for various saline concentrations is shown in Figure 6.2(b). As the solution becomes more resistive, the ability for the constant current source to maintain the set output current is seen to drop at both high and low frequencies. The drop-off at low frequencies is due to the increasing contact impedance between the electrode and electrolyte as the saline solution becomes



less concentrated. This increased impedance limits the amount of current that the constant current source can output. The drop-off at high frequencies is due to stray capacitances and resultant leakage current in the experimental setup. Data points for which the measured current drops below  $30 \mu\text{A}$  are discarded from analysis.

The dielectric properties measured for the saline solutions are shown in Figure 6.5. Based on the characterization for the saline solutions tested and the known ranges of dielectric properties for tissue, it is believed that the measured data can be calibrated adequately for the frequency range  $100 \text{ Hz} - 100 \text{ kHz}$ . Due to the concentration-dependence, and therefore impedance-dependence, of frequency data greater than  $100 \text{ kHz}$ , it is not feasible to use this data for monitoring strain-dependent properties of tissue.

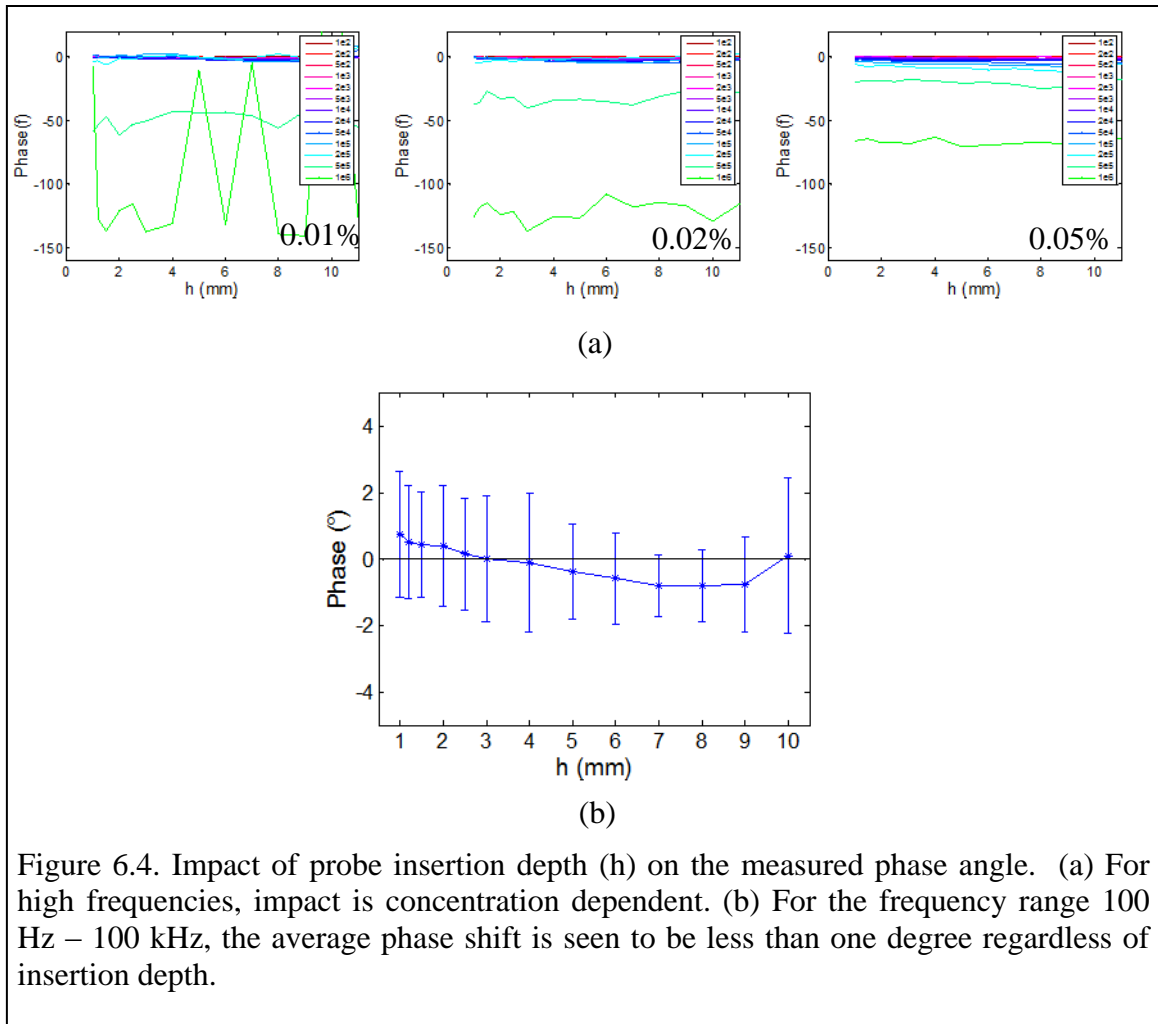


Figure 6.4. Impact of probe insertion depth ( $h$ ) on the measured phase angle. (a) For high frequencies, impact is concentration dependent. (b) For the frequency range  $100 \text{ Hz} - 100 \text{ kHz}$ , the average phase shift is seen to be less than one degree regardless of insertion depth.

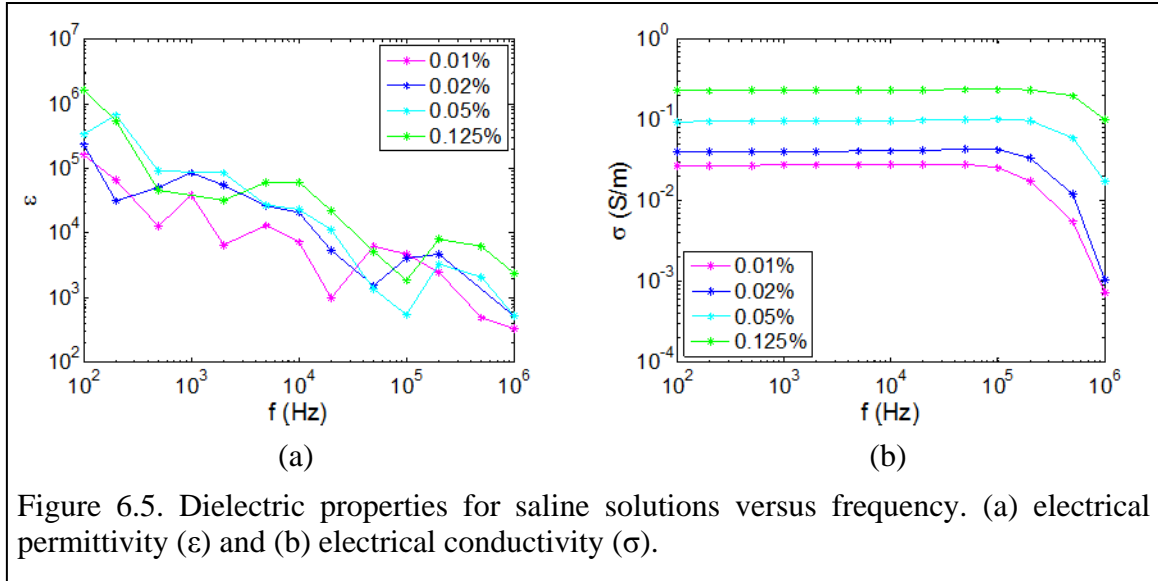


Figure 6.5. Dielectric properties for saline solutions versus frequency. (a) electrical permittivity ( $\epsilon$ ) and (b) electrical conductivity ( $\sigma$ ).

## 6.2.2 Experimental Procedure

A process flow chart for how the experiment was run is shown in Figure 6.6. For each test, a 25.4 mm plug of spleen tissue is cut out of a whole spleen for testing. The bottom of the tissue chamber is then found by incrementally lowering the bioimpedance probe until a load is detected on the load cell as described in Section 6.2.1. The linear stage is brought to its most upright position, and the tissue sample is placed in the acrylic tissue chamber. The linear stage is again incrementally lowered while monitoring the current across the outer two electrodes of the bioimpedance probe. Upon sensing current the bioimpedance probe, the BP is lowered an additional 100  $\mu\text{m}$  to ensure good contact with the tissue and the tissue thickness is determined based on this position and the bottom of the tissue chamber. Pressure is recorded for 5 s to calibrate out any offset and a frequency sweep is performed sending 60  $\mu\text{A}_{\text{RMS}}$  through the tissue. Voltage, current, and phase shift readings are taken on the PXI-5044. The tissue is then compressed to 10% strain level while monitoring the pressure on the tissue. The pressure relaxation is continuously monitored until a steady state readings is achieved and a frequency sweep is again performed on the tissue. This cycle is repeated until 80% strain level has been reached, at which point the linear stage is raised and the tissue sample is placed in 10% formalin for histology with a hematoxylin and eosin (H&E) stain.

### 6.2.3 Experimental Calibration

Three calibration steps were used to condition the data and compensate for the circuit, experimental set-up, and Hook Effect seen in the data collected. Each set of data was calibrated in the following order:

1. Compensate for bandwidth of the differential voltage measurement circuit
2. Compensate for insertion depth of the probe
3. Compensate for the Hook Effect seen at high frequencies

The differential voltage measurement circuit compensation for impedance magnitude was performed by

6-1

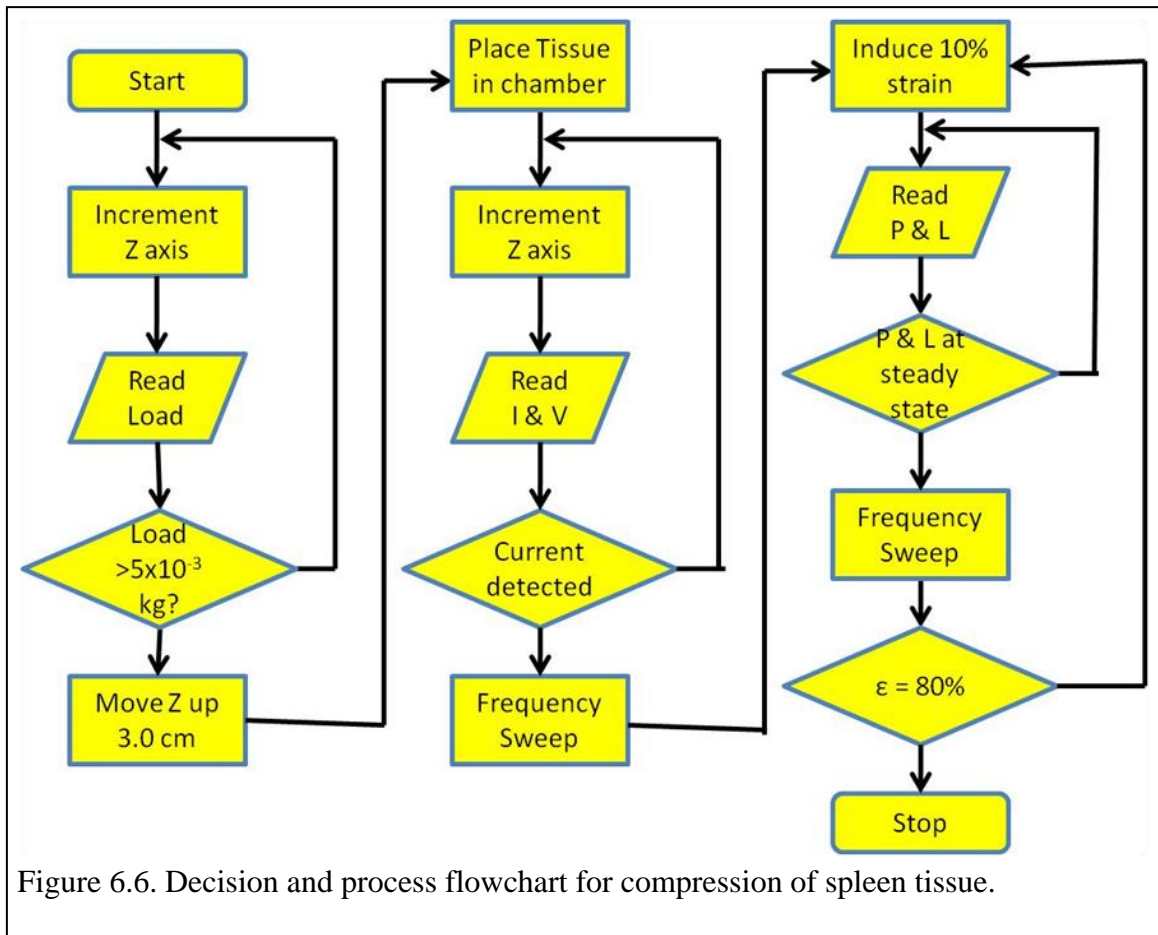


Figure 6.6. Decision and process flowchart for compression of spleen tissue.

where  $|Z|_{IA}$  is the compensated impedance magnitude,  $|Z|_{raw}$  is the raw data,  $f$  is the frequency of the impedance measurement, and  $dB$  is the decibel drop-off that the circuit imposes on the input voltage difference as a function of frequency.

The differential voltage measurement circuit compensation for impedance phase was performed by

6-2

where  $\theta_{IA}$  is the compensated impedance phase measurement,  $\theta_{raw}$  is the raw phase measurement, and  $\theta_{shift}$  is the phase shift that the circuit imposes on the output of the voltage difference amplifier as a function of frequency.

The data from Figure 6.3(b) is used to compensate the measured  $|Z|$  value for all bioimpedance measurements through the equation

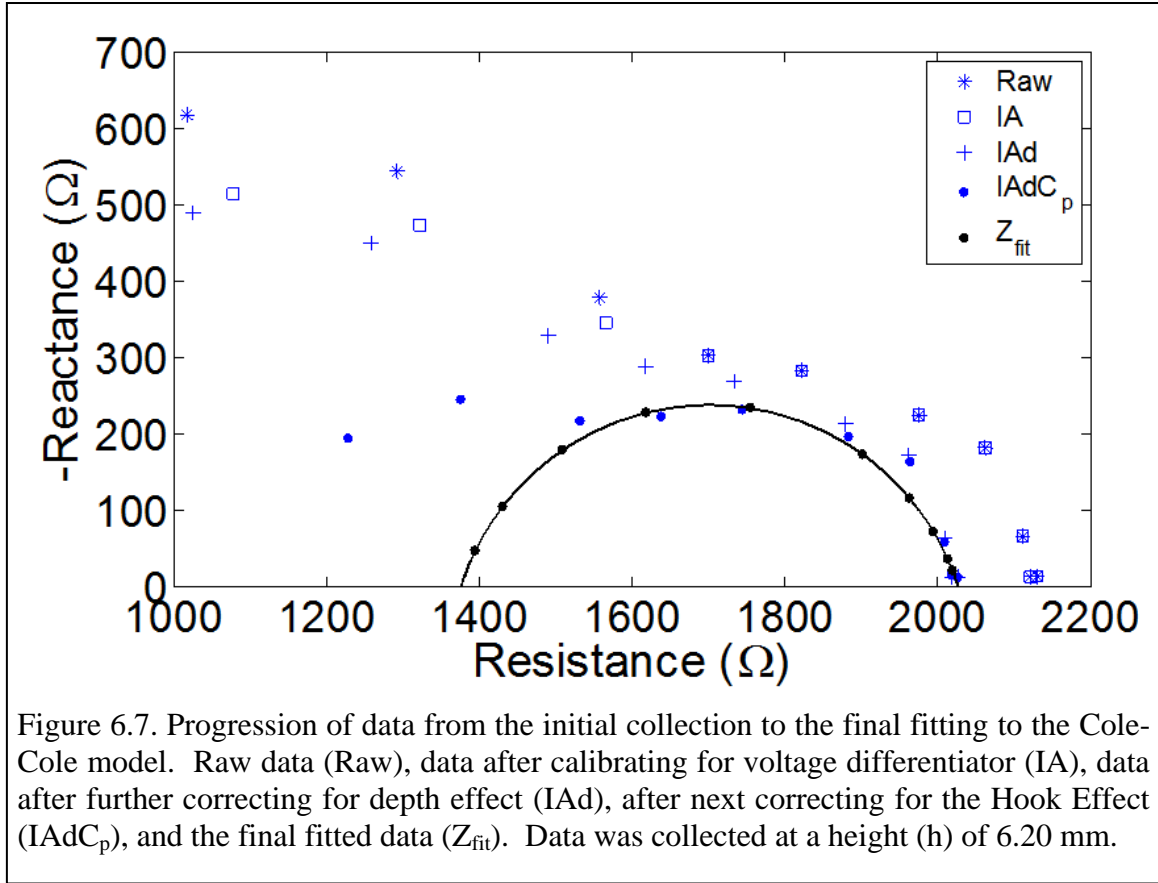
————— 6-3

where  $|Z|_{IAd}$  is the impedance magnitude calibrated for the circuit and insertion depth and  $d_{factor}$  is the insertion depth calibration factor. As shown in Figure 6.4, the phase shift due to insertion depth is negligible and is not compensated for in this analysis. The values and standard deviations for  $d_{factor}$  are shown in Table 6.1.

The Hook Effect is compensated for using the methodology of Buendía et. al [141] whereby the parasitic capacitance from the experimental set-up can be calibrated out using the following equation

6-4

where  $Z_{IAdCp}$  is the impedance magnitude compensated for the circuitry, insertion depth, and stray capacitance [141]. Additionally,  $j$  is  $\sqrt{-1}$ ,  $\omega$  is the angular frequency, and  $C_p$  is



the parasitic capacitance. The stray capacitance term ( $C_p$ ) can be estimated as the slope of the susceptance plotted against the natural frequency.

#### 6.2.4 Non-linear Least Squares Fitting

The final conditioned data ( $Z_{IAdC_p}$ ) was then passed into a non-linear least squares fitting algorithm using a trust-region algorithm to fit the  $Re\{Z_{IAdC_p}\}$  to the theoretical real part of the Cole-Cole model

$$\frac{R(\omega) - R_\infty}{R_0 - R_\infty} = \frac{1}{1 + (j\omega\tau)^\alpha}$$

6-5

where  $R(\omega)$  is the  $Re\{Z_{IAdC_p}(\omega)\}$ ,  $R_\infty$  is the resistance at infinite frequency,  $R_0$  is the resistance at zero frequency (DC),  $\tau$  is the relaxation time constant for the tissue, and  $\alpha$  is the dispersion coefficient.

### 6.3 Results

Both bioimpedance and pressure readings were recorded during the compression of tissue. Pressure readings were taken at a rate of 100 Hz from the beginning of compression until a suitable relaxation in the stress reading had occurred. Bioimpedance measurements were then taken over a frequency range of 100 Hz-1 MHz, however, as discussed in Section 6.2.1, only the range from 100 Hz – 100 kHz is used in the data fitting due to decreased current output and impedance-dependent changes seen in the saline solution measurements. Any data points at low frequencies for which the measured current dropped below 30  $\mu\text{A}$  were also removed from analysis.

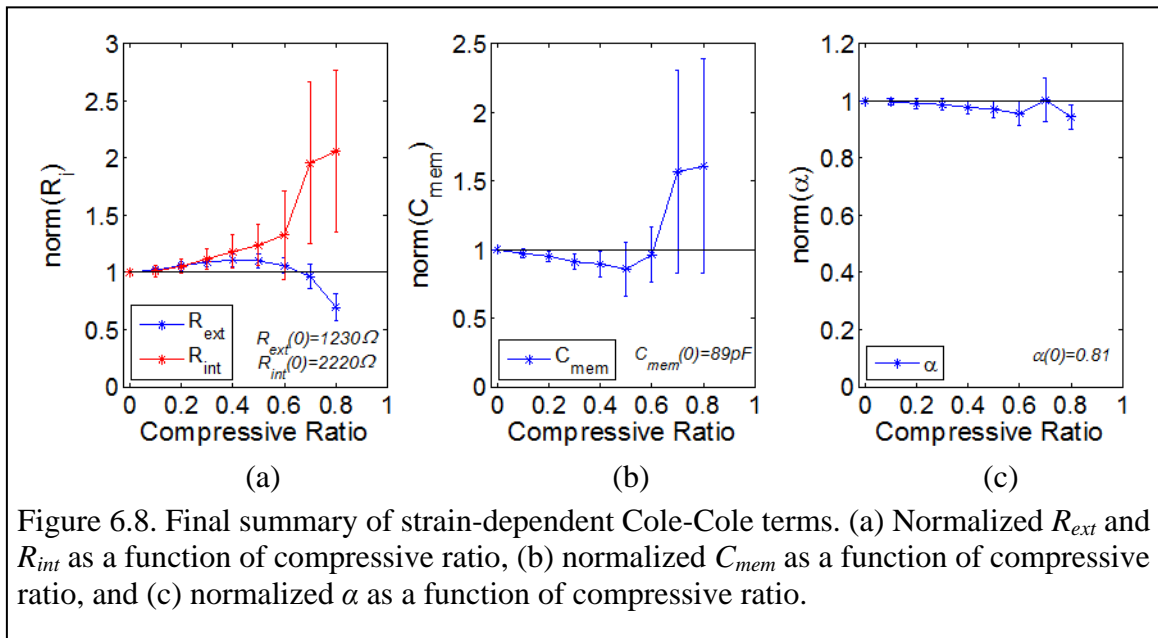


Figure 6.8. Final summary of strain-dependent Cole-Cole terms. (a) Normalized  $R_{ext}$  and  $R_{int}$  as a function of compressive ratio, (b) normalized  $C_{mem}$  as a function of compressive ratio, and (c) normalized  $\alpha$  as a function of compressive ratio.

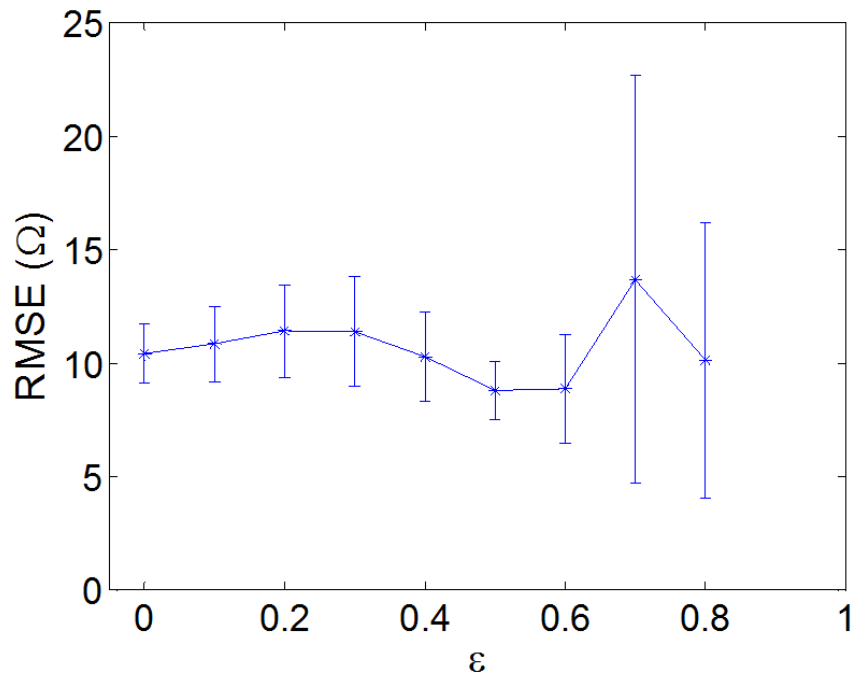


Figure 6.9. Mean and standard deviation (error bars) of the RMSE for data fitting to a Cole-Cole model for eight samples over 0-80% compression.

### 6.3.1 Bioimpedance Measurements

Data for an example bioimpedance measurement is shown in Figure 6.7 for porcine spleen tissue measured at 50% compression and a height of 6.20mm. The graph shows the progression of the data from its initial collection through the final fitting to a Cole-Cole model. Raw data (raw) is first compensated for magnitude and phase shifts derived from the circuit board (IA), as discussed in Section 5.4.3. This data is then calibrated for the effect of insertion depth (IAd), and finally for the Hook Effect (IAdC<sub>p</sub>). The calibration factor for insertion depth in Figure 6.7 was 1.051 and the parasitic capacitance was calculated to be 404 pF. The final fitted data ( $Z_{\text{fit}}$ ) is then plotted for each frequency point as well as a continuous function (black line). The root mean squared error (RMSE) for this fit was 18.8  $\Omega$ .

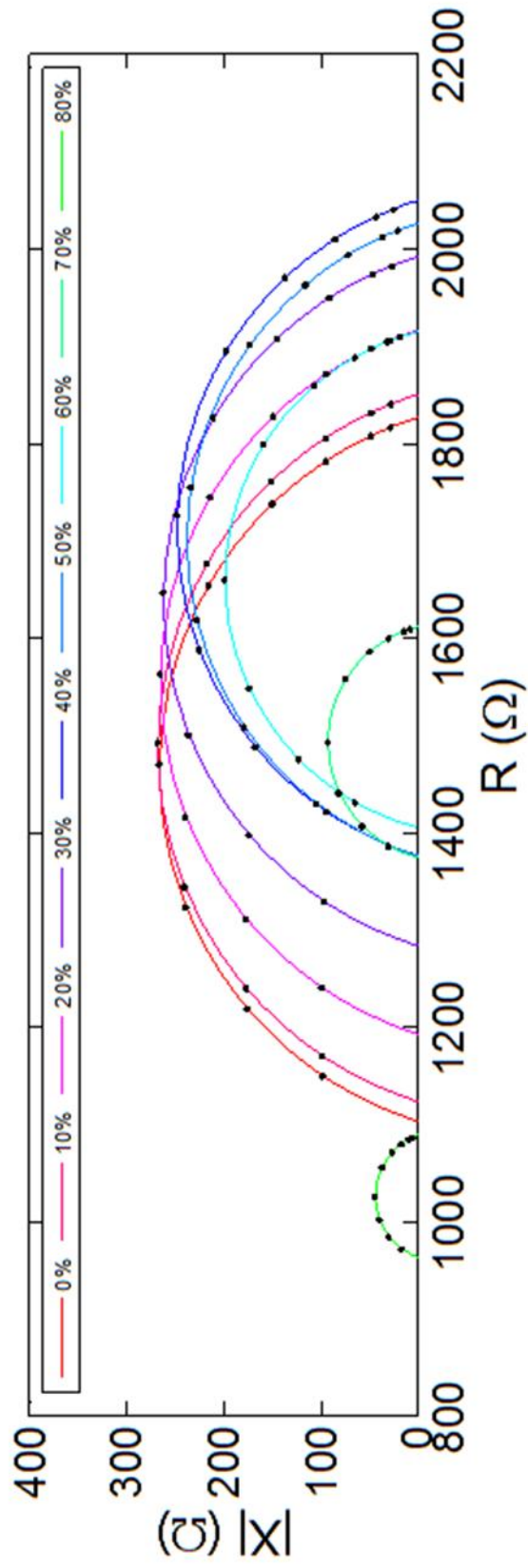
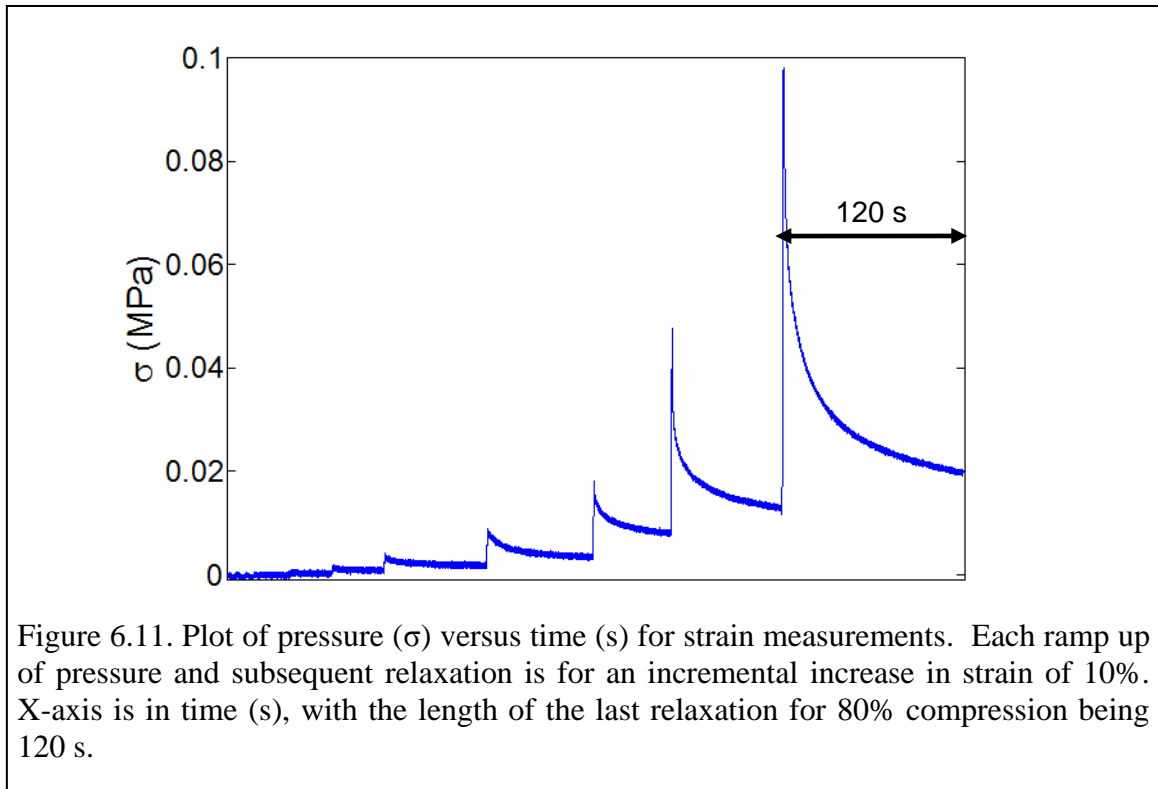


Figure 6.10. Overview of the development of the impedance loci during tissue compression. Note the shift of the loci to the right for lower compression levels and then a dramatic shift to the left and collapse of the loci at higher compression levels.





Overall, the RMSE values for the Cole-Cole model fits as a function of strain are shown in Figure 6.9 where the mean of the RMSE is seen to be less than  $15 \Omega$  over the whole range of compressions.

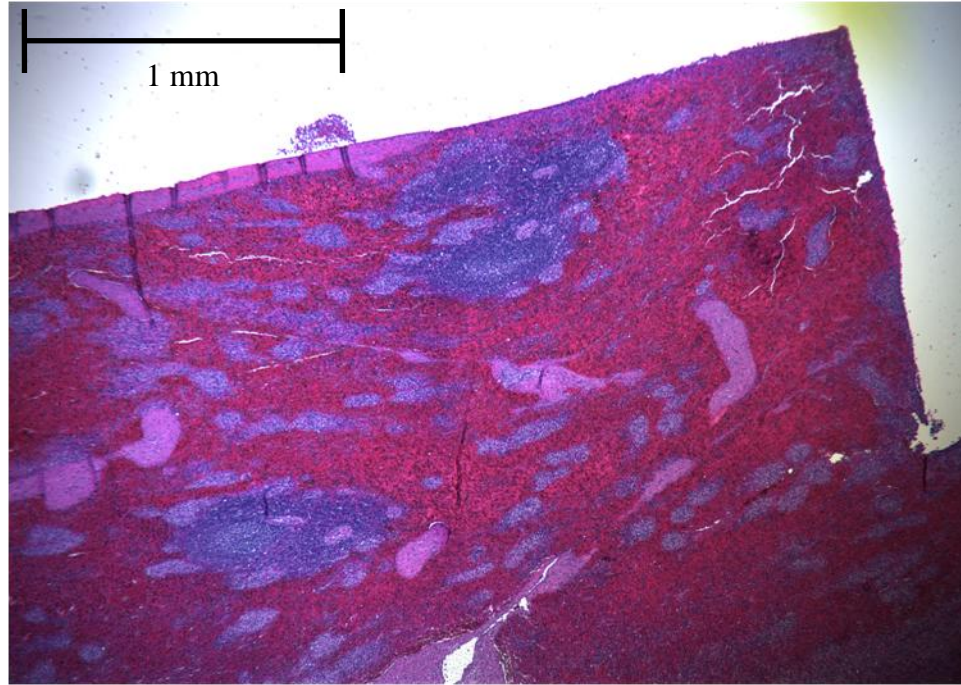
An overview of the development of the impedance loci is shown in Figure 6.10 for one of the tissue trials. It can be seen that the impedance loci initially increase before both collapsing and moving to the left at extreme compression levels.

### 6.3.2 Pressure Measurements

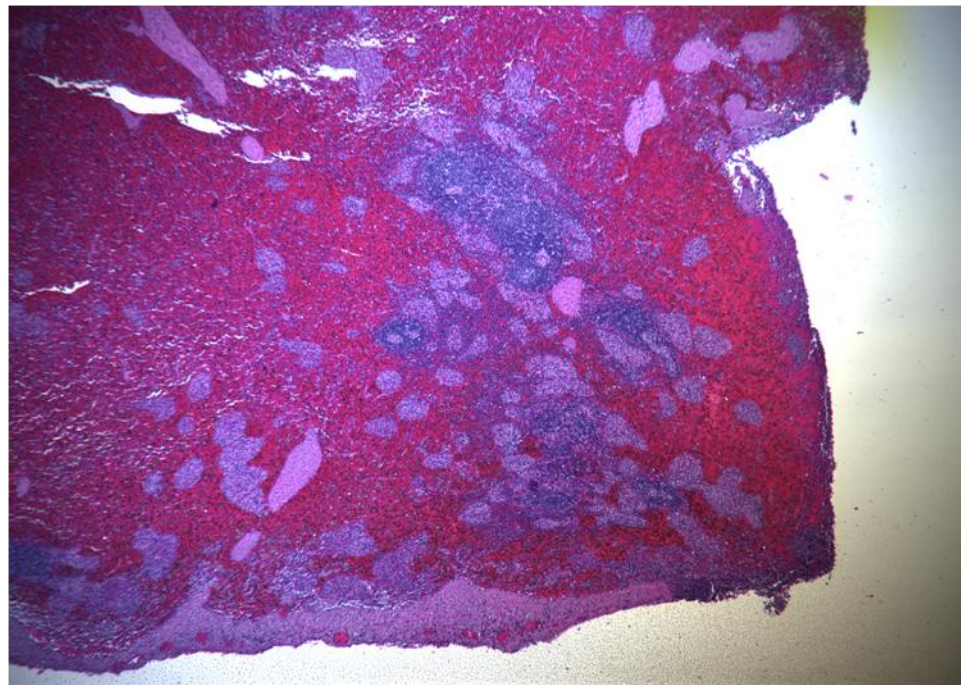
Pressure measurements were taken from the start of a strain application until a satisfactory amount of relaxation had occurred. Figure 6.11 shows the pressure on the tissue over time for each successive 10% strain put on the tissue. At higher strains, each increase in strain resulted in a more than doubling of the peak stress placed on the tissue.

### 6.3.3 Histology

Representative images at 10X magnification for 0% and 80% compression levels are shown in Figure 6.12 and 40X magnification in Figure 6.13. Much of the tissue looks

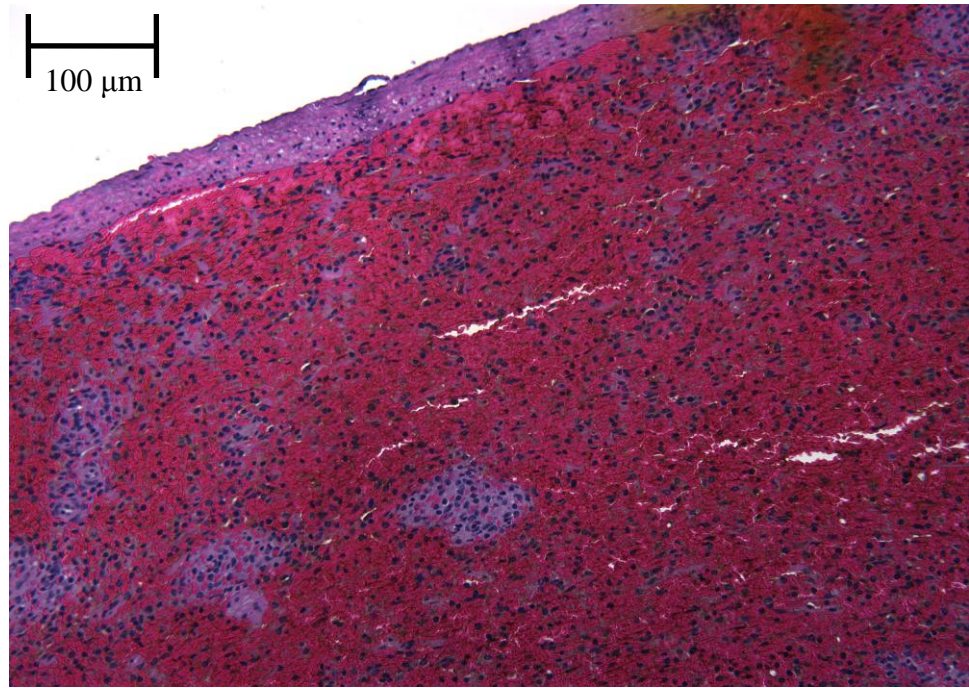


(a)

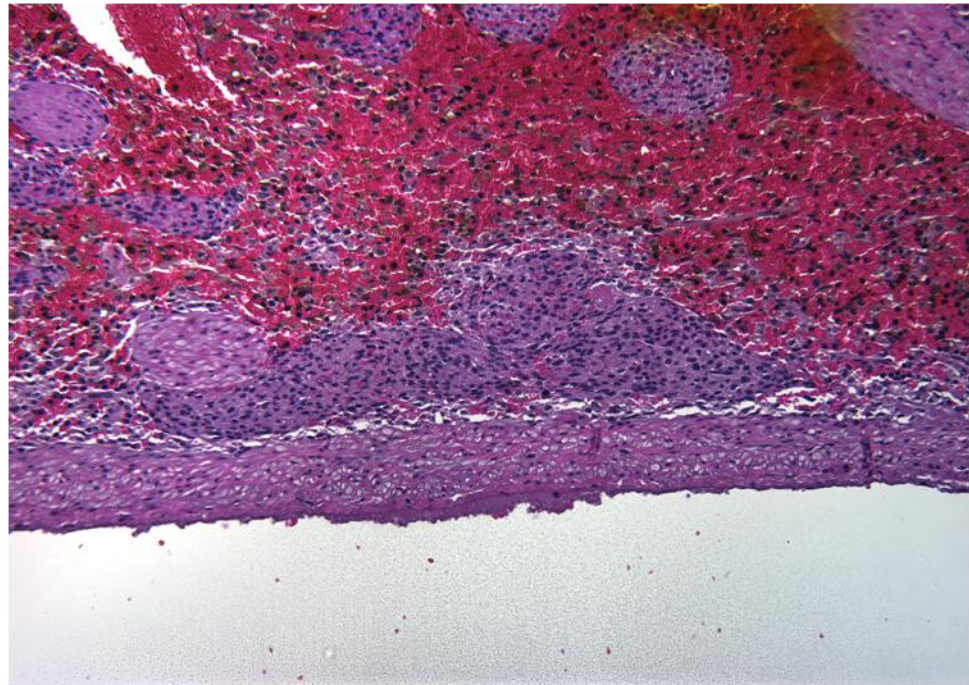


(b)

Figure 6.12. Histology at 10X magnification for (a) 80% tissue compression and (b) control.



(a)



(b)

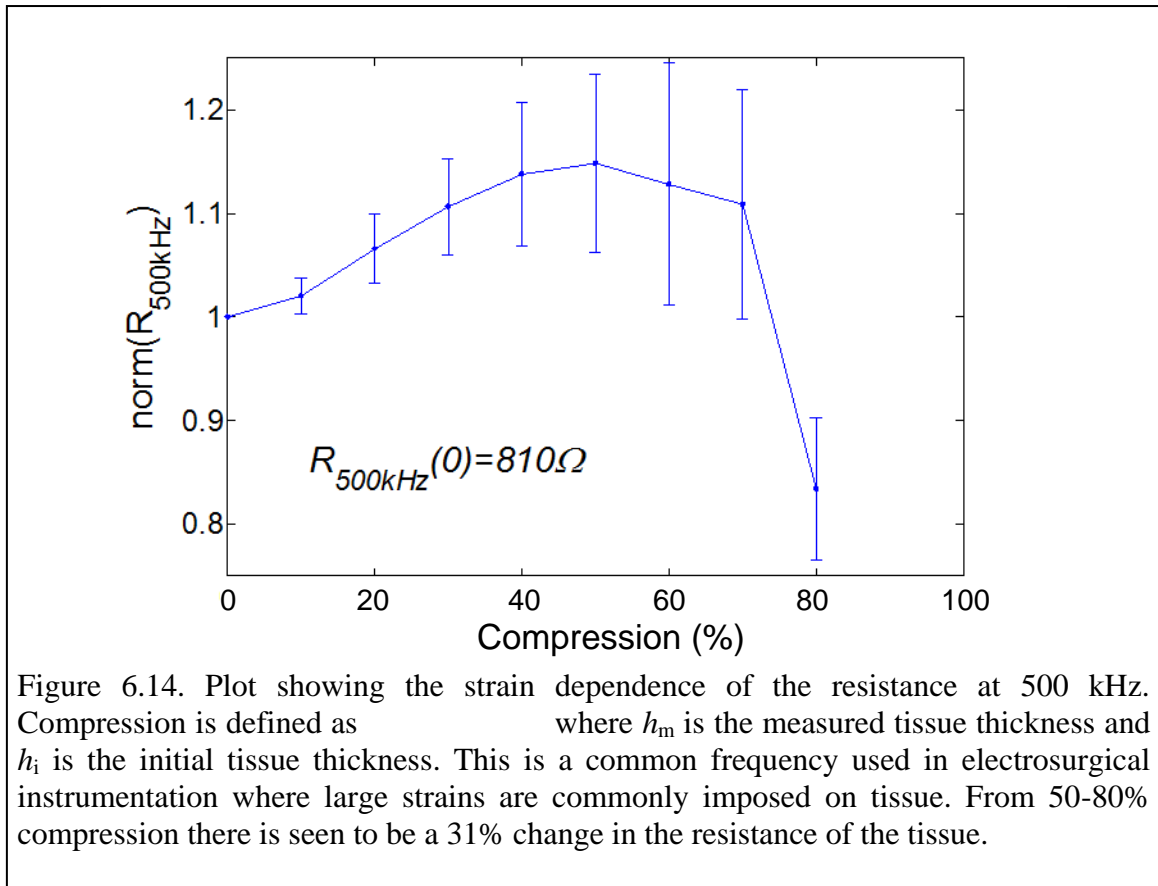
Figure 6.13. Histology at 40X magnification for (a) 80% tissue compression and (b) control.

quite similar between the different compression levels, but the capsule does appear to become more compressed at the higher compression levels. Zones of active white blood cell maturation are still evident even in the 80% compressed tissue samples. Of note is the increased ‘free space’ seen in the uncompressed histology slides as opposed to the relatively ‘squeezed’ appearance of the highly compressed tissue. This may be indicative of the loss of free interstitial fluid during compression.

#### **6.4 Discussions**

Bioimpedance data for porcine spleen tissue under compression show two distinct stages of change. Initially, under small strains (<40%), both  $R_\infty$  and  $R_0$  increase slightly from around 10% for  $R_0$  and around 25% for  $R_\infty$ . With increasing compression, however,  $R_0$  is seen to decrease while  $R_\infty$  is seen to increase quite rapidly. The bulk membrane capacitance sees an opposing trend to  $R_0$  where after an initial decrease at low compression levels the capacitance value begins to increase rapidly for increasing strain. In general, the dispersion term, intriguingly, remains fairly consistent over compression levels. Certainly major mechanical changes are occurring at high compression levels.

There are at least two distinct phenomena that could bring about such a trend in the bioimpedance readings. The first is the case where cell membranes are being ruptured. Whereas at low strains both interstitial and intracellular spaces are losing conductance, after a certain strain level the conductance of the interstitial space increases. During compression, the interstitial space is a medium between the intracellular and the open boundary of the tissue. Thus, while the intracellular space is losing fluid and ions to the outside of the tissue it is also gaining ionic and fluidic components from the intracellular space. Assuming the rupturing of cell membranes at some critical stress level due to increasing compression, much more of that fluid could be entering into the interstitial space than is being lost to the outside of the tissue, thereby creating a simultaneous drop in resistance for the interstitial space while increasing the resistance of the intracellular space. Additionally, the decreased capacitance initially could potentially be the result of cell membranes being brought into contact with other cell membranes, resulting in a ‘series’ capacitance which would decrease the capacitance. The increase of bulk membrane capacitance could be explained in that, once the cell ruptures, the membrane



no longer divides tissue compartments and thus has no capacitive impact. This would be the equivalent of removing a series capacitor, which would have the net effect of increasing the overall capacitance.

The second theory revolves around the mass exudation of tissue from the compressed space. In this scenario, cell membranes may not rupture, but the increasing stress from compression is enough to break the bonds of connective tissue holding the cellular matrix intact. While the membranes may not break, radially emanating pressure gradients may push the cells out of the measurement space, leaving behind mostly fluid. At high compression levels, what would be left behind is a reduce amount of cells representing both an increased resistance due to the lower volume and an increase capacitance due to the loss of ‘series’-ness in the cellular membranes.

Looking at the impact this has on electrosurgery, average normalized resistance data for eight trials are shown against the compressive ratio in Figure 6.14. Typical

electrosurgical strains imposed on tissue can easily exceed 50%. From 50-80% strains a 31% loss in resistance is seen, preceded by a 15% increase in resistance.

Histology proves to be inconclusive, but the ‘squeezed’ appearance of the highly compressed tissue does lend to the theory that free interstitial fluid was lost during compression. This correlates well with the fluid seen within the outside container of the tissue chamber; however, this fluid was not measured as to volume to determine if this could be an adequate explanation for the change.

It is well known that the electrical conductivity of tissue exhibits a temperature dependence of approximately 2%/°C [146]. Both high current densities and high strain rates can potentially increase tissue temperature. Due to this, the current used to drive the tissue load was purposely maintained at levels to ensure current densities remained below levels high enough to increase the temperature of the tissue. In addition, the circuitry was only powered up while measurements were being taken to avoid unnecessary temperature heating.

The velocity of the linear stage was maintained at 1.5 mm/s to ensure that strain rates were kept low enough to avoid unwanted development of thermal energy due to compression. Also, bioimpedance measurements were only taken after the tissue had reached a point of relaxation, allowing for any thermal energy generated during compression to dissipate. While thermal monitoring was not included in this current experimental setup, the addition of thermal monitoring would allow for thermal effects to be determined and compensated for.

## **6.5 Conclusions**

This research has quantified the impact that tissue compression has on bioimpedance measurements. Strains of 80% are seen to increase intracellular resistance by as much as 100%, bulk membrane capacitance by as much as 50% after an initial decline of 10%, and interstitial resistance is reduced by as much as 25% after an initial increase of 20%. As opposed to previous assumptions as to the loss of fluid during tissue compression, these findings suggest that just as much, if not more, fluid is lost from the intracellular space as compared to the interstitial space. This could be explained by the fluidic nature of the cellular membrane as well as the fairly porous ionic channels embedded with the

membrane. Histology performed on the tissue samples is inconclusive as to the exact nature of change in the highly compressed tissue, but given the appearance of relatively unharmed cellular structures, cell rupture is believed to not be one of the phenomena at play. However, mass exudation of tissue material from the compressed space may be satisfactory to address the bioimpedance changes seen in the tissue, as that cellular content could have moved back into the compressed space upon relief of the strain during testing. Performing histology on tissue samples while still under compression may best aid in determining the underlying mechanism of bioimpedance change seen in this data.

## Chapter 7 Conclusions

### 7.1 Major Achievements

The minimization of lateral thermal spread during bipolar electrosurgery has been identified as one of the major requirements needed to be overcome for the continued use of bipolar electrosurgical devices during prostatectomy and hysterectomy procedures [7]. To date, most bipolar devices attempt to mitigate this thermal spread by customizing algorithms to control the electrical energy being delivered to the tissue. However, to best shape these algorithms a better understanding of how the key physiological tissue parameters are changed during the procedure is required. This thesis aims to fulfill a portion of this gap by addressing how the compression of tissue changes the electrical properties of the tissue. The results from this thesis enhance the understanding not only of how the impedance of tissue changes under high compression, but also suggests mechanisms for how the physical makeup of the tissue changes during the compression. The results from this thesis can be used to develop bipolar devices that are capable of minimizing the thermal spread in tissue during electrosurgery.

The major achievements of this body of research are:

- *Real-time sub-surface tissue temperature measurement during energized tissue coagulation.* A thermistor-based measurement technique was used incorporating the use of polycarbonate fixtures around energized surgical devices to record tissue temperature in real-time at predetermined points away from the electrode. It is the first known successful attempt of measuring sub-surface tissue temperatures in real-time during energized dissection. The technique was used to compare various energized surgical devices, including monopolar (not included in this dissertation), bipolar, and ultrasonic modalities. This advance has the potential to enhance the surgeon's ability to minimize unwanted thermal damage to surrounding tissues during surgical procedures if incorporated into instrument



designs. Currently, for practical studies, traditional *in situ* dynamic thermography with thermal imaging cameras is limited to open cases.

- *Development of a finite element model for bipolar electrosurgery.* This study demonstrated the capability of using a finite element model (FEM) to study bipolar electrosurgical procedures and demonstrated the importance of incorporating appropriate temperature-dependent tissue properties, electrode geometry, and compression-dependent properties in the FEM model. It was shown that incorporating the temperature-dependent electrical conductivity in the FEM model resulted in a significant 20% decrease in temperature at a distance of 1.0 mm adjacent to the electrode. While a model without strain-dependent electrical conductivity more closely matched the peak temperature values of the experiment, a model developed utilizing a strain-dependent electrical conductivity matched the overall temperature profile, providing a better comparison of the heat transfer time scale.
- *Experimental validation of the use of compression and active cooling adjacent to bipolar electrodes for control of lateral thermal spread.* Experiments carried out with a standard bipolar electrosurgical device and a customized device allowing for continuous, active cooling adjacent to the validate the concept of using active cooling of electrosurgical instruments to minimize collateral thermal damage while maintaining adequate, and potentially increased, coagulative properties seen in current electrosurgical instrumentation. For coagulations of the mesentery and the spleen, temperatures lateral and outside the profile of the device were significantly different between the standard device and the actively cooled device, thus confirming that the use of active cooling is effective at protecting tissue near to electrosurgical electrodes from experiencing lethal levels of thermal energy. Comparing maximum temperatures at the centerline of both devices used to coagulate splenic tissue, times were seen to be not significantly different while maximum temperatures for the actively cooled device was significantly larger, leading to a potential increase in surgical efficiency as procedural times could be

decreased while offering minimized thermal damage with an actively cooled device.

- *Development of a bioimpedance measurement system using a new innovative constant current source.* A custom system has been developed for use in quantifying the effect of compressive strain on the electrical properties of soft tissues. Circuitry involving a unique method for producing a constant current, differential amplification of two voltages, and the monitoring of current input into tissue were developed and prototyped on a PCB board. The constant current source incorporates a DC feedback mechanism to maximize output impedance bandwidth that would otherwise be used to overcome transmitting DC current across the electrode/electrolyte barrier. A bioimpedance probe utilizing platinum electrodes flush to the face of an acrylic fixture was created to transmit and receive electrical data as well as provide compressive strain to tissue. Custom state-machine-based Labview software was developed to fully perform all the tasks involved in compressing tissue and monitoring the mechanical and electrical signals during the compression. The system was validated on passive RC networks mimicking a standard Cole-Cole model, saline solutions, and finally on uncompressed spleen tissue with results within the range of currently published literature values. A major advantage of this system is that it can be created at a relatively low cost as compared to commercially available products reported to perform similar functions.
- *Effect of compressive strain on bioimpedance of spleen tissue.* This research has quantified the impact that compressive strain of tissue has on bioimpedance measurements. Strains of 80% are seen to increase intracellular resistance by as much as 100%, bulk membrane capacitance by as much as 50% after an initial decline of 10%, and interstitial resistance is reduced by as much as 25% after an initial increase of 20%. As opposed to previous assumptions as to the loss of fluid during tissue compression, these findings suggest that just as much, if not more, fluid is lost from the intracellular space as compared to the interstitial space. This could be explained by the fluidic nature of the cellular membrane as well as the

fairly porous ionic channels embedded with the membrane. Given the appearance of relatively unharmed cellular structures seen in histology performed on the compressed tissue samples, cell rupture is believed to not be one of the phenomena at play during high compression levels. A mass exudation of tissue material from the compressed space may be the most satisfactory explanation to address the bioimpedance changes seen in the tissue.

## **7.2 Original Contributions**

The original contributions made to the literature within this research are listed below. The first four contributions were used in the application of a patent for the thermal management of electrosurgical devices [151]. The application was awarded Patent #7815641 on October 19<sup>th</sup>, 2010. The last three original contributions were developed for the analysis of tissue bioimpedance under compression. They allowed for the development of an extended Cole-Cole model that utilizes strain-dependent Cole-Cole parameters to predict the impedance changes in tissue due to compression. The list of original contributions are:

1. An experimental method using thermistors to achieve real-time sub-surface tissue temperature measurements
2. Development of a finite element model for the bipolar electrosurgical procedure capable of analyzing temperature- and strain-dependent electrical conductivity
3. Validation of the use of active cooling channels adjacent to energized electrodes for the minimization of lateral thermal spread during bipolar electrosurgery
4. Realization that adjacent cooling and compression may facilitate coagulation procedures due to higher midline temperatures achieved in shorter periods of time
5. Development of bioimpedance measurement system capable of outputting 60  $\mu$ A AC current from 100 Hz-100 kHz (>3dB) and is sensitive to a range of impedances from 5  $\Omega$ -5 k $\Omega$  impedances
6. Quantified the effect tissue compression has on the electrical properties of spleen tissue including the interstitial space, intracellular space, and bulk membrane capacitance.

7. Developed an extended Cole-Cole model incorporating strain-dependent values for  $R_0$ ,  $R_\infty$ , and  $\tau$ .

### 7.3 Future Work

Based on the results from experiments performed during this research as well as my own analysis of the work performed over the course of this dissertation, the following research is suggested to be performed in order to improve the experimental and modeling work presented as well as to move this research forward from the point it is currently at:

1. *Develop a low-pass filter for tissue temperature measurement during electrosurgery.* While the tissue temperature measurements taken by the thermistors were fairly independent of the voltage from the electrosurgical generator, preliminary data collected on using a customized Wheatstone bridge using a capacitor across the supply voltage lines acted as a very good low-pass filter to the data and may be a better method for collecting temperature data in such an electrically noisy environment. It may also allow for the use of more resilient thermocouples, which proved to be prohibitively sensitive in initial trials to the electrosurgical environment.
2. *Use pointed thermistor tips to improve tissue penetration during temperature measurement.* The thermistor tips could be sharpened to allow easier penetration into the tissue. While penetration was achieved with the current methodology, thermistors would occasionally break and hand pressure was normally needed to ensure that the thermistors penetrated the capsular layer of the tissue being coagulated. While sharpening thermistors would be a delicate and time intensive procedure, if successful it would prove easier to use during the actual experiment where time is more critical.
3. *Perform research to better understand the independent role of cooling and compression in the developed thermal management system.* Active cooling and compression of tissue was shown to be an effective method of controlling lateral thermal spread. However, the contribution of each component (the active cooling and tissue compression) to the reduction in thermal spread is unknown. Research can be performed using different fluid temperatures, flow rates, non-cooled

compressive devices of different thermal diffusivities, and varying compressive strains to quantify how each component in the thermal management system contributes to the overall reduction in lateral thermal energy diffusion. Monitoring the input and output fluid temperatures would allow for an estimation of the energy removed from the system and could be used as an efficiency benchmark for the STMS.

4. *Perform experiments where tissue bioimpedance is measured simultaneously with tissue pressure and strain.* The monitoring of tissue bioimpedance in real-time while the tissue undergoes compression could be performed to couple the exodus of tissue fluid from the tissue space to the bioimpedance measurements. In this research, bioimpedance testing was performed only after tissue relaxation had been achieved. This made it difficult to analyze the stress relaxation readings against bioimpedance. If bioimpedance testing is performed continuously while tissue is being compressed, bioimpedance data can be coupled to stress relaxation data for the analysis of what happens to tissue under high compression. In addition, by performing experiments with varying strain rates, it may be possible to separate cellular compression and fluid flow impacts on bioimpedance from each other. This data could be used to determine flow rates of fluid out of intracellular and extracellular spaces.
5. *Perform cyclic loading tests on tissue while measuring bioimpedance.* The monitoring of tissue bioimpedance under cyclic loading/unloading of the tissue is also another next logical step to take this research as the hysteresis known to occur during the loading and unloading of tissue can be analyzed from a bioimpedance standpoint to offer more complete conclusions as to what happens to tissue during compression at an intracellular and interstitial fluid level.
6. *Update finite element model (FEM) to incorporate strain-dependent electrical conductivity data.* The FEM of bipolar electrosurgery developed in Chapter 3 can now be updated to incorporate the bioimpedance of tissue under compression data from Chapter 6. Additionally, tissue compression was only crudely implemented in the initial model and could be more properly implemented with the pressure data collected during the experiments performed in Chapter 6. Lastly, this model

could be extended out to analyze the active cooling of tissue adjacent to the bipolar electrode in conjunction with the work suggested above in Point 3.

7. *Add thermal monitoring to the bioimpedance experimental setup.* The electrical conductivity of tissue is known to be highly sensitive to temperature at a rate of 2%/°C [146]. Considering the large effect tissue temperature can have on impedance measurements, the actual temperature of the tissue at the time of measurement should be collected along with the mechanical and electrical data. Both high current densities and high strain rates can potentially increase tissue temperature and should be minimized, or at least accounted for, in all impedance measurements.
8. *Develop a new bioimpedance probe.* A new bioimpedance probe design may allow for most of the stray capacitance issues to be resolved. Concentric ring electrodes positioned on the top and bottom of the compression cell can potentially mitigate some of the high frequency problems noticed in the current system. Each concentric ring electrode would consist of a central solid electrode used for voltage referencing while the outer concentric ring would be used to source current into the tissue. This would maximize the voltage readings as the differential voltage would be over the entire length of current input. It would also help to mitigate contact impedance issues as the overall surface area for current injection would increase dramatically. Also, field lines produced in the tissue would extend out radially into the tissue as opposed to the current design where field lines extend into the acrylic tissue holder.
9. *Add platinum black coating to bioimpedance electrodes to reduce contact impedance.* A known methodology for reducing contact impedance of electrodes is to apply a platinum black coating to the electrodes as described in detail in several publications [152, 153]. If this contact impedance is high enough it allows for stray capacitance issues in the experimental setup to dominate further down into lower frequencies. The platinum black process deposits a very thin layer platinum onto the platinum electrode resulting in the blackening of the electrode and thus the source of its name. This can be effective in reducing contact impedance from one to three orders of magnitude through the dramatic increase of

surface area to the electrode. While the platinum black film may be somewhat fragile, if it is cared for properly it can be a long lasting solution [82].

10. *Perform histology on tissue while maintaining compression on tissue throughout histological process.* Considering the inconclusive nature of the histology performed on the compressed tissue in Chapter 6, it is suggested that histology be performed on tissue samples undergoing continuous compression for the duration of processing. This would give a better understanding as to what the bioimpedance electrodes are ‘seeing’ during the electrical testing.

## **Appendices**



## Appendix A Gyrus PlasmaKinetic® Surgical Generator Overview

The Gyrus PlasmaKinetic® System Generator is an advanced electrosurgical generator developed by Gyrus Medical Inc. to provide more effective coagulation and cutting of tissues than when similar instruments are used with other electrosurgical generators [154]. The generator has two main modalities: Vapor Pulse Coagulation (VPC) and PlasmaKinetic Tissue Cutting (PK). Only the VPC modality is used in this research.

The VPC modality is said to produce controlled coagulation of basuclar pedicles using vapor-focused pulsed of energy. Tissue is uniquely coagulated using pulses of PlasmaKinetic energy compared to the continuous output employed in conventional bipolar generators [154]. This feature is said to provide controlled and repeatable outcomes under a variety of surgical situations.

The VPC modality has three separate modes associated with how the PlasmaKinetic energy pulses are applied. These modes are designed to accommodate the coagulation of various types of tissue during electrosurgery. A summary of these modes and how they are designed to be used is shown in Table A.1 [154]. Additionally, load curves as shown in the Gyrus PlasmaKinetic User Manual are shown in Figure A.1 [154].

Table A.1. Summary of VPC modes within the Gyrus PlasmaKinetic® Generator.

| <b>VPC Mode</b> | <b>Target Tissue Type</b>                      | <b>Maximum Output Voltage (V<sub>RMS</sub>)</b> |
|-----------------|--|---|
| VP1             | Low impedance tissue (thin tissue)             | 73  |
| VP2             | Medium impedance tissue                        | 100   |
| VP3             | High impedance tissue (fatty, vascular tissue) | 120   |

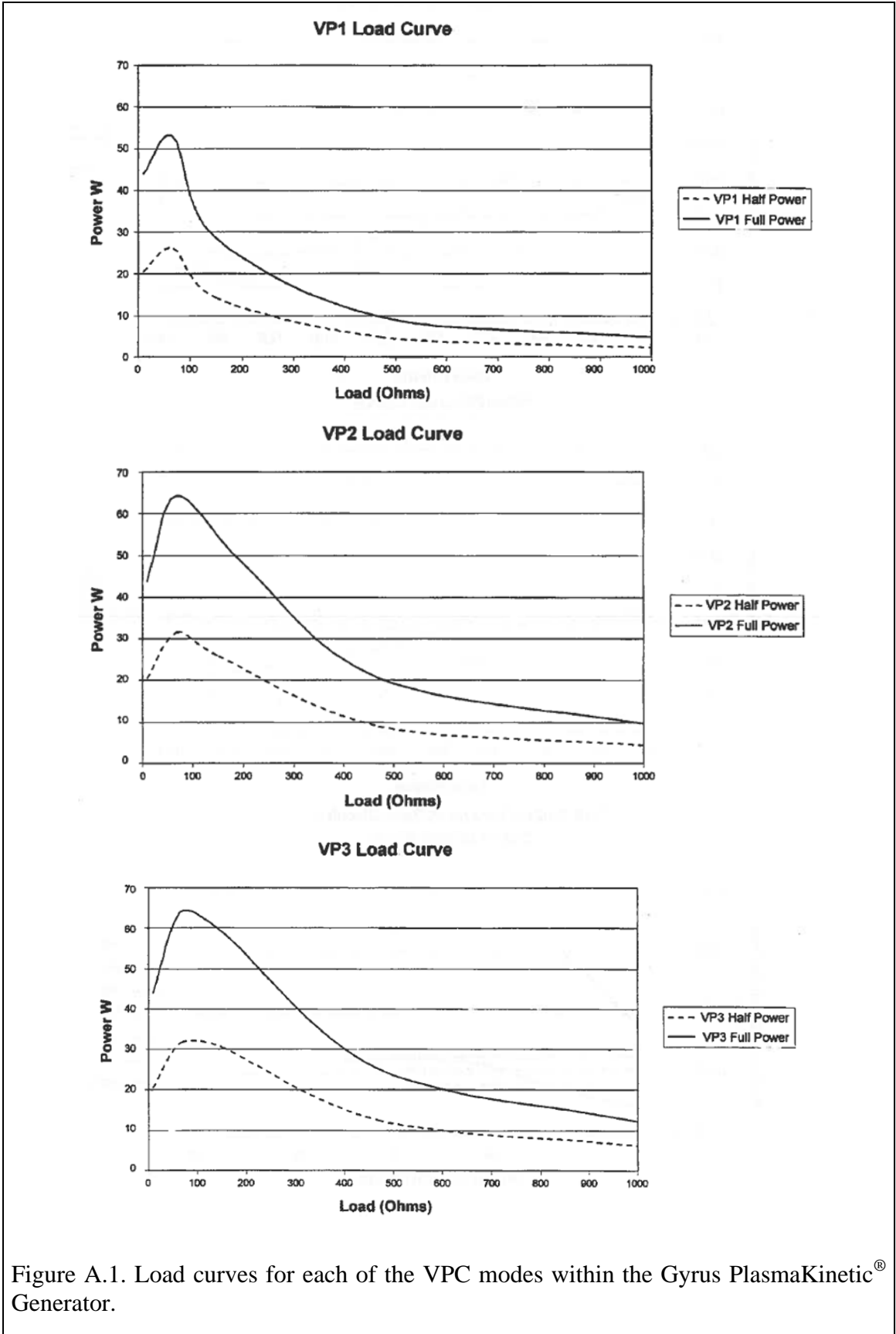


Figure A.1. Load curves for each of the VPC modes within the Gyrus PlasmaKinetic<sup>®</sup> Generator.

## Appendix B Cartesian and Polar Bioimpedance Representations

Due to its complex nature, electrical impedance data can be represented in a number of ways to help convey pertinent information. In general, impedance can be approximately modeled by combinations of resistive and reactive elements. The resultant complex impedance,  $Z^*$ , of any such network is presented by

$$A-1$$

where  $R$  is the real component of impedance,  $X$  is the reactive component, and [155].  $R$  and  $X$  are both measured in Ohms ( $\Omega$ ). Typically impedance data is plotted in the complex plane as shown in Figure B.(a) where the resistance is plotted on the x-axis and the reactance is plotted on the y-axis. Bioimpedance measurements typically show a capacitive reactance having a negative value. As it is standard to plot data in the upper right quadrant of a Cartesian plane, the negative reactance is typically plotted against the resistance.

Eq. A-1 is the Cartesian, or rectangular, representation of impedance. A polar form can also be defined with the modulus ( $|Z|$ ) and argument ( $\theta$ ) of the data written as

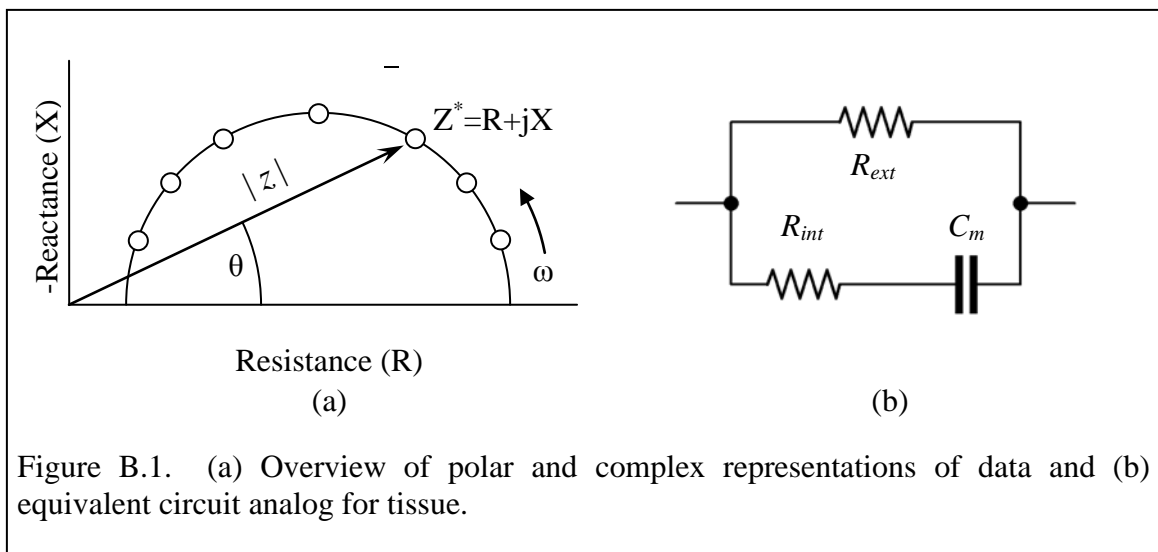
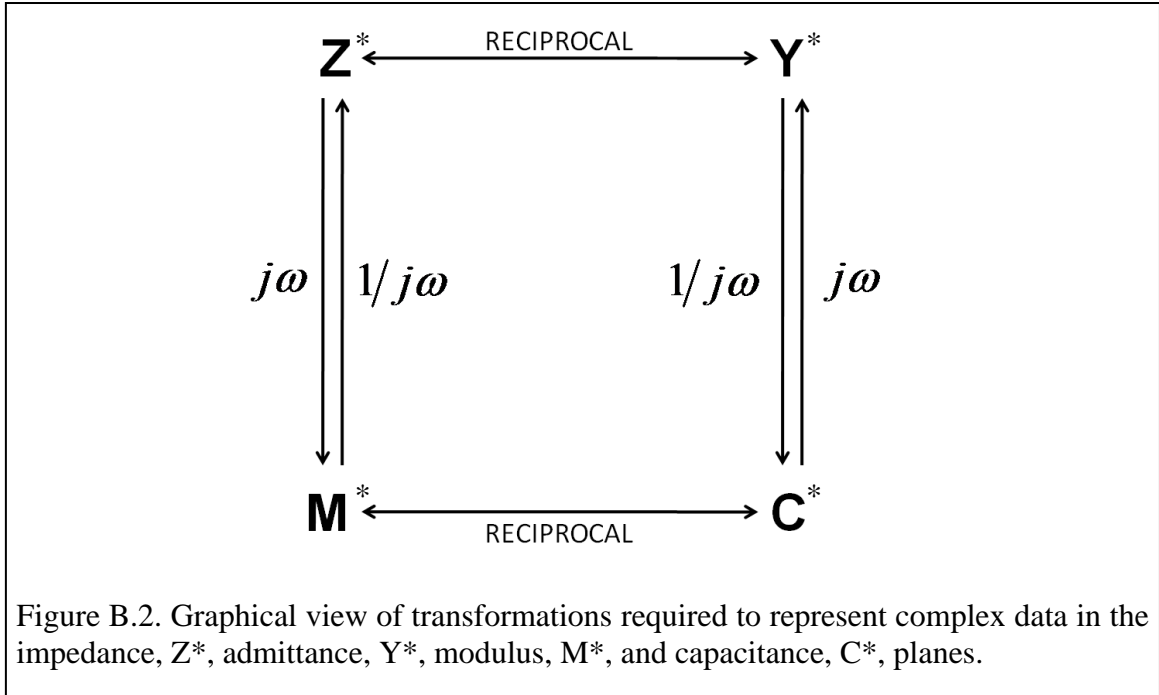


Figure B.1. (a) Overview of polar and complex representations of data and (b) equivalent circuit analog for tissue.



A-2

where  $|Z|$  has units of Ohms ( $\Omega$ ) and  $\theta$  has units of radians (rad) or degrees ( $^\circ$ ). The modulus and argument can be determined from the resistance and reactance using the following equations

$$\text{---} \tag{A-3}$$

$$\text{---} \tag{A-4}$$

Transformations of Cartesian impedance data result in other complex representations of the data. In total, four complex representations can be defined [156]. Taking the reciprocal of impedance ( $Z^*$ ) yields the admittance representation ( $Y^*$ ). Multiplying  $Z^*$  by  $j\omega$  yields the modulus representation ( $M^*$ ), where  $\omega$  is the angular frequency measured in rad/s. The inverse of  $M^*$  will yield the capacitance representation ( $C^*$ ). A graphical representation of these transformations is shown in Figure B..

The complex admittance ( $Y^*$ ), can be further defined as

A-5

where  $G$  is the conductance and  $B$  is the susceptance, both measured in Siemens ( $\Omega^{-1}$  or S). The susceptance can also be related to capacitance ( $C$ ), measured in F, through

A-6

A specific admittance ( $y^*$ ), measured in S/m, can be defined as [58]

A-7

where  $k$  is a geometric constant measured in  $m^{-1}$ ,  $\sigma_s$  is the static (DC) conductivity (S/m),  $\epsilon_s$  is the static permittivity, and  $\epsilon_0$  is the permittivity of free space ( $8.85 \times 10^{-12}$  F/m). Using Eqs. A-5 and A-7, the conductance and susceptance can be shown to be equal to [58]

— A-8

—— A-9

Other quantities of interest to bioimpedance are the complex conductivity ( $\sigma^*$ ) and complex permittivity ( $\epsilon^*$ ). The complex conductivity is defined as

A-10

where  $\sigma$  is the conductivity. It should be noted that the complex conductivity and specific admittance are identical terms. The complex permittivity ( $\epsilon^*$ ) is related to the complex conductivity through the relationship

A-11

For single relaxation time constant systems typical of biological tissue, plotting  $R$  against  $X$  in the impedance plane produces a semicircular arc as shown in Figure B.(a). This behavior can be represented by a parallel and series combination of resistances and capacitances of the form shown in Figure B.(b) [82]. A single time constant system can be written mathematically as

—— A-12

where  $R_\infty$  is the real axis intercept at high frequency,  $R_0$  is the real axis intercept at low frequency, and  $\tau$  is the time constant [156]. The frequency of the impedance data point at the apex of the loci can be determined through the equation

$$\text{---} \tag{A-13}$$

Rationalizing Eq. A-16 allows the impedance to be expressed in the form of Eq. A-1 yielding with the resistance and reactance values being equal to

$$\text{-----} \tag{A-14}$$

$$\text{-----} \tag{A-15}$$

$R_0$ ,  $R_\infty$ , and  $\tau$  can be used to determine the component values of the equivalent circuit analog shown in Figure B.(a) through the following equations

$$\tag{A-16}$$

$$\text{-----} \tag{A-17}$$

$$\tag{A-18}$$

It is important to note that the equivalent circuit representation cannot be derived solely on the basis of complex plane representations. Successful use of the equivalent circuit analogs greatly depends on the understanding of the morphology of the system of interest, especially at the cellular level [156].

## **Appendix C Bioimpedance Labview Program**

In order to automate the experimental procedure for compressing tissue while monitoring bioimpedance, a state-machine was developed in Labview<sup>®</sup> to efficiently move from each device within the experimental set-up and perform the needed operations.

A number of different pieces of hardware and sensors need to be controlled in order to efficiently perform bioimpedance monitoring of tissue under compression. Linear stages need to be controlled, a load cell and pressure sensor need to be monitored, a function generator needs to output a specified voltage and frequency, a DC power supply needs to power the bioimpedance measurement circuit only during operation, and an oscilloscope needs to receive and analyze voltage readings.

In addition, at some points in the experimental procedure it became important to monitor data from multiple devices simultaneously. As an example, during tissue compression, pressure readings and tissue thickness need to be monitored together in order to analyze the data during post-processing. The state-machine makes this process very efficient as both processes can be performed within a single ‘state’ of the program. When the data recording is completed, the program moves to a state to put the pressure sensor and linear stage into a wait state until they are needed again.

Six things are needed to efficiently implement a state machine within Labview and are identified. They are

- 1) While Loop
- 2) Case Structure
- 3) Shift registers
- 4) Cluster
- 5) Arrays
- 6) Enumerated Text Box

The while loop is used to keep the program in a wait state when it is not performing specific functions. A specific state, typically called the 'Wait' state, essentially waits for user input to perform a specific function. An additional 'Stop' state is used such that when the user chooses to stop the program all necessary steps to shut down the controlled hardware are initiated.

The case structure houses all of the states and describes how to transition in and out of them. Each function allowable to the user consists of several state sequences. Even though a certain state can be used by multiple functions, knowing which function was called allows for the state to properly direct the program to the next needed state. Once a function has been completed, the last state sends the user back to the 'Wait' state for the next command. Internal case structures within the primary case structure are used to make directional decisions as to which state to go to next based on data collected from the previous states.

Shift registers are essential for keeping track and organizing data as it is being collected. As each state is accomplished and data is collected, it is passed on to a database through the shift register to properly organize it. In addition, the shift register is used to pass data from one state to the next and is essential for the 'memory' of the program whereby the previous state (or multiple previous states) can be tracked. Knowing this information within a state allows for the state to properly direct the program to the next needed state for a given function.

Typically a cluster is used to store the program data as it is capable of housing multiple data types. Bundle by name and unbundle by name commands are used to call specific data from the cluster or write specific data to the cluster. In this program the cluster is shift registered so that it can continuously build a data array of experimental data.

Arrays are used to allow for the creation of expandable choices within the program. Within the 'Wait' state, an array of Booleans is continuously monitored by the program to determine when a certain function is called for by the user. The build array and search 1-D array commands are used to perform this monitoring.



An enumerated text box (ETB) is possibly the most critical component of the state machine. The ETB is used to house the names of each state accessible by the program. By setting the ETB definition to Strict Type the Enum can be automatically updated throughout the program wherever it is being used. This allows for additional states to be created and referenced without having to change every instance of the Enum within the program.

The block diagram (back panel) of the Labview program for the 'Wait' state is shown in Figure C.. Each of the state machine elements is shown highlighted by a rounded, transparent rectangle. Details for both the cluster and enumerated text box are also shown in Figure C.. The front panel of the program is shown in Figure C.. The user controls to initiate block diagram functions are shown as green toggle switches on the left hand side. These correspond to the array grouping in the block diagram in Figure C..

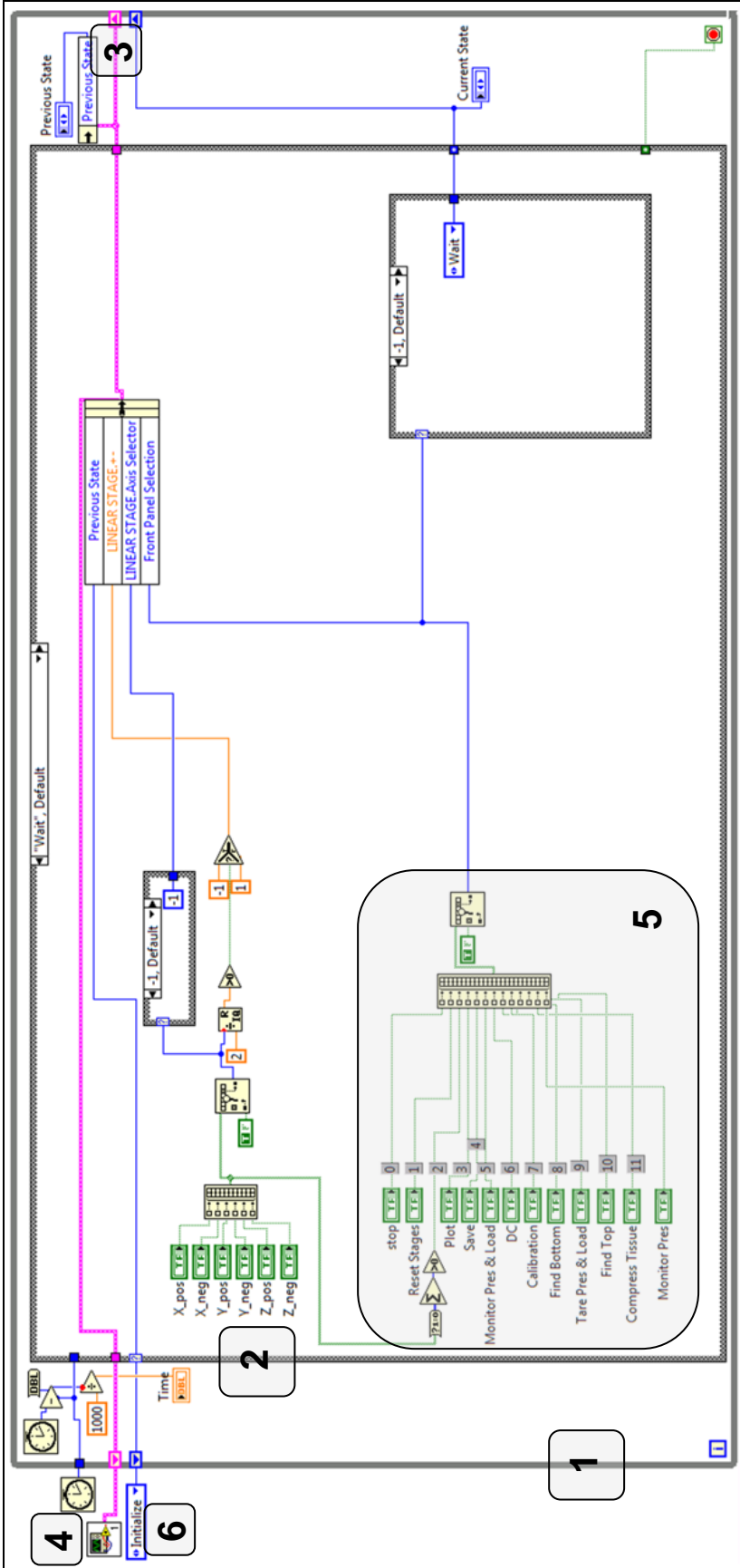


Figure C.1. Block diagram of the Labview program. The numbered rounded rectangles indicate (1) while loop, (2) case structure, (3) shift register, (4) cluster, (5) array, and (6) enumerated text box.

- "Initialize"
- ✓ "Wait", Default
- "Reset Stages"
- "Reset Z Axis"
- "Reset Y Axis"
- "Reset X Axis"
- "Jog Axis"
- "Update Position"
- "Plot Z Axis Position"
- "DC Power - Start"
- "DC Power - Monitor"
- "DC Power - Stop"
- "Data Test"
- "Load Start"
- "Load Monitor"
- "Load Pause"
- "Pres Monitor"
- "Pres Pause"
- "Pres & Load PowerUp"
- "Pres & Load Start"
- "Pres & Load Tare"
- "Pres & Load Monitor"
- "Pres & Load Graph"
- "Pres & Load Pause"
- "Configure Fx Gen"
- "Configure Sweep Parameters"
- "Perform Frequency Sweep"
- "Osci Measurement"
- "Osci Monitor Current"
- "Osci Plot Waveform"
- "Osci Configure Data"
- "Osci Save Image"
- "Plot Impedance Mag & Phase"
- "Plot Cole-Cole"
- "Save Data"
- "Stop"

The screenshot displays a software interface for tissue testing, organized into several functional panels:

- LINEAR STAGE:** Controls for Time, Z Position, Vector Space 2, Board ID, Velocity (c/s), Axis Selector, Vector Space, Axis Ratio, and Axes.
- DC POWER SUPPLY:** Controls for DC ID, voltage level 0, current limit 0, voltage level 1, current limit 1, Time, and Error.
- DAQ:** Controls for Load Task AI, Load Task AO, Pres Task AI, Pressure Task AO, Pres & Load Task AI, Load AO Channel, Load AI Channel, Pressure AO Channel, Pres AI Channel, Pres Tare, Load Tare, Time, Load, Pres, and Error.
- OSCILLOSCOPE:** Controls for Scope ID, Waveforms, Current Gain, Voltage Gain, Phase, Frequency, Time, Vrms, Irms, Tissue Thickness, Top of Tissue, Bottom Level, and Previous State.
- FX GEN:** Controls for Sweep #, Sweep\_i, Current Frequency, Sweep Frequencies, X array, Y Array, Initial Time, Compression, and Cycle.

At the bottom, the interface shows the File name: "Tissue Testing(Contact Impedance\2kOhm)" and the Main Folder: "F:\Documents\Tissue Machining\Impedance Analyzer Data\Constant Current Circuit\Tissue Testing\Saline Tests 2\".

(a)

Figure C.2. Detailed view of (a) the enumerated text box showing all of the states within the program and (b) the cluster containing all of the different data type variables used in the program.

(b)

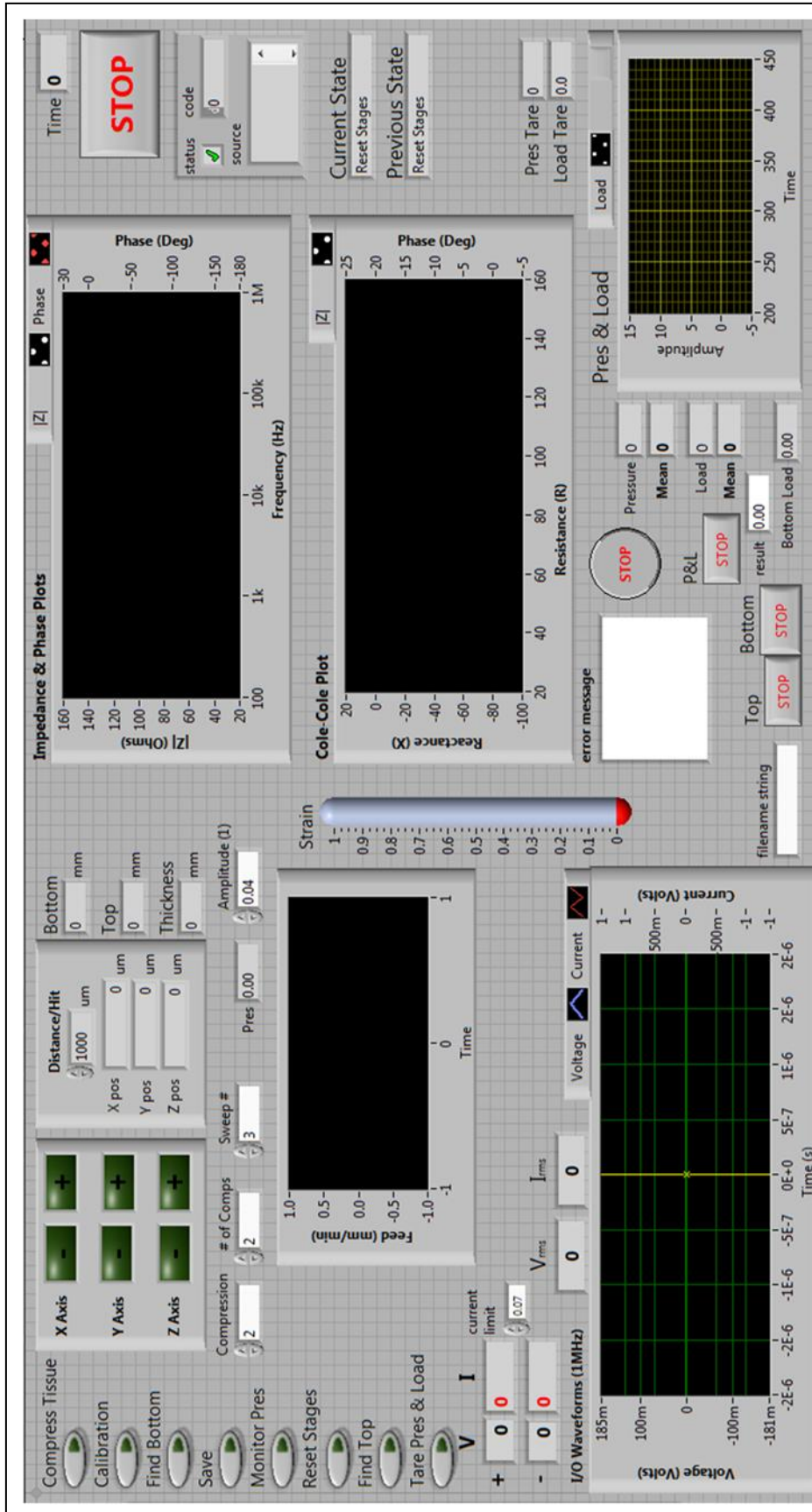


Figure C.3. Front panel of the bioimpedance Labview program.

## **Appendix D Bioimpedance Measurement Circuit Details**

The bioimpedance measurement circuitry was designed using Eagle 4.10 (CadSoft USA, Pembroke Pines, FL). The full schematic is shown in Figure D.. As opposed to the figures in Chapter 5, this figure shows power supply connections, DC bypass coupling capacitors, BNC coaxial cable connections, and voltage offset potentiometers all used to reduce noise in the circuit.

The board layout is shown in Figure D.(a) along with images of the top and bottom of the board in Figure D.(b). In the board layout blue markings correspond to bottom layer components and red markings correspond to top lay components. Green markings indicate through-hole components.

For the current to voltage converter subcircuit, an LM7171 IC chip was used. The front page of the LM7171 datasheet is shown in Figure . For the constant current source, an AMP03 IC chip was used for the modified Howland current pump. The front page of the AMP03 datasheet is shown in Figure . Two IC chips were used to allow for precise low currents and the elimination of DC bias current. The front page of the AD8065 datasheet is shown in Figure . The front page of the LM7171 datasheet is shown in Figure . The buffered voltage differentiator circuit is buffered by two AD711 IC chips in a voltage follower configuration. The front page of the AD711 datasheet is shown in Figure . The instrumentation amplifier used is the INA111. The front page of the INA111 datasheet is shown in Figure . An additional inverted gain is also applied to the output of the INA111 by an AD8065 IC chip. The front page of the AD8065 datasheet is shown in Figure .

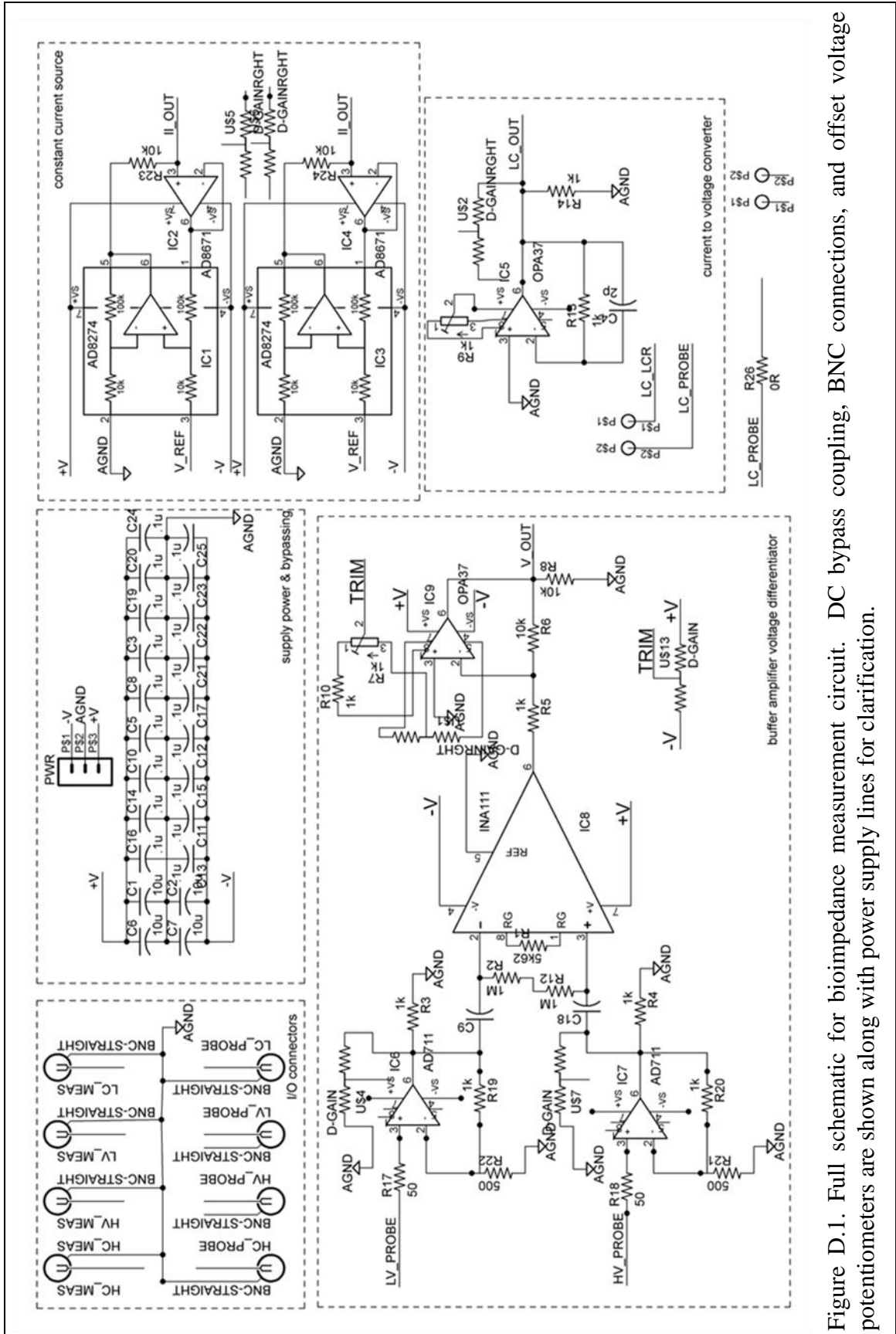


Figure D.1. Full schematic for bioimpedance measurement circuit. DC bypass coupling, BNC connections, and offset voltage potentiometers are shown along with power supply lines for clarification.

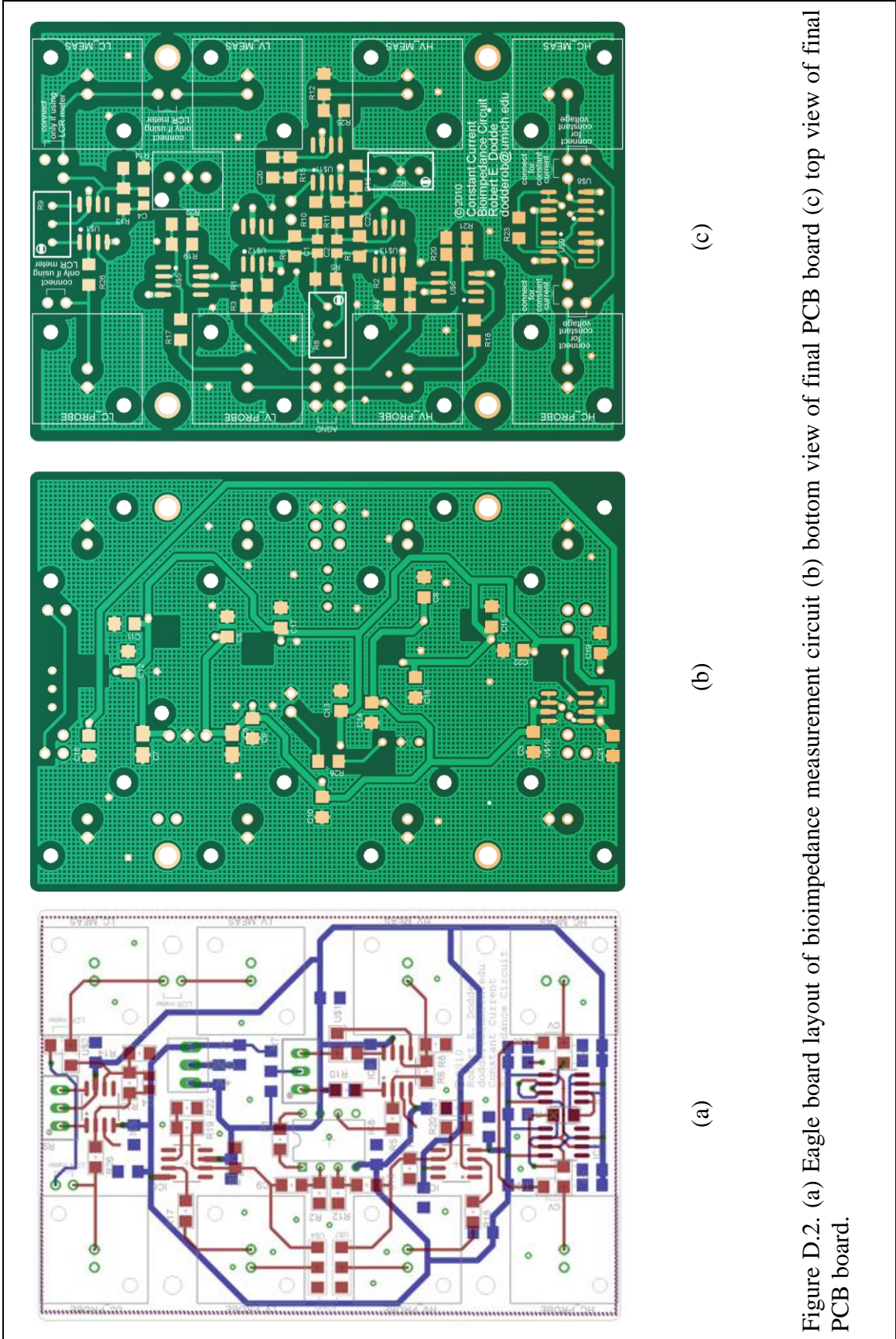


Figure D.2. (a) Eagle board layout of bioimpedance measurement circuit (b) bottom view of final PCB board (c) top view of final PCB board.

## AMP03

### FEATURES

- High CMRR: 100 dB Typ
- Low Nonlinearity: 0.001% Max
- Low Distortion: 0.001% Typ
- Wide Bandwidth: 3 MHz Typ
- Fast Slew Rate: 9.5 V/ $\mu$ s Typ
- Fast Settling (0.01%): 1  $\mu$ s Typ
- Low Cost

### APPLICATIONS

- Summing Amplifiers
- Instrumentation Amplifiers
- Balanced Line Receivers
- Current-Voltage Conversion
- Absolute Value Amplifier
- 4 to 20 mA Current Transmitter
- Precision Voltage Reference Applications
- Lower Cost and Higher Speed Version of INA105

### GENERAL DESCRIPTION

The AMP03 is a monolithic unity-gain, high speed differential amplifier. Incorporating a matched thin film resistor network, the AMP03 features stable operation over temperature without requiring expensive external matched components. The AMP03 is a basic analog building block for differential amplifier and instrumentation applications.

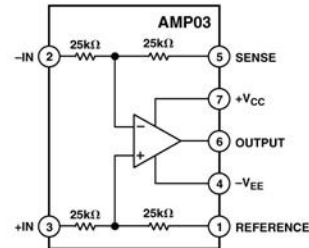
The differential amplifier topology of the AMP03 both amplifies the difference between two signals and provides extremely high rejection of the common-mode input voltage. By providing common-mode rejection (CMR) of 100 dB typical, the AMP03 solves common problems encountered in instrumentation design. As an example, the AMP03 is ideal for performing either addition or subtraction of two signals without using expensive externally matched precision resistors. The large common-mode rejection is made possible by matching the internal resistors to better than 0.002% and maintaining a thermally symmetric layout. Additionally, due to high CMR over frequency, the AMP03 is an ideal general amplifier for buffering signals in a noisy environment into data acquisition systems.

The AMP03 is a higher speed alternative to the INA105. Featuring slew rates of 9.5 V/ $\mu$ s and a bandwidth of 3 MHz, the AMP03 offers superior performance to the INA105 for high speed current sources, absolute value amplifiers, and summing amplifiers.

REV. F

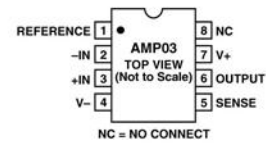
Information furnished by Analog Devices is believed to be accurate and reliable. However, no responsibility is assumed by Analog Devices for its use, nor for any infringements of patents or other rights of third parties that may result from its use. No license is granted by implication or otherwise under any patent or patent rights of Analog Devices. Trademarks and registered trademarks are the property of their respective owners.

### FUNCTIONAL BLOCK DIAGRAM

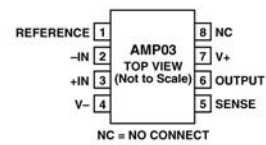


### PIN CONNECTIONS

#### 8-Lead PDIP (P Suffix)



#### 8-Lead SOIC (S Suffix)



#### Header (J Suffix)

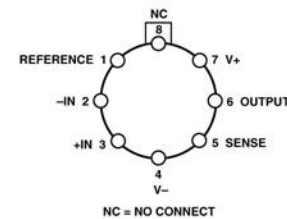


Figure D.3. AMP03 datasheet.



## AD711

### FEATURES

Enhanced Replacement for LF411 and TL081

#### AC PERFORMANCE

- Settles to  $\pm 0.01\%$  in  $1.0 \mu\text{s}$
- $16 \text{ V}/\mu\text{s}$  min Slew Rate (AD711J)
- $3 \text{ MHz}$  min Unity Gain Bandwidth (AD711J)

#### DC PERFORMANCE

- $0.25 \text{ mV}$  max Offset Voltage: (AD711C)
- $3 \mu\text{V}/^\circ\text{C}$  max Drift: (AD711C)
- $200 \text{ V}/\text{mV}$  min Open-Loop Gain (AD711K)
- $4 \mu\text{V}$  p-p max Noise,  $0.1 \text{ Hz}$  to  $10 \text{ Hz}$  (AD711C)
- Available in Plastic Mini-DIP, Plastic SOIC, Hermetic Cerdip, and Hermetic Metal Can Packages

#### MIL-STD-883B Parts Available

- Available in Tape and Reel in Accordance with EIA-481A Standard
- Surface Mount (SOIC)
- Dual Version: AD712

### PRODUCT DESCRIPTION

The AD711 is a high speed, precision monolithic operational amplifier offering high performance at very modest prices. Its very low offset voltage and offset voltage drift are the results of advanced laser wafer trimming technology. These performance benefits allow the user to easily upgrade existing designs that use older precision BiFETs and, in many cases, bipolar op amps.

The superior ac and dc performance of this op amp makes it suitable for active filter applications. With a slew rate of  $16 \text{ V}/\mu\text{s}$  and a settling time of  $1 \mu\text{s}$  to  $\pm 0.01\%$ , the AD711 is ideal as a buffer for 12-bit D/A and A/D Converters and as a high-speed integrator. The settling time is unmatched by any similar IC amplifier.

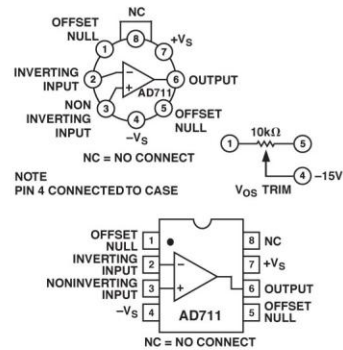
The combination of excellent noise performance and low input current also make the AD711 useful for photo diode preamps. Common-mode rejection of  $88 \text{ dB}$  and open loop gain of  $400 \text{ V}/\text{mV}$  ensure 12-bit performance even in high-speed unity gain buffer circuits.

The AD711 is pinned out in a standard op amp configuration and is available in seven performance grades. The AD711J and AD711K are rated over the commercial temperature range of  $0^\circ\text{C}$  to  $70^\circ\text{C}$ . The AD711A, AD711B and AD711C are rated over the industrial temperature range of  $-40^\circ\text{C}$  to  $+85^\circ\text{C}$ . The AD711S and AD711T are rated over the military temperature range of  $-40^\circ\text{C}$  to  $+125^\circ\text{C}$  and are available processed to MIL-STD-883B, REV. E.

### REV. E

Information furnished by Analog Devices is believed to be accurate and reliable. However, no responsibility is assumed by Analog Devices for its use, nor for any infringements of patents or other rights of third parties that may result from its use. No license is granted by implication or otherwise under any patent or patent rights of Analog Devices.

### CONNECTION DIAGRAMS



Extended reliability PLUS screening is available, specified over the commercial and industrial temperature ranges. PLUS screening includes 168 hour burn-in, as well as other environmental and physical tests.

The AD711 is available in an 8-pin plastic mini-DIP, small outline, cerdip, TO-99 metal can, or in chip form.

### PRODUCT HIGHLIGHTS

1. The AD711 offers excellent overall performance at very competitive prices.
2. Analog Devices' advanced processing technology and 100% testing guarantee a low input offset voltage ( $0.25 \text{ mV}$  max, C grade,  $2 \text{ mV}$  max, J grade). Input offset voltage is specified in the warmed-up condition. Analog Devices' laser wafer drift trimming process reduces input offset voltage drifts to  $3 \mu\text{V}/^\circ\text{C}$  max on the AD711C.
3. Along with precision dc performance, the AD711 offers excellent dynamic response. It settles to  $\pm 0.01\%$  in  $1 \mu\text{s}$  and has a 100% tested minimum slew rate of  $16 \text{ V}/\mu\text{s}$ . Thus this device is ideal for applications such as DAC and ADC buffers which require a combination of superior ac and dc performance.
4. The AD711 has a guaranteed and tested maximum voltage noise of  $4 \mu\text{V}$  p-p,  $0.1$  to  $10 \text{ Hz}$  (AD711C).
5. Analog Devices' well-matched, ion-implanted JFETs ensure a guaranteed input bias current (at either input) of  $25 \text{ pA}$  max (AD711C) and an input offset current of  $10 \text{ pA}$  max (AD711C). Both input bias current and input offset current are guaranteed in the warmed-up condition.

One Technology Way, P.O. Box 9106, Norwood, MA 02062-9106, U.S.A.  
Tel: 781/329-4700 [www.analog.com](http://www.analog.com)  
Fax: 781/326-8703 © Analog Devices, Inc., 2002

Figure D.4. AD711 datasheet.

### FEATURES

- Qualified for automotive applications
- FET input amplifier
- 1 pA input bias current
- Low cost
- High speed: 145 MHz, -3 dB bandwidth (G = +1)
- 180 V/ $\mu$ s slew rate (G = +2)
- Low noise
  - 7 nV/ $\sqrt{\text{Hz}}$  (f = 10 kHz)
  - 0.6 fA/ $\sqrt{\text{Hz}}$  (f = 10 kHz)
- Wide supply voltage range: 5 V to 24 V
- Single-supply and rail-to-rail output
- Low offset voltage 1.5 mV maximum
- High common-mode rejection ratio: -100 dB
- Excellent distortion specifications
- SFDR -88 dBc @ 1 MHz
- Low power: 6.4 mA/amplifier typical supply current
- No phase reversal
- Small packaging: SOIC-8, SOT-23-5, and MSOP-8

### GENERAL DESCRIPTION

The AD8065/AD8066<sup>1</sup> FastFET™ amplifiers are voltage feedback amplifiers with FET inputs offering high performance and ease of use. The AD8065 is a single amplifier, and the AD8066 is a dual amplifier. These amplifiers are developed in the Analog Devices, Inc. proprietary XFCB process and allow exceptionally low noise operation (7.0 nV/ $\sqrt{\text{Hz}}$  and 0.6 fA/ $\sqrt{\text{Hz}}$ ) as well as very high input impedance.

With a wide supply voltage range from 5 V to 24 V, the ability to operate on single supplies, and a bandwidth of 145 MHz, the AD8065/AD8066 are designed to work in a variety of applications. For added versatility, the amplifiers also contain rail-to-rail outputs.

Despite the low cost, the amplifiers provide excellent overall performance. The differential gain and phase errors of 0.02% and 0.02°, respectively, along with 0.1 dB flatness out to 7 MHz, make these amplifiers ideal for video applications. Additionally, they offer a high slew rate of 180 V/ $\mu$ s, excellent distortion (SFDR of -88 dBc @ 1 MHz), extremely high common-mode rejection of -100 dB, and a low input offset voltage of 1.5 mV maximum under warmed up conditions. The AD8065/AD8066 operate using only a 6.4 mA/amplifier typical supply current and are capable of delivering up to 30 mA of load current.

<sup>1</sup> Protected by U. S. Patent No. 6,262,633.

#### Rev. J

Information furnished by Analog Devices is believed to be accurate and reliable. However, no responsibility is assumed by Analog Devices for its use, nor for any infringements of patents or other rights of third parties that may result from its use. Specifications subject to change without notice. No license is granted by implication or otherwise under any patent or patent rights of Analog Devices. Trademarks and registered trademarks are the property of their respective owners.

### APPLICATIONS

- Automotive driver assistance systems
- Photodiode preamps
- Filters
- A/D drivers
- Level shifting
- Buffering

### CONNECTION DIAGRAMS

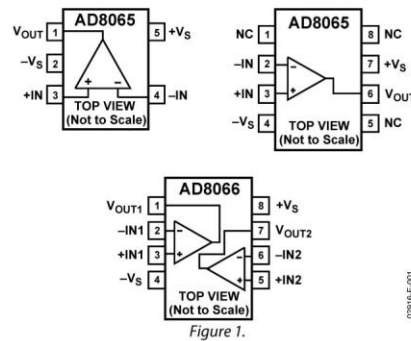


Figure 1.

The AD8065/AD8066 are high performance, high speed, FET input amplifiers available in small packages: SOIC-8, MSOP-8, and SOT-23-5. They are rated to work over the industrial temperature range of -40°C to +85°C.

The AD8065WARTZ-REEL7 is fully qualified for automotive applications. It is rated to operate over the extended temperature range (-40°C to +105°C), up to a maximum supply voltage range of  $\pm 5$ V only.

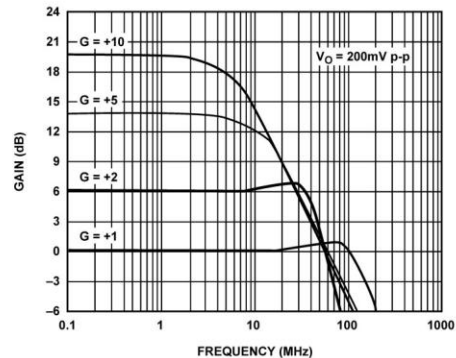


Figure 2. Small Signal Frequency Response



INA111

## High Speed FET-Input INSTRUMENTATION AMPLIFIER

### FEATURES

- FET INPUT:  $I_B = 20\text{pA max}$
- HIGH SPEED:  $T_s = 4\mu\text{s}$  ( $G = 100, 0.01\%$ )
- LOW OFFSET VOLTAGE:  $500\mu\text{V max}$
- LOW OFFSET VOLTAGE DRIFT:  $5\mu\text{V}/^\circ\text{C max}$
- HIGH COMMON-MODE REJECTION:  $106\text{dB min}$
- 8-PIN PLASTIC DIP, SOL-16 SOIC

### APPLICATIONS

- MEDICAL INSTRUMENTATION
- DATA ACQUISITION

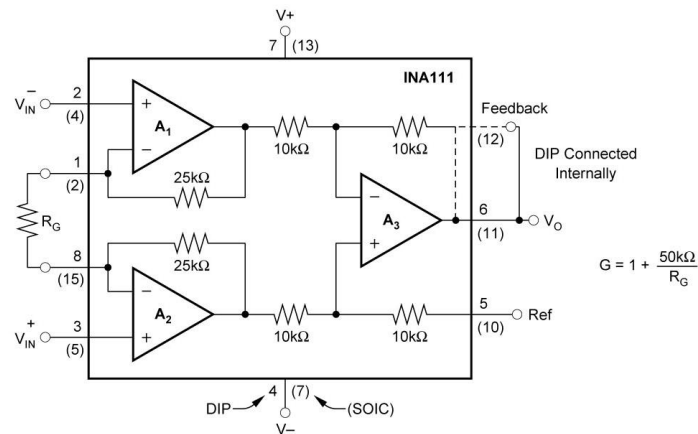
### DESCRIPTION

The INA111 is a high speed, FET-input instrumentation amplifier offering excellent performance.

The INA111 uses a current-feedback topology providing extended bandwidth (2MHz at  $G = 10$ ) and fast settling time ( $4\mu\text{s}$  to 0.01% at  $G = 100$ ). A single external resistor sets any gain from 1 to over 1000.

Offset voltage and drift are laser trimmed for excellent DC accuracy. The INA111's FET inputs reduce input bias current to under 20pA, simplifying input filtering and limiting circuitry.

The INA111 is available in 8-pin plastic DIP, and SOL-16 surface-mount packages, specified for the  $-40^\circ\text{C}$  to  $+85^\circ\text{C}$  temperature range.



International Airport Industrial Park • Mailing Address: PO Box 11400, Tucson, AZ 85734 • Street Address: 6730 S. Tucson Blvd., Tucson, AZ 85706 • Tel: (520) 746-1111 • Twx: 910-952-1111  
 Internet: <http://www.burr-brown.com/> • FAXLine: (800) 548-6133 (US/Canada Only) • Cable: BBRCORP • Telex: 066-6491 • FAX: (520) 889-1510 • Immediate Product Info: (800) 548-6132

Figure D.6. INA111 datasheet.

## LM7171

# Very High Speed, High Output Current, Voltage Feedback Amplifier

### General Description

The LM7171 is a high speed voltage feedback amplifier that has the slewing characteristic of a current feedback amplifier; yet it can be used in all traditional voltage feedback amplifier configurations. The LM7171 is stable for gains as low as +2 or -1. It provides a very high slew rate at 4100V/ $\mu$ s and a wide unity-gain bandwidth of 200 MHz while consuming only 6.5 mA of supply current. It is ideal for video and high speed signal processing applications such as HDSL and pulse amplifiers. With 100 mA output current, the LM7171 can be used for video distribution, as a transformer driver or as a laser diode driver.

Operation on  $\pm 15V$  power supplies allows for large signal swings and provides greater dynamic range and signal-to-noise ratio. The LM7171 offers low SFDR and THD, ideal for ADC/DAC systems. In addition, the LM7171 is specified for  $\pm 5V$  operation for portable applications.

The LM7171 is built on National's advanced VIP™ III (Vertically integrated PNP) complementary bipolar process.

### Features

(Typical Unless Otherwise Noted)

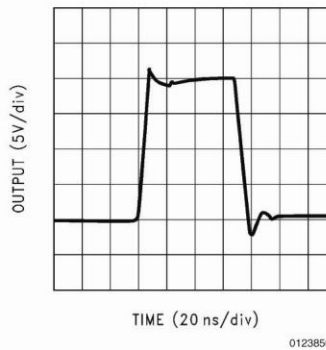
- Easy-to-use voltage feedback topology
- Very high slew rate: 4100 V/ $\mu$ s
- Wide unity-gain bandwidth: 200 MHz
- -3 dB frequency @  $A_v = +2$ : 220 MHz
- Low supply current: 6.5 mA
- High open loop gain: 85 dB
- High output current: 100 mA
- Differential gain and phase: 0.01%, 0.02°
- Specified for  $\pm 15V$  and  $\pm 5V$  operation

### Applications

- HDSL and ADSL drivers
- Multimedia broadcast systems
- Professional video cameras
- Video amplifiers
- Copiers/scanners/fax
- HDTV amplifiers
- Pulse amplifiers and peak detectors
- CATV/fiber optics signal processing

### Typical Performance

Large Signal Pulse Response  
 $A_v = +2$ ,  $V_S = \pm 15V$



VIP™ is a trademark of National Semiconductor Corporation.

## References

1. Lantis II JC. *Comparison of coagulation modalities in surgery*. Journal of Laparoendoscopic & Advanced Surgical Techniques. 1998;8(6):381.
2. Jiaquan X. *Deaths: Final Data for 2007*. National Vital Statistics Reports. 2010;58(19):135.
3. Brown JS, Sawaya G, Thom DH, Grady D. *Hysterectomy and urinary incontinence: a systematic review*. The Lancet. 2000;356(9229):535-9.
4. Walsh PC, Marschke P, Ricker D, Burnett AL. *Patient-reported urinary continence and sexual function after anatomic radical prostatectomy*. Urology. 2000;55(1):58-61.
5. Catalona WJ, Carvalhal GF, Mager DE, Smith DS. *Potency, continence and complication rates in 1,870 consecutive radical retropubic prostatectomies*. The Journal of Urology. 1999;162(2):433-8.
6. Su LM, Link RE, Bhayani SB, Sullivan W, Pavlovich CP. *Nerve-sparing laparoscopic radical prostatectomy: replicating the open surgical technique*. Urology. 2004;64(1):123-7.
7. Ong AM, Su L-M, Varkarakis I, Inagaki T, Link RE, Bhayani SB, et al. *Nerve sparing radical prostatectomy: effects of hemostatic energy sources on the recovery of cavernous nerve function in a canine model*. The Journal of Urology. 2004;172(4):1318-22.
8. Khan F, Rodriguez E, Finley DS, Skarecky DW, Ahlering TE. *Spread of thermal energy and heat sinks: implications for nerve-sparing robotic prostatectomy*. Journal of Endourology. 2007;21(10):1195.
9. Eggleston JL, Von Maltzahn WW. *Electrosurgical Devices*. In: Bronzino JD, editor. *The Biomedical Engineering Handbook*. 2<sup>nd</sup> Ed. ed. Boca Raton, FL: CRC Press; 2000.
10. Pearce JA. *Electrosurgery*. New York: Wiley; 1986.
11. O'Connor JL. *William T. Bovie and electrosurgery*. Surgery. 1996;119(4):390-6.
12. Greenwood J, Jr. *Two point coagulation: a follow-up report of a new technic and instrument for electrocoagulation in neurosurgery*. Archives of Physical Therapy. 1942;23(9):552-4.

13. Landman J, Kerbl K, Rehman J, Andreoni C, Humphrey PA, Collyer W, et al. *Evaluation of a vessel sealing system, bipolar electrocoagulation, harmonic scalpel, titanium clips, endoscopic gastrointestinal anastomosis vascular staples and sutures for arterial and venous ligation in a porcine model.* The Journal of Urology. 2003;169(2):697-700.
14. Owaki T, Nakano S, Arimura K, Aikou T. *The ultrasonic coagulating and cutting system injures nerve function.* Endoscopy. 2002;34(7):575-9.
15. Carbonell AM, Joels CS, Kercher KW, Matthews BD, Sing RF, Heniford BT. *A comparison of laparoscopic bipolar vessel sealing devices in the hemostasis of small-, medium-, and large-sized arteries.* Journal of Laparoendoscopic & Advanced Surgical Techniques. 2003;13(6):377-80.
16. Harold KL, Kercher KW, Sing RF, Pollinger H, Matthews BD, Heniford BT. *Comparison of ultrasonic energy, bipolar thermal energy, and vascular clips for the hemostasis of small-, medium-, and large-sized arteries.* Surgical Endoscopy. 2003;17(8):1228-30.
17. Campbell PA, Cresswell AB, Frank TG, Cuschieri A. *Real-time thermography during energized vessel sealing and dissection.* Surgical Endoscopy. 2003;17(10):1640-45.
18. Berjano EJ. *Theoretical modeling for radiofrequency ablation: state-of-the-art and challenges for the future.* BioMedical Engineering OnLine. 2006;5(24).
19. Berjano EJ, Hornero F. *A cooled intraesophageal balloon to prevent thermal injury during endocardial surgical radiofrequency ablation of the left atrium: a finite element study.* Physics in Medicine and Biology. 2005;50(20):N269-79.
20. Tungjitkusolmun S, Tsai JZ, Mahvi DM, Webster JG, Staelin ST, Haemmerich D, et al. *Three-Dimensional finite-element analyses for radio-frequency hepatic tumor ablation.* IEEE Transactions on Biomedical Engineering. 2002;49(1):3-9.
21. Panescu D, Mirotznik MS, Swanson DK, Wayne JG, Fleischman SD, Webster JG. *Three-dimensional finite element analysis of current density and temperature distributions during radio-frequency ablation.* IEEE Transactions on Biomedical Engineering. 1995;42(9):879-90.
22. Pearce JA. *Numerical models of bipolar electrode electrocoagulation current fields.* Proceedings of the 16th Annual International Conference of the IEEE Engineering in Medicine and Biology. 1994;16(2):794-5.
23. Sims C. *Histologic characteristics of laparoscopic saline-enhanced electrocoagulation of liver and splenic injuries.* Surgical Endoscopy. 2003;17(11):1739.
24. Takao T. *Effect of cautery with irrigation forceps on the remnant liver after hepatectomy in rats.* European Surgical Research. 1999;31(2):173.

25. Rampini PM. *Low-cost self-irrigating bipolar forceps*. Journal of Neurosurgical Sciences. 1997;41(3):313.
26. Dujovny M. *Bipolar jeweler's forceps with automatic irrigation, for coagulation in microsurgery*. Plastic and Reconstructive Surgery. 1975;56(5):585.
27. Gnerlich JL. *Saline-linked surface radiofrequency ablation: a safe and effective method of surface ablation of hepatic metastatic colorectal cancer*. Annals of Surgery. 2009;250(1):96.
28. Donzelli J, Leonetti JP, Bergstrom R, Wurster RD, Young MR. *Thermoprotective mechanisms of irrigation during bipolar cautery*. Archives of Otolaryngology - Head & Neck Surgery. 1998;119(3):153.
29. Zorn K. *Use Of Enseal<sup>®</sup> During Robotic Prostatectomy Pedicle Control: Cold Irrigation To Minimize Lateral Thermal Injury*. Journal of Endourology. 2009;23:A301-A.
30. Zorn KC. *Application of Ice Cold Irrigation During Vascular Pedicle Control of Robot-Assisted Radical Prostatectomy: EnSeal Instrument Cooling to Reduce Collateral Thermal Tissue Damage*. Journal of Endourology. 2010;24.
31. Sha D, Connolly R, Schwaitzberg S, Levine A. *The development of non-sticking, passively cooled electrosurgical instruments*. In: Enderle JD, Macfarlane LL, editors. *Proceedings of the IEEE 27th Annual Northeast Bioengineering Conference 2001*. p. 11-2.
32. Elliott-Lewis EW. *Evaluation of a new bipolar coagulation forceps in a thermal damage assessment*. Neurosurgery. 2009;65(6):1182-7.
33. Gerhard GC, Elliott WR, Selikowitz SM. *A programmable variable waveshape generator for electrosurgical research*. Medical Instrumentation. 1986;20(3):150-5.
34. Smaldone MC. *Laparoscopic nephrectomy using the EnSeal Tissue Seating and Hemostasis System: Successful therapeutic application of nanotechnology*. Journal of the Society of Laparoendoscopic Surgeons. 2008;12(2):213-6.
35. Geddes LA, Baker LE, Moore AG, Coulter TW. *Hazards in the use of low frequencies for the measurement of physiological events by impedance*. Medical and Biological Engineering. 1969;7(3):289-96.
36. McAdams ET. *Tissue impedance: a historical overview*. Physiological Measurement. 1995;16(3):A1.
37. Kohlrausch F. *Ueber platinirte Electroden und Widerstandsbestimmung*. Annalen der Physik. 1897;296(2):315-32.

38. Bouty E. *Sur la conductibilité électrique des dissolutions salines très étendues*. Journal de Physique. 1884;3(1):325-55.
39. Schwan HP. *Electrode polarization impedance and measurements in biological materials*. Annals of the New York Academy of Sciences. 1968;148(1):191.
40. Mirtaheri P. *Electrode polarization impedance in weak NaCl aqueous solutions*. IEEE Transactions on Biomedical Engineering. 2005;52(12):2093.
41. Onaral B, Schwan H. *Linear and nonlinear properties of platinum electrode polarisation. Part 1: frequency dependence at very low frequencies*. Medical and Biological Engineering and Computing. 1982;20(3):299-306.
42. Jaron D. *Nonlinearity of cardiac pacemaker electrodes*. IEEE Transactions on Biomedical Engineering. 1969;16(2):132.
43. Philippon M. *Les lois de la résistance électrique des tissus vivants*. Institut Royal des Sciences Naturelles de Belgique Memoires. 1921;7:387-403.
44. Fricke H. *A mathematical treatment of the electrical conductivity of colloids and cell suspensions*. The Journal of General Physiology. 1924;6(4):375.
45. McClendon JF. *Colloidal properties of the surface of the living cell. I. Conductivity of blood to direct electric currents*. Journal of Biological Chemistry. 1926;68(3):653-63.
46. McClendon JF. *Colloidal properties of the surface of the living cell. II. Electric conductivity and capacity of blood to alternating currents of long duration and varying in frequency from 260 to 2,000,000 cycles per second*. Journal of Biological Chemistry. 1926;69(2):733-54.
47. Cole KS. *Electric impedance of suspensions of spheres*. The Journal of General Physiology. 1928;12(1):29.
48. Cole KS. *Electric phase angle of cell membranes*. The Journal of General Physiology. 1932;15(6):641-9.
49. Cole KS. *Electrical conductance of biological systems*. Cold Spring Harbor Symposia on Quantitative Biology. 1933;1:107-16.
50. Maxwell JC. *A treatise on electricity and magnetism*. Oxford: Clarendon press; 1873.
51. Fricke H. *The electric capacity of suspensions with special reference to blood*. The Journal of General Physiology. 1925;9(2):137.
52. Fricke H. *The electric resistance and capacity of blood for frequencies between 800 and 4(1/2) million cycles*. The Journal of General Physiology. 1925;9(2):153.



53. Carter CW. *Graphic representation of the impedance of networks containing resistances and two reactances*. Bell System Technical Journal. 1925;4:387-401.
54. Cole KS. *Membranes, ions, and impulses: a chapter of classical biophysics*. Berkeley: University of California Press; 1968.
55. Cole KS, Cole RH. *Dispersion and absorption in dielectrics I. Alternating current characteristics*. Journal of Chemical Physics. 1941;9(4):341-51.
56. Cole KS, Cole RH. *Dispersion and absorption in dielectrics II. Direct current characteristics*. Journal of Chemical Physics. 1942;10(2):98-105.
57. Cole KS. *Permeability and impermeability of cell membranes for ions*. Cold Spring Harbor Symposia on Quantitative Biology. 1940;8:110-22.
58. Polk C, Postow E. *Handbook of Biological Effects of Electromagnetic Fields*. Boca Raton, FL: CRC Press; 1996.
59. Jaffrin MY, Morel H. *Body fluid volumes measurements by impedance: A review of bioimpedance spectroscopy (BIS) and bioimpedance analysis (BIA) methods*. Medical Engineering and Physics. 2008;30(10):1257-69.
60. Jaffrin MY. *Body composition determination by bioimpedance: an update*. Current Opinion in Clinical Nutrition and Metabolic Care. 2009;12(5):482-6.
61. Kotanko P. *Current state of bioimpedance technologies in dialysis*. Nephrology Dialysis Transplantation. 2008;23(3):808.
62. Zhu F. *Extracellular fluid redistribution during hemodialysis: bioimpedance measurement and model*. Physiological Measurement. 2008;29(6):S491.
63. Bayford RH. *Bioimpedance tomography (electrical impedance tomography)*. Annual Review of Biomedical Engineering. 2006;8:63.
64. Mudry KM, Plonsey R, Bronzino JD. *Biomedical imaging*. Boca Raton, Fla.: CRC Press; 2003.
65. Cherepenin VA. *Three-dimensional EIT imaging of breast tissues: system design and clinical testing*. IEEE Transactions on Medical Imaging. 2002;21(6):662.
66. Bagshaw AP. *Electrical impedance tomography of human brain function using reconstruction algorithms based on the finite element method*. NeuroImage. 2003;20(2):752.
67. Fung YC. *Biomechanics: mechanical properties of living tissues*. New York: Springer-Verlag; 1993.

68. Humphrey JD. *Continuum biomechanics of soft biological tissues*. Proceedings of The Royal Society A. 2003;459(2029):3-46.
69. Toms SR. *Quasi-linear viscoelastic behavior of the human periodontal ligament*. Journal of Biomechanics. 2002;35(10):1411.
70. Pioletti DP. *On the independence of time and strain effects in the stress relaxation of ligaments and tendons*. Journal of Biomechanics. 2000;33(12):1729.
71. Abramowitch SD. *An improved method to analyze the stress relaxation of ligaments following a finite ramp time based on the quasi-linear viscoelastic theory*. Journal of Biomechanical Engineering. 2004;126(1):92.
72. Miller K. *Constitutive modelling of abdominal organs*. Journal of Biomechanics. 2000;33(3):367-73.
73. Kim J. *Characterization of viscoelastic soft tissue properties from in vivo animal experiments and inverse FE parameter estimation*. Medical Image Computing and Computer Assisted Intervention. 2005;8(2):599.
74. Yang W. *Viscoelasticity of esophageal tissue and application of a QLV model*. Journal of Biomechanical Engineering. 2006;128(6):909.
75. Gao Z. *Constitutive Modeling of Liver Tissue: Experiment and Theory*. Annals of Biomedical Engineering. 2010;38(2):505-16.
76. Kohandel M. *Estimation of the quasi-linear viscoelastic parameters using a genetic algorithm*. Mathematical and Computer Modelling. 2008;47(3-4):266-70.
77. Madjidi Y, Shirinzadeh B, Banirazi R, Tian YL, Smith J, Zhong YM. *An improved approach to estimate soft tissue parameters using genetic algorithm for minimally invasive measurement*. In: Shi R, Fu WJ, Wang YQ, Wang HB, editors. *Proceedings of the 2009 2<sup>nd</sup> International Conference on Biomedical Engineering and Informatics, Vols 1-42009*. p. 781-6.
78. Kim J. *An efficient soft tissue characterization algorithm from in vivo indentation experiments for medical simulation*. The International Journal of Medical Robotics and Computer Assisted Surgery. 2008;4(3):277.
79. Mow VC, Kuei SC, Lai WM, Armstrong CG. *Biphasic creep and stress relaxation of articular cartilage in compression - Theory and Experiments*. Journal of Biomechanical Engineering. 1980;102(1):73-84.
80. Ateshian GA, Mow VC, Lai WM, Zhu WB. *An asymptotic solution for the contact of two biphasic cartilage layers*. Journal of Biomechanics. 1994;27(11):1347-60.

81. Ateshian GA, Grelsamer RP, Mow VC, Warden WH, Kim JJ. *Finite deformation biphasic material properties of bovine articular cartilage from confined compression experiments*. Journal of Biomechanics. 1998;30(11-12):1157-64.
82. Grimnes S, Martinsen OG. *Bioimpedance and bioelectricity basics*. London: Academic; 2008.
83. Dodde RE, Shih AJ, Advincula AP. *A novel technique for demonstrating the real-time subsurface tissue thermal profile of two energized surgical instruments*. The Journal of Minimally Invasive Gynecology. 2009;16(5):599-603.
84. Wang K, Advincula AP. *"Current thoughts" in electrosurgery*. International Journal of Gynecology & Obstetrics. 2007;97(3):245-50.
85. Dodde RE, Miller SF, Geiger JD, Shih AJ. *Thermal-Electric Finite Element Analysis and Experimental Validation of Bipolar Electrosurgical Cautery*. Journal of Manufacturing Science and Engineering. 2008;130(2):021015-1--8.
86. Pearce JA, Magnusen TA, editors. *Numerical models of bipolar electrode electrosurgical current fields*. Engineering in Medicine and Biology Society, 1994 Engineering Advances: New Opportunities for Biomedical Engineers Proceedings of the 16th Annual International Conference of the IEEE; 1994.
87. Pennes HH. *Analysis of Tissue and Arterial Blood Temperatures in the Resting Human Forearm*. Journal of Applied Physiology. 1948;1(2):93-122.
88. Chen MM, Holmes KR. *Microvascular contributions in tissue heat transfer*. Annals of the New York Academy of Sciences. 1980;335:137-50.
89. Chato JC. *Heat transfer to blood vessels*. Journal of Biomechanical Engineering. 1980;102(2):110-8.
90. Weinbaum S, Jiji LM, Lemons DE. *Theory and experiment for the effect of vascular microstructure on surface tissue heat transfer--Part I: Anatomical foundation and model conceptualization*. Journal of Biomechanical Engineering. 1984;106(4):321-30.
91. Arkin H, Xu LX, Holmes KR. *Recent developments in modeling heat transfer in blood perfused tissues*. IEEE Transactions on Biomedical Engineering. 1994;41(2):97-107.
92. Haines DE, Watson DD. *Tissue heating during radiofrequency catheter ablation: a thermodynamic model and observations in isolated perfused and superfused canine right ventricular free wall*. Pacing and Clinical Electrophysiology. 1989;12(6):962-76.

93. Tungjitkusolmun S, Eung Je W, Hong C, Jang-Zern T, Vorperian VR, Webster JG. *Finite element analyses of uniform current density electrodes for radio-frequency cardiac ablation*. IEEE Transactions on Biomedical Engineering. 2000;47(1):32-40.
94. Gabriel C, Gabriel S, Corthout E. *The dielectric properties of biological tissues: I. Literature survey*. Physics in Medicine and Biology. 1996;41(11):2231-49.
95. Oh SH, Lee SY, Seo JK, Kim T-S, Lee BI, Woo EJ, et al. *Electrical conductivity images of biological tissue phantoms in MREIT*. Physiological Measurement. 2005;26(2):S279-88.
96. Valvano JW, Cochran JR, Diller KR. *Thermal conductivity and diffusivity of biomaterials measured with self-heated thermistors*. International Journal of Thermophysics. 1985;6(3):301-11.
97. Schwan HP, Foster KR. *RF-field interactions with biological systems: Electrical properties and biophysical mechanisms*. Proceedings of the IEEE. 1980;68(1):104-13.
98. Schenk O, Gartner K. *Solving unsymmetric sparse systems of linear equations with PARDISO*. Future Generation Computer Systems. 2004;20(3):475-87.
99. Muntinga JH, Visser KR. *Estimation of blood pressure-related parameters by electrical impedance measurement*. Journal of Applied Physiology. 1992;73(5):1946-57.
100. González-Correa CA, Kalia N, Haggie SJ, Stoddard CJ, Brown BH, Smallwood RH, et al. *Virtual biopsies in Barrett's esophagus using an impedance probe*. Annals of the New York Academy of Sciences. 1999;873(Apr):313-21.
101. Richter S, Pistorius GA, Menger MD, Kollmar O, Schilling MK. *Efficacy and quality of vessel sealing: comparison of a reusable with a disposable device and effects of clamp surface geometry and structure*. Surgical Endoscopy. 2006;20(6):890-4.
102. Sutton PA. *Comparison of lateral thermal spread using monopolar and bipolar diathermy, the Harmonic Scalpel and the Ligasure*. British Journal of Surgery. 2010;97(3):428-33.
103. Lamberton GR. *Prospective comparison of four laparoscopic vessel ligation devices*. Journal of Endourology. 2008;22(10):2307-12.
104. Altman D, Granath F, Cnattingius S, Falconer C. *Hysterectomy and risk of stress-urinary-incontinence surgery: nationwide cohort study*. The Lancet. 2007;370(9597):1494-9.
105. Geddes LA. *The decrease in transthoracic impedance during successive ventricular defibrillation trials*. Medical Instrumentation. 1975;9(4):179-80.

106. King MJ. *A four terminal instrumentation system for the measurement of complex bioelectric impedance*. Milwaukee: Marquette University; 1978.
107. Yelamos D, Casas Ó, BragoS R, Rosell J. *Improvement of a Front End for Bioimpedance Spectroscopy*. *Annals of the New York Academy of Sciences*. 1999;873(1):306-12.
108. Gersing E. *Measuring electrical impedance of organs - instrumental equipment for research and clinical use*. *Biomedizinische Technik*. 1991;36(1-2):6.
109. Zagar T. *An instrumentation amplifier as a front-end for a four-electrode bioimpedance measurement*. *Physiological Measurement*. 2007;28(8):N57-N65.
110. Torrents JM, Pallas-Areny R. *Compensation of impedance meters when using an external front-end amplifier*. *IEEE Transactions on Instrumentation and Measurement*. 2002;51(2):310-3.
111. Yuxiang Y, Jue W, editors. *New Tetrapolar Method for Complex Bioimpedance Measurement: Theoretical Analysis and Circuit Realization*. *27th Annual International Conference of the Engineering in Medicine and Biology Society*; 2005 17-18 Jan. 2006.
112. Tong In O, et al. *Multi-frequency EIT system with radially symmetric architecture: KHU MarkI*. *Physiological Measurement*. 2007;28(7):S183.
113. Ragheb AO. *Tetrapolar electrode system for measuring physiological events by impedance*. *Medical and Biological Engineering and Computing*. 1992;30(1):115.
114. Pallás-Areny R. *Bioelectric impedance measurements using synchronous sampling*. *IEEE Transactions on Biomedical Engineering*. 1993;40(8):824-9.
115. McEwan A, et al. *Design and calibration of a compact multi-frequency EIT system for acute stroke imaging*. *Physiological Measurement*. 2006;27(5):S199.
116. Gary JS, et al. *A high-precision voltage source for EIT*. *Physiological Measurement*. 2006;27(5):S221.
117. Tsai JZ. *Dependence of apparent resistance of four-electrode probes on insertion depth*. *IEEE Transactions on Biomedical Engineering*. 2000;47(1):41-8.
118. Birkett A. *Bipolar current source maintains high output impedance at high frequencies*. *Electronic Design News*. 2005:128-30.
119. Cook RD, Saulnier GJ, Gisser DG, Goble JC, Newell JC, Isaacson D. *ACT3: a high-speed, high-precision electrical impedance tomograph*. *IEEE Transactions on Biomedical Engineering*. 1994;41(8):713-22.

120. Dössel O, Schlegel WC, Ar-Rawi AH, Moghavvemi M, Wan-Ibrahim WMA. *Wide Band Frequency Fixed Current Source for BIT and BIA*. In: Magjarevic R, editor. *2009 World Congress on Medical Physics and Biomedical Engineering*: Springer Berlin Heidelberg; 2009. p. 522-4.
121. Hongwei H, et al. *Comparison of a new integrated current source with the modified Howland circuit for EIT applications*. *Physiological Measurement*. 2009;30(10):999.
122. McCann MR-NaH. *Low-noise current excitation sub-system for medical EIT*. *Physiological Measurement*. 2008;29(6):S173.
123. Qureshi TR, et al. *Comparison of Howland and General Impedance Converter (GIC) circuit based current sources for bio-impedance measurements*. *Journal of Physics: Conference Series*. 2010;224:012167.
124. Ross AS. *Current source design for electrical impedance tomography*. *Physiological Measurement*. 2003;24(2):509.
125. Devices A. *High Precision, Low Cost Current Sources Using the AD8276 Difference Amplifier and the AD8603 Op Amp*. Circuit Note [serial on the Internet]. 2009; (CN-0099): Available from: [http://www.analog.com/static/imported-files/circuit\\_notes/CN0099.pdf](http://www.analog.com/static/imported-files/circuit_notes/CN0099.pdf).
126. Ackmann JJ. *Complex bioelectric impedance measurement system for the frequency range from 5 Hz to 1 MHz*. *Annals of Biomedical Engineering*. 1993;21(2):135-46.
127. Geddes LA. *The rectification properties of an electrode-electrolyte interface operated at high sinusoidal current density*. *IEEE Transactions on Biomedical Engineering*. 1987;34(9):669.
128. Coughlin RF, Driscoll FF. *Operational amplifiers and linear integrated circuits*. Englewood Cliffs, N.J.: Prentice-Hall; 1982.
129. Wojslaw CF, Moustakas EA. *Operational amplifiers: the devices and their applications*. New York: Wiley; 1986.
130. Clayton GB. *Operational amplifiers*. London ; Boston: Newnes-Butterworths; 1979.
131. Schwan HP. *Four-electrode null techniques for impedance measurement with high resolution*. *Review of Scientific Instruments*. 1968;39(4):481-5.
132. Kitchin C, Counts L. *A Designer's Guide To Instrumentation Amplifiers*. 3 ed: Analog Devices; 2006.
133. Gabriel C. *The dielectric properties of biological tissues: I. Literature survey*. *Physics in Medicine and Biology*. 1996;41(11):2231-49

134. Geddes LA. *Electrodes and the measurement of bioelectric events*. New York: Wiley-Interscience; 1972.
135. Jakosky JJ. *Exploration geophysics*. Newport Beach, Calif.: Trija Pub. Co.; 1961.
136. Littwitz C, Ragheb T, Geddes L. *Cell constant of the tetrapolar conductivity cell*. Medical and Biological Engineering and Computing. 1990;28(6):587-90.
137. Stogryn A. *Equations For Calculating The Dielectric Constant Of Saline Water*. IEEE Transactions on Microwave Theory and Techniques. 1971;19(8):733-6.
138. Bolton MP. *Sources of error in bioimpedance spectroscopy*. Physiological Measurement. 1998;19(2):235.
139. Mirtaheri P. *Designing a PtCO<sub>2</sub> sensor based on conductivity measurements*. 13<sup>th</sup> International Conference on Electrical Bioimpedance and 8<sup>th</sup> Conference on Electrical Impedance Tomography. 2007;17:300-3.
140. Scharfetter H. *A model of artefacts produced by stray capacitance during whole body or segmental bioimpedance spectroscopy*. Physiological Measurement. 1998;19(2):247.
141. Buendía R. *A novel approach for removing the hook effect artefact from electrical bioimpedance spectroscopy measurements*. Journal of Physics: Conference Series. 2010;224(1):012126.
142. Buendía R. *Experimental validation of a method for removing the capacitive leakage artifact from electrical bioimpedance spectroscopy measurements*. Measurement Science and Technology. 2010;21(11).
143. Bohren CF. *What did Kramers and Kronig do and how did they do it?* European Journal of Physics. 2010;31(3):573-7.
144. Gorter CJ. *On the theory of absorption and dispersion in paramagnetic and dielectric media*. Physica. 1936;3:1009-20.
145. Kronig RDL. *On the theory of dispersion of X-rays*. Journal Optical Society of America Review of Scientific Instruments. 1926;12(6):547-58.
146. Schwan HP, Foster KR. *RF-Field Interactions with Biological Systems: Electrical Properties and Biophysical Mechanisms*. Proceedings of the IEEE. 1980;68(1):104-13.
147. González-Correa CA. *Electrical bioimpedance readings increase with higher pressure applied to the measuring probe*. Physiological Measurement. 2005;26(2):S39.

148. Keshtkar A. *The effect of applied pressure on the electrical impedance of the bladder tissue using small and large probes*. Journal of Medical Engineering and Technology. 2008;32(6):505-11.
149. Kottam A. *Electric field penetration depth of myocardial surface catheters and the measurement of myocardial resistivity*. Biomedical Sciences Instrumentation. 2004;449:155-60.
150. Steendijk P, Baan J, Mur G, Van Der Velde ET. *The four-electrode resistivity technique in anisotropic media: theoretical analysis and application on myocardial tissue in vivo*. IEEE Transactions on Biomedical Engineering. 1993;40(11):1138-48.
151. Dodde RE, Shih A, Geiger J, Roberts W, Pipe K, Advincula A, inventors; The Regents of the University of Michigan, assignee. *Surgical instrument and method for use thereof*. United States of America patent 7815641. 2010.
152. Grimnes S, Martinsen OG. *Bioimpedance & Bioelectricity Basics*. San Diego: Academic Press; 2000.
153. Schwan HP. *Determination of Biological Impedances*. PhysTech in Biol Res 6. New York: Academic Press; 1963.
154. Gyrus PlasmaKinetic® Surgical Generator User Manual. Gyrus PlasmaKinetic® System. Maple Grove, MN: Gyrus Medical Inc.; 2004.
155. Smith GA. *Analysis of the current pathways associated with multifrequency impedance measurements of the lung*. Milwaukee: Marquette University; 1982.
156. Ackmann JJ, Seitz MA. *Methods of complex impedance measurements in biologic tissue*. Critical Reviews in Biomedical Engineering. 1984;11(4):281-311.